Play Fairway Analysis of the Snake River Plain, Idaho: Final Report

DE-EE0006733

John W. Shervais, Principal Investigator
Award Recipient: Utah State University

John W. Shervais [0000-0003-4370-7500]
James P. Evans [0000-0002-2181-3866], Dennis L. Newell [0000-0001-9628-739X]
Department of Geology, Utah State University, 4505 Old Main Hill, Logan, UT 84322-4505

Jonathan M. Glen [0000-0002-3502-3355], Drew Siler [0000-0001-7540-8244],
Jacob DeAngelo [0000-0002-7348-7839], Jared Peacock [0000-0002-0439-0224]
US Geological Survey, 350 N Akron Rd, Moffett Field, CA 94035

Patrick Dobson [0000-0001-5031-8592], Erika Gasperikova [0000-0003-1553-4569],
Eric Sonnenthal [0000-0003-2987-3481]
Lawrence Berkeley National Laboratory, 1 Cyclotron Road, Berkeley CA 94720

Lee M. Liberty [0000-0003-2793-8173]
Center for Geophysical Investigation of the Shallow Subsurface, Boise State University, Boise, ID 83725

Dennis L. Nielson
DOSECC Exploration Services, LLC., 2075 Pioneer Rd., Suite B, Salt Lake City, UT 84104

Sabodh Garg
Geologica Geothermal Group, Inc, 9920 Pacific Heights Blvd, Suite 150, San Diego, CA 92121

Ghanashyam Neupane [0000-0003-4492-6203]
Idaho National Laboratory, Idaho Falls, ID 83415

Charles Visser, Neil Snyder
National Renewable Energy Laboratory, 15013 Denver West Parkway, Golden, CO 80401

William Schermerhorn [0000-0002-0167-378X], Tait Earney [0000-0002-1504-0457], Brent Ritzinger [0000-0002-5379-1390]
US Geological Survey, 350 N Akron Rd, Moffett Field, CA 94035

Keywords: Snake River Plain, Geothermal Exploration, Play Fairway Analysis, GIS

Acknowledgment: This material is based upon work supported by the Department of Energy, Office of Energy Efficiency and Renewable Energy (EERE), Geothermal Technologies Office, under Award Number DE-EE0006733.

Disclaimer: This report was prepared as an account of work sponsored by an agency of the United States Government. Neither the United States Government nor any agency thereof, nor any of their employees, makes any warranty, express or implied, or assumes any legal liability or responsibility for the accuracy, completeness, or usefulness of any information, apparatus, product, or process disclosed, or represents that its use would not infringe privately owned rights. Reference herein to any specific commercial product, process, or service by trade name, trademark, manufacturer, or otherwise does not necessarily constitute or imply its endorsement, recommendation, or favoring by the United States Government or any agency thereof. The views and opinions of authors expressed herein do not necessarily state or reflect those of the United States Government or any agency thereof.

Table of Contents

Acronyms list

2D	Two-dimensional
3D	Three-dimensional
ArcGIS	Integrated collection of GIS software products from ESRI
AFB	Air Force Base
BSU	Boise State University
GIS	Geographic Information System
CCRS	Composite Common Risk Segment
COM	Craters of the Moon
CRS	Common Risk Segment
CSRP	Central Snake River Plain
DEM	Digital Elevation Map
EGS	Enhanced/Engineered Geothermal System
EM	Electromagnetics
ESRP	Eastern Snake River Plain
GPS	Global Positioning System
IDW	Inverse Distance Weighting
IDWR	Idaho Water Resources
IGS	Idaho Geological Survey
INL	Idaho National Laboratory
LBNL	Lawrence Berkeley National Laboratory
LIDAR	Light Detection And Ranging (remote sensing technology)
LoK	Level of Knowledge
MH	Mountain Home
MT	Magnetotellurics
NGDS	National Geothermal Data System
NREL	National Renewable Energy Laboratory
PoS	Probability of Success
QFFDB	USGS Quaternary Fault Database
RBF	Radial Basis Function
SMU	Southern Methodist University
SROT	Snake River Olivine Tholeiite
SRP	Snake River Plain
SRRA	Snake River Regional Aquifer
USGS	United States Geological Survey
USU	Utah State University
WSRP	Western Snake River Plain

Snake River Plain Play Fairway Analysis: EE0006733
Executive Summary

OVERVIEW

The Snake River Plain (SRP) volcanic province overlies a thermal anomaly that extends deep into the mantle; it represents one of the highest heat flow provinces in North America. The Yellowstone hotspot continues to feed a magma system that underlies much of southern Idaho and has produced basaltic volcanism as young as 2000 years old. It has been estimated to host up to 855 MW of potential geothermal power production, most of which is associated with the Snake River Plain volcanic province in Idaho, which lies outside the area of Yellowstone National Park (*Neely, K.W. and Galinato, G., 2007, Geothermal power generation in Idaho: an overview of current developments and future potential, Open File Report, Idaho Office of Energy Resources*).

Our goals for this study were to: (1) adapt the methodology of Play Fairway Analysis for geothermal exploration to create a formal basis for its application to geothermal systems, (2) assemble relevant data for the SRP from publicly available and private sources, and (3) build a geothermal play fairway model for the SRP and identify the most promising plays using tools developed within readily-available Geographic Information System software. Our ultimate goals are to lower the risk and cost of geothermal exploration throughout the geothermal industry, and to stimulate the development of new geothermal power resources in Idaho.

The success of play fairway analysis in geothermal exploration depends critically on defining a systematic methodology that is grounded in theory (as developed within the petroleum industry over at least three decades) and incorporates the key factors (e.g., heat source, permeability, and seal) that form the geologic and hydrologic framework of distinct classes of geothermal systems (i.e., play types). This project has contributed to the success of this approach by cataloging the critical parameters of exploitable hydrothermal systems and establishing risk matrices that evaluate these parameters in terms of both *probability of success* and *level of knowledge*. These matrices were used as guidelines to construct an approach using ArcGIS (an industry and governmental standard for geographic analysis) that allowed us to compile a range of different data types, with distinct characteristics and confidence values, and to process them in a consistent and systematic fashion across the entire study area.

Most of the study area is underlain by a basaltic volcanic province that overlies a mid-crustal intrusive complex, which in turn provides the long-term heat flux needed to sustain a geothermal system. This geologic combination represents a new conceptual model for geothermal systems that includes aspects of volcano-hosted, and structurally controlled Basin-and-Range systems. Basin-and-Range systems underlie part of the study area; rhyolite domes and granite batholith systems are also present but were not evaluated quantitatively in this study.

This study was carried out in three formal phases: **Phase 1**: data compilation and evaluation (October 2014-October 2015); **Phase 2**: new data collection in focus areas in the central and western SRP (November 2015-September 2017); **Phase 3**: new data collection and drilling of a validation slim hole in Camas Prairie (October 2017-June 2020).

PHASE 1

The first task during Phase 1 was to adapt Play Fairway Analysis to geothermal systems. This was done by building a series of conceptual models for geothermal systems in general and for SRP-related geothermal systems in particular. These efforts focused on three critical parameters for exploitable hydrothermal systems: *Heat, Permeability,* and *Seal*. Data used for the assessment of *Heat* were heat flow, the distribution of volcanic vents, groundwater temperatures, thermal springs and wells, helium isotope anomalies, and reservoir temperatures calculated from water chemistry. Data used for the assessment of *Permeability* were stress orientation, mapped post-Miocene faults and lineaments derived from horizontal gradients in magnetics, deep gravity, and mid-crustal gravity. Data used for the assessment of *Seal* included the distribution of impermeable lake sediments and clay-seal developed by hydrothermal alteration below the regional aquifer.

Phase 1 studies were restricted to data compilation and evaluation. Data resources compiled and analyzed included published and unpublished geologic maps (largely USGS and Idaho Geological Survey), heat flow from the USGS, Southern Methodist University (SMU), and the National Geothermal Data System, water data from the Idaho Department of Water Resources, the USGS Quaternary fault database, the Idaho Geological Survey's post-Miocene fault database, and USGS potential field (gravity, magnetics) data. Data on water chemistry and calculated reservoir temperatures was shared by other DOE-funded research groups (e.g., Cannon et al., 2014; Dobson et al., 2015). The decision was made to compile and analyze these data using a Geographic Information System (GIS) in order to evaluate large quantities of disparate data types efficiently and objectively (DeAngelo et al., 2016).

GIS Methodology

Raw data were compiled into an ArcGIS database with multiple *data layers* for each parameter. These *data layers* were processed using either density functions or interpolations to produce *evidence layers*. Because different data types have different uncertainties associated with their collection, each *evidence layer* has its own *confidence layer*, which reflects geographic variations in these uncertainties. *Risk maps* represent the product of *evidence* and *confidence layers* and are the basic building blocks used to construct *Common Risk Segment (CRS)* maps for *Heat, Permeability*, and *Seal*. In a final step, these three maps were combined into a *Composite Common Risk Segment (CCRS)* map for analysis.

Processing raw data layers into evidence layers involved either density functions to calculate the density of distribution of an attribute (e.g., volcanic vent or fault segment) or interpolation, to calculate a continuous surface from point data (e.g., heat flow, groundwater temperatures). Density functions are used for data that are by nature discontinuous, and where the geographic location of that data is important. Interpolation is used for properties that are by nature continuous, but which can only be sampled at specific points. Our method for interpolation was *Empirical Bayesian Kriging*, a geostatistical process that produces an estimate of the value of a property at each point and a standard error surface that quantifies the uncertainty.

Python scripts were used in ArcGIS to automate data processing and to enhance the flexibility of the data analysis. These Python scripts are repeatable, scalable, modifiable, transferrable, and when complete, will automate the task of data analysis and the production of CRS and CCRS maps. Our ultimate goal is to produce a toolkit that can be imported into ArcGIS and applied to any geothermal play, with fully tunable parameters that will allow for the production of multiple versions of the CRS and CCRS maps in order to test for sensitivity and to validate results.

Phase 1 Results

Our Phase 1 assessment suggests that important undiscovered geothermal resources are located in several areas of the SRP (Shervais et al., 2016). Our Phase 1 results identify eight areas with multiple prospects, each of which may contain resources that equal or exceed the 10 MW Raft River geothermal plant in Basin-and-Range province in southeastern Idaho. Four of these areas are in the Western Snake River Plain (WSRP) and include blind systems (*i.e.,* those with no observed surface expression); two are in the Central Snake River Plain (CSRP), and two are Basin-and-Range play types in eastern and southeastern Idaho. One site in the WSRP (on Mountain Home Air Force Base) has a confirmed resource that is at least 10-12 km long, parallel to a buried fault system (*Nielson et al, 2018*). Our identified prospects exhibit higher favorability on *CRS* and *CCRS* maps than either of our training sites, and have regional extents that generally exceed both of our training sites. These data strongly support the conclusion that commercial resources exceeding 100 MW are present in southern Idaho, most of them blind systems in southwest Idaho. The Camas Prairie site was chosen as the second site despite its expected low temperatures (~110ºC) because it met several other criteria needed to satisfy Phase 2 objectives – not the least of which was that the expected depth to the target reservoir was relatively shallow (~600 m) and thus attainable within the expected budget constraints.

PHASE 2

Phase 2 work focused on new data collection in three of the areas identified during Phase 1: the regions around Mountain Home Air Force Base and the Bostic 1A well, and Camas Prairie. These data included new geophysical surveys (magnetotelluric, active source seismic reflection, potential field gravity and magnetic), geologic field campaigns (mapping and radiometric dating

of volcanic vents, whole rock geochemical analyses of volcanic rocks, structural mapping of faults and lineaments), and hydrologic studies (distribution of hot springs, water chemistry and isotopic composition, He isotope studies). Phase 2 also included thermal modeling using data compiled during Phase 1 and an updated play model concept.

Thermal Modeling and Updated Conceptual Model

Based on data acquired during Phase 1, our conceptual model for SRP-type geothermal systems was updated and published. Thermal modeling to test this conceptual model was carried at LBNL using the software program TOUGHREACT V3.3, and a natural state model was developed for the Mountain Home area using Leidos' STAR geothermal reservoir simulator (Garg et al., 2016; Nielson et al., 2017). Both models supported the updated conceptual model, which was used to finalize focus area selection.

Geophysical Studies

Gravity and magnetic field campaigns were carried out in all regions by the U.S. Geological Survey (USGS) Geothermal Division (Menlo Park, California). The USGS collected data at 1659 gravity stations and over 725 line-km of ground magnetic data for this project. They also collected hundreds of rock-property measurements on outcrops and samples to constrain potential field modeling and integrated ground water well logs into our analyses. Seismic reflection surveys were carried out by the Center for Geophysical Investigation of the Shallow Subsurface (CGISS), Boise State University. CGISS collected ~56 km of seismic data along five roads in Camas Prairie. 3D magnetotelluric (MT) surveys were carried out around Mountain Home Air Force Base (AFB) and in Camas Prairie, with 96 station installations.

Field Studies

Field studies included detailed geologic mapping in Camas Prairie, and the collection of basalt samples from Camas Prairie and the Mountain Home area for ^{39}Ar-^{40}Ar dating of the volcanic vents. Basalt samples were also analyzed for major and trace element composition by X-ray fluorescence (XRF) spectrometry. Geologic mapping focused on fault traces, orientations, and slip directions as indicated by slickenlines on shear surfaces.

Water Chemistry

Natural springs and well waters were sampled throughout the region and analyzed for major and trace element composition. These data were then used to calculate equilibrium reservoir temperatures using multicomponent geothermometry. Samples were also taken for H, He, and O isotope analysis.

Phase 2 Results

Focused geologic, geochemical, and geophysical studies were conducted to refine previous PFA assessments of selected areas within the Western SRP (Shervais et al., 2017). Geophysical studies around Mountain Home and Bostic included gravity, magnetic, and magnetotelluric surveys (Glen et al., 2017). The gravity and magnetic data were used to define subsurface lineaments (interpreted as faults) that were digitized and added to the permeability evidence layers. This was critical as almost no faults are exposed on the surface, except near the margins of the plain where range front faulting has affected basalt flows. These data also define a basement high that trends ~275º -- slightly oblique to the ~300º trend of the western SRP and its range front fault system. Inversion of 3D MT data reveal a conductive layer (seal) that correlates with the Quaternary to Pliocene lacustrine sediments and thins to the NE.

Geophysical studies in the Camas Prairie region define a complex basin structure with three sub-basins, EW-trending range front faults (which extend north of the southern range front), NE-trending faults (in the western half of the prairie) and NW-trending faults (in the eastern half of the prairie). These latter two systems are separated by The Pothole fault system, which offsets a volcanic crater dated at 692 ka (see below). The Pothole fault system localizes a number of hot springs along its extent. Inversion of 3D MT data reveal a conductive layer (seal) that is restricted to areas with known current or former hot springs, suggesting an alteration-derived clay cap. Seismic reflect lines were run only in Camas Prairie. They provide high resolution data on fault locations and dips, and confirm interpretations based on gravity data.

Volcanologic field studies were carried out to document the location and age of volcanic vents in both areas. Location data were added to existing maps to produce a comprehensive catalogue of vent locations. Radiometric ^{39}Ar-^{40}Ar dating of basalts document a range of ages, from 4.54 Ma in the lower part of the MH-2 drill core, to 2 ka in the mountains north of Mountain Home, and NW of Camas Prairie. Young (< 1 Ma) high-K basalts are common in the western SRP around Mountain Home and are interpreted to represent the heat source for the most recent geothermal systems. Field studies documented structural complexities in the Camas Prairie area, with two dominant fault sets (WNW and ENE). Fault striations are most commonly dextral-normal. These orientations are more or less consistent with the attitudes of the major features at depth in the Camas basin, as interpreted from the geophysical studies described above. Our new water chemistry for Camas Prairie and the Mount Bennett Hills show that cooler groundwater and spring samples are Ca-HCO_3-type waters, whereas hot spring and thermal well samples are Na-HCO_3-type waters. A mixing trend is observed between Ca-HCO_3 and Na-HCO_3 water types.

PHASE 3

During Phase 3 we completed collection of data begun during Phase 2 and selected a site in Camas Prairie to drill a validation well up to 2000 feet deep. This validation well (USU Camas-1) was drilled along a fault system associated with hot spring activity that separates two distinct structural domains and offsets Pleistocene volcanic features. This well was drilled in two separate field campaigns (2018, 2019) that included collection of cuttings, core, and water samples. The well was logged using geophysical logging tools and a reservoir test was carried out.

Geophysical Studies

Geophysical studies included the addition of 21 MT stations to the Camas Prairie array, and the addition of two active source seismic surveys oriented approximately perpendicular to the trend of the Pothole fault system (Glen et al., 2018). The new MT stations allowed a more robust 3D inversion of the MT data, while the new seismic lines documented the precise locations and dips of faults in the target area for our planned test well. In addition, 293 new gravity stations were added to improve regional coverage in areas with sparse control and to provide detailed coverage along a series of profile lines in the target area for the planned test well.

Field studies

Mapping in the foothills adjacent to the Pothole fault system shows that surface faulting in the Barron's Hot Springs-Pothole area consists of two distinct structural trends: NW (~285-295°) and NNW (~325°). Faults of both domains dip predominantly NE and exhibit dextral-normal to normal slip. Both systems offset late Pleistocene basalts, documenting late Pleistocene to Quaternary ages.

Data Integration, Modeling, and Site Selection

The GIS workflow was updated during Phase 3 to facilitate its performance and ease of use at a range of scales, from regional to highly focused local areas. Our methodology was tested by applying it to the Washington State PFA project, comparing their results with results produced by our approach using their data inputs. Our semi-automated approach produces essentially the same results as those obtained by the Washington State PFA group using a more hands-on approach.

Our updated GIS workflow was used to integrate new data (produced during Phases 2 and 3) into detailed CRS and CCRS maps of the Camas Prairie area. The results pointed to highly favorable sites for a test well along the Pothole fault system. Gravity, magnetic, and seismic data were combined to develop structural cross-sections that further constrained potential test well locations. A structural analysis of the Pothole fault system suggests a zone of extension

corresponding to its intersection with the blind range front fault system. The zone of extension was chosen as the site for our test well.

Geothermal Test well USU Camas-1

The geothermal test well USU Camas-1 was drilled by the USGS Research Drilling unit under a separate contract with DOE. The well was drilled in three stages: (1) rotary drilling through basin fill sediments to bedrock (347 m depth), and setting casing into bedrock; (2) rotary drilling through bedrock to 490 m depth; and (3) diamond core drilling through bedrock to 618 m total depth. Stages 1 and 2 were drilled in September through October 2018; Stage 3 was drilled in October 2019. Cuttings were collected every 10 feet during Stages 1 and 2, and continuous core was collected during Stage 3. Wireline geophysical logs were collected in the open holes for each stage, and a lithologic log was constructed from cuttings and core.

Temperature logs collected during and after drilling indicate isothermal temperatures of ~80ºC below ~300 meters depth. Water samples collected in 2018 and 2019 subsequent to drilling operations were analyzed for major and trace elements. Multicomponent geothermometry obtained from a flowing well sample collected in July 2019 indicates equilibrium reservoir temperatures of ~124ºC, somewhat higher than our original predicted temperatures of ~110ºC and the maximum measured downhole temperature of 81ºC. Lithologic logs indicate that hydrothermal flow is associated with fracture permeability in the basement granites. Propylitic (hydrothermal) alteration is common in both core and cuttings, but its age is unknown. Shervais et al. (2020) summarizes the results of the Phase 3 investigations.

SUMMARY AND CONCLUSIONS

This project has developed a systematic and reproducible approach to geothermal Play Fairway Analysis within ArcGIS that uses Python scripts to automate creation and evaluation of evidence layers based on a range of geologic, geochemical, and geophysical data. This approach can be applied to other geothermal exploration targets, as we have documented with the Washington State PFA data, either by adding new evidence layers or by applying zero weight to evidence layers that lack data.

Application of our method to southern Idaho has revealed several areas with high geothermal potential. Two of these areas were selected for more detailed study: Mountain Home and Camas Prairie. Additional data were collected for each of these areas, which allowed us to update and refine our conceptual model and data analysis to select potential drilling targets in each. Drilling of a geothermal test well (USU Camas-1) validated the underlying geologic model and our pre-drilling predictions. The Camas Prairie geothermal test well successfully documented a geothermal resource as predicted by our PFA model based on measures of permeability, heat and seal. The Camas site was not expected to be a high temperature resource, although the final

equilibrium reservoir temperature exceeded our pre-drilling predictions. Although the geothermal system under Camas Prairie is relatively small, our model predicts multiple large resources beneath other portions of the western SRP.

Benefit to the Public

Access to clean, renewable energy is becoming more imperative each year. Geothermal energy is a clean, renewable resource that is always on – making it the ideal source for base load electrical production. Wind and solar are popular renewable technologies, but have limitations: wind does not always blow, and solar output is limited by clouds and night. Geothermal energy is especially useful when combined with solar for peak daylight energy consumption. A further benefit is that hydrothermal water produced for the generation of electricity may be cycled through direct use applications, such as space heating for greenhouses or buildings, before it is re-injected to replenish the geothermal reservoir.

Idaho sits upon a unique geothermal resource that could potentially rival Nevada for power output. Our project has documented that geothermal resources fueled by volcanism in southern Idaho are regional in extent and may be tapped in zones of high permeability formed by faults. Many of these faults are exposed on the surface, but others are buried beneath thick blankets of clay-rich sediments that provide both a seal for the hot water resource and a layer of insulation for the underlying thermal anomaly.

The goal of our project was to reduce the risk for private developers and thus remove barriers to further exploration and development. The methodology and tools developed by this project have helped to identify where these resources are located, to estimate their volume, and in time, to locate the best places to drill in order to harness this resource. Furthermore, these methods and tools are transferable to other regions with different geothermal resources and may be used throughout the geothermal industry.

I. PHASE 1 ACTIVITIES AND RESULTS

1.0 INTRODUCTION

The Snake River Plain (SRP) volcanic province in southern Idaho (Figure 1) formed in response to movement of the continental lithosphere over a deep-seated mantle thermal anomaly ("hotspot") that has thinned the lithosphere and fueled the intrusion of hot basaltic magma into the lower and middle crust, forming a layer over 10 km thick (*Shervais et al., 2006a, 2006b*). The heat from these intrusions drives the high heat flow and geothermal gradients observed in deep drill holes throughout the Snake River Plain (SRP: *Blackwell, 1980, 1989; Brott et al., 1978, 1981; Lewis and Young, 1989*). The SRP is one of the highest heat flow regions in the United States. Idaho was ranked third among western states for potential geothermal power production, with 855 MW of near-term economic potential resources, by the Geothermal Task Force of the Western Governors' Association (*Western Governors' Association, 2006).* Identification of blind resources could spur commercial development (*Nielson et al., 2012; Nielson and Shervais, 2014*) in this undeveloped area.

Play Fairway Analysis is an approach to exploration pioneered by the petroleum industry that integrates data at the regional or basin scale in order to define favorable trends for exploration in a systematic fashion. It then interrogates these data to highlight which plays have the highest likelihood of success (*prospects*). *Play Fairway Analysis* provides greater technical rigor than traditional exploration approaches and facilitates quantitative risk-based decisions even when data are sparse or incomplete (*Shell Exploration and Production, 2013*).

Play Fairway Analysis is a mature methodology in petroleum, but it is a new exploration technique for the geothermal industry. Past techniques were based on conceptual models of systems as a whole, or targeted individual sites, and current exploration methodologies address those conceptual models *(Ward et al., 1981)*. The geothermal industry has evolved from drilling hot spring occurrences to blind exploration of known or inferred geothermal trends, and has identified distinct geothermal play types (*e.g., Moeck, 2014*), but has not adopted Fairway analysis. This study represents a new approach that we believe will aid in the discovery of buried or blind geothermal systems. A key challenge is to adapt this analysis in a way that provides meaningful results and measurable return on investment *(Nielson et al., 2015)*.

Our study area encompasses almost all of southern Idaho, spanning six degrees of longitude (~500 km EW) and over 2.5 degrees of latitude (~300 km NS), or about 150,000 km^2 (Figure 1). Our goals for Phase 1 were: (1) adapt the methodology of *Play Fairway Analysis* for geothermal exploration by creating a formal basis for its application to geothermal systems, (2) assemble relevant data for the SRP volcanic province from publicly available and private sources, (3) build a geothermal play fairway model for the Snake River Plain that would allow us to identify the most promising plays, and (4) develop an exploration plan to further evaluate the most promising plays. Our specific objectives included defining the critical elements that characterize a viable geothermal system (heat source, reservoir, migration pathways for recharge, and seal), integration of the diverse data sets that may be used to characterize these critical elements within a single analytical platform (ArcGIS), and interrogation of these data to produce *Common Risk*

Segment maps and *Composite Common Risk Segment* maps *(e.g., Shell Exploration and Production, 2013)*.

1.1 Summary of Project Activities: Phase 1

The Project Team met at least once each quarter for extended discussions and analysis. Conference calls or web-based conferences were held in months without in-person meetings. Project activities focused initially on defining critical elements, methodology, and data compilation. Emphasis shifted first to refining and extending the methodology to produce risk maps, and finally to data analysis. Most work was carried out within ArcGIS, but some data exploration was done using *Google Earth* and *Google Maps*®. Data compilation was distributed to appropriate team members based on expertise, and those team members were responsible for later analysis of their data layers.

An important aspect of our work was the recruitment of an Industry Advisory Board comprising representatives of the geothermal industry (USGeothermal, Ormat), developers (US Navy), and consultant (Mink Geohydro, Inc.). Our team also includes two consultants with longtime connections to geothermal modeling (Leidos, Inc) and slim hole well development (DES, Inc). These strong industry connections were valuable for keeping our efforts focused on real-world problems, and for understanding industry practices.

Problems and Departures: The only significant problem encountered was with petroleum industry software tools designed to assist in play fairway analysis (*e.g. Exprodat*® extensions for ArcGIS). These tools proved to be too specific to the petroleum industry to adapt or apply in any meaningful way to geothermal. This is in large part due to the fact that petroleum plays are generally stratigraphic, so these tools rely on the distribution and thickness of source rocks, reservoir rocks, and cap rocks to assess exploration risk. In geothermal, only *Seal* is stratigraphic, and then only in some circumstances. *Heat* source may be localized or regional, whereas *Permeability* is structurally controlled.

We dealt with this issue by placing more emphasis on Python scripting within ArcGIS to carry out the steps required for fairway analysis. This required significant support from USGS GIS programmers. The impact of this shift on the project was positive because it allowed us to produce custom scripts that can be used throughout the geothermal industry without the need to license expensive petroleum industry software. It also allowed us to focus specifically on the critical elements of geothermal systems. The tools produced are repeatable, scalable, modifiable, transferrable, and when complete, will be essentially fully automated.

1.2 The Play Fairway Concept in Petroleum: The Exploration Play

The term ***Play*** is imprecisely defined in petroleum exploration, but there is "...general agreement that the play describes groups of accumulations and prospects that resemble each other closely geologically..." (*Doust, 2010*). These similarities include reservoir rocks, source rock maturity, migration paths and traps. Importantly, the play has a requirement that petroleum be economically recoverable (*Norwegian Petroleum Directorate, 2003*). *Fugelli and Olsen (2005)* state that an exploration play is validated when at least one economic discovery is made. In petroleum, plays are often defined by stratigraphy and/or structural style, and, for instance, one well may intersect more than one play. The Play Fairway is the area of maximum possible extent of reservoir rocks in the play (*Fugelli and Olsen, 2005*). For geothermal, we propose that the Play Fairway be defined by the maximum possible extent of potential heat sources, in our case, the Snake River Plain volcanic province.

Play Risk is defined by the confidence in (1) the geological model and (2) the database available (*Fugelli and Olsen, 2005*). These may be depicted as a confidence matrix with confidence ranked as low, medium and high. Within a fairway, there can be a dramatic difference in data availability and quality (for instance seismic data absent, 2D or 3D). This type of analysis also provides a basis for identifying areas where additional data collection is necessary to reduce exploration risk. *Common Risk Segment (CRS)* maps define areas that contain the same general *Probability of Success* (*PoS*) for individual model components, based on our *Level of Knowledge* (*LoK*) for these components. Each map indicates high, medium and low risk areas for each element under consideration. In petroleum exploration, the risk elements are the reservoir, source, charge and trap. For geothermal systems, we consider risk elements to be the heat source, permeable reservoir volume, recharge and seal. *Composite Common Risk Segment* (CCRS) maps incorporate the information from the individual CRS maps and define the "sweet spots" that will lead to prospect definition.

In petroleum assessment, the CRS maps lead to a volumetric potential evaluation that is based on reservoir size versus probability of occurrence. In general, small systems have a much higher probability of occurrence than large systems, and the number and size of these systems may be estimated using log-normal plots of cumulative probability versus field size *(e.g., Shell Exploration and Production, 2013).* There is a lack of comparable data for most geothermal areas. *Brook et al. (1979)* noted a relationship between characteristic temperature of a hydrothermal system and size where higher temperature systems were larger. This relationship was confirmed by *Nielson (1993)* but may not hold true for all geologic environments *(e.g., Wilmarth and Stimac, 2015).*

1.3 Play Fairway Analysis Concept Adapted to Geothermal Exploration

The fundamental parameters required for petroleum plays are source rocks, reservoir rocks, migration pathways, and seals. To be considered a prospect, plays must also contain structural or stratigraphic traps, and have a thermal history conducive to hydrocarbon generation at a time – the critical moment – when all of the other required elements (e.g., reservoirs, pathways, seals, traps) were in place. Petroleum fairway analysis begins at the basin scale, and progressively

focuses in on the play scale, and finally at the prospect scale. Our challenge was to adapt this methodology to geothermal systems in a way that preserves the fundamental strengths of the scientific approach and risk-based aspects developed by the petroleum industry, but which makes sense for geothermal systems.

In this section, we correlate the fundamental parameters required for petroleum plays with what we regard as their equivalent parameters in geothermal systems. The analogies are imperfect in some cases but represent our best judgment, based on our collected experience over decades of geothermal and/or petroleum exploration.

1.3.1 Heat (the Source)

A high-level heat source is the principal requirement for a high-temperature geothermal system that is within economically accessible drilling depths. The SRP is one of the highest heat flow provinces in North America and is associated with extensive Plio-Pleistocene volcanism. Within that province, we looked for areas where temperatures are enhanced by repeated or high-level magmatism. Using the Mountain Home corehole MH-2 as an example, there are hydrothermal breccias that are probably formed at temperatures >350ºC and indicate proximity to an intrusive (*Nielson et al., 2012*).

In order to identify areas underlain by these complexes and associated heat sources, we used a wide range of geological, geochemical, and geophysical data, including: regional heat flow data; the age, size, composition, and density distribution of basaltic vents; gravity and magnetic field data; magnetotellurics (MT); seismic surveys; groundwater temperatures; and estimates of deep reservoir temperatures derived from isotopic, cation, and multicomponent geothermometers (*e.g., Cannon et al., 2014*). He isotopic values were also utilized in a supporting role to identify fluids that contain He with a significant mantle component (R/Ra > 1.5) (*Dobson et al., 2015*). Rhyolite domes and lavas are less common (e.g., Big Southern Butte), but may also form an important heat source if they are underlain by relatively shallow magma chambers. In some areas, heat appears to come from circulation within the crust (e.g., Twin Falls area), in settings that resemble traditional Basin and Range geothermal systems.

1.3.2 Permeability (the Reservoir)

Geothermal reservoirs are almost exclusively reliant on fracture permeability, associated with fracturing related to tectonic and magmatic processes. Surface exposures of bedrock are amenable to mapping of structural features such as faults and lineaments, but in many settings sedimentary basins adjacent to topographic highs mask evidence of bedrock faulting and surface ruptures typically degrade quickly. In addition, the presence of extensive, young volcanic lava flows obscures older faults in the subsurface.

Fractures are difficult to characterize in the subsurface, but their presence can be predicted by steep gravity gradients, alignment of volcanic vents, petrophysical analyses of wireline log data, and an understanding of the relationships between lithology, lithostratigraphy, and mechanical properties. Analysis of fault trace maps and quantitative structure/stress analysis have been used to help locate permeability associated with large, mapped structures. Geothermal permeability is

typically highest within step-overs (transfer zones), accommodation zones, and fault intersections (*e.g., Faulds et al., 2013*); these are high priority targets for identification and mapping. MT and magnetics provide information for identifying zones of alteration produced by interaction of geothermal fluids with the host rock. Geothermal reservoirs also discharge fluids that are often detectable by fluid geochemical methods, enhanced groundwater temperatures, or hot springs and other surface manifestations. The existence of thermal features highlights the presence of permeable flow paths through which thermal waters migrated up to the surface.

The reservoir volume must be of adequate size to warrant commercial production. In addition, due to the high cost of drilling geothermal production wells (*Mansure and Blankenship, 2011, 2013*), we decided for this study that systems must be accessible by wells no deeper than 3 km. Commercial production is also dependent on production rate of wells and their thermal decline, which reflect the sustainability of the resource.

1.3.3 Permeability (Migration Pathways, Recharge)

Recharge by the migration of water into the geothermal system is critical to maintaining a long-lived resource. The hydrology of the SRP is complex. In the central-eastern SRP, the upper parts of the Snake River Regional Aquifer (SRRA) are reasonably well known; however, the deeper parts are understood only from deep holes, such as the Kimama hole drilled during Project Hotspot, and from electromagnetic (EM) and MT data (*Whitehead, 1986; Lindholm, 1996*). Deep groundwater circulation is even less well known in the western SRP, where lake sediments dominate. Evidence for deep groundwater circulation is found in hot springs and thermal wells characterized by low $^{3}He/^{4}He$ ratios (<0.1), which show that deep magmatic sources and mantle are not involved. Important recharge paths provided by tectonic faulting allow fluids to penetrate beneath lake beds and into geothermal reservoirs. As a result, we consider migration pathways in concert with reservoir permeability.

1.3.4 Seal (Cap)

An impermeable seal is a common feature of many geothermal systems (*Anderson et al., 2000*), and is often seen as a critical feature for the preservation of an active geothermal system (*Cummins, 2016*). In the absence of a seal, thermal fluids will escape to form surface hot springs (and accentuate heat release to the surface via advective heat transfer) or will mix with cold waters in shallower aquifers. Overlying sediments, which have lower thermal conductivities than the volcanic reservoir rocks, also act as a thermal blanket to retain heat. Project Hotspot demonstrated that lake sediments, hyaloclastites (glassy volcanic sediments), and altered basalts all may serve as effective reservoir seals in the SRP region. The distribution of lake sediments in the SRP is documented by surface exposure and well logs. Hydrothermally altered basalts and hyaloclastites may be mapped using magnetotelluric and magnetic surveys *(Bouligand et al., 2014)*. In addition, detailed studies of core from deep drill holes in the eastern SRP show that the base of the regional SRP aquifer is marked by pervasive clay alteration in the basalt groundmass, as well as a shift from convective geotherms (within the aquifer) to conductive geotherms (below the aquifer) (*e.g., Morse and McCurry, 2002; Shervais et al., 2013*). The distribution of this aquifer has been documented by *Lindholm* (*1996*) using resistivity surveys and well data.

1.4 Conceptual Models

Four play-types are defined for our area of investigation in southern Idaho: (a) ***SRP basaltic sill*** systems that involve fault-controlled permeability, a basaltic sill complex heat source, and a seal consisting of lake sediments (in the western SRP) or clay alteration of basalt (typical of the eastern SRP); Craters of the Moon, a very young basaltic rift, represents a subset of this type (*Nielson and Shervais, 2014; Nielson et al., 2015)*; (b) ***Shallow silicic domes***, which may create their own permeability during intrusion; examples of this type include the Big Southern Butte, Cedar Buttes, and other silicic domes (*Adams et al, 2000; Pribnowa et al, 2003; McCurry and Welhan, 2012; Welhan et al., 2014*); (c) ***Basin-and-Range systems*** that involve fault-controlled permeability and deep heat sources, such as the Raft River system *(e.g., Faulds et al., 2013)*; and (d) ***Granite batholith systems*** such as those occurring across the Idaho Batholith *(e.g., Young, 1985; Druschel and Rosenberg, 2001)*.

In the following sections we describe the characteristics of each system, with emphasis on the newly proposed *SRP-type basaltic sill play (Nielson and Shervais, 2014)*.

1.4.1 SRP Basaltic Sill systems

Although the SRP demonstrates young volcanic activity that is both widespread and voluminous, there has been relatively little geothermal exploration. We believe that this is the consequence of the lack of hot spring activity (except on the margins of the province) and the largely basaltic nature of the volcanism. Basaltic terrains are not generally considered to be viable exploration targets for high-temperature geothermal systems (with the exception of exposed mid-ocean ridge environments such as Iceland). *Smith and Shaw (1975)* pointed out that basalt is channeled rapidly from depth to the surface through fractures forming dikes that cool rapidly. In contrast, rhyolitic magmas commonly form chambers in the shallow crust and are therefore more capable of providing a larger and longer-lived heat source for hydrothermal circulation.

However, there are well-documented hydrothermal geothermal systems in areas of basaltic volcanism without associated rhyolites. The southeastern rift of Kilauea Volcano on the island of Hawaii hosts the Puna geothermal system. Active extension and dike intrusion provides a continuous source of basaltic magma. *Teplow et al. (2009)* document a dacite melt intersected by injection well KS-13 at depths of 2480 to 2488 m in the Puna field. Although there are no exposed flows of dacitic composition, the authors speculate that this dacite has differentiated from basalt. They have calculated that the magma intersected by drilling had a temperature of about 1050ºC, and on the basis of thermal arguments, they suggest a body with a minimum circular dimension of 1 km and a thickness of at least 100 m.

Another well-documented geothermal system specifically related to basaltic volcanism is located on the Reykjanes peninsula in Iceland *(Fridleifsson et al., 2014)*. The character of the heat source has yet to be determined, but it is hypothesized to be either a sheeted dike complex or a major gabbroic intrusive body. Drilling in the Krafla field, where there is young rhyolite volcanism, intersected magma of rhyolite composition. Petrologic studies have shown that the magma was formed through the partial melting of altered basalt *(Elders et al., 2011; Zierenberg*

et al., 2013). A common feature of the above examples of active hydrothermal systems related to basaltic heat sources is the presence of high-level magma chambers that have sufficient volume and longevity to sustain convective circulation. As the above examples also show, felsic melts may be formed through partial melting or differentiation, and these rocks may not be exposed at the surface.

Within the SRP, a number of studies have presented evidence for high-level basaltic magma chambers (sill complexes). Young basaltic volcanism is present throughout the region, with vents as young as 200 ka or less in the western SRP (WSRP) *(Shervais et al., 2002; White et al., 2002; Shervais and Vetter, 2009),* and ≤2,000 years old in the eastern SRP (ESRP) *(Kunz et al,, 1982; Shervais et al,, 2005).* Additional observations include:

- Documentation of a mafic sill or sill complex in the mid-crustal region beneath both the ESRP and WSRP by seismic methods *(e.g., Hill and Pakiser, 1967; Prodhehl, 1979; Sparlin et al, 1982; Peng and Humphries, 1997).*
- Geochemical evidence for a layered mafic sill complex beneath both the ESRP and WSRP, based on fractionation-recharge cycles in basalt flows sampled as drill core *(Shervais et al., 2006; Jean et al 2012).*
- The Graveyard Point Sill, exposed near the southern margin of the WSRP, documents a single layered basaltic sill up to 160 m thick *(White, 2007)* confirming the existence of sills inferred from seismic data and lava chemistry.
- High-resolution gravity mapping by the USGS defines an ~EW trending gravity high that lies at an oblique angle to the axis of the WSRP; this gravity high has been interpreted as a horst block, and may be cored by a mafic sill complex *(Shervais et al., 2002; 2013).* The alignment of this gravity high is approximately parallel to a fault system mapped north of Mountain Home, which lies at an oblique angle to the range front fault system *(Shervais et al., 2002).*
- Further support for the presence of a sill complex comes from olivine gabbro xenoliths in basalt from Sid Butte, which lies just a few km west of the Kimama drill site *(Matthews, 2000; Jones, 2017).* These xenoliths have modes and compositions appropriate for basalt fractionation at mid-crustal levels and suggest that basalts found on the surface were processed through this sill complex.
- A magmatic origin for many thermal features associated with the SRP is supported by geochemical and isotopic studies, which indicate anomalously high $^{3}He/^{4}He$ and magmatic methane in thermal springs and well water *(Dobson et al. 2015; Conrad et al., 2015).*

We propose that the main geothermal play type in Snake River Plain derives its enthalpy from a layered basaltic sill complex in the middle to upper crust (Nielson and Shervais, 2014). The SRP basaltic sill complex is long-lived because each individual sill is ~100-200 m thick, and the intrusion of multiple sills into the same level of crust pre-heats this crust, minimizing heat loss from subsequent intrusions (*Nielson et al, 2017*). Basaltic sills tend to pond at levels of neutral buoyancy *(Ryan, 1987),* and subsequent intrusions will also cluster near this level, at or just above previously intruded sills.

Conduits for heated fluids are provided by faults that have been mapped along the margins of the plain, measured by borehole imaging in some deep wells, and inferred from high-resolution gravity and magnetic surveys. In the WSRP, these faults trend essentially parallel to the long axis of the gravity high, which is interpreted to represent an uplifted horst block (*Glen et al, 2017*). The location and orientation of these faults are thought to be controlled by the distribution of sill complexes within the crust: crust modified by sill intrusion will tend to act as a rigid block, localizing strain along its margins. Because the horst block lies near the central axis of the WSRP, these conduits may conduct fluid upwards far from the range front system.

However, these fluids do not reach the surface, as no thermal features are observed in the center of the WSRP. The thick section of fine-grained sediment in the upper part of the Mountain Home section is thought to provide a cap on the geothermal system. This cap both prevents the system from discharging at the surface and seals the system against the ingress of cold water.

If this conceptual model is valid, we would expect to find similar subsurface resources and fracture systems in the WSRP associated with both the northern and southern flanks of the gravity high and possibly over the central part of the high where cross-faults are indicated. This model may also apply to the ESRP, which has a well-imaged crustal sill complex, gabbro xenoliths in basalt that show processing of magma through crustal magma chambers, and very young basaltic volcanism (≤2 ka in age) documenting an active magmatic system. The ESRP also features lacustrine sediments that could serve as a seal for the geothermal system.

These geothermal plays may constitute a significant recoverable geothermal resource and will be assessed quantitatively in light of this model.

1.4.2 Shallow silicic dome systems

Shallow silicic systems may form either as extrusive volcanic domes or as laccolith-style intrusions *(i.e.,* cryptodomes) that uplift pre-existing surface strata. These systems are noted for several characteristics: (a) the extrusive domes and cryptodomes are inferred to root in larger magma bodies at some depth below the surface; (b) thus, the domes represent cupolas of limited areal extent that contain relatively little long-lived heat internally, but which overlie much larger high-enthalpy magma systems; (c) wall rocks directly adjacent to these domes and cryptodomes may be highly fractured by intrusion of the domes, providing conduits for hot fluids to move upward from the underlying magma body (*Bacon et al, 1980; Adams et al, 2000; Pribnow et al, 2003; Schmitt and Hulen, 2008; Wright et al, 2015*). More commonly, these open fractures along the margins allow the downflow of cold water, resulting in temperatures below those predicted from thermal modeling of the intrusion (*Pribnow et al, 2003; Melosh, 2015*).

Silicic domes and cryptodomes are not common in the Snake River Plain: only six are found in the ESRP, along with one fractionated dacite vent (Cedar Butte), and they are rare elsewhere (*McCurry et al. 1999; Spear and King, 1982*). The China Hat domes, which lie SE of the SRP, in a zone transitional between the volcanic plain and the Basin and Range, may also be considered within this venue (*McCurry et al, 2011, 2015; McCurry and Welhan, 2012; Welhan et al, 2014*).

1.4.3 Basin and Range-style systems

The Basin-and-Range province in Nevada contains a large number of generally amagmatic geothermal systems; similar systems may exist in SE Idaho. Most systems are not associated with young volcanism and are thought to result from active extension and high heat flow (*Faulds et al., 2004; Blackwell et al 2002*). Heat flow ranges from 50 to ~120 mW/m^2 (average ~90 mW/m^2: Blackwell and Richards, 2004). Most of the higher temperature geothermal systems are found in the northwestern part of the Basin and Range, with many having subsurface temperatures up to ~200°C, even though volcanism ended 3 to 10 Ma (*Faulds et al., 2004, 2010*). The lack of recent volcanism suggests that upper crustal magmatism is not a heat source for most of the geothermal activity in this region.

Geothermal activity in the northwestern portion of the Basin and Range is facilitated by transtensional extension, with high rates of Neogene extension and dextral offset in the Walker Lane (*Colgan et al., 2004; Faulds, 2004*). Geothermal fields in northern Nevada appear to be controlled largely by NNE-trending normal faults, which are oriented perpendicular to extension and thus favor dilation and deep circulation of geothermal fluids (*Blackwell et al., 2002; Johnson and Hulen, 2002; Faulds et al., 2004, 2006*). Many geothermal systems in the Basin and Range are likely to be blind systems with no surface manifestations (*Coolbaugh et al., 2007; Williams et al., 2009*).

1.4.4 Granitic Batholith systems

Geothermal systems in the Idaho batholith are included here for completeness but are not a focus of our study, and for the most part lie outside our study area. Previous work on geothermal systems within the batholith have concluded that the present day thermal waters represent older, possibly late Pleistocene meteoric water that has circulated along deep-seated fault systems and reequilibrated in part with the granite (*Druschel and Rosenberg, 2001; Young, 1985; Criss and Taylor, 1983; Anderson et al., 1985; Street, 1990*). Reservoir depths are estimated to be 2.4 to 6.7 km, with temperatures of 85° to 160°C (*Druschel and Rosenberg, 2001*).

1.4.5 Engineered Geothermal systems (EGS)

Engineered geothermal systems (EGS) are a special category where permeability is created artificially by hydraulic fracturing of hot rocks. These systems typically require permeability created between an injection well (where water is introduced under pressure) and one or more production wells (where this water is recovered after it is heated by flow through the fractured rock). As a result, the primary requirement is Heat; primary permeability should be low. Our project was not designed to explore for EGS, but can easily be adapted to do so, as we note later in this report.

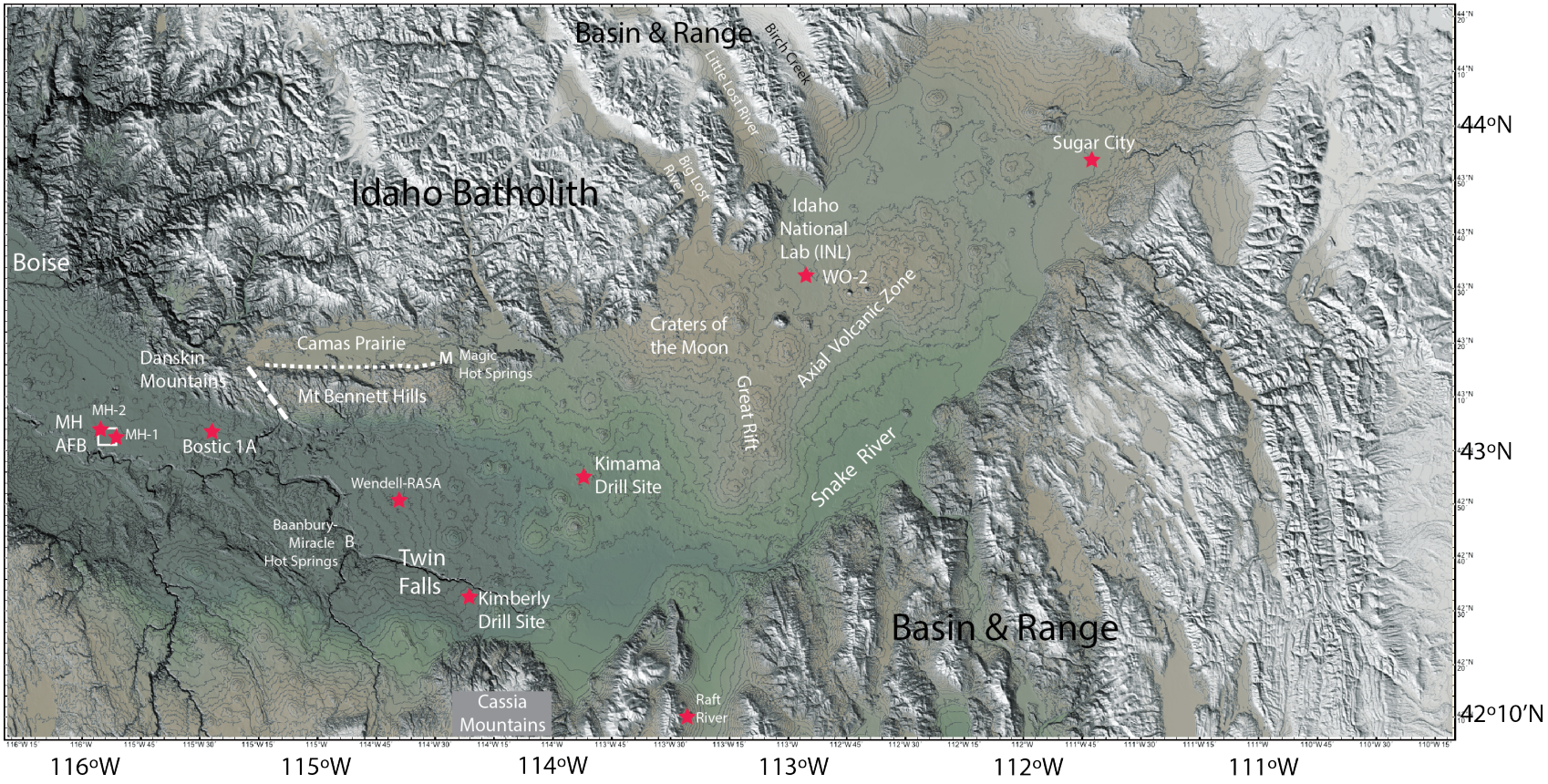

Figure 1. Location map of Snake River Plain, showing the study area, along with major towns, geographic features, and deep wells (red stars). Features:Craters of the Moon National Monument; Great Rift; Mount Bennett Hills; Camas Prairie; Danskin Mountains; Idaho National Laboratory; Axial Volcanic Zone. Other sites: B: Banbury Hot Springs, M: Magic Hot Springs. Deep wells: RR: Raft River complex, MH-1: Mtn Home #1; MH-2: Mtn Home #2, KB: Kimberly, KA: Kimama, SC: Sugar City, WO2: WO2 (INL site).

2.0 APPROACH

Our approach was to analyze direct and indirect indicators of geothermal potential in order to identify the three critical geothermal resource parameters: *heat source, permeable reservoir,* and *seal (Nielson et al., 2015)*. The project was divided into three phases. Phase 1 assessed the distribution and viability of plays throughout the SRP region using existing data sources, and identified areas where new data collection was needed to confirm these resources. Phase 2 focused on the collection of new field data and thermal modeling. Phase 3 focused on a specific prospect identified in Phase 2 (Camas Prairie), with additional data collection and the drilling of an exploration slimhole to validate our approach.

2.0.1 Software and Data Handling

Our workflow is modified from the petroleum industry, using industry-standard tools for data integration and modeling where appropriate. We used *ArcGIS,* with extensions for spatial and geostatisical analysis, as our primary software tool for several reasons. It is capable of integrating and analyzing a wide range of spatial data types, and it has become the standard platform for geospatial analysis in industry, academia, and government. Most geothermal enterprises already have GIS professionals on staff and use ArcGIS for a range of functions. A second strength of ArcGIS is its extensibility through the use of Python scripts. Python is a scripting language that is used by advanced GIS professionals to create new tools that can be incorporated into the Arc toolbox, where they can be accessed and applied by less skilled GIS technicians. *The use of custom Python scripts is a critical component not anticipated in our original proposal and has had a fundamental impact on our approach to data analysis.* The Python scripts allowed us to compile raw data layers within ArcGIS, extract these layers and process them to create evidence layers and common risk segment map layers that can be imported back into ArcGIS for display and interrogation.

Other software tools used in this study include the *IHS Kingdom* and *Petra*, used to construct 3D stratigraphic models, *Oasis Montaj*®, which integrates 3D geophysical data modeling with ArcGIS layers, and *3DStress*, which analyzes fault dilation tendency and fault slip tendency based on the regional stress field. Estimates of reservoir temperatures using thermal spring and well water compositions were calculated using *RTEst*, a multicomponent geothermometer (Palmer et al., 2014). Analysis of geospatial data outside of the ArcGIS framework was carried out using *Google Earth Pro*® and *Google Map*. Both tools import Arc shapefiles that have been exported in kmz or kml format, and also import tabular data files (csv or Excel format) for data exploration (e.g., volcanic vent mapping). Thermal modeling was carried using Leidos's STAR geothermal reservoir simulator (*Pritchett, 2011*) and *Toughreact* (*Xu et al., 2011*).

A shared Google Drive folder was created to facilitate the exchange and archiving of data files. This guaranteed that everyone associated with the project had access to the same data files and facilitated the exchange of data files, which can range in size to hundreds of megabytes. It also allowed us to have a central repository for all of our data sets in order to avoid inconsistencies between users. On project completion, these data were uploaded to the Geothermal Data Repository (GDR).

2.0.2 Workflow

The Snake River Plain was divided into three main regions based on differences in tectonic and volcanic setting, which differ in their stratigraphy and structure (Figure 1). The main regions are (1) the eastern SRP, including Craters of the Moon-Great Rift along its western margin, (2) the central SRP, comprising the axial portion of the plain between Craters of the Moon-Great Rift on the east and Hagerman-Bliss on the west, as well as the Bruneau-Jarbidge eruptive center, the Mount Bennett Hills, and the Camas Prairie, and (3) the western SRP graben and adjacent regions. Subregions comprise areas of interest adjacent to the margins of the plain, including Basin-and-Range areas north and south of the ESRP, the Idaho Batholith, which lies largely north of the WSRP and CSRP, and the Owyhee Plateau, which lies south of the WSRP.

A *resource attribute worksheet* was created at our kick-off meeting to summarize important properties (heat, permeability, seal) and the types of data needed to establish them (*e.g.,* heat flow, volcanic vents, faults, gravity and magnetic lineations, *etc*). The *resource attribute worksheet* also included data sources and links where known, or ideas on where appropriate data might be found. This worksheet was expanded as work progressed, but the basic data elements laid out in this worksheet remained the dominant factors in our analysis throughout Phase 1.

Critical element risk matrices were produced for several play types and attributes that assess model favorability against data confidence or assess an attribute for model favorability. The primary focus for these risk matrices was on heat source and reservoir quality (permeability). The critical element risk matrices were based in part on the resource attribute worksheet, which defined many of the critical elements of source, reservoir and seal, and in part on our evaluation of the uncertainty expected within each data type. Reservoir seal is more difficult to assess, since it consists of either impermeable sediments, whose distribution is relatively well known, or alteration self-seal, which is difficult to predict, but may be inferred from resistivity studies (*e.g., Lindholm, 1996*). These critical element charts were not used directly but were used conceptually to structure how these data were handled within ArcGIS. Our approach is similar to that used by *Coolbaugh et al. (2002, 2005)* for a GIS-based weights of evidence approach to the Basin-and-Range that has been validated by subsequent studies.

2.0.2 Changes in Approach During Phase 1

Early in our efforts we explored the use of *Team-GIS* from *Exprodat LCC*, a set of petroleum industry extensions to *Arc* for play fairway analysis. It was our hope that these tools could be adapted relatively easily to geothermal exploration and would provide a robust application of petroleum industry expertise. Unfortunately, these tools turned out to be extremely specific to petroleum exploration and proved to be impractical to adapt to geothermal exploration in any meaningful way.

This discovery led us to move forward by developing our own custom Python scripts for geothermal fairway analysis. Because Python is native to ArcGIS, scripts can be compiled into a "toolkit" that can imported into ArcGIS for use by others. This approach allows us to "automate" the Fairway Analysis, by providing a series of user tunable weights for combining evidence layers within a given CRS map, for applying confidence layers to evidence layers, and for

combining CRS maps into composite CRS maps. It also allows us to use tools built into ArcGIS for functions such as density maps and data interpolations. An extended discussion of these issues is provided in the *Methods* Section.

2.1 Data Compilation

Data were compiled from a range of public and private sources, both published and unpublished, and imported into ArcGIS to create a series of data layers for later analysis (**Appendix A**). The data collected include geologic maps at scales from 1:24,000 to 1:250,000, structural features (faults, lineaments), vent locations, ages, and types from geologic maps and other sources, heat flow from the USGS and SMU databases, groundwater temperatures (USGS, IDWR), existing regional gravity data as well as newly collected high resolution profile data, and processed potential field data yielding subsurface structural interpretations and Curie temperature depths, passive seismic velocity, magnetotelluric and crustal thickness data from *Earthscope*, regional EM data from USGS reports, the location of 56 commercially-available active source seismic lines and other public domain seismic lines, distribution, thickness and age of lacustrine sediment seals, the distribution and temperatures of thermal springs and wells from IDWR and NGDS, water chemistry and stable isotope chemistry from USGS and from partner GTO-funded projects, and He isotopes from partner GTO-funded projects. Significant data types and sources are listed below**.**

2.1.1 Geologic Maps

Geologic maps used for the project (many available as GIS shapefiles) include those published by the USGS and Idaho Geological Survey (IGS), and unpublished maps. Most of the SRP and adjacent areas are covered by 1:100,000 1º sheets or 1:125,000 county maps, most of which are compiled from mapping done originally at 1:24,000 scale (7.5' quadrangle) or in a few cases, 1:62,500 scale (15' quadrangle). A few areas are represented by older 1:250,000 scale maps (2º sheets). Regardless of scale, all of these maps are available in high resolution PDF format, which enables us to import the trimmed map sheets into Arc GIS or Google Earth and to rubber-sheet them into geographic coordinates as image files. These were used to compile vent locations and sizes. A GIS-based geologic map of the state provided a starting point for the overall geology as well as the distribution of lacustrine sediments in the western SRP.

2.1.2 Heat Flow, Thermal Gradients, and Groundwater Temperatures

Heat flow and thermal gradient drillhole data were compiled from USGS and Southern Methodist University (SMU) Geothermal Lab databases (*e.g., Williams and DeAngelo, 2008; 2011; Blackwell et al., 1989; Blackwell and Richards, 2004*), plus data from the National Geothermal Data System. Heat flow data are not evenly distributed, with the highest density of measurements found in the WSRP and across the border in eastern-most Oregon. Gradient wells in the eastern SRP are clustered at the INL site and along the eastern edge of the plain near Island Park caldera, with scattered coverage elsewhere. Large data gaps are found in the axial region from Idaho Falls to Hagerman (on the western edge of the Central SRP (CSRP)). These gaps correspond largely to the distribution of the Snake River aquifer, which renders

measurement of conductive thermal gradients impossible in all but the deepest wells. Further, if thermal gradients are estimated from bottom hole temperatures and surface temperatures, the resulting gradient will be too shallow and give erroneously low heat flow. We have used data on aquifer distribution and thickness to correct for this effect where possible, both in the Snake River Aquifer system and in the smaller but still important system on the Mountain Home plateau (see section 2.1.9 Aquifers). In addition, new heat flow data from two Hotspot wells and one older well provide important new control points within these data gaps.

Groundwater temperature reflects thermal flux from below. Groundwater and surface flow from the mountains of eastern Idaho and Wyoming is characterized by temperatures ~8ºC, which represents the baseline temperature of the Snake River aquifer in the eastern and CSRP. Groundwater temperatures increase gradually from NE to SW in this region in response to thermal flux from below the aquifer (*e.g., Blackwell et al 1992; Smith, 2004; McLing et al., 2014*). Further, groundwater temperatures are uniformly high in the WSRP due to the thick insulating layer of lacustrine sediments. Because groundwater temperatures respond well to the underlying heat flux, they can be used as a proxy for heat flux to supplement the more limited heat flow database.

2.1.3 Volcanic Activity

Areas with high concentrations of young volcanic vents are likely to overlie magma chambers or recent sill intrusions, making them a proxy for magmatic heat centers in the crust. Vent locations for basalts and rhyolites were compiled from a range of sources and cross-checked against topographic features and geologic maps for accuracy and completeness. Radiometric ages, though rare, were compiled where available, and all vents were classified by age using radiometric ages, magnetic polarity, or stratigraphic relations from geologic maps. Vents were binned into six age groups, as follows:

Group	Age Range	Stratigraphic Age	Polarity	Weight
Group 1:	<75 ka	Holocene plus	Normal	1.0
Group 2:	75 – 400 ka	Late Pleistocene	Normal	0.95
Group 3:	400 – 780 ka	Middle Pleistocene	Normal	0.90
Group 4:	0.78 – 2.58 Ma	Early Pleistocene	Mostly Reverse	0.8
Group 5:	2.58 – 5.23 Ma	Pliocene	Mixed	0.7
Group 6:	>5.23 Ma	Miocene-older	Mixed	0.5

In order to correct for age-related degradation of small vents (e.g., cinder and spatter cones), which are over-represented in young volcanic fields, a size factor was assigned to each vent ranging from 0.1 for small cinder or spatter vents to 1.0 for shield volcanoes. Parasitic vent clusters caused by lava erupting onto wet lake beds were given a weight of 0.01.

Composition codes were assigned to track types of lava erupted. Since relatively few flows have published chemistry, many flows were assigned a composition code based on their location,

e.g., all Holocene plus vents of the Craters of the Moon-Great Rift field are Type 2 evolved basalts, whereas all other basalts of the central and eastern SRP are SROT *(e.g., Kuntz 1992; Putirka et al 2009; Shervais et al, 2005; 2006; Shervais and Vetter 2009; Jean et al, 2013; Hughes et al 2002; Geist et al 2002;* see Appendix A*)*.

2.1.4 Faults and Lineaments

Faults and lineaments were compiled largely from two sources: (1) USGS Quaternary fault database (QFFDB: *Machette et al, 2003*), and (2) Idaho Geological Survey database of Miocene and younger faults. Additional faults were compiled from geologic maps and reports (e.g., Project Hotspot Final Report). The Idaho Geological Survey (IGS) database is more extensive but contains less information, so where duplicate records occur the USGS record was retained and the IGS record discarded. Individual fault strands were digitized into numerous short segments, each of which was considered a separate fault segment during data processing (e.g., density counts). As discussed below, all fault segments were evaluated for slip and dilation tendency within the regional stress field, and these tendency values (0-1.0) were used as weights in the density functions (see **Methods**, below).

In addition to mapped surface faults, we also digitized subsurface lineaments from maximum horizontal gradients in gravity and magnetic anomalies. These lineaments are interpreted to represent major structural discontinuities in the subsurface. These data are crucial for most of the SRP because exposed faults are rare within the plain, but these structures are known to host geothermal permeability at depth (*e.g., Shervais et al., 2014*). As with the mapped surface faults, these lineaments are evaluated for slip and dilation tendency within the regional stress field, and these tendency values are used as weights in the density functions.

2.1.5 Geophysical Data

Geophysical data used in this study included: gravity and magnetic potentials, resistivity, MT and regional stress data compiled by the USGS, including new high-resolution gravity and magnetic data produced by Project Hotspot and the distribution of subsurface lineaments derived from maximum horizontal gradients in gravity and magnetic data.

Seismic reflection and refraction lines, including lines shot by Chevron in the 1980s, are available mostly for the WSRP, with other lines in the overthrust belt of SE Idaho. Boise State University (BSU) completed the analog to digital conversion of about 210 km of seismic lines from the WSRP, including six lines from the *Seismic Data Exchange* inventory of seismic profiles from the WSRP (160 km) and seven digital profiles from other sources (50 km). This inventory does not include the short profiles collected by BSU projects. These data are publicly available, owned by participants, or for sale by the Seismic Data Exchange.

Crustal scale seismic profiling data (refraction and receiver function analyses) and earthquake seismic data (NEIC and INL) from southern Idaho are compiled and integrated into our analyses. These datasets include seismic profiles published across the WSRP by *Hill and Pakiser (1967)* and by *Sparlin et al. (1982), Peng and Humphreys (1998), and DeNosaquo et al. (2009)* for the ESRP. USArray (Earthscope) seismic and magnetotelluric results provide the lithospheric

framework, crustal thickness, and identify highly conductive regions beneath southern Idaho (*e.g., Eager et al., 2001; Smith et al., 2009; Gao et al., 2009; Kelbert et al., 2012*).

Gravity data from Project Hotspot (1866 new gravity stations) were combined with gravity data from the surrounding areas (including parts of ID, OR, NV, UT, WY and MT) downloaded from the PACES data portal (*Pan-American Center for Earth and Environmental Studies, 2009*). Existing data provided regional coverage between detailed high-resolution gravity profiles and extended profiles beyond the plain. The regional magnetic grid used in this report was derived from the Magnetic Anomaly Map of North America (*Bankey et al., 2002*). We have also used a higher resolution grid for the State of Idaho (*McCafferty et al., 1999*).

Additional datasets integrated into our analyses include geodetic results from *Payne et al. (2013)* and local magnetotelluric and resistivity survey results. These surveys, summarized by *Stanley (1982)* across the ESRP and *Whitehead (1992, 1996)* across the SRP have provided the framework for resistive sedimentary basin geometries and more conductive aquitards that may cap blind geothermal systems.

2.1.6 Mechanical Properties of Reservoir Rocks

Rock mechanical properties of core, correlated with borehole geophysical logs, are available only for two deep wells drilled by Project Hotspot: the 1923 m deep Kimama drill hole and the 1812 m deep Mountain Home 2 drill site (*Kessler, 2014*). The Kimama site is typical of the CSRP and ESRP and provides an analogue for what to expect in any deep holes drilled in this part of the study area. Lithology and alteration in the Kimama core can be correlated with core from other deep drill holes in the CSRP and ESRP (e.g., the 1524 m WO-2 well on the INL site, the 343 m deep Wendell-RASA well NW of Twin Falls, and the 696 m deep Sugar City well near Rexburg, Idaho). The Mountain Home site is typical of the western SRP, and can be correlated with core from other deep holes in this area (*e.g.,* 2743 m deep Bostic 1A well, 4389 m deep JN James well, and the 2750 m deep Deer Flat well).

2.1.7 Geochemistry and Geothermometry of Geothermal Wells and Thermal Springs

Measured temperatures, geochemistry and geothermometry of geothermal wells and thermal spring waters were obtained from USGS, IGS, and NGDS databases, as well as from ongoing studies being carried on by researchers at INL, the University of Idaho, and LBNL. We have partnerships with two DOE-funded research projects, which have been gracious enough to share their current data with us:

- Pat Dobson and Mack Kennedy, LBNL: *Use of He isotopes for Geothermal Resource Identification in the Cascades and Snake River Plain*.
- Earl Mattson, Travis McLing, Hari Neupane (INL), Mark Conrad (LBNL), Tom Wood, Cody Cannon, Wade Worthing (U-Idaho): *Geothermometry Mapping of Deep Hydrothermal Reservoirs in Southeastern Idaho*.

These data include results from recently developed multicomponent geothermometers as well as traditional cation methods (*e.g., Spycher et al., 2014; Palmer, 2014; Neupane et al., 2014*) and new and compiled He isotope data (*Dobson et al., 2015*).

Measured water temperatures are used to document hot water springs and wells, but these are often too low because of cooling or mixing with cooler waters. Geothermometry based on silica, cations, or multiple components is used to circumvent this problem by estimating reservoir temperature, assuming it is in equilibrium with common rock-forming minerals and their associated alteration products (*e.g., Giggenbach and Goguel, 1989; Powell and Cumming, 2010; Spycher et al., 2014; Palmer et al., 2014*). There is often significant variation among different thermometers, which may reflect chemical disequilibrium or dilution with non-thermal waters.

He isotopes are measured in terms of $^{3}He/^{4}He$ relative to atmospheric composition (R/Ra). ^{3}He is stable (not produced by radioactive decay), whereas ^{4}He is created by radiogenic decay of heavy elements to form alpha particles (^{4}He nuclei). Since these elements (U, Th and their decay products) are concentrated in continental crust, ^{4}He increases in the crust over geologic time, resulting in extremely low crustal $^{3}He/^{4}He$ ratios (<0.1 R/Ra largely). Values R/Ra > 1.0 require input from a mantle reservoir that preserves primitive He isotope ratios; this is commonly accomplished by the intrusion of mantle-derived mafic magma (*e.g., Kennedy and van Soest, 2007*). Thus, high $^{3}He/^{4}He$ ratios record both relatively recent mantle-derived magmatism, and the presence of highly permeable pathways that allow this He (released by degassing magmas) to move quickly through the crust, where it is captured by groundwater and sampled.

2.1.8 Aquifer Systems

The Snake River Plain is characterized by major aquifer systems that can have a significant impact on heat flow measurements and on the drilling depth needed to achieve sufficiently high temperatures for power production. Data for the distribution, thickness, and impact of these aquifers is obtained largely from publications of the USGS and the Idaho Department of Water Resources: *Whitehead (1986), Whitehead and Lindholm (1985), Lindholm (1996), Whitehead (1992), Garabedian (1992), Wood and Anderson (1981), Smith (2004)*.

The most significant is the Snake River Regional Aquifer system of the ESRP-CSRP. This system is fed by inflow from the Big and Little Lost Rivers, Birch Creek, and Henrys Fork River, and it emerges in a series of spectacular springs in the Thousand Springs-Hagerman area, 200-300 km SW of its recharge areas. Deep wells show that the aquifer extends to depths of 200-550m in the ESRP and 980m in the CSRP. The base of the aquifer is defined by the change from convective, nearly isothermal gradients within the aquifer, and conductive gradients below (*Smith 2004*). The distribution and thickness of this aquifer has been delineated from electrical resistivity and well data by *Lindholm (1996)* and *Whitehead (1992)*.

The Snake River Regional Aquifer is bounded on its southern and western margins by the Snake River canyon. Local aquifers, such as the Twin Falls low-temperature geothermal aquifer system, flow towards the Snake River from mountain ranges in the south (*Street and DeTar, 1987; Garabedian, 1992; Lindholm, 1996; Whitehead, 1992*).

In the WSRP, aquifers are limited by the distribution of impermeable lacustrine sedimentary rocks, and surface drainages include the Bruneau, Jarbidge, Owyhee, and Boise Rivers, as well as the Snake. Gravel deposits comprise shallow aquifers in the Boise area, and a perched aquifer in the Mountain Home area. The plateau between Boise and Mountain Home is capped by up to

300 m of basalt that hosts localized aquifers. These basalts are underlain by impermeable lacustrine sediments (*Newton, 1991; Wood 1994; Wood and Clemens, 2002*).

2.1.9 Lithology and Wireline Logs of Deep Wells

Lithologic and borehole geophysical logs were compiled for deep wells, e.g., test wells at the INL site, USGS water resource and geothermal test wells, passive geothermal wells (Boise, Twin Falls districts), and wildcat petroleum exploration wells. The most complete records are from Project Hotspot (EE0002848), which drilled deep (1.8 to 1.9 km deep) holes at three locations across the SRP (*Hotspot Final Report, National Geothermal Data System (NGDS)*). These wells provided about 5300 m of core and a complete set of wireline logs for each drill hole. Other deep holes that provided more limited data (typically lithologic logs, but some with wireline logs and temperature data) include INEL-1 and WO-2 (1524m) at the INL site, Sugar City (696m) and Wendell-RASA (343m) in the ESRP and CSRP, and MH-1 (1342m), Bostic 1A (2743m), JN James (4389m), Champlin Petroleum Upper Deer Flat No. 11-19 (2750m), and Anschutz Federal #1 (3391m) in the WSRP (*Doherty, 1979; McIntyre, 1979; Embree et al., 1978; Doherty et al, 1979; Arney et al, 1982; Whitehead and Lindholm, 1985; Hackett et al, 1994; Breckenridge et al, 2006; Jean et al, 2013*).

Most water wells in the central and eastern SRP are too shallow to reveal much information, but an exception to this is the Twin Falls Warm Water district, which contains a large number of moderately deep wells (150m to 670m depth) that tap into a low-temperature geothermal aquifer at 37ºC to 42ºC, used for passive space heating. Because they are located along the southern margin of the CSRP, these wells typically penetrate basalt and bottom in rhyolite lavas or welded ash flow tuffs. These wells lie outside the basaltic Snake River Aquifer and provide information on a distinct hydrologic system that lies largely south and west of the Snake River. Relatively shallow (≤250m) well data from the Burley and American Falls area are important for establishing the extent and thickness of lacustrine sediments from paleo-Lake Burley and paleo-Lake American Falls, which represent the most important lake seals in the ESRP (*Neal Farmer, IDWR, personal communication, 2010; Desborough et al, 1989; Phillips and Welhan, 2006, 2011*).

2.1.10 Cadastral Data

The Snake River Plain PFA study area encompasses a wide variety of political, land use, cultural, infrastructural, and environmental attributes. Cadastral data (*i.e.,* data relating to ownership of land and its uses) was assembled using the *Geothermal Prospector* mapping tool developed by NREL for the DOE Geothermal Technologies Office. *Geothermal Prospector* is designed to assist users in determining locations that are favorable to geothermal energy development.

Key regional cadastral data layers include: Political (Federal, State, Tribal lands), Land Ownership (Private, BLM restricted, NFS restricted, DOD restricted, Other restricted), Environmental (Areas of critical environmental concern, Brownfields, BLM closed areas, National Forest Service closed areas, Wilderness areas and study areas, Greater Prairie

Chicken/Sage Grouse range), Infrastructure (operating geothermal plants, developing geothermal projects, Transmission corridors), and Resource (*Known Geothermal Resource Areas* (KGRA)).

Geothermal exploration and development is possible across the vast majority of the Snake River Plain study area. Cadastral maps show those areas in which geothermal exploration and development can be expected to be closed or restricted. Among the closed or restricted areas are certain Federal lands (BLM, NFS, Wilderness, and DOD), State lands, Tribal lands, and lands designated as environmentally sensitive under various jurisdictions. Private lands may be accessible for geothermal development on a case-by-case lease basis. Land accessibility and geothermal leasing status will be examined in finer detail in the selected fairway and prospect areas identified in Phase 2 of the SRP Geothermal Play Fairway Analysis Project.

2.2. GIS Methodology

Our GIS approach is similar to that used by earlier investigations that pioneered the use of ArcGIS in geothermal exploration (*e.g., Coolbaugh et al, 2002, 2005; Noorollahi et al, 2008; Trumpy et al, 2015*). Data were imported into ArcGIS shapefiles, with each shape file representing a different data layer. GIS specialists at the USGS geothermal program prepared Python® scripts to automate the process of risk segmenting using ArcGIS functions and custom processing. Our Python scripts are *repeatable, scalable, modifiable, transferrable*, and when complete, will *automate* the task of data analysis and the production of CRS and CCRS maps. A complete description of the data layers and supporting files may be found in the Geothermal Data Repository (*https://gdr.openei.org/submissions/1287*).

2.2.1 Terminology

We have developed a uniform terminology for discussing the various GIS layers as data move through the assembly of the CRS maps. These terms apply to all data types and allow the science team to converse more cogently with the GIS technicians. These layers are: (1) Data layers, (2) Evidence Layers, (3) Confidence layers, (4) Risk maps, (5) Common Risk Segment (CRS) maps, and (6) the Composite Common Risk Segment map.

(1) Data Layers represent the raw data imported into ArcGIS prior to data processing. These data may include points, lines, or polygons, all of which must include geographical coordinates.

(2) Evidence layers are created by applying geostatistical functions to *Data layers*. Typically, these include application of either a *density function* (simple or kernel density), which calculates the occurrence of objects within a given area, or a data *interpolation* function, which calculates intermediate values from a finite array of data points. *Simple Density Functions* assess data density by counting all instances of a data type within a specified radius of each data point and dividing by the area of the search radius; this density value is applied to the entire area. *Kernel Density Functions* assess data density (e.g., vents, fault segments) by counting all instances of a data point within a specified radius of a single point and dividing by the area of the search radius. This density is then distributed from a maximum at the location of the data point to zero at the full radius of the search area using a quadratic function. Data points may be weighted

prior to counting. For example, fault segments are weighted by both dilation tendency and slip tendency, as determined by the 3DStress software, on a scale from zero to 1.0.

Data interpolation for point or line sources is carried out with either a *radial basis function* (RBF), *inverse distance weighted* (IDW), or by *Kriging*, depending on data density and desired result. The RBF and IDW functions are exact interpolators, so no variance or standard errors are predicted. *Empirical Bayesian Kriging* (EBK) is an iterative geostatistical interpolation method that uses an intrinsic random function as the kriging model, taking into account uncertainties in estimating the semivariogram. Standard errors of prediction are more accurate than other kriging methods, and the results are more accurate for small datasets than other kriging methods (*Arc Online Help Manual*).

(3) Confidence Layers reflect data uncertainties, which are assessed using a combination of fuzzy logic (user assigned uncertainty weights for non-interpolated data) and Kriging standard error (a Bayesian method for interpolated data). Examples of non-interpolated data include data derived from geologic mapping, such as volcanic vent locations and faults. The confidence layer for these data is based on published map scale (high certainty for 1:24,000 scale, lower certainty for 1:250,000 scale). Examples of interpolated data are heat flow and groundwater temperatures, which are interpolated from a finite number of well locations. The confidence layers for interpolated data are typically derived from the standard error of the Kriged surface.

Note that each data type will have its own confidence layer, which depends on how the data are collected, and on the distribution of data points. For example, heat flow and groundwater temperatures both have confidence layers derived from the standard error of their interpolated surface, derived by *Empirical Bayesian Kriging (EBK),* but their confidence layers are distinct because each has its own standard error surface. This standard error surface depends not only on the distribution of data (*e.g.,* distance to its nearest neighbors), but also on the contrast in values between adjacent data points, with large contrasts increasing the standard error.

(4) Risk Maps are the result of applying the Confidence layer to the Evidence layer. Risk maps are produced for each primary evidence layer by multiplying each pixel in the evidence layer (which shows likelihood of a resource characteristic being present) with its corresponding pixel in the appropriate confidence layer (which assesses likelihood of data being reliable or complete). Since each evidence layer has its own confidence layer, this calculation must be made before the layers for different evidence types are assembled into the *Common Risk Segment* map.

(5) Common Risk Segment (CRS) Maps are the weighted sum of a multiple *Risk Maps* within a given category, producing a CRS map for each characteristic: Permeability, Heat, and Seal. Because each CRS map represents the sum of multiple risk layers, and not all layers are equally diagnostic, the sum is weighted to emphasize those layers that are thought to contribute most strongly to the characteristic in question, or to balance layers with different data densities that may contribute equally to that characteristic.

(6) Composite Common Risk Segment (CCRS) Maps are the weighted product of the three *Common Risk Segment Maps*, one each for *Permeability, Heat, and Seal*. It highlights areas where all three critical elements required for a viable geothermal resource are present.

2.2.2 GIS Programming

The main GIS workflow of the study is carried out using Python®. Python is a scripting language that can execute any geoprocessing tool in ArcMap and can be used to perform custom data manipulation and organization. Python scripts are used in ArcGIS to automate data processing and to enhance the flexibility of the data analysis. As noted above, our Python scripts are repeatable, scalable, modifiable, transferrable, and when complete, will automate the task of data analysis and the production of CRS and CCRS maps. Our ultimate goal is to produce a toolkit that can be imported into ArcGIS and applied to any geothermal play, with fully tunable parameters that will allow for the production of multiple versions of the CRS and CCRS maps in order to test for sensitivity and to validate results.

Density functions are used for data that are by nature discontinuous, and where the geographic location of that data is important. Examples include fault segments and volcanic vents. *Simple density functions (SDF)* count the number of like objects within a given radius (*e.g.,* 10 km) and calculate the density by dividing the sum by the area of the search radius. The calculated density is assigned to the entire radius. *Kernel density functions (KDF)* distribute the calculated density to the center of the area and use a quadratic function to reduce the density to zero at the circumference of the search radius. In our project, for example, we apply a kernel density function to individual fault segments twice: first using *dilation tendency* as the weight factor, then using *slip tendency* as a weight factor.

Interpolation is used for properties that are by nature continuous, but which can only be sampled at specific points. There are a number of interpolation methods in the *Geostatistical Analyst Wizard*, such as *Inverse Distance Function (IDF)* and *Radial Basis Function (RBF)*. Our preferred method for interpolation is *Empirical Bayesian Kriging (EBK)*, a geostatistical process that produces an estimate of the value of a property at each point on a continuous surface, and a standard error surface that quantifies the uncertainty in the interpolation. *Standard Kriging* methods use existing data locations to predict the values at unknown locations. EBK uses existing data as a starting point to estimate data values at all locations, then uses those values to create a new set of starting values using an intrinsic random function, and so on through a series of iterations. As a result, EBK returns a more generalized interpolation and a more robust estimate of standard errors.

Because the results of density functions and interpolations can cover a wide range of values, in some cases it is convenient to normalize the results (typically from 0 to 1.0) in order to compare them more easily. In other cases, the un-normalized values are preferred in order to retain information on scale.

After *Evidence Layers* are produced from the raw data layers, they are sampled at a specified grid size to produce a table that arrays grid locations versus the returned values for each individual evidence layer. This can be thought of as a raster array consisting of pixel elements. For this project we chose a grid size of 2 km square; this can be increased for broader scale studies, or decreased for higher resolution in smaller study areas. Confidence layers are sampled at the same grid scale and confidence values for each grid cell (pixel) are paired with the

appropriate evidence value. *Risk Maps* are produced by multiplying the value of the evidence layer pixel times its corresponding confidence pixel:

[Evidence Layer1][Confidence Factor1] + [Evidence Layer2]*[Confidence Factor2] + [etc]*

To produce the *Common Risk Segment (CRS) maps*, multiple risk maps are combined using the same approach: the value of each grid cell (pixel) in each risk map is added to the value of its corresponding grid cell in another risk map. The values for any Risk Map can be weighted using intra-CRS weight factors that are applied before the Risk Maps are summed:

[Risk Map 1][RM1 Weight Factor] + [Risk Map 2]*[RM2 Weight Factor] + [etc]*

Similarly, the final *Composite Common Risk Segment (CCRS)* map is produced by taking the values for each grid cell in a CRS map and adding it to the values for the corresponding grid cells in the other CRS maps. In all cases, these values may be multiplied by an inter-CRS weight factor before summation, as with Risk Maps (above).

The overall workflow for these processes is shown in Figure 2. The CRS map for Heat Source reflects the summation of 5 separate risk maps (*heat flow, volcanic vents, groundwater temperatures, thermal reservoir temperatures and He-isotope anomaly*) produced by multiplying each evidence layer by its confidence value. Similarly, the Permeability CRS map reflects eight different evidence layers (*mapped faults, magnetic lineations, deep gravity lineations, and mid-crustal gravity lineations*, each summed once with *dilation tendency* weight and *slip tendency* weight). The CRS for Seal is simply sum of lacustrine sediment and aquifer distribution. Finally, the CCRS map is the weighted sum of the three CRS maps.

This workflow was automated with the use of Python scripts, which allow the user to set weight factors for confidence layers (typically 1.0 for highest confidence to 0 for no confidence), kernel density functions (*e.g.,* age and size factors), and for intra-CRS and inter-CRS Risk Maps. Other user selectable values include the grid cell size, search radius for density functions, and upper and lower limits for heat flow values. Intra- and inter-CRS weight factors are taken as integers and the ability to vary these factors will be a major issue in sensitivity analysis.

At this point the Python script must be edited manually to change these values, but Phase 2 work will include building an *ArcMap Toolbox* tool to allow control of some values. This will allow the user to exclude certain input values that are not relevant to their study area by setting the weight factor to zero, and to adjust other values to determine the settings that are most appropriate to their study. It will also allow users to undertake a sensitivity analysis to see which values are most affected by small changes in their component weight factors, and to validate the chosen values against known resources.

The resulting maps may be visualized using *equal intervals*, *equal areas* (*quintiles*), or *natural breaks,* which are based on natural groupings inherent in the data. We generally use *equal interval segments* for evidence layers, and *natural break segments* for CRS and CCRS maps, in order to emphasize natural groupings of regions with similar characteristics.

2.2.3 Confidence

Confidence levels are assigned using a *fuzzy logic* approach (user defined limits that range from zero to one). Fuzzy logic is appropriate for geologic data sets because most geologic data cannot be assigned *Boolean* "1 or 0" (yes-no) values. For interpolated surfaces using EBK the values are chosen based on the standard error map, with high confidence at the lowest standard errors (1.0) and progressively lower confidence at higher standard errors (values less than 1.0). If standard error exceeds a given cutoff value, the confidence is set to zero, effectively eliminating that region from consideration. For example, for the RTEst multicomponent geothermometer, grid cells in the confidence layer with a standard error greater than ±30ºC are set to zero confidence.

For density functions of data based on geologic mapping (*e.g.,* faults), the scale of mapping and map publication are significant: are all faults in a given map area indicated on the geologic map? To what extent were mapped faults simplified due to publication scale? As a result, for map-based data we rely on map scale as measure of confidence, with larger scale maps (1:24,000) having higher confidence scores than small scale maps (1:250,000).

ArcGIS segments data using a semivariogram, which describes the distribution of data in space or more precisely, the "*spatial autocorrelation of the measured sample points*" (*ArcGIS Resource Center*). The semivariogram is used by ArcGIS processing to segment spatial data, as described above, using *equal intervals*, *equal areas* (*quintiles*), or *natural breaks.* The segmented data represent the probability of values occurring within a given segment.

We note that it is not appropriate to take variation about a mean of sample measurements as a measure of data confidence since the variation is in fact the signal we are trying to measure. For example, the confidence level for our gravity data is based on station spacing and on the inherent measurement error at each station. Variations about the mean are what produce the horizontal gradients used to infer the location of subsurface structural discontinuities.

2.3 Evaluation of Stress and Strain

Faulds et al. (2013) have shown that most productive hydrothermal resources in the Great Basin occur in complex fault interaction zones that have dilational and slip components that result in open fractures along some part of the fault. In order to assess the impact of stress and strain to reservoir favorability, we have applied standard methods for assessing the effects of stress and strain to our study area. These calculations were applied to each segment in a digitized fault or lineament, and the results were used to weight that segment in the kernel density functions described above.

2.3.1 Slip and Dilation Tendency

Critically stressed fault segments have a relatively high likelihood of acting as fluid flow conduits (*Zoback and Townend, 2001; Ito and Zoback, 2000; Townend and Zoback, 2000; Barton et al., 1995, 1998; Morris et al., 1996; Sibson, 1994, 1996)*. As such, the tendency of a fault segment to slip (slip tendency; T_s) (*Morris et al., 1996*) or to dilate (dilation tendency; T_d) (*Ferrill et al., 1999*) provides a quantitative indication of the likelihood of a certain fault segment

to be critically stressed, for either slip or dilation, relative to another fault segment. The slip tendency of a surface is defined by the ratio of shear stress to normal stress on that surface:

$$T_s = \tau / \sigma_n \qquad (\textit{Morris et al., 1996})$$

Dilation tendency is defined by the stresses acting normal to a given surface:

$$T_d = (\sigma_1 - \sigma_n) / (\sigma_1 - \sigma_3) \quad (\textit{Ferrill et al., 1999})$$

where τ is the resolved shear stress on the fault plane, σ_n is the resolved normal stress on the fault plane, σ_1 magnitude of the minimum stress, and σ_3 is the magnitude of the maximum stress. Slip and dilation tendency are both unitless ratios of the resolved stresses applied to the fault plane by ambient stress conditions. Values range from a maximum of 1, a fault plane ideally oriented to slip or dilate under ambient stress conditions to zero, a fault plane with no potential to slip or dilate. Slip and dilation tendency values were calculated for each fault segment and each discrete magnetic and gravity lineation in the focus study area. As dip is not well constrained or unknown for many faults mapped within the study area, fault dip was assumed to be 70° for all faults. Magnetic and gravity lineations are assumed to be vertical. The resulting along-fault and fault-to-fault variation in slip or dilation potential is a proxy for along fault and fault-to-fault variation in permeability or fluid flow potential.

2.3.2 Stress Magnitudes and Directions

Azimuthal stress field variation within the study area was approximated based on regional published data and the data from the World Stress Map (www.world-stress-map.org/) *(Blake and Davatzes, 2011, 2012; Hickman and Davatzes, 2010; Moeck et al., 2010; Moos and Ronne, 2010; Heidbach et al., 2008; Davatzes and Hickman, 2006; Robertson-Tait et al., 2004; Hickman et al., 1998, 2000*) and unpublished data (*Kessler, 2013*). For faults within the study area we applied either a normal faulting stress regime, where the vertical stress is larger than the maximum horizontal stress, which is larger than the minimum horizontal stress ($S_v > S_{Hmax} > S_{hmin}$) or a strike-slip faulting stress regime where the maximum horizontal stress is larger than the vertical stress which is larger than the minimum horizontal stress ($S_{Hmax} > S_v > S_{hmin}$). The normal or strike-slip polarity of the applied stress field was determined from the polarity of the focal mechanisms used to calculate stress in the World Stress Map (Heidbach et al., 2008). For each fault segment, the normal or strike slip stress field polarity was selected based on the nearest focal mechanism to that fault segment. Based on visual inspection of the limited stress magnitude data in and proximal to the study area, we used stress magnitudes such that $S_{hmin}/S_{Hmax} = 0.527$ and $S_{hmin}/S_v = 0.46$, which are consistent with complete and partial stress field determinations from Coso (California), Desert Peak, Fallon and Dixie Valley (Nevada) (*Blake and Davatzes, 2011, 2012; Hickman and Davatzes, 2010; Davatzes and Hickman, 2006; Robertson-Tait et al., 2004; Hickman et al., 1998, 2000)*.

2.3.3 Strain

Each fault segment in the study area was also parameterized based on strain. Spatial correlations between high-temperature geothermal systems and both Holocene faulting *(Bell and Ramelli, 2007, 2009)* and elevated strain-rate *(Faulds et al., 2012)* suggest that active tectonism is an important factor in generating and maintaining permeability pathways necessary for robust geothermal upflow. Deformation rates, calculated based on geodetic data and quantified as the 2nd invariant of the strain-rate tensor *(Kreemer et al., 2012)*, were applied to each fault segment and are considered as a proxy for permeability.

2.4 Thermal Modeling of the WSRP Geothermal System

A hydrothermal system contains a convecting fluid mixture that is heated at depth and then rises towards the surface as a consequence of buoyancy. The system is not only nonisothermal but is also in a continuous state of flow. The development of a natural-state model requires a variety of geological, geophysical, geochemical and hydrological data sets. A computer-based simulation of the natural fluid and heat flow in the geothermal reservoir offers the framework for synthesizing these evolving data sets into an integrated geohydrological model. Such natural-state modeling also helps in the evolution of the conceptual model by revealing inconsistencies and physical shortcomings in the preliminary conceptual model of the reservoir.

Assessment of the natural-state model was carried out by comparing theoretical predictions of quantities such as reservoir pressure and temperature, and surface heat and mass discharge with field measurements. This process provides insight into reservoir parameters such as formation permeability distribution, and boundary conditions for heat and mass recharge at depth. The natural-state model can also be used to evaluate the effects of gaps in the database on future reservoir performance. Planning of future drilling and well tests for reservoir verification can then be based on resolving major uncertainties in the evolving model for the geothermal reservoir. For fields that have not yet been exploited, or have been in operation for only a few years, the natural-state information comprises the bulk of the data available for reservoir modeling.

Determination of the natural state requires solving an inverse problem and is accomplished by a procedure amounting to successive approximation. The quasi-steady (or stationary) state depends mainly upon the boundary conditions imposed upon the perimeter of the system volume (e.g., pressure, temperature, deep heat flux, and hot fluid sources) and upon the distributions of formation properties (such as porosity and permeability) believed to prevail within it. Thus, given estimates of the boundary conditions and formation properties, the corresponding stable state is found. This solution may be examined to see how well it matches known facts about the system (such as measured downhole pressures, temperatures, fluid state, advective zones within the reservoir and distribution of surface discharge). Appropriate adjustments are then made in the boundary conditions and/or formation properties in an effort to improve agreement between measurements and computed results, and the problem is solved again. In this way, the natural state is found in an iterative fashion involving repetitive calculations of the pseudo-steady state.

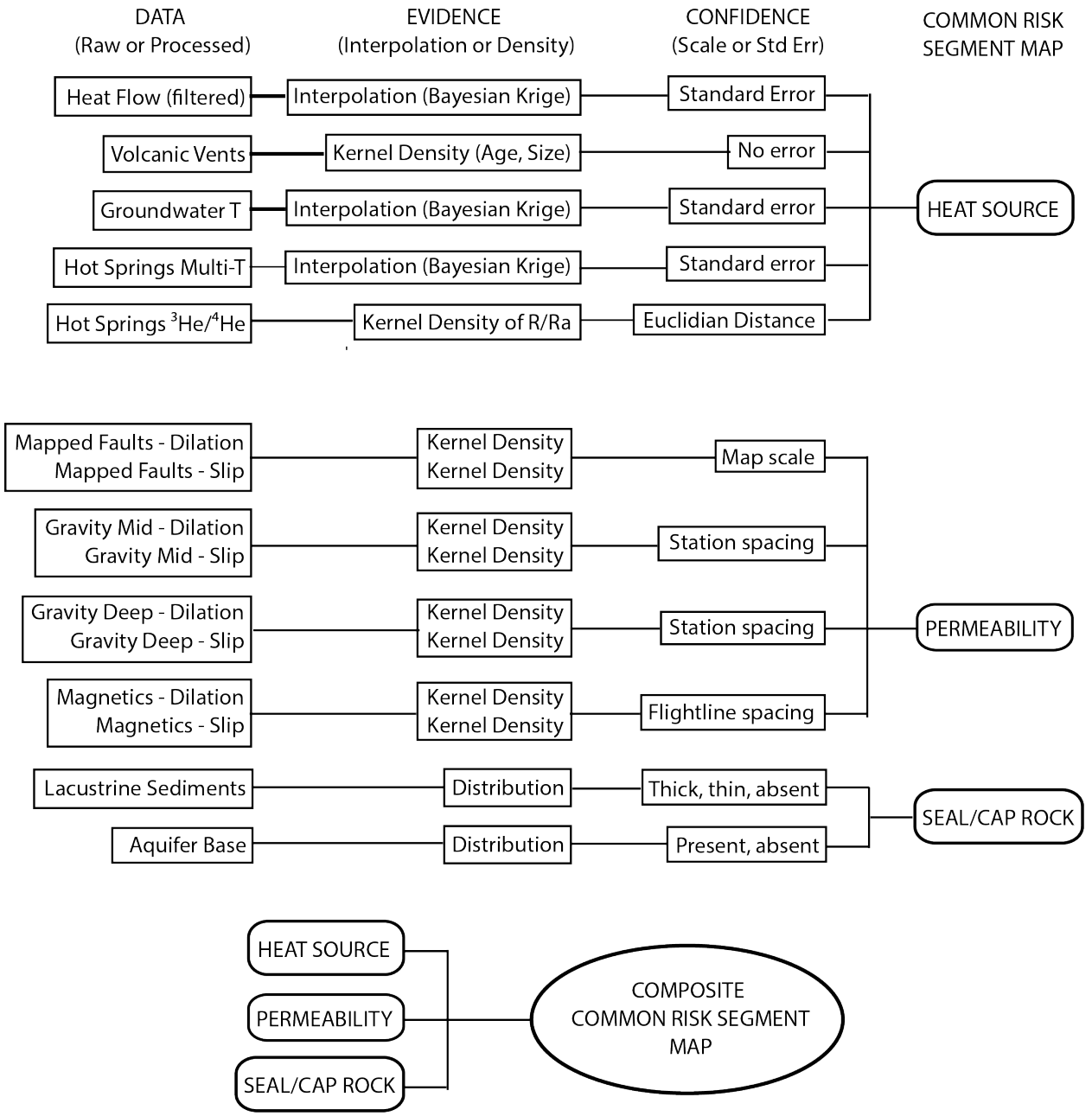

Figure 2. Flow chart showing data layers processed in ArcGIS and their confidence evaluation (1-risk), grouped by HEAT, PERM, and SEAL. Lineaments are processed for dilation and slip before processing to evidence layers. Kernel density functions quantify the distribution of point/line sources, while Empirical Bayesian Kriging interpolates discretely sampled functions to estimate continuous functions. Seals are evaluated as simply present or absent.

A complete description of the methodology and results from Phase 1 is presented in *Mountain Home Geothermal Area: Preliminary Natural State Model*. This report and related publications are found in the Geothermal Data Repository: *https://gdr.openei.org/submissions/943.*

3.0 PHASE 1 RESULTS: APPLICATION TO CONCEPTUAL MODELS

In this section, we discuss the application of our approach to our conceptual models for the different play types, with particular emphasis on basaltic sill complex plays, since the other play types have long been recognized and discussed in the literature. In contrast, the *SRP basalt sill* complex play type has only recently been differentiated from related play types, e.g., volcano-based plays and Basin-and-Range type plays (*Nielson and Shervais, 2014*). The SRP basaltic sill complex play type has characteristics intermediate between these related play types, warranting an extended discussion of how the evidence layers relate to heat, permeability and seal for this type of play.

3.1 Application to the Basalt Sill Conceptual Model

Preliminary conceptual models were presented by *Nielson and Shervais (2014)* for the SRP geothermal system, in which the ultimate heat source is mantle-derived mafic magma that intrudes the middle to upper crust to form a long-lived sill complex-layered mafic intrusion, and by *Nielson et al (2015)* for adaption of Play Fairway Analysis from petroleum systems to geothermal systems. Below we outline the application of our approach described above to these conceptual models. The maps in this section are Risk Maps, derived from evidence layers (density functions or interpolations) by application of their confidence layers. Evidence layers, CRS maps, and CCRS maps produced during Phase 1 are archived in the Geothermal Data Repository (GDR) (*https://gdr.openei.org/submissions/733*). Map files in kmz format are also archived in the GDR *(https://gdr.openei.org/submissions/734)*.

3.1.1 Source (Heat)

There are several potential indicators of heat source: heat flow, volcanic vent distribution, groundwater temperatures, and hot springs or wells. Heat flow is uniformly high across much of the SRP (~90 to 110 mW/m^2), except in the ESRP, where shallow thermal flux is masked by advective transport of heat through the immense Snake River Aquifer (Figure 3). The influence of the aquifer on the heat flow pattern is demonstrated by comparing heat flow determined using all thermal gradient wells with heat flow determined using only those wells deep enough to penetrate the aquifer in the east. The effect of the aquifer is to suppress conductive gradients above and within the aquifer, so that temperatures greater than 150ºC require wells deeper than 2.5 to 3.0 km (i.e., up to 1 km deeper in the ESRP). This effect can be corrected using mapped distribution and thickness of the aquifer (*e.g., Whitehead, 1986; Lindholm 1996*), or we can use heat flow values calculated from both shallow and deep wells in the eastern SRP. This results in a heat flow map that already reflects the effects of aquifer cooling.

In contrast, areas of the CSRP and WSRP lie outside the influence of the regional aquifer and are characterized by high thermal gradients (~65-75ºC/km) and high heat flow (~100-110 mW/m^2). However, a small aquifer exists along the northern margin of the WSRP between Boise and Mountain Home that appears to have a similar effect on heat flow measurements in that area. We have accounted for this effect by culling shallow wells with low heat flow from our database in areas that are affected by aquifer cooling.

Because the recent transmission of lava to land surface is indicative of subsurface emplacement of magma (heat source), an alternate measure of potential heat is the distribution of young volcanic vents. These vents are generally younger (<780 ka) and more common in the ESRP, with very dense concentrations found in Craters of the Moon-Great Rift area, on the INL site, along the Axial Volcanic Zone, and in the Spencer-High Point rift area. Young vent clusters also occur in the Blackfoot volcanic field of SE Idaho, and in the WSRP, where they are often characterized by primitive compositions and high mantle potential temperatures (*Shervais and Vetter, 2009*). The WSRP also has high concentrations of slightly older early Pleistocene vents, often in the form of hydrovolcanic mounds or maars, indicating eruption through water or water-saturated sediments. Vents of the Owyhee Plateau and the Oregon-Idaho Graben are largely late Miocene in age, with rare Pliocene vents. The youngest vents (≤50 ka) are found in the Craters of the Moon-Great Rift cluster; however, almost all of these vents lie within the Craters of the Moon National Monument and are thus off-limits to geothermal development.

Groundwater temperatures are a proxy for heat flow because they reflect warming of meteoric water (often in the form of snow melt) as it moves slowly through an aquifer. This effect is seen most clearly in the ESRP-CSRP, where groundwater with temperatures around 9ºC infiltrates the NE end of the SRP and gradually warms to about 13-14ºC in the CSRP (*e.g.,* Kimama well). *Blackwell et al. (1992)* calculated that this increase in temperature along the hydrologic gradient requires about 330 MW of heat energy. This in turn requires ~190 mW/m^2 heat flow – higher than typically observed heat flow. In the WSRP, groundwater ranges from ~13-16ºC, with higher temperatures of 20-30ºC in thermal areas near Boise and Grandview. The base temperature is similar to that measured at the western end of the CSRP, suggesting a similar heat flux, with the higher temperatures reflecting advective transport.

A final set of potential indicators of heat source, hot springs and thermal wells, are most commonly located on the margins of the SRP, e.g., the Boise Thermal District and the Twin Falls Thermal District, both of which are characterized by moderate fluid temperatures (30-40ºC) and have been used for district space heat for decades (*e.g., Street and DeTar, 1987*). The most prominent hot spring districts are Banbury-Miracle (on the Snake River west of Twin Falls) and Magic-Camas (north of the Mount Bennett Hills). Both areas are associated with regional-scale fault intersections and are characterized by high reservoir temperatures calculated using multicomponent geothermometers (*Neupane et al., 2014*) and high $^3He/^4He$ ratios (*Dobson et al., 2015*). The high $^3He/^4He$ isotope ratios imply recent heat source emplacement (magmatic input) from great depth along faults which penetrate the crust. High temperature thermal fluids (~150ºC) were also encountered in an exploration well on Mountain Home Air Force Base (*Shervais et al., 2012; Lachmar et al., 2012; Nielson et al., 2012*), indicating a previously unidentified permeable zone at depth.

We quantified these various measures of heat by combining interpolated evidence layers (heat flow, groundwater temperatures) and density function evidence layers (density of volcanic vents), along with spot data for thermal springs and wells, e.g., multicomponent thermometry and $^3He/^4He$ isotope anomalies. Heat flow and groundwater temperatures were interpolated using an empirical Bayesian Kriging function in ArcGIS, whereas volcanic vents were processed using

a kernel density function weighted by age and size, as described in Methods. The resulting CRS map for Heat Source (Figure 3) highlights several areas with high thermal potential, discussed in Section 4.0.

3.1.2 Reservoir/Recharge (Permeability)

Reservoir and recharge permeability is assessed using the weighted sum of mapped faults, magnetic lineaments, upper to mid-crustal gravity lineaments, and deep crustal gravity lineaments, each processed for both slip tendency and dilation tendency. Each of these data layers was processed using a kernel density function in ArcGIS to produce eight evidence layers. In order to address data confidence (a measure of risk), each evidence layer is multiplied by its corresponding *confidence layer* to produce a *Risk Map* for that evidence layer. Finally, all of the Risk Maps are summed to produce the *Common Risk Segment* map for permeability (Figure 3).

Risk maps for the deepest lineaments are weighted more heavily than those for shallow (magnetic) or surface features (mapped faults), which reflect the difficulty in imaging deeper structures and their correlation with large structural offsets in the basement. It also reflects the fact that surface faults are mapped with great precision in some areas, resulting in high fault densities in places where there may be little structural offset. Weights were adjusted empirically to ensure that known subsurface structures (*e.g.,* the seismically imaged central gravity high in the WSRP) and our training sites appear on the CRS map as favorable structures.

Faulds et al. (2013) have shown that most productive hydrothermal resources in the Great Basin occur in complex fault interaction zones that have a dilational component that results in open fractures along some part of the fault (i.e., accommodation zones, fault intersections, and step-overs). A proxy for fault intersections at the regional scale of this study is fault density, where high fault densities tend to favor multiple intersections. In Phase 2 studies we will focus on specific regions and add fault interaction zones as an evidence layer.

3.1.3 Seal

According to our model *(Nielson and Shervais, 2014)*, the SRP geothermal system has two potential seals: (a) fine-grained lacustrine sediments, which are largely impermeable and (b) self-seal of volcanic rocks by hydrothermal alteration. The first is relatively easy to map; the second much more difficult. The distribution of lake sediments is well known in the WSRP, where regional formations consisting largely of lacustrine sediments are widespread (e.g., Bruneau, Glens Ferry, and Chalk Hills Formations; early Pleistocene, Pliocene, and Miocene in age). These formations were deposited by paleo-Lake Idaho, which filled the WSRP for much of its existence, and provide an impermeable seal 0.5-1.6 km thick (*Wood and Clemens, 2002*). These formations continue into the CSRP, but gradually pinch out from west to east (e.g., Jean et al., 2013). Their extent is well known and can be delineated using the state geologic map.

The Camas Prairie, north of the Mount Bennett Hills, is another large sedimentary basin with extensive basin fill, as documented by *Cluer and Cluer (1986),* based on mapping and gravity surveys. They document up to 500 m of sedimentary fill, with a depo-center running EW along the axis of the prairie. Detailed well logs document a basin-wide layer of clay ~30 m thick

that extends from Camas Creek in the north to the Mount Bennett Hills in the south (*Walton, 1962*). In the ESRP, there are three areas with lake deposits: the Burley area, with up to 100m of sediment, the American Falls area, with 10-30m of sediment, and paleo-Lake Terreton, along the northern margin of the northeastern SRP (*Neal Farmer, IDWR, personal communication, 2010; Desborough et al, 1989; Phillips and Welhan, 2006, 2011; Anderson et al, 1996, 1997*). All of these paleo-lake deposits are attested in numerous well logs, so their areal extent is relatively well established despite the general lack of surface outcrops. The outline of paleo-lake Burley appears to coincide with younger sedimentary deposits in Burley. Paleo-lake Terreton is the least well known, forming thin horizons at varying depths in the general region of current Mud Lake.

For a lacustrine sedimentary seal to be effective, it must be relatively thick and continuous. We grouped the lake seals into three groups: > 100 m thick (paleo-lake Idaho and Camas Prairie), 30-100 m thick (paleo-lake Burley), and <30 m thick (paleo-lakes American Falls and Terreton). We assigned the highest score for seal effectiveness to the thickest sediments, a lower score to the 30-100 m group, and consider any sediments <30 m thick to be too thin to form an effective seal (Figure 3).

For a traditional geothermal reservoir within volcanic deposits at depth, a permeable zone needs to be capped by a zone of alteration. Because volcanic deposits are highly heterogeneous, and the thermal resource is at great depth, self-seal by alteration is difficult to ascertain without core data. *Sant (2012)* has documented that the base of the Snake River Aquifer is controlled by the onset of clay alteration in basalt groundmass. Thus, we interpret the base of the Snake River Regional Aquifer to represent the top of a hydrothermal seal that confines hydrothermal systems below it as well as the aquifer above.

These risk maps combine to create a *CRS map for seal* (Figure 3). This Seal CRS shows that adequate seal should be present throughout most of the SRP.

3.2 Application to Other Play Types

Other play types, *e.g.,* silicic domes or Basin-and-Range plays, have different conceptual models and thus different requirements for CRS maps. Nonetheless, our methodology, outlined above, is still applicable to these plays, and the same tools can be used to evaluate them. Below we outline the application of our approach described above to these conceptual models.

3.2.1 Source (Heat)

Potential indicators of heat source for *Basin-and-Range* and *Batholith* plays include heat flow, groundwater temperatures, and data from hot springs or wells. Since these plays are not magmagenic (at least outwardly), the density and distribution of volcanic vents is not a factor. As a result, we have produced a separate heat CRS map for these plays that does not include vent density (volcanic vent evidence layer weight set to zero).

For *silicic domes and cryptodomes*, the dominant indicator of heat source is the dome itself, supplemented by heat flow, groundwater temperatures, and data from hot springs or wells. The occurrence of basaltic vents is encouraging but not required for this play type. Due to the limited

occurrence of silicic domes in our study area, we have not produced a separate heat CRS map for this play type.

3.2.2 Permeability (Reservoir/Recharge)

Reservoir and recharge permeability for *Basin-and-Range* and *Batholith* play types is assessed using the same factors applied to the *Basalt-sill* play type: mapped faults, magnetic lineaments, upper to mid-crustal gravity lineaments, and deep crustal gravity lineaments, each processed for both slip tendency and dilation tendency. The permeability CRS maps for these plays are thus identical to that for the basalt-sill play. *Silicic domes and cryptodomes* are inferred to create their own permeability along the margins of the domes during intrusion, which limits their permeability CRS to an annulus around the perimeter of the dome. However, if a dome is associated with a fault-controlled lineament, the hydrothermal reservoir may extend away from dome along this lineament. Because of their limited extent, we have not produced a separate permeability CRS map for silicic domes.

3.2.3 Seal

Potential reservoir seals for the other play types (*Basin-and-Range, Batholith, and Silicic domes/cryptodomes*) are basically the same as for the basalt-sill play type: (a) fine-grained lacustrine sediments, which are largely impermeable and (b) self-seal by hydrothermal alteration. In general, for these plays, self-seal is likely to be more important than clay-rich lacustrine sediments, although clay-rich sediments are important in some Basin-and-Range plays. Given the difficulty in assessing the existence or extent of self-seal in the subsurface without drill data, we must rely on the basalt-sill play seal CRS for a general assessment and evaluate any potential prospects in the "other" category individually.

3.2.4 Engineered Geothermal Systems (EGS)

Engineered geothermal systems ("hot dry rock") are a special case where primary permeability is low; the only requirement is for high temperatures at shallow depth. These resources are created by fracturing hot rocks at depth to create limited permeability between injection wells (where water is introduced) and production wells (where the heated water is extracted). Our methodology can be adapted to EGS exploration by selecting for areas with high Heat signatures with little or no Permeability. Since primary permeability is not present, there is no need to a seal or cap in EGS systems. As a result, only the Heat CRS map and an inverse Permeability map are needed.

4.0 RESULTS: PLAYS AND PROSPECTS

4.1 Basalt Volcanic-Sill Complex Systems

The primary target for geothermal exploration in the Snake River Plain of southern Idaho is the large, volcanic-hosted system related to the Yellowstone-Snake River Hotspot, described in our conceptual models (*e.g., Nielson and Shervais, 2014*). The heat source for this system is inferred to be a thick (>10 km) mafic sill complex that underlies the entire SRP (*Hill and Pakiser, 1967; Prodehl, 1979; Sparlin et al, 1982; Peng and Humphries, 1998; DeNosquao et al 2009*). The repeated intrusion of mafic sills 100-300 m thick mimics the thermal effect of a single large felsic intrusion, with the youngest sills emplaced into a pre-heated crust that inhibits rapid cooling and crystallization. This sill complex is exposed in the western-most SRP at Graveyard Point (*White 2007*) and has been sampled as xenoliths in the central SRP (*Potter, 2013*). The existence of a layered mafic complex is also attested by cyclic variations in composition of SRP basalts in core (*Shervais et al, 2006; Jean et al, 2013*).

4.1.1 Distribution of Heat

The distribution of heat throughout the SRP volcanic province was assessed using measured thermal gradients, interpolated heat flow values, groundwater temperatures, the distribution of volcanic vents (weighted by age, size, and composition), measured temperatures of thermal waters from springs and wells, calculated ionic and multicomponent temperatures of thermal waters from springs and wells, and the distribution of high $^{3}He/^{4}He$ in thermal waters.

Geochemical and helium isotope data on a limited number of thermal springs and wells were obtained from cooperating projects led by INL and LBNL. Multicomponent geothermometers indicate high reservoir temperatures for hot springs along the southern margin of the Mount Bennett Hills, MH-2 artesian hydrothermal water, Banbury Hot Springs, and hot springs along the margins of the ESRP. Helium isotope data present a similar picture, with high $^{3}He/^{4}He$ ratios found in Camas Prairie hot springs, Banbury hot springs, Arco, and the Blackfoot area. Interestingly, hot springs in the Camas Prairie-Mount Bennett Hills region with high $^{3}He/^{4}He$ ratios do not have the highest multicomponent temperatures, and hot springs with the highest multicomponent temperatures do not have the highest $^{3}He/^{4}He$ ratios.

The *CRS map for Heat Source* (Figure 3) highlights several areas with high thermal potential: (a) large portions of the WSRP, including the Boise thermal district, areas south and west of Boise (Marsing-Kuna area), the Mountain Home area (both the town and Air Force Base (AFB)), the Castle Creek-Bruneau KGRA, and part of Bruneau-Jarbidge eruptive center; (b) the CSRP, including the Camas Prairie-Mount Bennett Hills region, Magic Hot Springs, and the Banbury-Miracle Hot Springs area; and (c) the ESRP, including Craters of the Moon and Great Rift, the Arco area (adjacent to the INL FORGE site), and the Spencer-High Point rift, which trends EW and intersects the margin of Island Park caldera. Each of these areas is discussed in detail in following section (Section *4.3: Potential Prospects – An Assessment*).

4.1.2 Distribution of Potential Reservoir/Recharge Permeability

Faults are restricted to the margins of the SRP, with high densities in three areas (outside of the Basin and Range regions). Buried structures, defined by high horizontal gradients in the gravity and magnetic anomalies, suggest significant permeability along the northern and southern margins of a major gravity anomaly in the WSRP.

The *Common Risk Segment map for Reservoir/Recharge Permeability* (Figure 3) highlights several highly favorable areas: (a) the WSRP, where high permeability is found in linear trends sub-parallel to the WNW-trend of the western plain range front faults or to the oblique trend of the central gravity high; (b) the CSRP, where high permeability is found in the Camas Prairie-Mt Bennett Hills area, near Fairfield, Idaho; (c) the ESRP, focused largely on the Arco rift zone that extends northward up the Big Lost River valley and southward past Big Southern Butte; and (d) the Blackfoot-Gem Valley region of SE Idaho. The Arco rift is notable because it encompasses the range front fault responsible for the M 6.9 Borah Peak earthquake of 1983, which created new scarps up to 100m high (*Crone et al, 1987*). It also parallels the Craters of the Moon-Great Rift volcanic rift zone trend.

The dominance of the WSRP is not surprising considering it is in part a graben-like structure with a central horst block forming the axial gravity high (*e.g., Wood 1994*). Structurally controlled permeability is associated both with the range-front faults and with subsurface lineaments inferred from gravity and magnetics. The occurrence of hidden permeability was confirmed by Hotspot well MH-2, which encountered an artesian geothermal system at 1745m depth (*Nielson and Shervais, 2014*). The inflow zone was about 4m thick and characterized by less than 50% core recovery (versus nearly 100% recovery above and below that zone).

The Camas Prairie-Mount Bennett Hills trends are interesting because they lie at sharp angles to both the WSRP and ESRP. An accommodation zone between the Mt Bennett Hills and Danskin Mountains forms a major zone of permeability at the west end of the area, while NW-trending faults with high dilation and slip tendencies intersect the Camas Prairie rift (*Cluer and Cluer, 1986*).

The lack of definable permeability in the ESRP (aside from the Arco rift) implies that Basin and Range structures do not, for the most part, transect the plain.

4.1.3 Distribution of Seals

The *CRS map for Seal* (Figure 3) shows that the distribution of seal is extensive, with most areas having either significant thicknesses of lacustrine sediments (WSRP, Camas Prairie, Burley area) or a basal aquifer seal (ESRP). Hot springs located along the margins of the SRP show where the seal does not exist or has been broached by faulting.

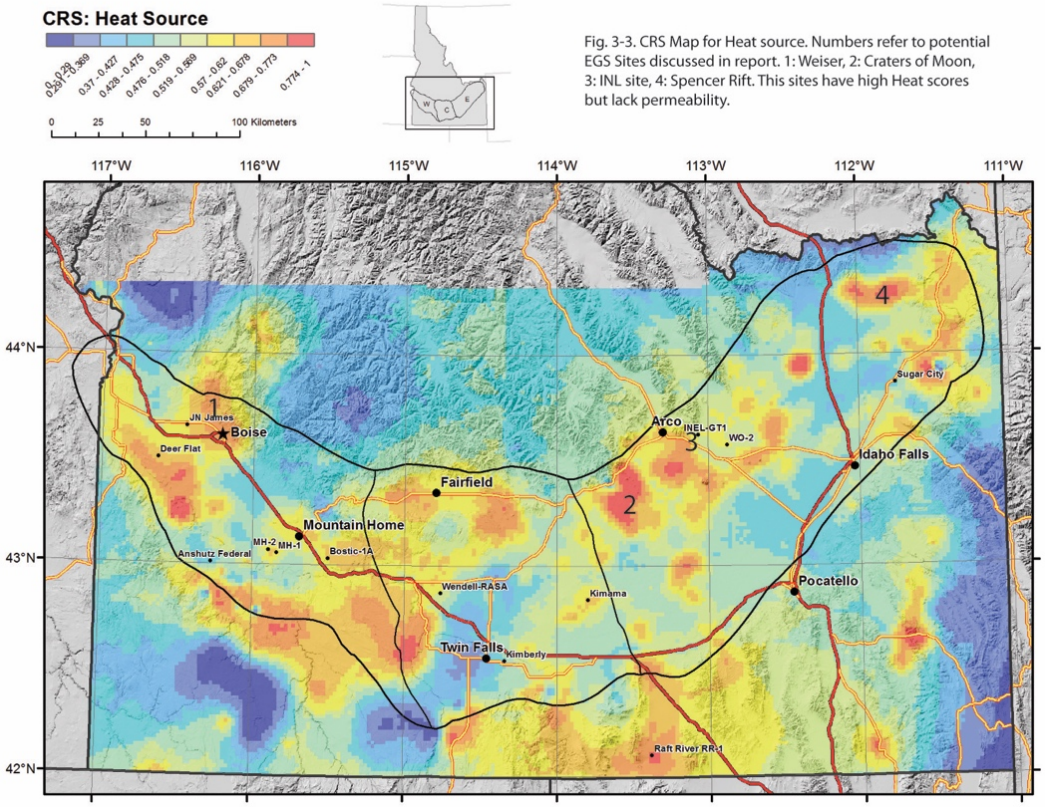

Fig. 3-3. CRS Map for Heat source. Numbers refer to potential EGS Sites discussed in report. 1: Weiser, 2: Craters of Moon, 3: INL site, 4: Spencer Rift. This sites have high Heat scores but lack permeability.

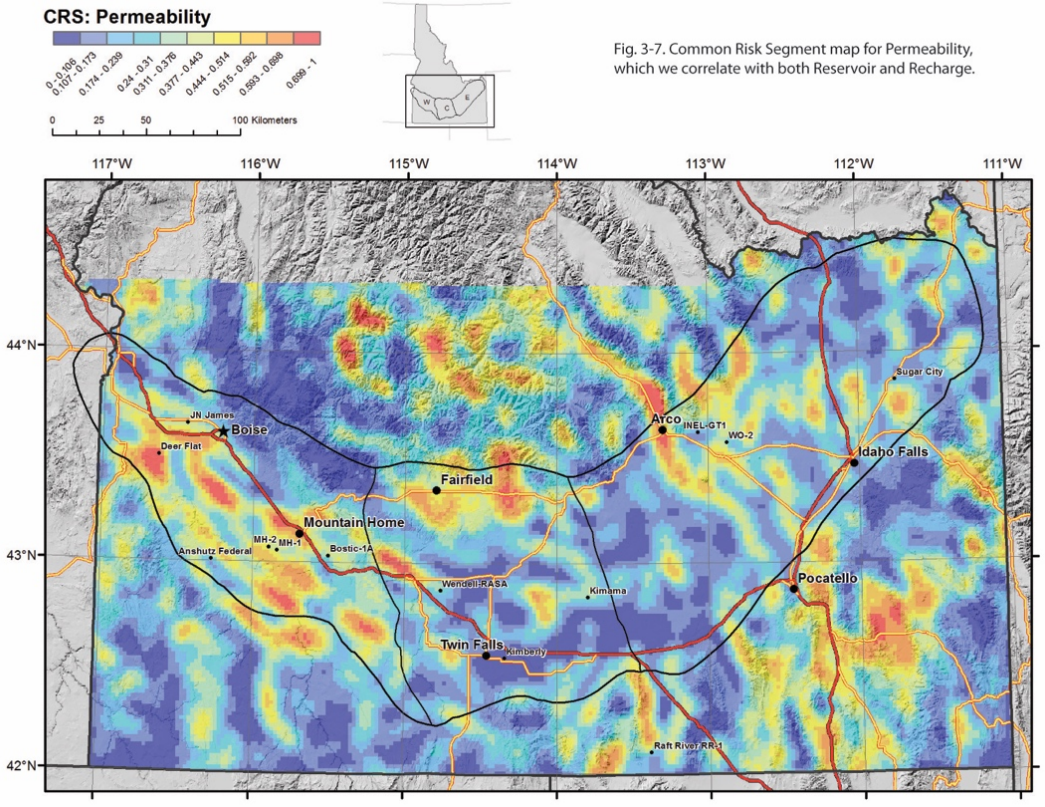

Fig. 3-7. Common Risk Segment map for Permeability, which we correlate with both Reservoir and Recharge.

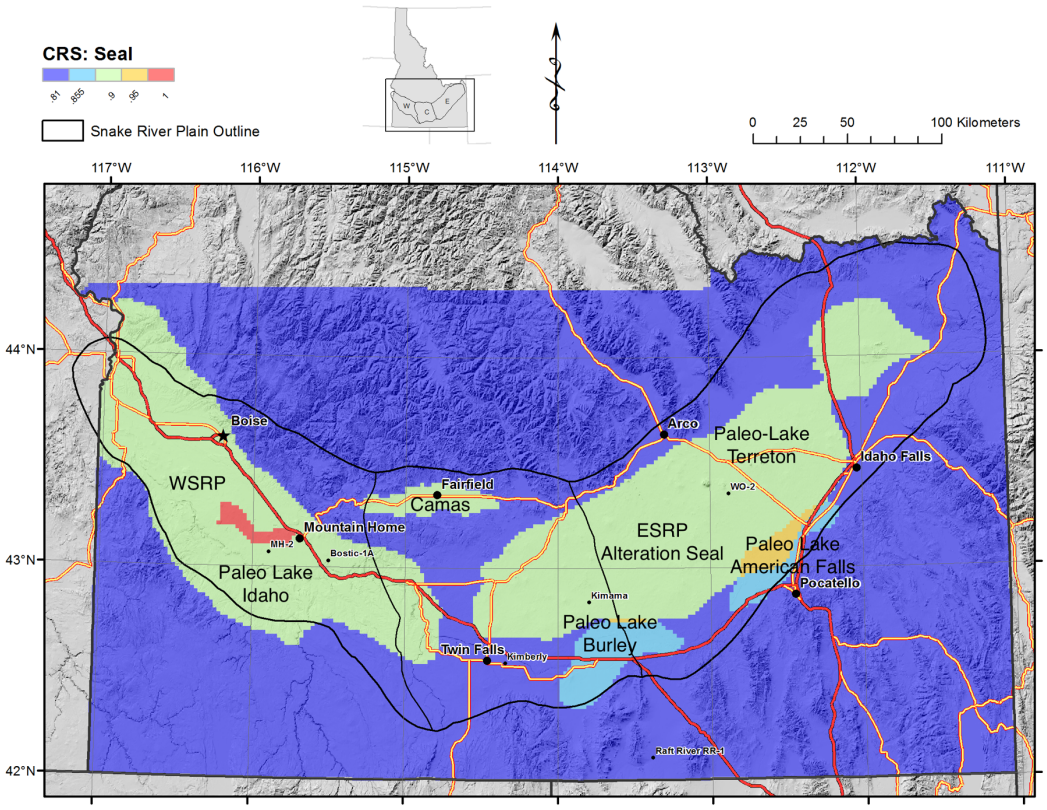

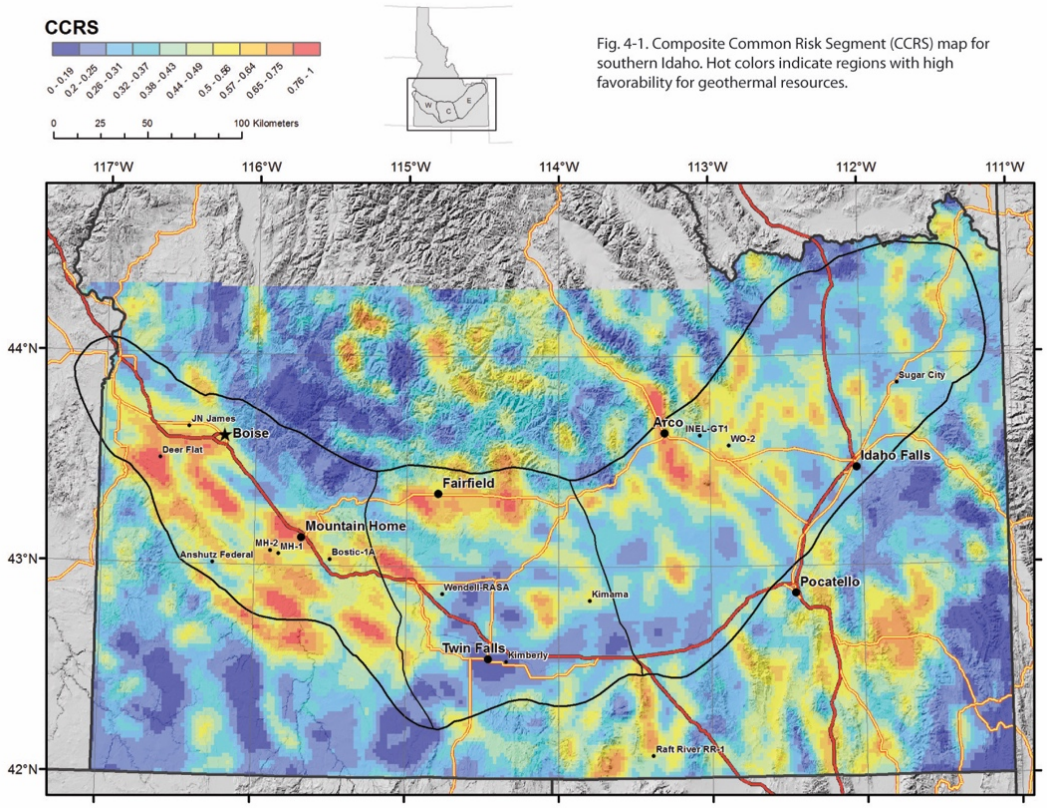

Fig. 4-1. Composite Common Risk Segment (CCRS) map for southern Idaho. Hot colors indicate regions with high favorability for geothermal resources.

Figure 3. Preceeding two pages. Composite Risk Segment (CRS) and Combined Composite Risk Segment (CCRS) maps of southern Idaho. CRS Heat (upper left) estimates distribution of heat, CRS Perm (upper right) shows distribution of permeability, CRS Seal (lower left) shows distribution of seal. The CCRS map (lower right) combines all three, and shows areas with high geothermal potential in which all three factors (Heat, Permeability, Seal) are present. Hot colors = higher potential. The CCRS map is very similar to the permeability map, reflecting the dominant control of permeability on geothermal potential. All maps incorporate confidence. Full size versions of these maps are available in the Geothermal Data Repository (GDR) (*https://gdr.openei.org/submissions/733*). Map files in kmz format are also archived in the GDR *(https://gdr.openei.org/submissions/734)*.

4.2 Other Systems

Other play types in southern Idaho include Basin-and-Range plays in SE Idaho and north of Arco, rhyolite domes in the eastern SRP, and granite plays in the Idaho batholith. Here we discuss the heat, permeability, and seal characteristics of these play types in Idaho.

4.2.1 Distribution of Heat

The distribution of heat sources in areas not related to the SRP volcanic province is based largely on heat flow and the occurrence of thermal features (measured temperatures of thermal waters from springs and wells, calculated ionic and multicomponent temperatures of thermal waters from springs and wells, and the distribution of high $^{3}He/^{4}He$ in thermal waters). Heat flow is relatively high in SE Idaho, coincident with Basin-and-Range structures, although the volcanic fields around Blackfoot are not as high as the Raft River area farther south.

Heat flow around shallow silicic domes is low in the center of the SRP where the regional aquifer dominates the heat budget (Big Southern, Middle, and East Buttes), but slightly higher on the margins south of the Snake River (Buckskin and Ferry Buttes). Similarly, rhyolite buttes in the Blackfoot area (China Cap, China Hat) are affected by massive cold water flow into Blackfoot Reservoir (attested by a Unocal well drilled adjacent to the domes in the 1980s).

Heat flow is somewhat elevated in the southeastern part of the Idaho Batholith (90-100 mW/m^2), which supports a number of thermal springs and pools in the Salmon River drainage. The highest heat flows are found north of Boise, in the Weiser embayment area (Crane Creek Hot Springs), which was proposed as a FORGE site.

4.2.2 Distribution of Potential Reservoir/Recharge Permeability

The *Common Risk Segment map for Reservoir/Recharge Permeability* (Figure 3) developed for basalt-sill complex plays also applies to Basin-and-Range plays and granite plays, but not to the rhyolite dome plays, which are assumed to create their own permeability during intrusion. Potential plays in the Basin-and-Range include the Raft River area, the Arbon Valley-Deep Creek Mountains, the Cache-Portneuf Valleys, the Blackfoot-Gem Valley area, and the Arco rift north of Arco (Fig. 3-7). This permeability is largely attested by surface faults with some range front faults reflected in deep gravity lineations. In the Idaho Batholith, permeability is indicated in the Salmon River drainage and an area just to the west. However, there is no permeability associated with the heat anomaly at Crane Creek north of Boise.

4.2.3 Distribution of Seals

The presence of seal in the other play types, which fall outside the Snake River Plain, is difficult to evaluate on a regional basis because neither of the seal types defined for the SRP basaltic-sill complex plays (lacustrine sediments, aquifer-defined self-seal) apply to the other play types. Thus, the occurrence of seal must be evaluated on a case by case basis for individual plays on a strictly local scale. Such an analysis is beyond the purview of this investigation.

4.3 Potential Prospects: An Assessment

A preliminary assessment of plays and potential prospects based on the results discussed above suggests several areas where undiscovered geothermal resources may be found based on indicators of sufficient heat source and probable sufficient permeability below a sealed zone. In this section, we present an overview of geothermal potential within specific regions of the SRP and conclude with a discussion of the sites that we believe have significant potential for exploitation. The following discussion is based on the *CRS maps for Heat, Permeability, and Seal* and on the Composite CRS map, which sums the contributions of each CRS map across the entire study area (Figure 3).

4.3.1 Western Snake River Plain (WSRP)

The WSRP presents numerous opportunities for geothermal exploration (Figure 4). It is characterized by relatively high heat, based on its heat flow, high groundwater temperatures, and the extensive distribution of early to mid-Pleistocene basalt volcanoes, with some vents as young as ~200,000 years. Volcanic vents form clusters that follow the southern margin of the axial gravity high, and parallel the northern margin, with a dense cluster at its western end. The vent distribution corresponds to subsurface lineaments highlighted in the permeability CRS map, which combine to make an excellent exploration target. The viability of these prospects is attested by our training site, Project Hotspot well MH-2, which was located on the southern margin of this gravity high and encountered hot (~150ºC) water at 1745m depth.

Kuna-Marsing area A-1: The southern margin of the gravity high defines lineaments that trend from around MH-2 NW towards the Marsing area (Figure 4; A1). Volcanic vents following this trend are early Pleistocene in age, with a few younger vents in the dense cluster around Melba, at the NW terminus of this trend. The northern margin trends from Mountain Home NW towards Kuna (Figure 4, A1). Young (mid- to late Pleistocene, <780,000 years old) high-K/high-Mg basalt vents are found along near the town of Mountain Home on the northern margin of the axial gravity high, and form a dense cluster at the west end of this trend, centered around Kuna Butte. These basalts have high mantle potential temperatures and appear to have erupted after delamination of the continental lithosphere (*Shervais and Vetter 2009*).

Mountain Home A-2: A second prospect is located near the town of Mountain Home (Figure 4; A2). This area lies along the northern margin of the axial gravity high and adjacent to the range front fault system *(Shervais et al, 2002)*. The Mountain Home area includes the Bostic-1A well, which was the focus of a hot dry rock investigation in the 1980s (*Arney 1982; Arney et al, 1982*). The area NW of town contains numerous intersecting faults of late Pleistocene age and younger (mid- to late Pleistocene, ≤300,000 years old) high-K/high-Mg basalt vents (*Shervais et al, 2002*). One of the intersecting fault sets trends ~NW (parallel to the range front system), while the other trends almost EW (sub-parallel to the trend of the axial gravity high). The nexus of intersection faults lies at the NW end of the Danskin Mountains, where the Danskin rhyolites give way to granites of the Idaho Batholith. This region lies north of the MH-2 training site, and MT coverage could be extended to provide more training data.

Castle Creek-Bruneau A-3: A third prospect encompasses the Castle Creek-Grandview-Bruneau KGRA (Figure 4; A3). This area is characterized by high heat flow and high inferred permeability, based largely on WNW-trending faults with high dilation tendency. There are also deep and mid-crustal gravity lineaments that parallel the surface faults, suggesting that the structural discontinuities penetrate relatively deeply into the crust. Geothermal waters in wells and hot springs have temperatures of 30ºC to >80ºC (Young and Lewis, 1982; Young et al, 1990; Berenbrock 1993). There are no installed power plants. Basalt vents have Pliocene or older ages, suggesting that the heat source must be relatively deep in the crust.

Deadman Flat A-4: The final area on the CCRS map is Deadman Flat, which lies south of Glenns Ferry on the northern rim of the Bruneau-Jarbidge eruptive center (Figure 4; A4). This area is characterized by high heat flow, despite the fact that most volcanic vents are late Miocene in age (although a few are late Pleistocene). It is also a region of high inferred permeability, based on surface faults with high dilation tendency, and on deep gravity lineations. This area lies at the nexus of WNW-trending faults that parallel WSRP structural trends and NNW-trending of the Basin-and-Range province to the south. This region is relatively remote and undeveloped, and is not likely to be a high priority.

4.3.2 Central Snake River Plain (CSRP)

The CSRP is characterized by a low density of young volcanic vents compared to the eastern SRP, but this is due in part to the older loess-covered surface of the vents here and to the rapid degradation of small cinder and spatter satellite vents that are common in the ESRP. Basalt vents in the CSRP are typically 100 ka to 400 ka along the Axial Volcanic Zone, and older (up to 2-3 Ma) along the margins. However, the Holocene Shoshone flow erupted from Black Butte Crater on the northern margin of the plain, just south of Magic Hot Springs, and other Holocene to late Pleistocene vents are found nearby in the Mount Bennett Hills. Many of the vents in CSRP region are enormous, with diameters up to 20 km across and flow fields that extend 35-40 km from the vent (*e.g., Shervais et al, 2005*).

Deep heat flow is marginally higher than in the ESRP although shallow heat flow is still suppressed. Groundwater temperatures are markedly higher in the CSRP compared to the east, reflecting the effect of continuing heat flux from below as the aquifer waters move from their source in eastern Idaho to their outlets in the Thousand Springs area NW of Twin Falls.

Thermal resources are indicated by the presence of numerous hot springs throughout the region, typically along the margins of the plain (*e.g.,* the Banbury-Miracle HS area, the Magic Reservoir-Camas Prairie HS area, and Latty HS on the SW edge of the Mount Bennett Hills) and by the widespread warm water of the Twin Falls thermal district (*Street and deTar, 1987; Street, 1990; Baker and Castelin, 1990*). Thermal spring waters in the Banbury-Miracle, White Arrow (Mount Bennett Hills south-side), Latty (Mount Bennett Hills SW edge), and Magic Reservoir areas are characterized by high calculated equilibrium reservoir temperatures *(Neupane et al, 2015*). Thermal spring waters in the Banbury-Miracle, White Arrow, Camas Prairie, and Magic Reservoir areas are characterized by high $^{3}He/^{4}He$ ratios, and the presence of magmatic methane (*Dobson et al 2015*).

Camas Prairie-Mount Bennett Hills B-1: The primary region of interest in the CSRP is the Camas Prairie-Mount Bennett Hills area (Figure 4, B1). Heat flow is high and there is minor late Pleistocene to Holocene volcanism. Permeability is very high, with high-dilation NW-trending faults intersecting NE-trending or EW-trending faults. In the Mount Bennett Hills, NW and NE-trending faults intersect the EW-trending range front faults (largely buried) along the southern margin of the prairie, and a major WNW-trending fault system cuts across both the Camas Prairie and Mount Bennett Hills near the center of the range. Thermal features include hot springs with high measured temperatures, high multicomponent geothermometry temperatures of 90-110ºC *(Neupane et al., 2014)* and He-isotope anomalies R/Ra >2.1 *(Dobson et al, 2015).*

King Hill B-2: The second region of interest in the CSRP is King Hill (Figure 4; B-2). This area lies at the southern end of the WSRP range front fault system, where it merges with the accommodation fault system that separates the Mount Bennett Hills from the Danskin Mountains (Figure 4). Volcanic vents are scarce, but heat flow is relatively high, and NW-trending surface faults are supported by gravity lineaments, which create a zone of high favorability in the Permeability CRS map (Figure 3). Thermal features include hot springs with multicomponent geothermometry temperatures of 175-200ºC *(Neupane et al., 2014)* and He-isotope anomalies that vary from R/Ra <1 to 1.9 *(Dobson et al, 2014)*.

Because of their high favorability on our CRS maps and other data, the Camas Prairie-Mount Bennett Hills and King Hill areas will be one of the main focal points in our Phase 2 work. These systems may represent hybrids of the basaltic sill and Basin-and-Range play types.

Banbury B-3: The Banbury-Miracle Hot Springs area west of Twin Falls (Figure 4; B-3) is a long-established thermal district *(Young and Lewis, 1982; Lewis and Young, 1982, 1988).* This area represents a zone of fault intersections between NS-trending Basin-and-Range faults exposed in the Cassia Mountains to the south and NW-trending faults of the WSRP, creating a NE-trending intersection zone that projects through Banbury hot springs. Multicomponent geothermometry is relatively low (130-160ºC; *Neupane et al, 2014)* but He-isotope anomalies that vary from R/Ra 1.6 to 2.0 *(Dobson et al, 2014)*. Heat flow is high but young volcanic vents are scarce. The area SW of Banbury appears favorable but has no surface manifestations. While the Banbury-Miracle region is moderately favorable on the CCRS map, its limited size and conflicting indicators suggest that it will not be a primary target for further exploration.

4.3.3 Craters of the Moon-Great Rift

One of the highest concentrations of the youngest volcanic vents (Holocene to 75 ka) is found in Craters of the Moon (COM)-Great Rift region, which defines the divide between the ESRP and CSRP (Figure 1). The volcanic rocks here are as young as 2000 ka, and the presence of an active rift system suggests that this is an active volcanic region. The rift zones are favorably oriented for dilation, although there is no indication of tectonic fracturing.

There are no potential hydrothermal prospects in the Craters of the Moon-Great Rift region, however, there may be EGS potential. Deep heat flow is relatively high, but heat flow based on shallow as well as deep wells much lower, and groundwater temperatures are still relatively low as well. This reflects the effect of the Snake River regional aquifer, which underlies much of the

COM-Great Rift region, suppresses conductive thermal gradients, and increases the drilling depth needed to achieve temperatures over 150ºC.

A further problem is that most of this region is now part of the expanded Craters of the Moon National Monument and is off-limits to geothermal development. There may be limited opportunities outside the Monument but permitting problems are likely.

4.3.4 Eastern Snake River Plain (ESRP)

The ESRP is characterized by dense clusters of vents in the EW-trending Spencer-High Point rift, in the vicinity of Mud Lake (NE of INL), and along the Axial Volcanic Zone, which marks the central axis of the SRP. Although there are some Holocene vents, most volcanic activity was late Pleistocene (Brunhes normal epoch, ≤780,000 years). The Axial Volcanic Zone contains three rhyolite domes (<700 ka) that post-date basalt, an older rhyolite cryptodome, and an evolved dacite volcano (Cedar Butte). There are two rhyolite cryptodomes on the southern margin. As with the COM-Great Rift, deep heat flow is high, but heat flow based on shallow wells is much lower, and groundwater temperatures are low.

The ESRP faces many of the same problems found in the COM-Great Rift region. The Snake River aquifer underlies much of the eastern SRP, there is no surface faulting except along the margins, and there is little indication of buried permeability from gravity or magnetics. *Payne et al. (2008, 2012)* present GPS strain data that document extension in the Basin and Range regions north and south of the SRP, whereas the SRP itself moves as a coherent block with uniform velocity. This implies relative motion along the interface between the SRP and the adjoining mountain areas, but at this time there is no indication of faulting or earthquakes along these boundaries.

The evidence for naturally occurring hydrothermal systems in the ESRP is limited due to the lack of indicators of reservoir permeability and the presence of the Snake River Aquifer under much of the region. However, there may be potential for Engineered (*aka* Enhanced) Geothermal System (EGS) development along the margins of the ESRP where the aquifer is thin or absent (e.g., the INL Forge site or the Spencer-High Point rift area). Both areas have indications of high heat (high groundwater temperatures at the INL Forge site, extremely high young vent densities in the Spencer-High Point rift), despite the lack of evidence supporting the presence of natural permeability. Both areas lie outside the major influence zone of the Snake River Aquifer.

4.3.5 Basin-and-Range Plays

There are two Basin-and-Range plays that may represent potential prospects (not counting our Training site at Raft River): the Arco Rift-Big Lost River Valley in central Idaho, and the Blackfoot-Gem Valley region of SE Idaho (Figure 4).

Arco Rift C-1: The Arco Rift-Big Lost River Valley is characterized by high heat flow (>90 mW/m^2) and high favorability on the Heat CRS map (Figure 3), and by extremely high favorability on the Permeability CRS map (Figure 3), resulting in very high favorability on the Composite CRS map (Figure 4; C-1). This favorability extends about 40 km north up the Big Lost River valley, and 25-30 km south into the SRP. The continuation of the permeability trend across the SRP is driven largely by a deep gravity lineament that extends to Pocatello and may represent a Basin-and-Range type structure that transects the entire SRP. The Big Lost River valley is filled with alluvium, so it is not known whether or not there is an effective seal. This valley is also the location of the Big Lost fault responsible for the M6.9 Borah Peak earthquake, making this a potentially hazardous site for a power plant.

Blackfoot C-2: The Blackfoot-Gem Valley area may be transitional to an SRP-type system in that the NNW-trending fault systems are transected at a strongly oblique angle by the NNE-trending volcanic field, which includes abundant basalt vents and several rhyolite domes (Figure 4; C-2). The Basin-and-Range structures here enter Idaho trending roughly NS, then gradually curve around to the NNW, becoming approximately in line with their companion structures on the north side of the SRP. There are a number of hot springs SW of the volcanic field which lie on approximately the same trend (*Janecke, personal communication, 2015*).

The Blackfoot-Gem Valley region has been studied extensively by McCurry and colleagues (*McCurry et al, 2011, 2015; McCurry and Welhan, 2012; Welhan et al, 2014).* A test well drilled by Unocal in the 1980s encountered a major flow of cold water moving towards Blackfoot reservoir. However, a 3 km deep well drilled NE of the reservoir in 1979 by Conoco measured a bottom hole temperature of 190ºC – similar to the Bostic 1A well in the WSRP (*Fleischmann, 2006*). *Welhan et al. (2014)* suggest that this resource comprises a large area with high heat flow (~100-220 mW/m^2) that is masked by structural relations in the SE Idaho over thrust belt.

4.3.6 Potential EGS Prospects

All of the prospects discussed so far have been hydrothermal prospects, which combine heat source with reservoir/recharge permeability and seal. EGS prospects require only the heat source, and do not require high primary permeability. There are several locations within our study area that meet these criteria (Figure 3):

(1) Weiser Embayment-Crane Creek: this area is characterized by high heat flow with little or no permeability. Fault systems in this area trend NS to NNE and have extremely low slip and dilation tendencies. This area was the focus of a proposed FORGE site and parts of it are under lease for geothermal development.

(2) Craters of the Moon: this area has high heat favorability on the Heat CRS map, based entirely on the concentration of volcanic vents, but heat flow is apparently low. However, it lies entirely within a National Monument and is thus off limits to development.

(3) The INL site east of Arco: this area is characterized by high heat flow and high favorability on the Heat CRS map. It lies on the northern margin of the SRP where the regional aquifer is thin (<230m) so the effect of aquifer cooling on thermal gradients is minimal. This area was the focus of a proposed FORGE site.

(4) Spencer-High Point rift: this area is the closest volcanic field to Yellowstone but lies well outside the Park boundaries. Heat flow is high (90-105 mW/m^2) and it has the highest vent density outside of Craters of the Moon. The Permeability CRS shows very low favorability except for the margins of Island Park caldera, defined by faults with low dilation tendencies.

Although the identification of EGS prospects lies outside the purview of this award, their locations are a by-product of our GIS methodology. Our approach has identified two areas that are subject to active EGS exploration (INL, Crane Creek), one area that is "off-limits" (Craters of the Moon), and one new area (Spencer rift). We will discuss cadastral issues below in our evaluation of commercial viability, but note here that the Spencer-High Point region has BLM and private land available for development, has no large excluded zones, and is adjacent to a 368 corridor.

4.4 Data Gaps

The analysis presented here represents a major data collection and processing effort, using regional data sets and geologic maps for the most part, and using proxies, such as fault and lineament density, in place of detailed structural analysis of intersections, step-overs, and accommodation zones.

4.4.1 Field-related Data Gaps

All of the areas identified (Fig. 4) have basically the same data gaps:

- Detailed field relations at the prospect scale are of variable detail. Field checking of each potential prospect is needed to confirm its structural and geologic setting, look for detailed fault interactions (step-overs, intersections, etc.), confirm mapped features, and evaluate for further work.
- Poor age control on volcanic vents in areas A-1 to A-4, and B-1. We will need to acquire 15-20 Ar-Ar dates across the area to better constrain age ranges.
- There are no MT data with upper crustal resolution anywhere in our study area; all of our potential prospects will need MT data acquisition.
- Only one area (part of A-1, Fig. 4-2) has existing seismic, which must be purchased from the Seismic Data Exchange. We will need to acquire some active source seismic that transects buried structures of interest in all other areas.

- Most of the WSRP and CSRP have high resolution gravity surveys, but the Mt Bennett Hills-Camas Prairie region do not. We will need to extend our high-resolution gravity work into this region (USGS).
- Most of the INL projects work on water geochemistry has focused on the ESRP and CSRP. We need to extend this work into the WSRP to determine potential reservoir temperatures.
- Regional scale cadastral data must be confirmed in the field and in areas of special interest, and land ownership determined from county records.

4.4.2 Modeling Data Gaps

Modeling gaps represent ongoing analysis of our old data and incorporation of new data:

- Refine our GIS tools and Python scripts to simplify application to other regions; retroactively apply tools to entire SRP as it is refined for detailed prospect studies.
- Refine and extend our conceptual models and apply them to detailed prospect studies.
- Thermal Reservoir Models will be refined in the WSRP and extended to other areas.

These data gaps were addressed during Phase 2 of our PFA study.

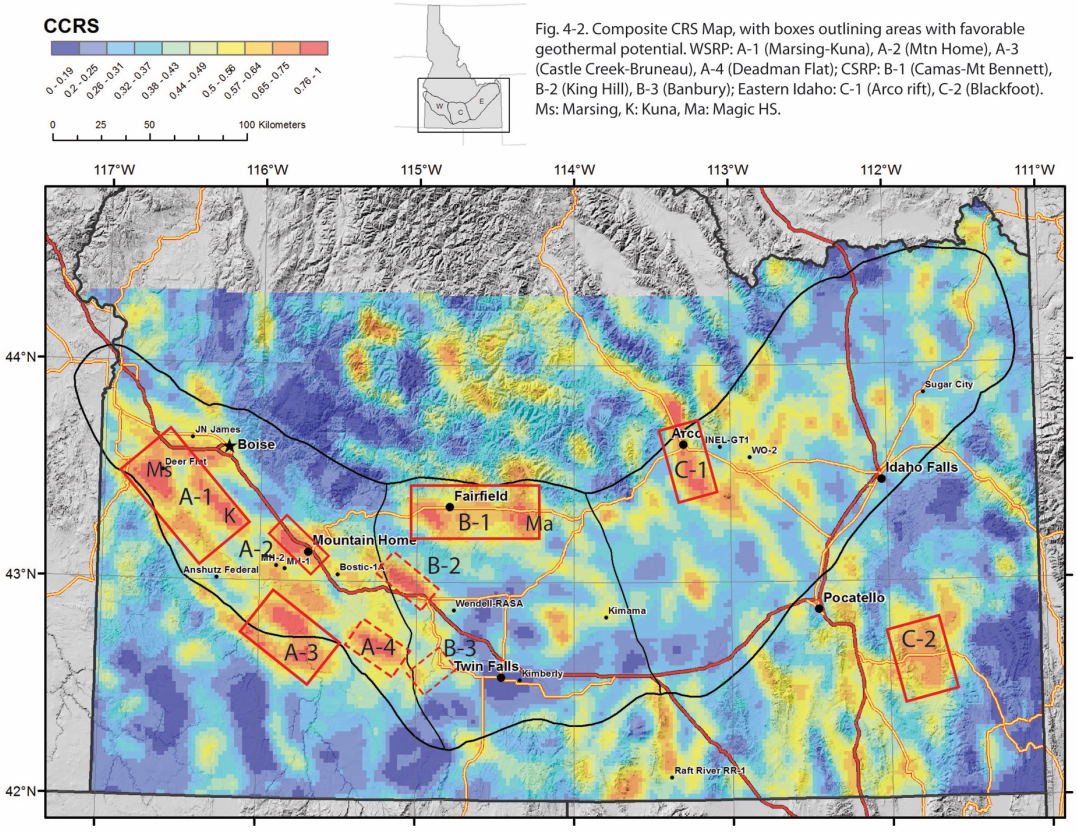

Figure 4. CCRS map for southern Idaho showing regions with high geothermal potential discussed in text.

II. PHASE 2 ACTIVITIES AND RESULTS

5.0 PLAY MODEL: MAFIC HEAT SOURCES AND BASALTIC SILL COMPLEXES

5.1. Our Updated Play Model Concept

A large number of hydrothermal systems are powered by underlying mafic magmatic systems. These include systems in the Reykjanes Peninsula, Iceland, the Puna District in Hawaii, and mid-ocean ridge spreading centers, which represent the largest manifestation of geothermal energy on the planet. Several studies now relate the geometry of mafic heat sources to the rates of magma supply versus tectonic extension (*e.g., Wohlitz and Heiken, 1992*). High extension rates relative to magma supply result in feeder dikes that accommodate the rapid ascent of magma to the surface, whereas high magma supply rates relative to extension produce sill complexes or plutons.

The Snake River Plain (SRP) in Idaho is a large basaltic province associated with the Yellowstone mantle plume and is part of the largest heat flow anomaly in the USA (Blackwell, 1989; Blackwell and Richards, 2004). The eastern SRP represents the track of the Yellowstone hotspot – a deep-seated mantle plume that has remained relatively fixed in space as the North American plate moved to the southwest (Smith et al., 2009). As the plate moved over the plume, large silicic caldera complexes formed. As the magma chambers beneath these calderas solidified and were able to sustain brittle fracturing, basalts were able to reach the surface and form the extensive lava flows that define the Snake River Plain surface geology. Our Phase 2 PFA region was located in the western and central parts of the Snake River Plain (Figure 5).

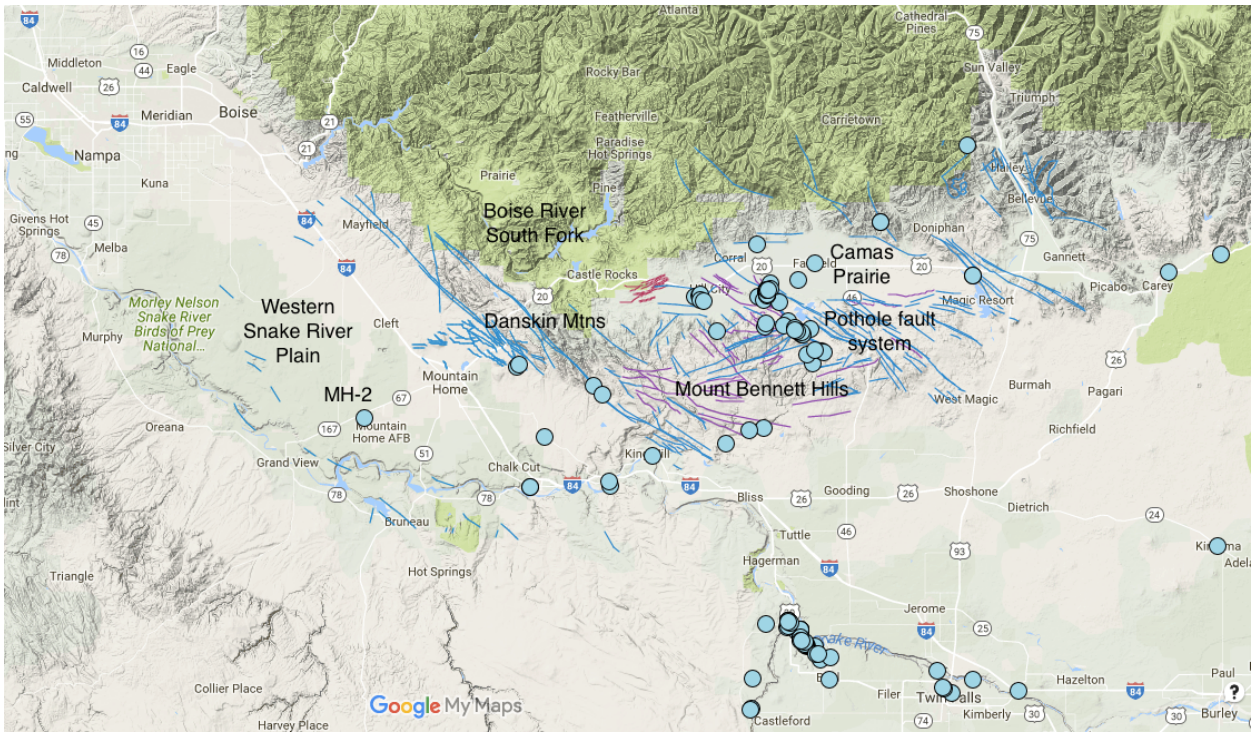

Figure 5. Location map for Snake River Plain PFA. Mapped faults in blue and purple, blue dots are water samples from springs and wells.

High-resolution seismic imaging carried out over several decades has established the presence of a mid-crustal sill complex at 10-20 km depth (Smith et al., 2009; DeNosaquo et al., 2009). Geologic mapping and deep drill cores have documented the thickness and distribution of surface basalt flows. Basalt geochemistry shows that this sill complex comprises a series of layered magma chambers, which evolved by fractional crystallization and magma recharge and fed surface eruptions (*Shervais et al., 2006; Jean et al., 2013*). Taken together, these data document a magma flux of ~10^4-10^5 km^3/Ma under the eastern and central SRP, with little or no extension perpendicular to its boundaries (*e.g., Payne et al., 2012*). This flux is similar to the one reported for Hawaii (10^5 km^3/Ma). Resurgent basalt volcanism (<800 ka, and as young as 2100 yr BP) formed long after the plume passed, driven by back-flow of plume material to the west. These resurgent basalts are also plume-derived, postulated to result from delamination of subcontinental lithospheric mantle (*Shervais and Vetter, 2009*). Numerical models of thermal evolution during sill injection show that a single sill will result in heating of the surrounding rocks to over 300ºC after 20,000 years (Nielson and Shervais, 2014; Nielson et al., 2017); multiple sill injections will result in the continuous accumulation of heat as the ambient temperature of the host rocks is raised with each injection (*Garg et al., 2017*).

Our play model concept proposes that heat flux in the shallow portion of the SRP is driven by the accumulated effect of multiple sill injections over the last several million years, with the most recent magmatic activity as young as 2000 years (Figure 6). We postulate that high heat flux is present throughout the SRP; however, in the eastern SRP it is masked by thick cold-water aquifers, thus requiring drilling to greater depths to encounter high temperatures and raising the costs of exploration drilling. In contrast, the western SRP (WSRP) is characterized by a thick (1.0-1.5 km) layer of lacustrine sediments with low thermal conductivities that act both as an insulating blanket on the underlying geothermal systems, and as a seal that prevents the convective transport of heat away from the system. This effect is documented by deep wells in the WSRP that all have conductive thermal gradients of ~75ºC/km (*Nielson et al., 2012; Garg et al., 2016*).

A primary requirement for finding blind geothermal resources in this setting is the ability to identify zones of high permeability at depth, below the insulating sediments, in areas with high heat flux. Our model postulates that these high permeability zones have characteristics similar to known geothermal resources in the Basin and Range province; that is, they represent faults with high slip or dilation tendencies relative to the local or regional stress field (e.g., Jolie et al. 2017). This concept is built into our GIS processing method, which weights fault and lineament segments for slip and dilation tendency. Further, we draw upon work of Kessler et al. (2017), who assess *in situ* stress, fracture density and distribution, and the mechanical properties of core from the MH-2 drill hole in the western SRP, based on core and borehole image logs.

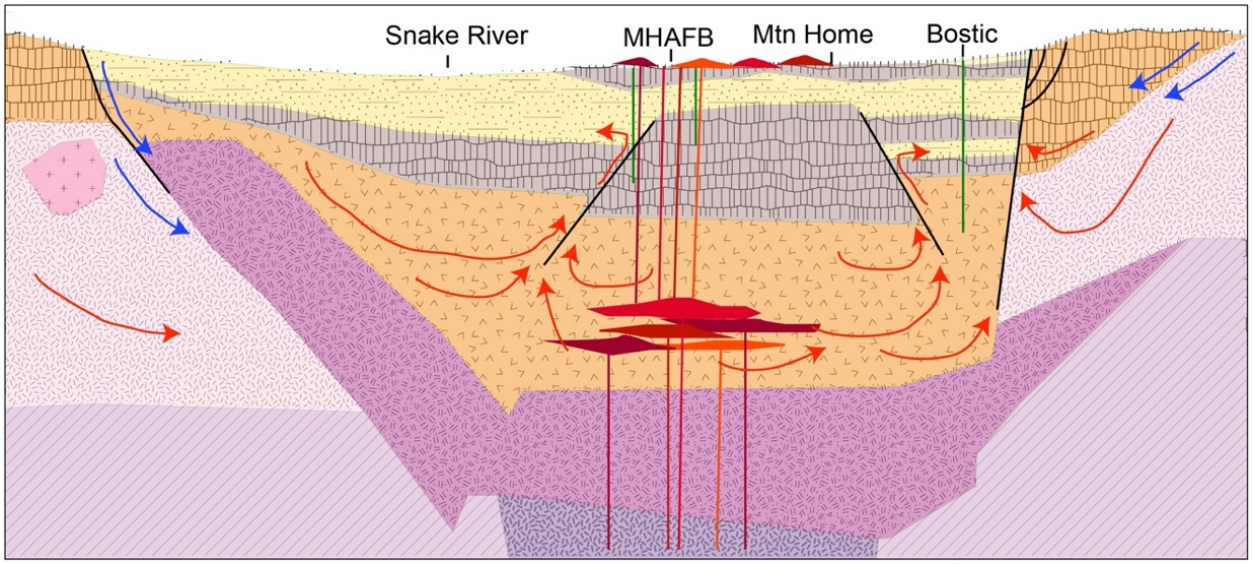

Figure 6. Cartoon illustrating our conceptual model of the structure and geothermal system of the western SRP relevant to the Mountain Home and Bostic study areas. Young basalt: grey patterned; marginal basalts: orange-patterned; Lake Idaho sediments: stippled yellow; Miocene rhyolites: checked orange pattern. Older volcanic rocks (dark pink) form a basin-wide sag structure, with young sills intruded around 2 km below present surface. This young sill complex (≤355 ka) drives hydrothermal circulation of deep convecting fluids. High extension with respect to magma supply results in feeder dikes and rapid ascent to the surface whereas high magma supply with respect to extension produces sills or plutons. We have proposed that the Graveyard Point Sill, located in western Idaho, is an analog for the buried mafic heat source of the Mountain Home geothermal system. On the basis of field mapping (e.g., White, 2007), we estimate that the Graveyard Point sill had an average thickness of 100 m, a total volume of about 3 km^3, and was emplaced at a temperature of ~1200ºC.

Thermal modeling was carried out to validate our conceptual play model and constrain conditions that may have led to the current thermal regime (*Nielson et al., 2017; Garg et al. 2017*). These models, which are discussed in the next section, support our conceptual model, reproducing temperatures observed in metamorphic and fluid inclusion studies, as well as measured temperature gradients in deep wells.

5.2 Natural State Thermal Model of the Mountain Home Region, WSRP

A 3D numerical model was developed using Leidos' STAR geothermal reservoir simulator (Pritchett, 2011) using updated data from Phase 2 (*Leidos Natural State Model Technical Report; https://gdr.openei.org/submissions/943*). To perform model computations, it is essential to prescribe distribution of thermo-hydraulic properties (e.g., permeability, porosity, thermal conductivity, specific heat, etc.) for the entire grid-volume, and boundary conditions along the faces of the model grid. During the development of the natural-state model for the Mountain Home geothermal prospect presented below, the boundary conditions (i.e., heat flux along the bottom boundary, pressure specification along the top boundary) and the formation permeabilities were freely varied in order to match the observed temperature profiles in wells. Several such calculations were carried out; only the final case is described here.

The model volume is divided into a 25x20x25 grid in the x- and y- and z-directions (east, north, and vertically upwards). The model area is only a small fraction (about 6%) of the area considered in the regional model (Garg et al., 2016). In the absence of pressure transient data from any of the wells in the area, the vertical permeability values were determined during the development of the numerical model in order to match the measured well temperatures. The horizontal permeability values in the model are largely unconstrained. Rock types assigned to individual grid blocks are in part based on MH-1 and MH-2 lithological logs, and interpretation of gravity and MT surveys. Intrinsic rock density, rock grain specific heat, global thermal conductivity, and porosity values are based on published data (e.g., Hyndman and Drury, 1977; Eppelbaum et al., 2014; Blackwell, 2013).

Starting from an essentially arbitrary cold state with the observed heat flux, the computation was marched forward in time for ~625,000 years. The maximum time step used was 25 years. For most of the computational period, the thermal energy continues to increase and the fluid mass declines. Initially the change is rapid; it moderates over time. After about 500,000 years, the change is quite small over a time scale of 50 to 100 years. The computed temperature values at cycle 25,000 (~625,000 years) were compared with the available data.

5.3 Thermal-Hydrologic Modeling of the Play Model

The Graveyard Point Sill (White, 2007) is exposed on the western side of the SRP and has been proposed as an analog for the heat source for the geothermal system intersected in MH-2 (Nielson and Shervais, 2014). We estimate that its original thickness was 200 m with lateral dimensions of 5 x 3 km for an original volume of 3.0 km^3.

A simulation of the sill hydrothermal cooling history was performed to determine whether the maximum temperatures deduced from fluid inclusions in the Mountain Home core (Atkinson et al., 2017) could develop through emplacement of the sill at a depth of about 2 km and how long the thermal pulse lasts after emplacement (Nielson et al., 2017). There is also evidence of boiling from two-phase fluid inclusions at temperatures of 340-350°C (Atkinson 2015; Atkinson et al., 2017) that should be observable in the simulations.

Simulations of the hydrothermal system and sill cooling history were performed using the coupled thermal-hydrological-chemical simulator TOUGHREACT V3.3 (*Sonnenthal et al., 2014; Xu et al., 2011*). TOUGHREACT V3.3 considers multiphase fluid and heat flow with temperature-dependent heat capacities and thermal conductivities, along with kinetic and equilibrium mineral-water-gas reactions, aqueous and gaseous species diffusion and advection. It simulates conductive heat transport in grid blocks that are initially, or attain, magmatic and/or supercritical temperatures for water. Therefore, the surrounding hydrothermal system can be adequately modeled with a simplified cooling model for the intrusive body.

The dual-permeability model considers global matrix-matrix and fracture-fracture flow, and local fracture-matrix flow. This includes heat conduction and advection, as well as fluid (water and/or steam) advection. The fault is given anisotropic permeability with a fracture density twice that in the surrounding host rock. The matrix permeability in the fault is also increased to reflect breccia zones. The local fracture-matrix interface area is given by the number of fractures in each

direction times the fracture-matrix area of each fracture locally. Estimated hydrological, thermal, and transport properties are given in Nielson et al. (2017). The thermal conductivity is fixed at 1.8 W/m/K. The magma was kept at the fixed higher heat capacity value (1522.3 J/kg/K) to approximate the effects of the latent heat of fusion.

Our simulations using TOUGHREACT V3.3 and estimated size, emplacement temperature and depth of emplacement of the Graveyard Point Sill support our hypothesis that a similar intrusion in the Mountain Home area could provide the heat required for hydrothermal brecciation and match observed fluid inclusion data (Atkinson, 2015; Atkinson et al., 2017). We believe that the simulations can be refined with additional data, particularly dating of the hydrothermal brecciation event observed in the MH-2 core.

6.0 SELECTION OF FOCUS AREAS

Our first task in Phase 2 was to assess regions deemed favorable in Phase 1, and to select a limited number of these areas for more detailed analysis, including acquisition of new data to fill gaps in knowledge. This task was carried out with assistance of our Industry Advisory Board (including representatives from *USGeothermal, Ormat,* the *U.S. Navy*, and a geothermal consultant), and resulted in the selection of three areas that appeared to be highly favorable, with sufficient existing data, so that the data gaps could be addressed with the budget available and within the prescribed period of performance (i.e., essentially shovel-ready). This takes into account issues such as permitting. These areas are discussed below.

6.1 Mountain Home – Western Snake River Plain

The Mountain Home study area represents a blind high-temperature geothermal system that is not associated with any mapped faults or surface geothermal manifestations. Initial investigations of the resource were prompted by elevated geothermal gradient estimates (65ºC/km) determined from a wildcat oil well (Bostic 1A, 2949 m) drilled in 1973 at a location 20 km southeast of the town of Mountain Home (Figure 1). A deep (1342 m) geothermal exploratory well (MH-1) was drilled in 1986 as part of an effort to assess resources at the Mountain Home Air Force Base (MH-AFB). A temperature of 93ºC logged at a depth of 1207 m (Lewis and Stone, 1988), and an estimated thermal gradient of 69ºC/km, suggests that temperatures at depths in the range of 1500–1800 m are high enough to support binary cycle power generation that could meet the base's present maximum electrical power requirements of 14 megawatts (*Breckenridge et al., 2012*), and potentially provide power to the town of Mountain Home or supply power to the grid. Subsequently, a second deep (1821 m) well (MH-2) documented artesian flow and 135-140ºC water (*Nielson et al., 2012*) at a depth of 1745 m.

The stratigraphy at Mountain Home, constrained by core from the MH-1 and MH-2 drill holes, consists of an upper section of basalt (~150-200 m thick) overlying ~600 m of fine-grained lake sediments, and a basal sequence of basalts with minor sedimentary layers. The sequence of low permeability lake sediments that overlie the geothermal system at Mountain Home likely help maintain the resource by insulating the reservoir, preventing upward migration of the thermal fluids, and inhibiting mixing with cold meteoric water that could degrade the resource (*Shervais et al., 2016*). MH-AFB has had a longstanding commitment to supporting

research of the base's geothermal resources that would make them an ideal partner in future exploration and eventual development of this resource.

6.2 Bostic (Western Mount Bennett Hills) – Western Snake River Plain

A region ~20 km east of Mountain Home, between the town of Glenns Ferry and the Mount Bennett Hills, was first identified as an area with elevated geothermal potential based on findings from the Bostic 1A exploratory oil well that yielded a measured bottom hole temperature (at 2931 m) of 195ºC (*Arney et al., 1982*). These findings motivated subsequent studies of the area, including geothermal evaluations of the Bostic well by Unocal and a hot dry rock investigation led by Los Alamos National Laboratory (*Arney, 1982; Arney et al., 1982*). Although this area has estimated potential for development of high-grade enhanced geothermal system (EGS) resources, with predicted temperatures exceeding 200-250°C at depths of 4-6 km (*Tester et al., 2006; Williams and DeAngelo 2011*), no further exploration of this resource has taken place since the efforts in the 1980s. In addition to its potential as an EGS resource, the broader region may have viable targets for development of conventional hydrothermal resources. Surface hydrothermal springs north of Bostic in the Danskin Mountains and Mount Bennett Hills yield temperatures of 175-200ºC using multicomponent geothermometry (*Neupane et al., 2014*).

6.3 Camas Prairie-Mount Bennett Hills

Our Phase 1 analysis identified the Camas Prairie in south central Idaho as a region with a potential commercial resource (e.g., capable of ≥10 MW of electric power generation) based on its presumed heat, permeability, and presence of basin-filling sediments (*Shervais et al., 2016*). It was chosen for this study based on the results of the Phase 1 play fairway analysis and because it is a relatively under-characterized geothermal system (*e.g., Stoker and Gertsch, 1980*).

The Camas Prairie is an E-W elongate valley situated between the Idaho Batholith and the central SRP that is thought to have formed as a rift basin in response to passage of the Yellowstone hotspot and subsequent down warping in the SRP (*Cluer and Cluer, 1986*). The Prairie is bounded on the north by late Cretaceous to early Tertiary granitoids of the Idaho Batholith and by the Eocene Challis volcanics. The valley fill consists of poorly sorted Pliocene and Holocene age sediments derived mainly from the north. Interbedded with these sediments are young volcanic units that flowed out from eruptive centers in the Mount Bennett Hills. The Mount Bennett Hills consist of basalt overlying rhyolite basement. Basin development is loosely constrained to between 5 and 1.8 Ma based on limited age control on rifted silicic and basin-filling basalts (*Cluer and Cluer, 1986*).

The Camas Prairie rift basin resembles other extensional basin-and-range systems, like those in the Great Basin. These systems generally involve amagmatic, moderate temperature resources associated with the circulation of geothermal fluids along deep crustal structures that tap a region of high crustal heat flow. In the Camas Prairie, however, direct surface evidence for major basin-controlling and intra-basin structures is limited. The geothermal system involves contributions from magmatic sources, based on the presence of Quaternary volcanism in the southern part of the basin, and it has elevated heat flow similar to the rest of the Snake River Plain (Blackwell, 1989). The youngest flows are associated with The Pothole – a Pleistocene basaltic vent and associated flows that are cut by a northwest-trending fault.

Camas Prairie hosts several hot springs and wells that are exploited for direct use applications and display high measured temperatures and high multicomponent geothermometry temperatures. This includes the now inactive Barron's Hot Springs, which displayed measured surface temperatures of 72°C; a nearby well has a maximum measured temperature of 91ºC at a depth of 91 m below surface (*Mink, 2010*). Geochemistry of Barron's Hot Springs yields predicted reservoir temperatures suggestive of low to moderate temperature systems (*Neupane et al., 2014*). Although this suggests it may be able to support electric power generation using binary cycle technology, more data are needed to demonstrate adequate flows and production temperatures. The close proximity of the resource to power transmission infrastructure along U.S. Highway 20 would help facilitate development of the resource.

7. PHASE 2 DATA ACQUISITION

The three areas chosen for more detailed assessment all contain data gaps that needed to be filled during Phase 2. These gaps differed between regions, so not all data types were acquired in each area: only those data needed to fill critical gaps. See Figure 7 for focus area locations.

7.1 Field Mapping and Sampling (USU, USGS)

Geologic field studies included detailed structural mapping to constrain fault geometries, and sampling of young volcanic rocks and vents for whole rock geochemistry and ^{40}Ar-^{39}Ar geochronology. Structural mapping focused on faults and fault intersections along The Pothole fault system (Camas Prairie). Data collected include strike and dip direction of polished surfaces, striated surfaces, or topographically apparent faults. This work was supplemented by fault locations taken from geologic maps in the Camas Prairie-Bennett Hills region, and by new mapping using satellite imagery and topography, with confirmation by field checking.

A wide range of volcanic vents were sampled, including vents in the WSRP near Mountain Home, The Pothole in Camas Prairie, and young vents along the South Fork of the Boise River. In addition, three samples were selected from the MH-2 well on MH-AFB (Project Hotspot) to document the stratigraphic age range intersected by that well. Twelve samples were sent to the Geochronology Laboratory at Oregon State University for ^{40}Ar-^{39}Ar dating and analyzed for major and trace elements by XRF spectrometry. Additional age data were compiled from published sources to supplement the new ages.

7.2 Magnetotelluric Surveys (LBNL)

The MT survey was carried out in August-September 2016, with 33 stations acquired around the two deep drill holes (MH-1 and MH-2) on MH-AFB and 63 stations on Camas Prairie (**Appendix B**). The Mountain Home station array was designed to tie into the deep drill hole stratigraphy, and to capture structures identified in previous high-resolution gravity surveys (*Geothermal Data Repository https://gdr.openei.org/submissions/1249*). Sixty-three stations acquired in Camas Prairie (*https://gdr.openei.org/submissions/1103*) covering the same area surveyed by our new seismic, gravity and magnetic campaigns. Six stations were acquired along a profile crossing a previously identified gravity anomaly near the Bostic 1A deep drill hole. We obtained data from a Unocal MT survey of the Bostic area, which was reprocessed to supplement our new data. Collectively, these data indicate the presence of a thick electrically conductive (low resistivity) layer in all three locations corresponding to the known distribution of lacustrine

sediments and possible alteration zones that are interpreted to represent a seal above any potential geothermal resource (*Glen et al., 2017*).

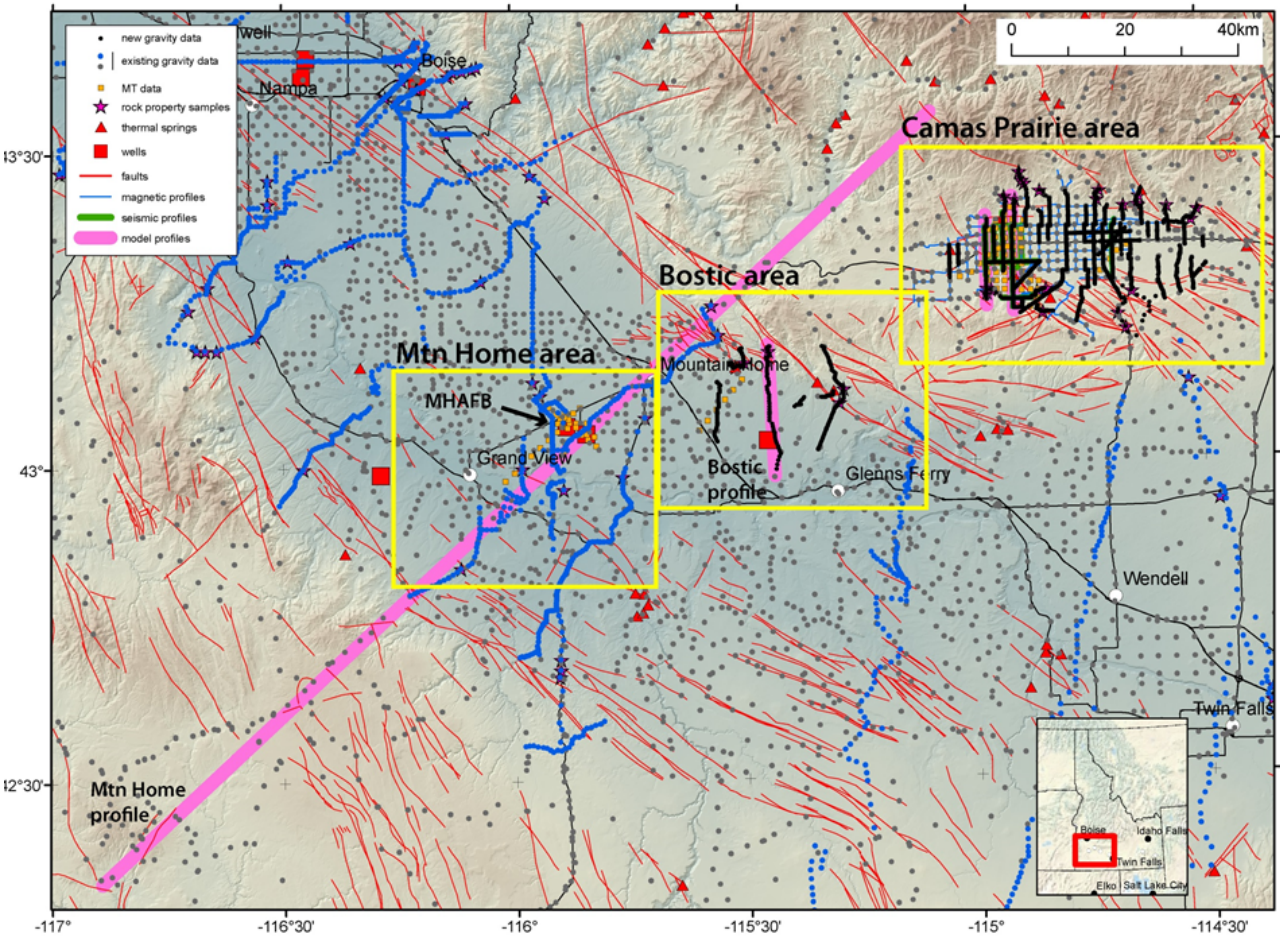

Figure 7. Shaded topographic index maps of the WSRP showing the three focus areas for new field surveys (outlined with yellow boxes; Mountain Home, Bostic, and Camas Prairie). Shown are seismic reflection profiles, MT stations, gravity stations, magnetic traverses, modeled profiles, rock property sample locations Also shown are modeled profiles, faults and thermal springs (Glen et al., 2017).

7.3 Seismic Reflection Surveys (Boise State University)

Boise State University (BSU) acquired ~56 km of active source seismic data along five north-south and two east-west county roads in Camas Prairie (Figure 7; *Glen et al., 2017*). Data were acquired using the BSU seismic land streamer and accelerated weight drop system that allowed survey rates of five km per day at four-meter source spacing. Data were processed and interpreted with industry-standard seismic processing software (ProMAX, Kingdom), where reflectors on cross lines were utilized to map key stratigraphic and structural boundaries. Seismic data are archived in the GDR at *http://gdr.openei.org/submissions/1102*.

7.4 Gravity and Magnetic Surveys (USGS)

The USGS collected data at 1659 gravity stations and over 725 line-km of ground magnetic data for this project (Figure 7, **Appendix C**). They also collected hundreds of rock-property measurements on outcrops and samples (including magnetic susceptibility, density, and magnetic

remanence) to constrain potential field modeling and integrated ground water well logs into our analyses. These data have been used, along with previously acquired data from Project Hotspot (*e.g., Shervais et al., 2013; Shervais, 2014; Liberty et al., 2015; Kessler et al., 2017*) to define basement structures (faults and lineaments), and to create detailed crustal density models (*e.g.,* Figure 10).

7.5 Water Chemistry (LBNL, INL, USU)

Natural springs and water wells were sampled in the Camas Prairie, Mount Bennett Hills, and WSRP regions, and several previously sampled locations were resampled to assess seasonal variations. These samples were analyzed for major and trace elements, and stable isotopes of oxygen, hydrogen, and helium. The chemical data were used to compute equilibrium reservoir temperatures using cation, silica, and multi-component geothermometry, while oxygen and hydrogen stable isotopes were used to identify the source of geothermal fluids and potential water–rock interaction, and helium isotope ratios were used to track mantle volatile inputs.

8.0. RESULTS

8.1. Mountain Home - Western Snake River Plain

8.1.1 Field Mapping and Sampling: The Mountain Home region is characterized by two fault systems: a range-front fault system that strikes about 300° and an oblique fault system that strikes about 275° (*Shervais et al., 2002*). Surface faults are only exposed north of Mountain Home, close to the range front, but subsurface systems with similar orientations may be inferred from lineations defined by steep gravity and magnetic gradients.

New ^{40}Ar-^{39}Ar ages are presented in **Appendix D** and Figure 8. Volcanic vents in the Mountain Home region include older tholeiitic basalts and younger high-K transitional alkali basalts (*Shervais and Vetter, 2009*). Older tholeiitic basalts include surface flows (789.4 ka to 1.22 Ma) and samples from MH-2 drill core (2.19 to 4.54 Ma). The younger high-K basalts range from 519.1-354.2 ka in the western SRP, and from 87.3 to 2.1 ka along the South Fork Boise River, just 60 km to the north of Mountain Home. The transition from old tholeiitic basalt to young high-K basalt occurs circa 700 ka (*Shervais and Vetter, 2009*). High-K basalt is ubiquitous in the WSRP and along the South Fork Boise River to the north, where they range from 100 ka to 2.1 ka (±4 ka) in age.

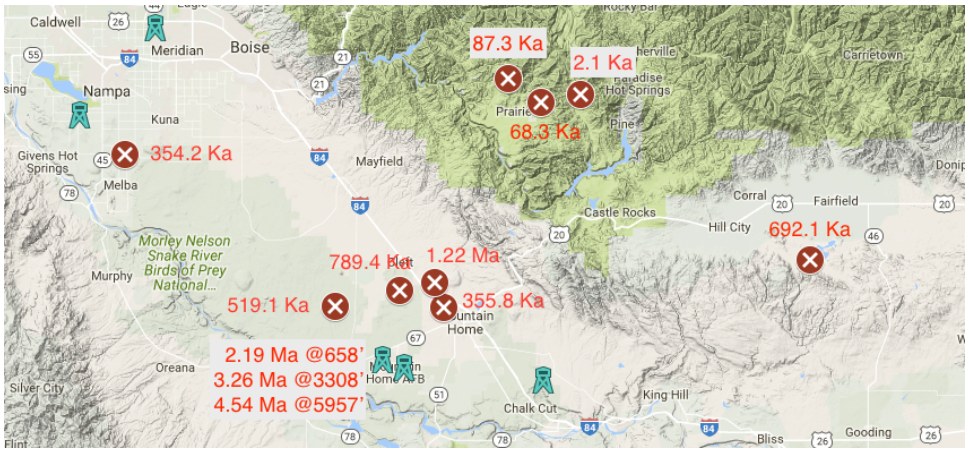

Figure 8. Map with locations of newly dated basalts, which range in age from 4.54 Ma (bottom of MH-2 well) to 2.1 Ka (Fall Creek).

8.1.2 Magnetotelluric Surveys: A 3D MT inversion was made with the Mountain Home data. The resistivity structure recovered by this inversion is shown in Figure 9. Low resistivity (1-10 Ohm-m) distribution in the 3D resistivity cube outlines the lateral and depth extent of a seal for a potential geothermal reservoir *(https://gdr.openei.org/submissions/1249)*. This includes both sedimentary layers and possible alteration zones. The uppermost resistive layer (200-500 Ohm-m) is representative of near surface unaltered porous basalts, whereas increased resistivity (50-70 Ohm-m) underneath the low resistivity structure is representative of crystalline volcanic units that could be associated with the presence of geothermal fluids. Similar structures were recovered on the eastern side of the basin, close to Bostic 1A, using MT data collected in 1980 by Unocal.

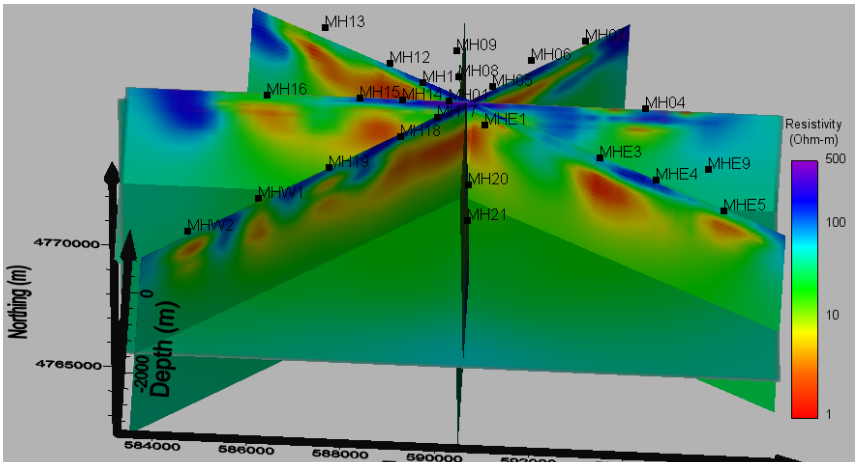

Figure 9. Fence diagram of final resistivity structure recovered by 3D MT inversion. Low resistivity zones represent potential clay seals from lake sediments or alteration, or both. Crossing point on the fence panels is the MH-2 deep well. Within the basin, a sedimentary layer, at some places up to 1,400 m thick, has a low resistivity and overlies higher resistivity volcanic formations.

8.1.3 Seismic Reflection Surveys: No new seismic data were collected during Phase 2; however, data collected during Project Hotspot were reassessed, along with available commercial seismic data. Legacy seismic reflection data within the WSRP region are of varying quality, but the bulk of data were acquired for oil/gas exploration in the deep sedimentary basin locations to the west of Mountain Home and to the south of Boise, Idaho. These data define bedrock depth, volcanic rock interbeds, and offset strata and related faults. Geothermal and groundwater focused seismic profiling related to the Bostic 1A borehole (*Arney, 1982*), the MH-2 borehole (*Liberty et al., 2015*), and the Boise geothermal system (*Liberty, 1998*) also provide insights into stratigraphy and structures for the upper few km beneath the WSRP margins. US Array lithospheric-scale seismic tomography and receiver function data also provide context of crustal and mantle heat sources, crustal thickness, and plume-related geometries.

8.1.4 Gravity and Magnetic Surveys: A regional potential field model was developed for the WSRP based on high-resolution gravity data collected across the plain. The seismic reflection results associated with the MH-2 borehole (*Liberty et al., 2015*) and new MT data were used to refine this model. A regional potential field model was developed for the WSRP that extends through the Mountain Home resource area, largely based on high-resolution gravity data collected across the plain. Regional lithospheric structure of the model was constrained by a N-S-trending deep seismic refraction line, extending from Boise to Elko, NV that crosses the

profile at Mountain Home (*Hill and Pakiser, 1967; Prodehl, 1970*). In addition, seismic reflection results associated with the MH-2 borehole (Liberty et al., 2015) and data from 33 new MT stations, collected as part of this study across the MH-AFB and extending 20 km along the SW-NE profile, were used to inform the interpretation of structures around the base.

The dominant feature along the profile is a prominent gravity high that extends nearly the full length of the WSRP (Figure 10). This high is primarily modeled as a dense mafic root and sill complex intruded into the lower and middle crust. Also contributing to the high, however, is a horst block in the upper crust consisting largely of dense mafic lavas (*Glen et al., 2017*). Both wells (MH-1 and MH-2) drilled at the MH-AFB are located over the prominent gravity high (Figure 10) and extend into basalts interpreted to mark the top of the horst.

8.1.5 Water Chemistry: There are no flowing springs in the Mountain Home region at this time, as historically active springs, located at the eastern end of the Danskin Mountains, have dried up. Previous work on water recovered from MH-2 (*Atkinson, 2015*) show that it is unlike any other thermal waters that occur in the SRP region: the primary anion is sulfate, it has high $\delta^{18}O$-δD values that fall on a mixing line between meteoric and volcanogenic waters, and its multicomponent equilibrium temperature is ~150ºC, similar to measured downhole temperatures.

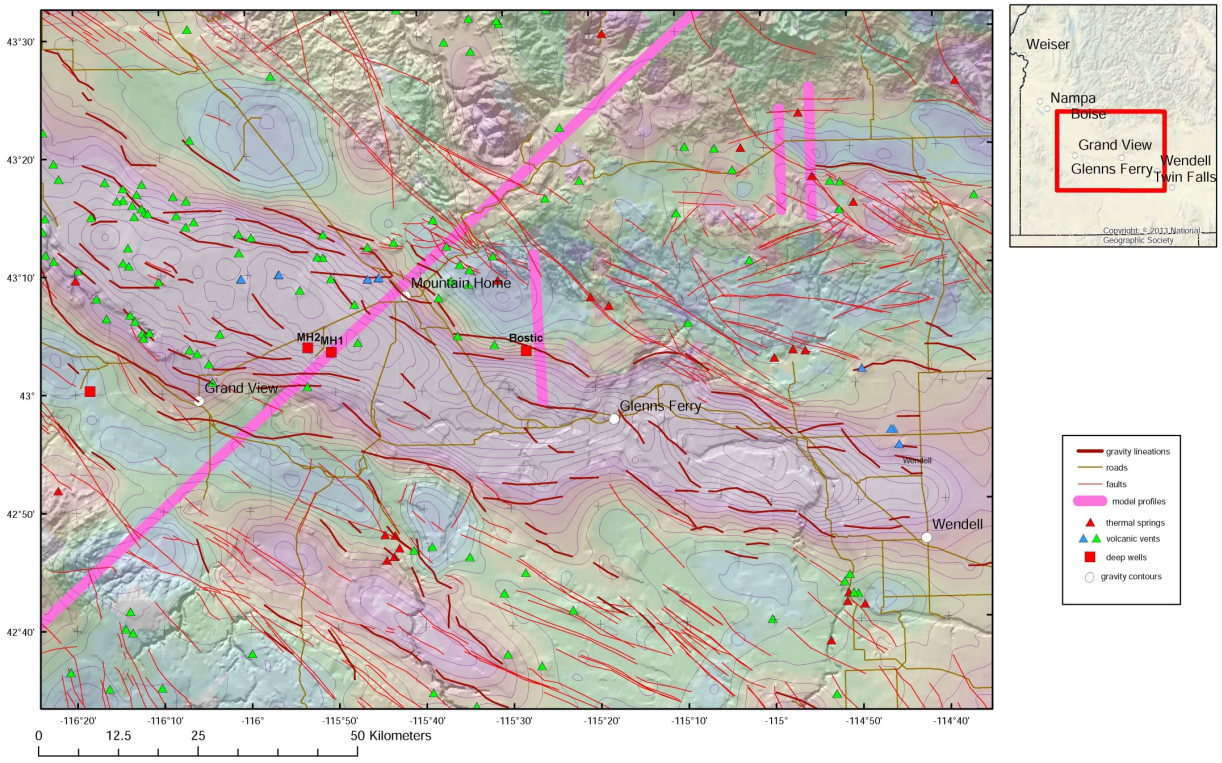

Figure 10. Colored residual isostatic gravity and shaded topographic relief map of the western SRP showing volcanic vents, thermal springs, and deep drill holes. Also shown are geophysically-inferred structural features (gravity lineations) based on maximum horizontal gradients of residual isostatic gravity. Geophysical grids are superimposed on a topographic base map. Pink lines are modeled cross-sections.

8.2 Bostic (Glenns Ferry) - Western Snake River Plain

8.2.1 Magnetotelluric Surveys: A 2D MT survey collected in 1980 by Unocal was reprocessed to evaluate potential seals in the Bostic area; this survey reveals structures similar to those in the Mountain Home area. Low resistivity (1-10 Ohm-m) indicates the depth extent of a seal for a potential geothermal reservoir. This includes both sedimentary layers and possible alteration zones. The uppermost resistive layer represents near surface unaltered basalts, whereas increased resistivity beneath the low resistivity structure is representative of volcanic formations (basalt, rhyolite) that could be associated with the presence of geothermal fluids.

8.2.2 Gravity and Magnetic Surveys: The potential field model of the Bostic area was derived from detailed gravity data collected along a line extending from the Bostic 1A well northwards to the Danskin Mountains (Figure 10) and from an aeromagnetic survey of the Mountain Home KGRA (U.S. Geological Survey, 1982). In addition, legacy seismic data and new MT data, collected as part of this study along a NE-trending line situated northwest of the modeled profile, were used to inform the interpretation of modeled structures.

The profile is characterized by a prominent gravity anomaly on its southern end, which corresponds with the central SRP gravity high. The Bostic 1A well is situated along the northern shoulder of this high, presumably within the structural horst. The model indicates the presence of two distinct intrusive bodies emplaced in the upper crust (extending to within 1 km of the surface) that were modeled to account for several 100 nT magnetic anomalies observed along the profile. This feature corresponds with a roughly 3x7 km wide anomaly seen in the aeromagnetic map (not shown).

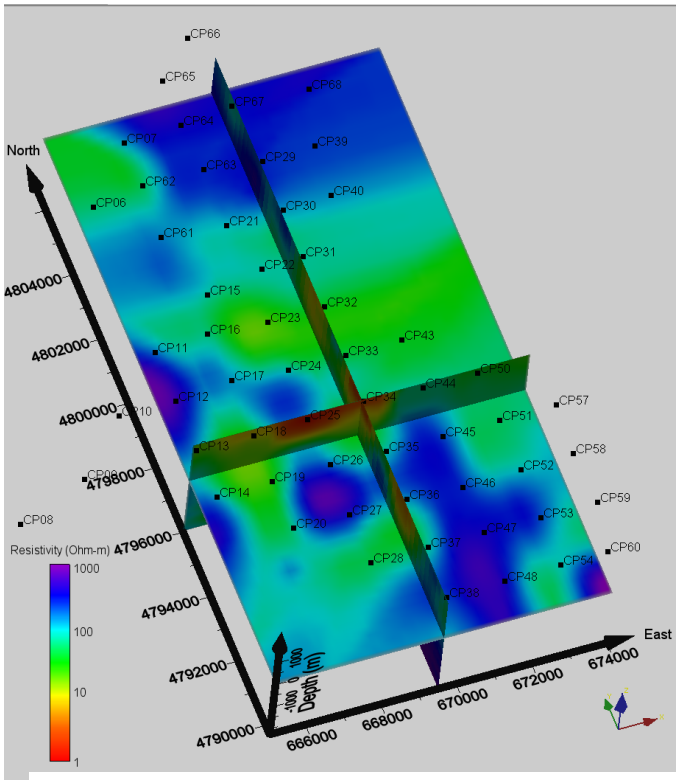

Figure 11. Fence diagram from 3D composite resistivity cube and depth slice of final resistivity structure recovered by MT inversion at Camas Prairie. The outline of the basin east of stations CP15-17 is clearly seen by change in resistivity from low (green color) to high (blue color) to the SW.

The potential field model reflects minor faulting following the interpretive schematic cross sections of Arney et al. (1984). This is primarily intended to illustrate the regional presence of such structures (note that a complex of faults occurs off-axis of the profile to the northeast of Mountain Home), whereas along this particular profile, the potential field data suggest that only a couple of the illustrated structures within the region north of the Bostic well have any significant geophysical expression that might suggest they involve appreciable offset and extend into basement.

8.2.3 Water Chemistry: The closest thermal springs to the Bostic region are at its northern end, at the western end of the Mount Bennett Hills. These include Latty Hot Springs and Prince Albert Hot Springs. Both have equilibrium reservoir temperatures estimated at 193-197ºC, based on the RTEst multicomponent geothermometer – among the hottest for springs in the SRP region (*Neupane et al., 2014, 2017*).

8.3 Camas Prairie-Mount Bennett Hills

8.3.1 Field Mapping and Sampling: Young volcanic rocks in Camas Prairie are tholeiitic basalts erupted around 700 ka, but the South Fork Boise River high-K basalts crop out less than 100 km to the NW (Figure 8). The Camas Prairie-Mount Bennett Hills region contains two dominant fault sets that strike WNW and ENE. In general, the WNW-trending faults are found in the eastern Mount Bennett Hills, east of The Pothole fault, whereas the ENE-trending faults are found in the western Mount Bennett Hills, west of The Pothole fault (Figure 5).

Geologic reconnaissance mapping of The Pothole fault system for this project documents more complex structures. The Pothole fault system is characterized by two dominant fault sets, which strike WNW and NNW. Both are predominantly east/northeast dipping. Fault striations were most commonly dextral-normal and secondarily normal. These orientations are more or less consistent with the attitudes of the major features at depth in the Camas basin, as interpreted from the geophysical studies described above. Relative ages of these fault sets could not be determined by cross-cutting relationships, however, the NNW-striking faults cut Cretaceous basement, the Oligocene Challis Volcanic Group, and The Pothole volcanic crater (circa 700 ka), so these fault systems remained active into the late Pleistocene. We expect that right-stepping geometries between the two WNW- and NNW-striking, right-oblique fault systems (releasing steps) are more conducive to permeability development and geothermal circulation than left-stepping (restraining steps) geometries.

8.3.2 Magnetotelluric Surveys: 2D inversions of MT data along several N-S and W-E profiles in Camas Prairie recovered resistivity structures that support the gravity and magnetic data interpretation. The outline of the basin east of stations CP15-17 (Figure 11) is clearly seen by a change in resistivity from low-to-high in the SW (*https://gdr.openei.org/submissions/1103*).

8.3.3 Seismic Reflection Surveys: Five 7-10 km long south-north seismic profiles and two 5-8 km long west-east profiles were acquired along section roads (one mile spaced) within the Camas Prairie (*https://gdr.openei.org/submissions/1102*). The focus of the seismic profiling effort was to identify permeable faults and to characterize the sedimentary cover that overlies basement. Seismic results suggest bedrock (volcanic rocks or granite) depths of <1.0 km beneath the southern margin of Camas Prairie, and define a complex network of active faults that correspond to locations of elevated groundwater temperatures (Figure 12). These faults offset basement (inferred to be older volcanic and granitic rocks), and overlying strata, and show that the depocenter of the basin is located towards its southern margin. Multiple, basin-wide unconformities are identified with late Quaternary sediment fill of less than 0.2 km along the basin margins.

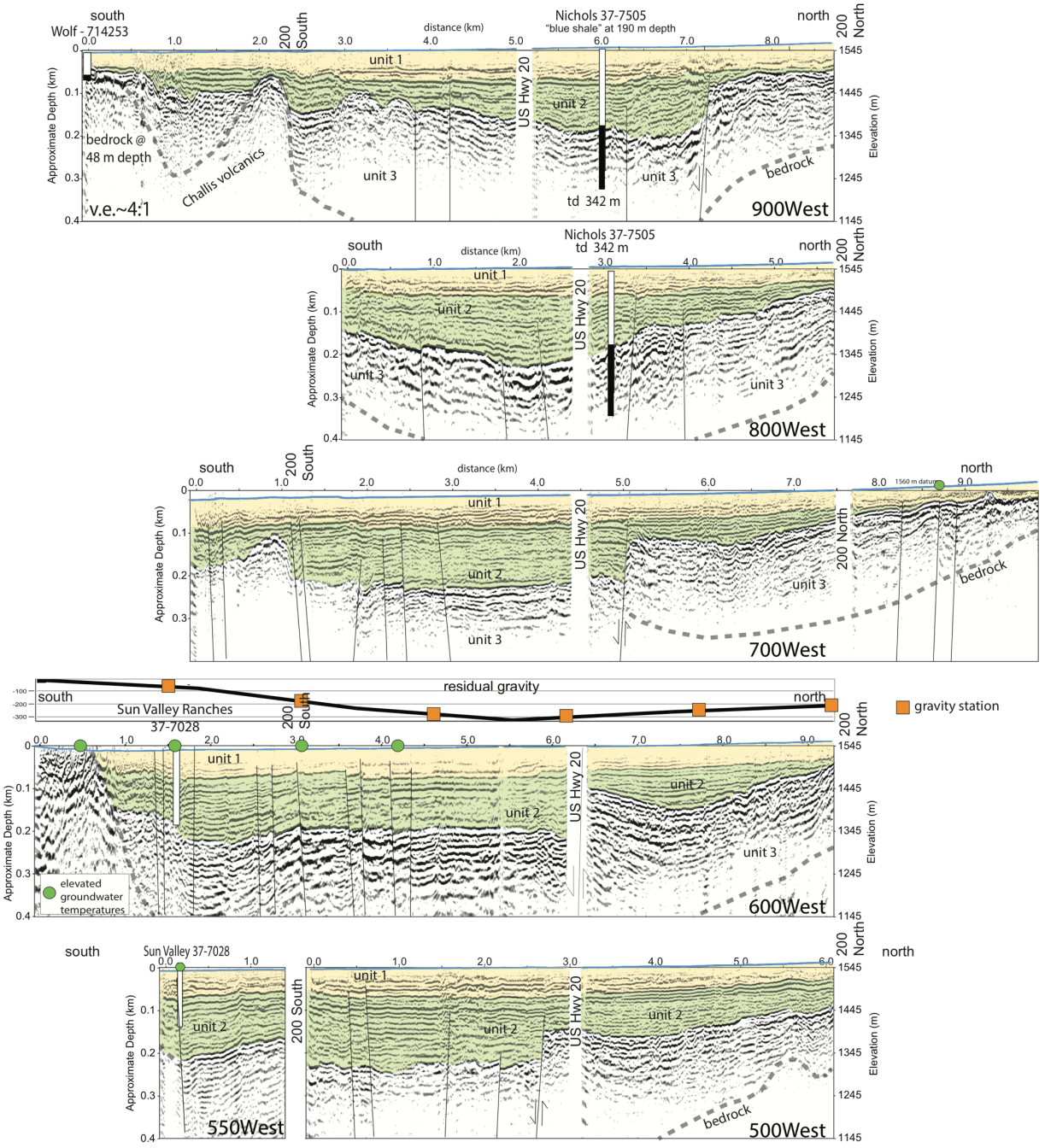

Figure 12. Seismic reflection profiles across Camas Prairie; locations shown in Figure 5 (600W to 900W profiles). All profiles run NS. Numerous faults in basement are evident as offsets in highly reflective markers. A major buried EW-trending fault lies under US HW20. The 600W profile shows location of thermal springs (green dots) relative to seismically identified faults. These faults correlate with offsets in gravity and magnetic potential fields and are being integrated into the overall structural models.

8.3.4 Gravity and Magnetic Surveys: Gravity and magnetic maps were gridded from a combination of new and existing data collected throughout the Camas Prairie valley and surrounding regions (Figure 13). Analyses of residual isostatic gravity and magnetic grids delineate a number of intrabasin structures that have little or no surface manifestation. These structures reflect two dominant sets of trends: W to WNW-trending structures that likely reflect the major basin-bound structural grain, and a NW-trending set that appears to control the major subbasin geometry of the valley.

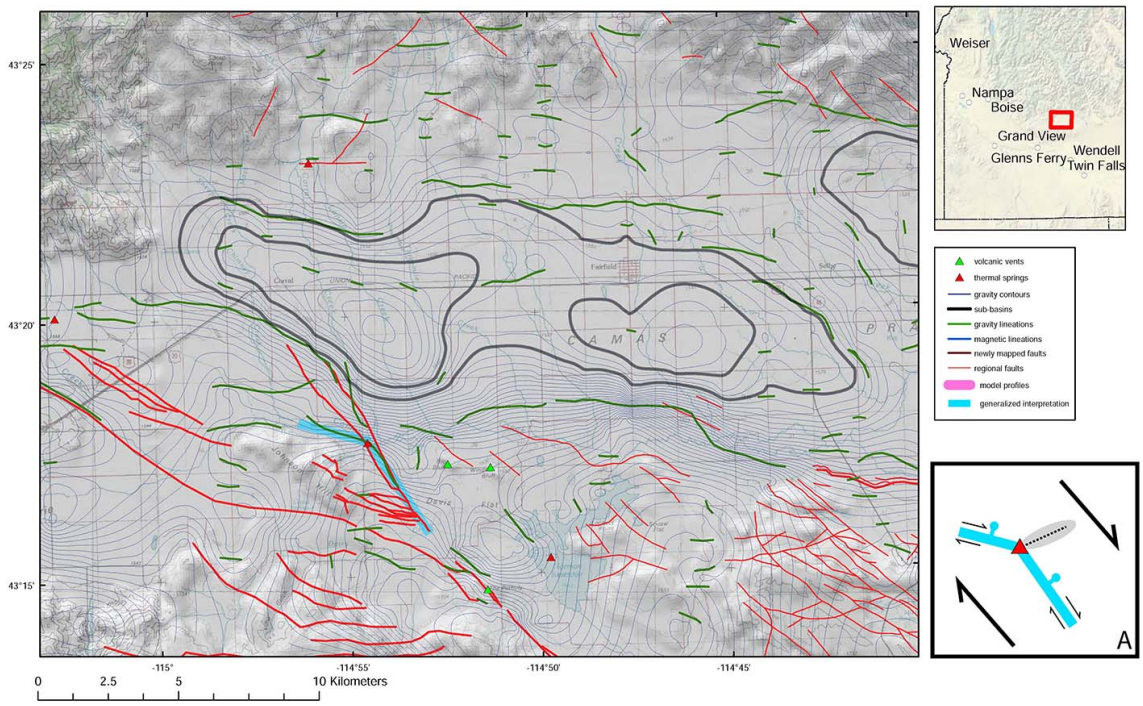

Figure 13. Topographic map of the Camas Prairie study area showing contours of the residual isostatic gravity, volcanic vents, thermal springs, deep drill holes, and profile model locations. Inset shows releasing step in Pothole system. Geophysically inferred structural features (gravity lineations) based on maximum horizontal gradients of residual isostatic gravity are shown in green. Faults (red) are derived from a number of sources including Garwood et al. (2014) and new mapping performed as part of this study.

Potential field modeling was performed along two profiles at the western end of the valley (lines 600W and 900W). Seismic data collected along these lines constrain the upper several hundred meters of the models. The models reveal a deep (500-1000 m) structurally controlled sedimentary basin that displays offsets along numerous structures imaged in the seismic profiles and reflected in the potential field data. MT results support structures identified by gravity or seismic data and provide depths to the base of basin sediments to constrain gravity inversions. The modeled basin is floored by crystalline basement that is, at least partly, capped with volcanic flows presumably derived from sources in the Mount Bennett Hills. The model also reveals that

the basin stratigraphy includes interbedded volcanic flows that are offset along the same structures identified in the seismic profiles.

Regional gravity mapping indicates the valley's subsurface consists of several NW-elongate sub-basins characterized by isolated gravity lows (Figure 13). The deepest of these inferred sub-basins, which resides on the western end of the Prairie just north of Barron's Hot Springs, reflects the deepest part of the basin (up to 1 km). This area coincides with anomalously high groundwater temperatures and may represent the primary geothermal reservoir for fluids that feed the springs and shallow thermal wells in this area. A steep gradient bounding the southwest side of the gravity low likely reflects the more structurally active part of the basin. Seismic results show diminishing offsets of shallow strata from southeast to northwest away from Barron's Hot Springs, intersecting fault systems beneath the central basin region, and offset of the shallowest reflectors that support ongoing NW-trending basin extension.

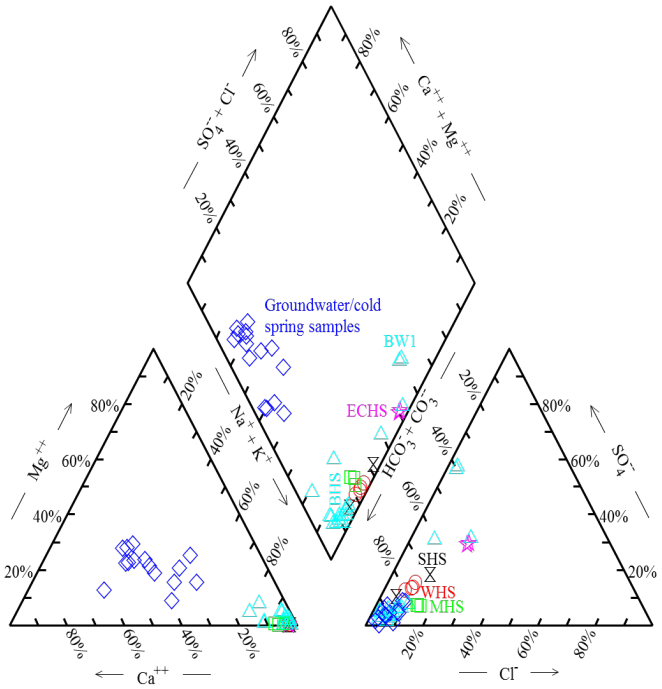

Figure 14. Piper diagram representing chemistry of water samples from Camas Prairie area. Samples are grouped as groundwater/cold springs (blue diamonds), Barron Hot Springs area (BHS cyan triangles; BW1 indicates recent (2014, 2016) water chemistry data of high sulfate water samples of the Barron Well 1), Sheep/Wolf Hot Springs (SHS black hourglasses), Wardrop Hot Springs area (WHS red circles), Elk Creek Hot Springs (ECHS magenta stars), and Magic Hot Springs area (MHS green squares; *Neupane et al., 2017*).

The steep gradient bounding the sub-basin in the western end of the valley is aligned with inferred NW-trending structures that extend through Barron's Hot Springs. The location of the hot springs appears to be related to the intersection of this NW-trending structure with more easterly-oriented basin-bounding structures that delineate the southern edge of the valley.

5.3.5 Water Chemistry: Our new water chemistry results for the Camas Prairie and Mount Bennett Hills (*Neupane et al., 2017*) show that, in general, cooler groundwater and spring samples are Ca-HCO_3-type waters, whereas hot spring and thermal well samples are Na-HCO_3-type waters (Figure 14). A mixing trend is observed between Ca-HCO_3 and Na-HCO_3 water types. Oxygen and hydrogen stable isotopic results show that most samples exhibit a small shift in $\delta^{18}O$ to values higher than local meteoric water; a few samples show significant shift to higher values, indicative of oxygen isotope exchange during high-temperature water-rock interaction in hydrothermal systems.

In general, water chemistry and isotopic compositions indicate that hydrothermal waters in Camas Prairie are dominantly meteoric in origin with some modification from water-rock interaction at elevated temperature (*https://gdr.openei.org/submissions/983)*.

We used multicomponent and conventional (quartz, Na-K, Na-K-Ca) geothermometry to estimate reservoir temperatures in Camas Prairie (*Neupane et al., 2017*). Our geochemical and geothermometry analysis indicates two areas of interest, one on the northern side and the other on the southern side of the Prairie, with estimated reservoir temperatures as high as 200ºC and 110ºC, respectively. Water geochemistry suggests that these correspond to geothermal resource types: one associated with the Idaho Batholith (to the north), and a second (to the south) related to Quaternary volcanism and intrusions within the Snake River Plain province.

9.0 DATA ANALYSIS

9.1 Detailed Stress-Strain Analysis

The orientation of stress fields is a critical part of defining reservoir characteristics. For the whole SRP the vast majority of the area appears to be under a normal faulting stress regime, but there are a few places where the stress data suggest strike-slip, oblique-slip, and thrust faulting stress regimes. We used the nearest stress data point to define the stress regime for each lineation. Our detailed structural mapping of fault systems in Camas Prairie allowed us to evaluate local stress regimes and the strain response to that stress, yielding refined estimates of the local stress fields and their orientation. The stress data are used to weight fault and lineament slip and dilation tendencies, both of which are proxies for permeability on these structures (e.g., *Jolie et al., 2015; Siler et al., 2017*). These data were integrated with regional stress and strain estimates from previous studies (*e.g., Payne et al., 2012; Kessler et al., 2017*).

9.2 GIS Analysis

Our GIS work involved two related efforts: first, to revise and update our approach to data handling to simplify data input and analysis, and second, to reassess our weights and parameters from Phase 1 in order to improve data products in Phase 2.

9.2.1: GIS Methodology: We recast our initial GIS methodology (*DeAngelo et al., 2016*) into a format that allows input of data weighting, including intra- and inter- CRS weight factors, from a look-up table that can be easily reprogrammed to evaluate new combinations of data and weights. We also prepared high resolution (500 m for MH region and 100 m for Camas Prairie) CRS and CCRS maps to aid in prospect evaluation, carried out a sensitivity analysis on our CRS maps to reveal which data types they are most sensitive to, and prepared new CRS maps with different combinations of weight factors to evaluate how different expert opinions affect the final products. We also validated our GIS methodology by utilizing the input data set developed by the Modoc Plateau play fairway project (*Siler et al., 2017*) and compared their output maps with those generated using our methodology; good agreement was observed.

New data and model results from Phase 2 were collated with existing data to update our CRS and CCRS maps for the Snake River Plain, and for our primary focus areas: (1) the WSRP blind systems near Mountain Home, Idaho, and the Bostic 1A deep well, and (2) the central Camas Prairie region near Fairfield, Idaho. As in Phase 1, the distribution of heat was assessed using measured thermal gradients, interpolated heat flow values, the distribution of volcanic

vents (weighted by age, size, and composition), groundwater temperatures in non-thermal wells, measured temperatures of thermal waters from springs and wells, calculated cation, silica and multicomponent geothermometry of waters from thermal springs and wells, and the $^{3}He/^{4}He$ ratios of thermal waters (*DeAngelo et al., 2016; Shervais et al., 2016; Neupane et al., 2014, 2017; Dobson et al., 2015*).

Permeability was assessed using the weighted sum of mapped faults, magnetic lineaments, and gravity lineaments (*DeAngelo et al., 2016; Shervais et al., 2016*). Fault and lineament segments were weighted using slip and dilation tendencies, based on new data for regional stress orientation (*Glen et al., 2017; Kessler et al., 2017*). As in Phase 1, structural intersections were assessed using density functions as a proxy for fault/lineament density, where high fault (or lineament) densities tend to favor multiple intersections (*Shervais et al., 2016*).

On a regional scale there are two potential seal types: (a) fine-grained lacustrine sediments, which are largely impermeable, and (b) self-seal of volcanic rocks by hydrothermal alteration (*Nielson and Shervais, 2014*). Locally, we were able to use 2D and 3D arrays of MT stations to document the occurrence of low resistivity seals in both of our focus areas.

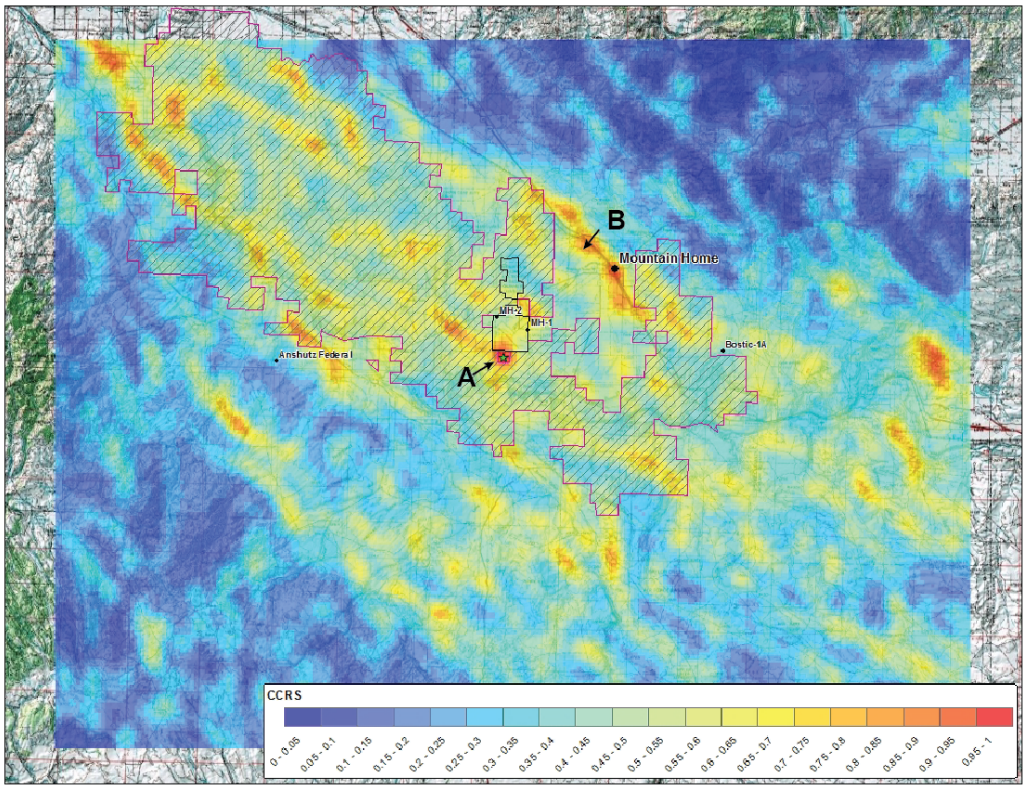

Figure 15. Phase 2 CCRS map for WSRP and Mountain Home region. Areas of high prospectivity are seen near Mountain Home AFB (A), Mountain Home city (B), and in the far NW near Caldwell, Idaho. The area around Mountain Home city appears to lack a clay cap seal, and we have no new data near Caldwell. Our preferred site is south of older drill holes on MH-AFB (A, star). The map shows the BLM Morley Nelson Birds of Prey Conservation Area (pink outline with cross hatch) and MH-AFB (black cross-hatch).

9.2.2 CRS and CCRS Maps: We prepared new high-resolution CRS and CCRS maps for the western SRP near Mountain Home and for Camas Prairie (Figures 15 and 16). In addition to being gridded at 500 m and 100 m pixel size, respectively, gravity and magnetic lineaments were reanalyzed at higher resolution, MT and seismic data from our new surveys were included, along with updated values for helium isotopes, equilibrium geothermometry temperatures, and vent ages. We used new values for intra- and inter-CRS layer weights, based on multiple expert opinions. For the local Phase 2 maps, a 2500m search radius for kernel density functions was applied to reflect the higher density data coverage (a 10000m search radius was used in Phase 1 for the initial regional evaluation; see Appendix E for local CCRS maps).

Since our Phase 1 maps were prepared at the regional scale, it was necessary to prepare both Phase 2 *and* Phase 1 maps using the same analytical routine (i.e., same study area size, grid size, weighting parameters, etc.) in order to evaluate how our new data impacted our CCRS maps. Specifically, because our new data are focused on areas near MH and the Camas Prairie, the new higher resolution maps for Phase 2 were prepared at a local scale (Figures 15, 16; also see Appendix E).

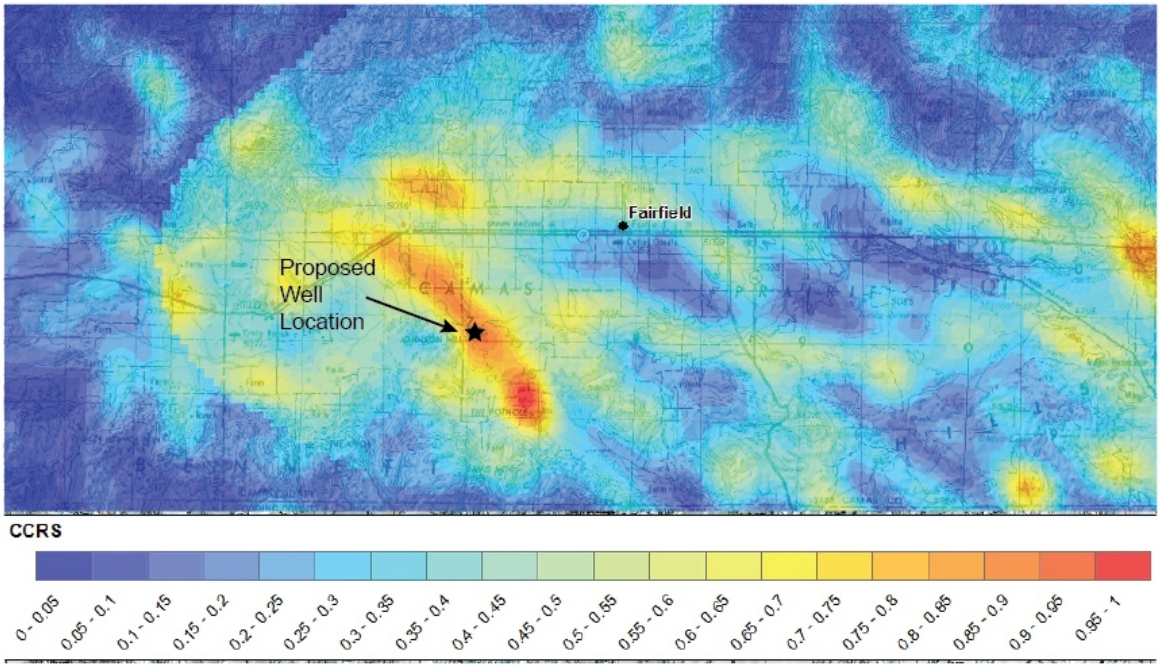

Figure 16. Phase 2 CCRS map for Camas Prairie region. The prime target area stands out as red-orange region along The Pothole fault system (not labelled). The proposed exploratory well location near Barron Hot Springs is indicated by the star. This site was ultimately drilled in Phase 3.

10. DATA INTEGRATION – VALIDATION WELL SITE SELECTION

10.1 Mountain Home – Western SRP

The focus of our planned work for the Mountain Home region is to drill a deep slim well to validate our PFA model for identifying permeability in blind systems. Previous studies have confirmed the presence of an elevated thermal gradient over a large area near Mountain Home, so additional thermal gradient drilling would not be productive.

Mountain Home region is characterized by high geothermal gradients and exhibits high geothermal potential on CRS and CCRS maps in areas associated with the regional gravity high that underlies the region (Figure 15). The flanks of this structure are especially favorable because they likely represent large offset fault traces and associated fracture zones on the margins of an uplifted horst block. The lineaments that highlight these structures are defined by high gradients in the isostatic gravity anomaly, which delineate offsets in dense basaltic basement (*Glen et al., 2017*). In addition, young volcanic activity associated with the high-K transitional alkaline suite, which ranges in age from 519 ka to 355 ka locally, and as young as 2.1 ka <50 km north, implies deep magmatic intrusive activity, which provides a heat source for ongoing geothermal activity.

Our CCRS maps for the Mountain Home area have been updated with revised internal weights, new age data, new MT data for clay alteration and seal, and new higher resolution mapping of lineaments defined by steep gradients in the gravity and magnetic anomalies (Figure 15). In addition, we have added the presence of a regionally extensive mid- to upper crustal sill complex (interpreted from gravity data) as a contributor to the HEAT CRS. The intrusion of these sills over a prolonged period of time adds heat to the crust incrementally, and prepares the ground for the youngest intrusions, that drive the most recent geothermal system. This concept is supported by high thermal gradients in deep core holes on Mountain Home AFB (Figure 17).

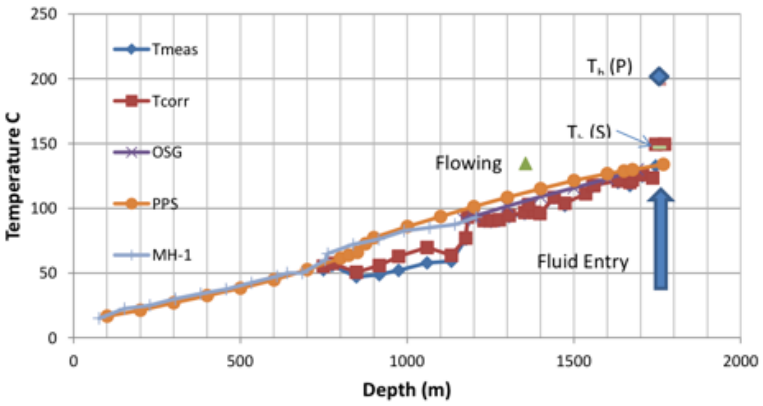

Figure 17. Temperature-depth curves for WSRP in holes MH-1 and MH-2. T_{meas} = measured high temperature with the temp while logging tool, T_{corr} = corrected temperature using the F(α,τ) method, OSG = Operational Support Group temperature log, PPS = gradient log by Pacific Process Systems; MH-1 is gradient for drill hole MH-1. T_h (P) and T_h (S) show primary and secondary fluid inclusion temperatures; Atkinson (2015) has measured primary inclusion temperatures to 368ºC. The green triangle shows the temperature recorded in the hole while fluid was flowing to the surface. The location of the fluid entry at 1745 m is shown. Thermal gradients are similar in other deep WSRP holes.

A formal assessment of recoverable geothermal energy for the MH-AFB region (*heat in place*), using area, reservoir thickness, and temperature estimates from well data (the deep holes MH-1 and MH-2), our magnetotelluric survey, and natural state model, and conservative recovery factor values (0.025, 0.15) estimates >79MW with 90% probability, and >204MW with 50% probability.

In the Mountain Home region, potential drilling sites are constrained by the *Morley Nelson Snake River Birds of Prey Conservation Area*, a BLM special use area that limits potential drill site locations (Figure 15). There are two prospective sites where drilling is possible: (A) in the area under and south of MH-AFB, and (B) just west of the town of Mountain Home and south of I-84 (Figure 15). The favorability of Site B is driven largely by the density of young volcanic vents in this area. However, detailed MT cross-sections derived from our 3D MT data model show that the conductive clay cap, which is ~1400 m thick under MH-AFB, pinches out and disappears to the NE (Figure 18). It is replaced by resistive rocks interpreted to be basalt based on detailed geologic mapping and water well logs. In contrast, sites located on MH-AFB (Site A) are underlain by a conductive clay cap (interpreted to include both lake sediments and altered volcanic rocks, based on core from the deep drill holes) that ranges from 250 m to 1750 m depth (Figure 18). This is underlain by resistive rock interpreted to be unaltered basalt, which would form the hydrothermal reservoir if fractured.

The resource at Mountain Home AFB is blind and likely located at depths of 1.5 to 2.3 km based on deep wells on the northern portion of the base. Validating our methodology here will require drilling to intersect permeability, since the geothermal gradients are well-known and regional in extent. The MH-AFB site also has the possibility of U.S. Air Force (USAF) funding for ongoing exploration and development and likely has a relatively simpler permitting and permissions process.

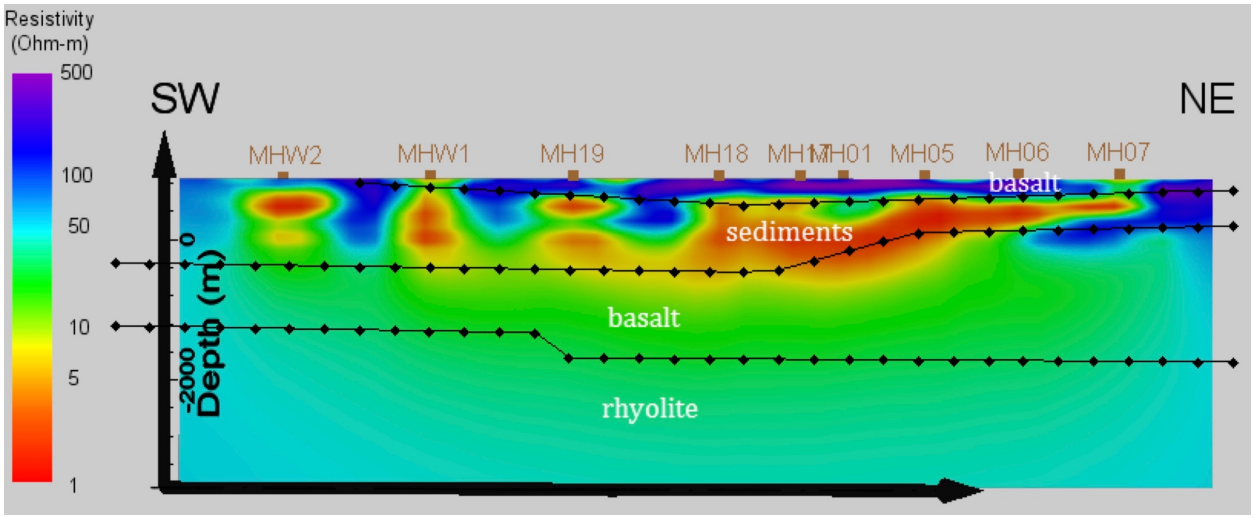

Figure 18. MT transect from 3D processing array, from SW corner to NE corner. The conductive clay cap is thick under MH-AFB, but pinches out to the NE, where it is replaced by resistive basalts. The town of Mountain Home lies farther to the NE.

10.2 Bostic – Western SRP

The Bostic region, anchored on the Bostic 1A wildcat well, has a more limited data set than the other areas. The primary addition was a Unocal MT traverse from the 1980's which was obtained from their data repository, and several new high-resolution gravity traverses (*Glen et al., 2017*). Despite the high temperature gradient in the Bostic 1A well (65ºC/km), it lacks other indicators of high heat potential, and does not appear to have permeability at depth. As a result, it

still appears as an area of low geothermal potential on CCRS maps of the WSRP (e.g., Figure 15) and will not be further considered.

10.3 Camas Prairie–Mount Bennett Hills

In the Camas Prairie region, prospective areas are found along The Pothole fault system, where it forms oblique intersections with numerous small faults to the south and west (Figure 5). The resource here is indicated by thermal springs that cluster along the fault systems, thermal and irrigation well geochemistry indicating >110°C reservoir conditions, and elevated $^{3}He/^{4}He$ ratios (~2 R_A) in groundwater suggesting a recent magmatic volatile source. A failed water well that was drilled to 550 feet (~168 m) near the Pothole Fault encountered a temperature of 91°C at a depth of 300 feet (~90 m) (*Mink, 2010*); this well confirms the presence of shallow hot outflow associated with this geothermal system. Volcanism is somewhat older (1.45 Ma to 692 ka), but it is also less than 50 km NW from The Pothole crater to the 2.1 ka vent on the Boise River. This high prospectivity is documented in our CCRS maps (Figure 16) and reinforced by field mapping that suggest high dilation in fault intersections, based on dip and slip directions observed on faulted surfaces. MT survey data indicate a region of conductive clay cap within our target zone. Target depths were expected to be as shallow as ~0.5 to 0.7 km.

III. PHASE 3 ACTIVITIES AND RESULTS

11.0 STATEGY AND APPROACH FOR PHASE 3

Our primary goal for Budget Period 3 was to validate our methodology by drilling a slim hole designed to intersect permeability in a hydrothermal system. Prior to drilling we carried out additional studies to pinpoint an exact site location within the target area. Additional goals were to update current geologic and validation models developed in Budget Periods 1 and 2, document our GIS methodology, and to prepare a user-friendly system to facilitate its application in other regions. Our work plan was predicated on the recommendations of geothermal industry representatives at the post-Stanford USGS meeting in 2017, who suggested that proper validation required intersecting a resource and performing reservoir testing to document its viability.

Our new higher resolution CRS and CCRS maps showed that two of our focus areas, Mountain Home and Camas Prairie, have high potential for geothermal resources. The first of our two scenarios postulated support from the U.S. Air Force to drill on or near Mountain Home Air Force Base (MH-AFB). The goal of this validation site was to intersect a hydrothermal reservoir at ~2 km depth. Since geothermal gradients are well-known in this part of the western SRP, a simple thermal gradient well would not provide a sufficient test of our methodology. If successful, this hole would validate our methodology, and further the USAF goal of energy independence for its bases. This option was not chosen because of problems coordinating our funding with possible USAF funding, and on recommendation of our Technical Monitoring Team.

The second scenario was to drill a validation well in the Camas Prairie area. The goal of this hole was to intersect permeability and heat in basement rocks in an area with elevated $^{3}He/^{4}He$ ratios and high thermal gradients, but our analysis of the local geology shows that the depth to basement is relatively shallow (<700 m). As result, a validation drill hole at Camas Prairie would be much less expensive and allow for extensive reservoir testing and analysis. This option was chosen upon the recommendation of our Technical Monitoring Team.

A 3D visualization of the MT data for Camas Prairie confirmed our results from gravity, magnetic, and seismic data, showing offsets in basement conductivity that correspond to the Pothole fault system and the presence of a clay cap over the suspected geothermal area.

12.0 PHASE 3 DATA ACQUISITION AND RESULTS

We identified a preliminary drilling target location in Camas Prairie from our Phase 2 studies. In order to finalize a specific drill site and drilling plan, we addressed some additional site-specific data gaps (Figures 19, 20). We also devoted a subset of resources to further site assessment around Mountain Home AFB, in support of potential future projects in collaboration with the USAF. Data gaps included a seismic survey across the potential drill site to locate fault systems at depth, field mapping, and additional gravity, magnetic and MT sites. Data acquisition and results are grouped here as the techniques used and areas studied are the same as in Phase 2.

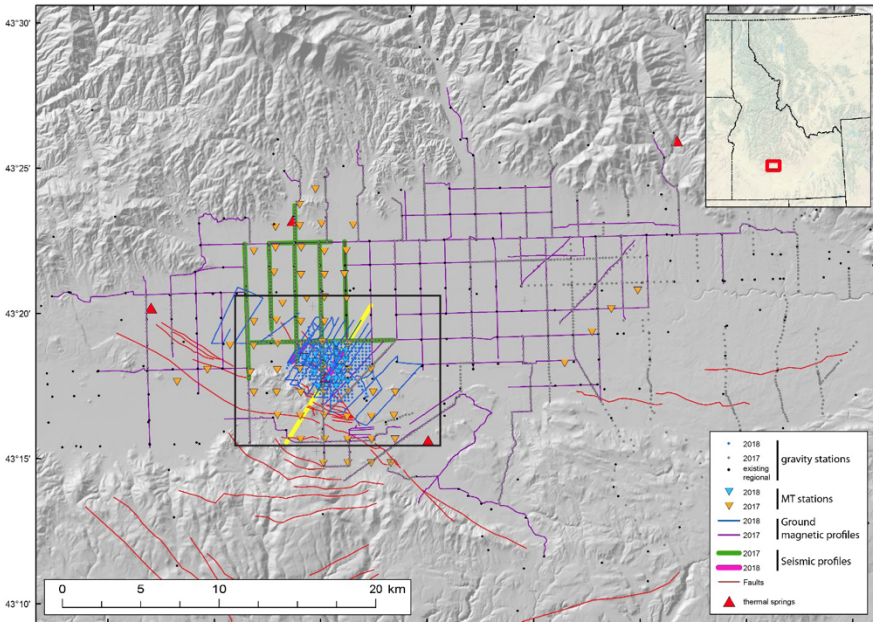

Figure 19. Regional shaded topographic index map of the Camas Prairie study area showing existing and newly collected seismic reflection profiles, MT stations, gravity stations, and magnetic traverses. Modeled profile shown in Figure 22 is depicted with yellow line. Faults are from USGS (2006) and Glen et al. (2017). The black box shows the extent of the Barron's Hot Springs area of Figure 20.

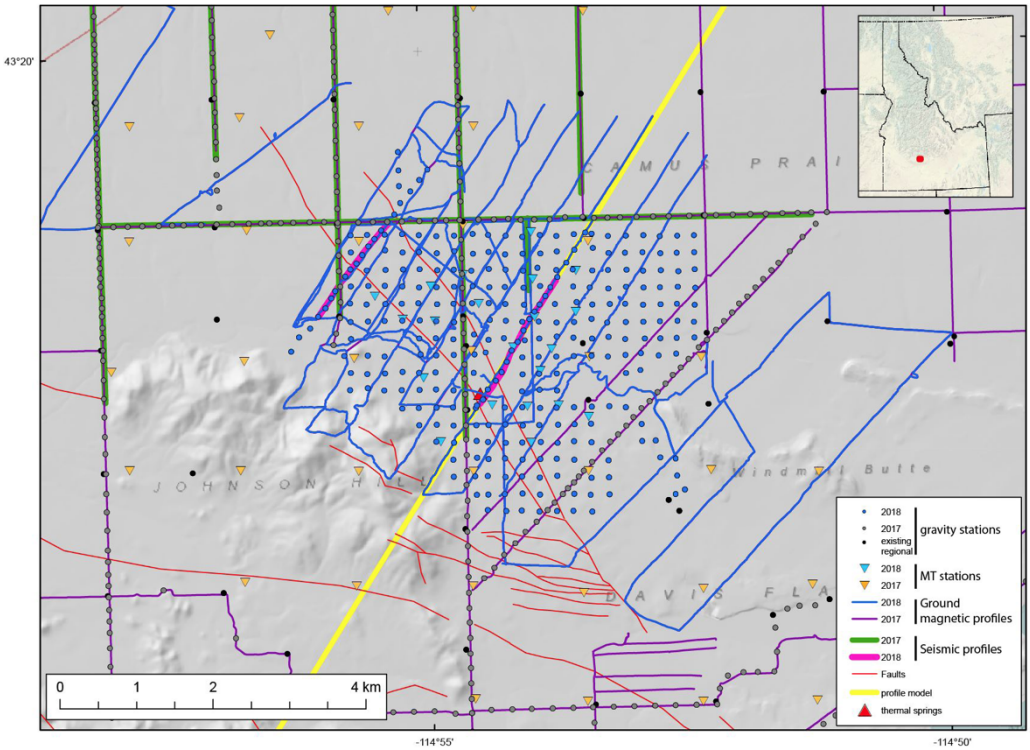

Figure 20: Shaded topographic index map of the Barron's Hot Springs focus area showing locations of gravity, magnetic, seismic and MT data. Barron's Hot Springs is shown by the red triangle at the center of the map.

12.1. Field Mapping and Sampling

Additional detailed field mapping was carried out to identify structurally complex areas with high fluid flow potential. These studies focused on The Pothole fault system and the numerous splays associated with this structure.

Mapping efforts, as part of this study, have involved reconnaissance mapping in the Camas Prairie along the southwestern foothills close to the Barron's Hot Springs and the Pothole, and analysis of aerial photos of the broader Mount Bennett Hills in the Camas and Bostic areas. Surface faulting in the Barron's Hot Springs-Pothole area consists of two distinct structural trends: NW (~285-295°) and NNW (~325°). Faults of both domains dip predominantly NE. Both structural domains pervasively cut the Pleistocene Pothole and other basalts, indicating that the faulting is Pleistocene or younger in age. Striated surfaces and relative offset of contacts and marker beds indicate that the dominant sense of slip is dextral-normal to normal.

Rock-property measurements were performed on outcrops, hand samples, and paleomagnetic cores taken from the study area in order to constrain the potential field models. These include 50 density measurements (dry bulk, grain and saturated bulk densities), 253 outcrop magnetic susceptibility measurements on 28 individual sites, and 26 remanence measurements made on Macon Flat and Pothole basalt flows). Model rock properties are based on these measurements, which include all the principal rock units from the study areas, as well as data derived from published and unpublished databases involving similar lithologies.

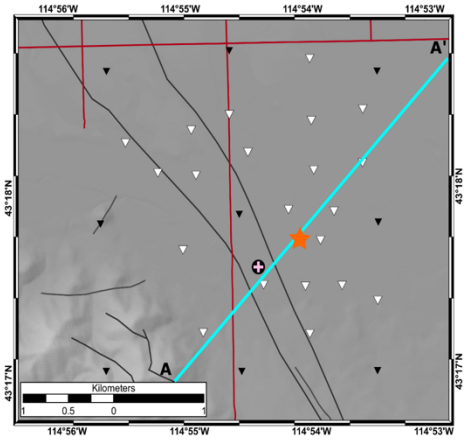

Figure 21: MT stations from Phase 3 are denoted as white triangles, Phase 2 as black triangles. The drill hole is shown by orange star. The Pothole fault zone is the northwest trending black lines. Profile line A-A' in Figure # is in cyan.

12.2. Magnetotelluric (MT) Surveys

Magnetotellurics (MT) is a passive electromagnetic geophysical method that measures the Earth's electrical response to natural time-varying magnetic fields that diffuse into the Earth and induce electrical currents in the subsurface. Depth of penetration of the diffusing magnetic field depends on subsurface resistivity and the frequency of the inducing magnetic field, where more resistive rocks and lower frequencies allow for deeper penetration. Typical depths are from 10's of meters to kilometers.

MT measurements in the field are done by using induction coils to measure the time-varying magnetic field for frequencies between 1000–0.001 Hz, and electric dipoles to measure the Earth's electrical response. A total of 63 MT stations were occupied in the Camas Prairie during Phase 2, and an additional 21 stations were added during Phase 3 characterization of the focus area around the Barrons Hot Springs (Figure 21).
(See https://gdr.openei.org/submissions/1103).

MT response functions were modeled in three-dimensions (3D) using the code ModEM developed by Egbert and Kelbert (2012) and Kelbert et al. (2014). Input data were edited using the EDI editor in MTpy (*Krieger and Peacock, 2014*) to remove obvious outliers in the data and suppress bias in the modeling. All data were interpolated onto 23 frequencies in the range of 500-0.001 Hz. Resistivity models were developed in two steps, one for the regional data, and another for the focus area around the BHS. The regional model had dimensions of 117 x 102 x 49 cells (280 km x 280 km x 200 km), with cell size of 200 m x 200 m within the station area, increasing by a factor of 1.4 outside. A total of 59 stations were inverted for the regional model. The focus area around the BHS had dimensions of 66 x 66 x 49 cells (180 km x 180 km x 200 km), with cell size 100 m x 100 m within the station area, increasing by a factor of 1.4 outside. A total of 30 stations were inverted for the local model. The regional model was used as an a priori model for the focused model. The thickness of the first layer of the models was set to 10 m and increased logarithmically downwards. Inversions were run on NASA's high-end computing capability (HECC) Pleiades supercomputer, where average run times were on the order of 60 hours.

The 3D resistivity model images two main structures that appear to control the location of the Barron's Hot Spring (Figure 22). The deeper structure is resistive and has a northwest trend following regional faults and controls basin geometry. The resistivity agrees with intrusive and extrusive felsic rocks with little porosity. The northeast edge of the resistive body coincides with the Pothole fault and dips towards the northeast at a steep angle (Figures 23, 24). The conductive anomaly is shallower and on the northeast side of The Pothole fault. The conductivity represents saturated porous sedimentary rocks with mixed clays and lacustrine deposits. A conductive zone underlies the Barron's Hot Springs and is bounded by the Pothole Fault and an un-named east-west fault.

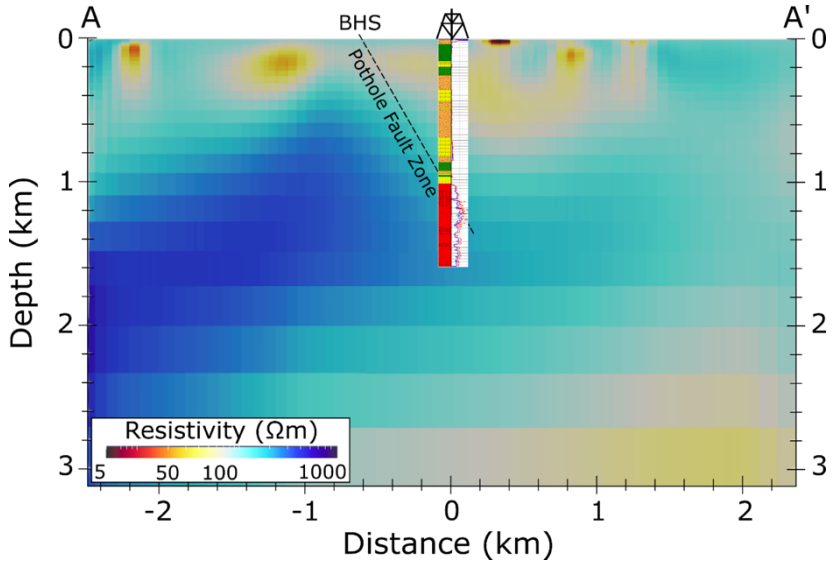

Figure 22: Profile A-A' from the 3D resistivity model. The resistivity well log and lithology are plotted at the drill hole location. BHS: Barron's Hot Spring.

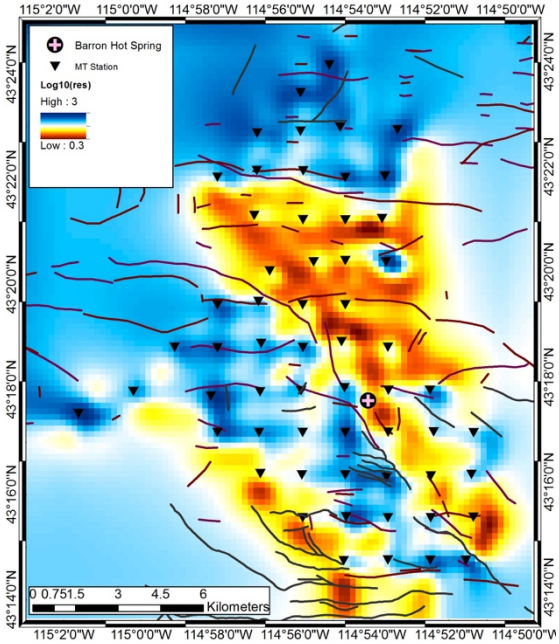

Figure 23: Depth slice from 3D MT model at 500 meter depth, showing contrast in resistivity on either side of The Pothole fault system.

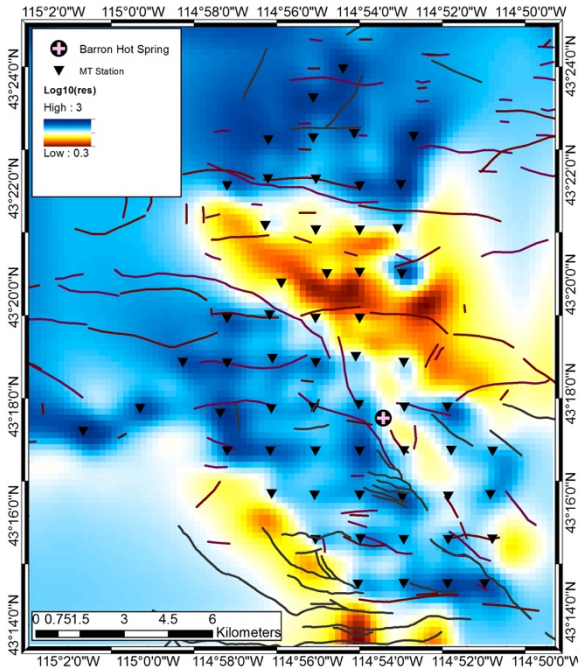

Figure 24: Depth slice of 3D resistivity model at 1000 meter depth, showing resistivity contrast on either side of The Pothole fault system.

12.3. Seismic Reflection Survey

Seven seismic reflection profiles were acquired on section roads (one mile spaced) within the Camas Prairie during Phase 2 (~53.3 km of data). During Phase 3, approximately 3.5 km of data were collected along two NE-trending profiles across the focus area (Figure 25). These profiles were termed Bakstrum and Barron. The focus of the Phase 3 seismic profiling effort was to identify faults that may be permeable pathways for upwelling geothermal fluids. The objective was to characterize the sedimentary cover that overlies basement in the vicinity of the proposed borehole and to identify offset reflectors that may indicate dilational normal faulting. While the road-based Phase 2 data were acquired using the Boise State seismic land streamer and accelerated weight drop system, Phase 3 data were acquired by hand, planting 10 Hz geophones and acquiring accelerated weight drop shot data every 5 m. Data were processed and interpreted with industry-standard seismic processing software (Halliburton's SeisSpace), where reflectors on Phase 2 cross lines were utilized to constrain the depth to key stratigraphic and structural boundaries. Topographic changes along the Bakstrum profile measured about five meters and topography varied by about two meters along the Barron profile. Both profiles were acquired across farm fields with no cultural noise interference.

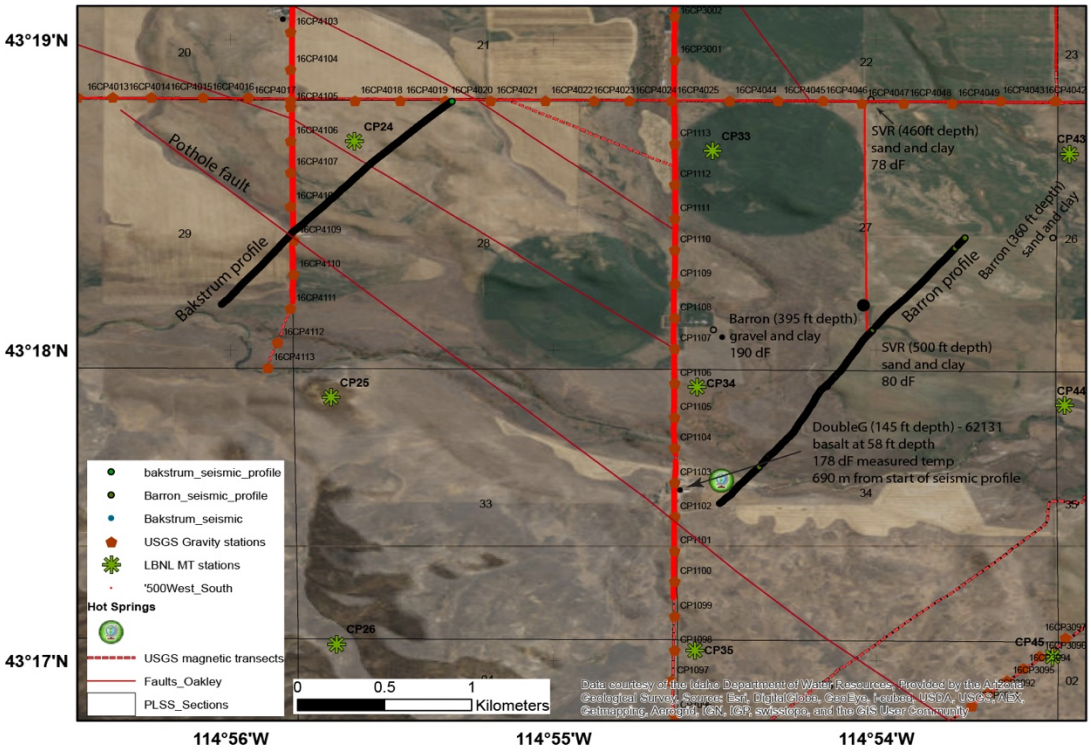

Figure 25. Aerial photographic map of the Bakstrum and Barron seismic profiles (black lines) in the vicinity of the Barron hot springs. Mapped faults (thin red lines) are from Phase II seismic profile (bold red lines) interpretations.

Both seismic profiles produced high quality reflectivity to characterize geologic targets in the upper few hundred meters. The Bakstrum profile, located approximately one mile to the west of the Barron hot springs, was acquired from 700 West, northeast to 200 South (Figure 25). The profile shows a strong-amplitude basement reflector at ~100 to 150 m depth (Figure 26). Above this prominent reflector, we identify mostly flat-lying strata consistent with lacustrine and fluvial deposits. We note an unconformity that lies within the sedimentary section, and this same boundary was identified with Phase 2 data. We interpret this boundary to represent a hiatus in sedimentary deposition during basin formation. We identify offsets on both bedrock and overlying reflectors, consistent with post-deposition faulting. The offset reflectors extend to within 20 m of the land surface at some locations, consistent with late Quaternary or younger motion. We identify the largest offset fault near position 1273 with a measured 44 m bedrock offset and a 77º dip to the east. The sedimentary basin is deepest to the east of this fault and this location along the Bakstrum profile may represent the best location for geothermal targets.

Approximately one mile to the east of the Bakstrum profile, we acquired the southwest to northeast trending Barron seismic profile. This profile extends from Barron hot springs near 600 West, northeast to near the intersection of 500W and 200S (Figure 25). Along the southwest half of the profile, a high amplitude reflector lies within the upper 30 m of the land surface. We interpret this reflector to represent the basalt basement surface. At position 2175, this shallow bedrock reflector terminates and we identify a 250 m wide zone between positions 2175 to 2225 that lack coherent reflectors. Farther to the northeast, we identify parallel reflectors that dip gently to the southwest. These reflectors are best observed in the upper 400 m, and are consistent with lacustrine and fluvial deposits that were identified in water wells of the region. Between the region that shows shallow bedrock and the region that shows near flat-lying strata, we interpret a fault or fault zone that defines the western margin of a sedimentary basin. These reflectors within the basin increase in dip with increasing depth, consistent with post-deposition tilting from fault motion. Elevated temperatures in nearby boreholes suggest the fault is a conduit for upwelling geothermal waters.

Seismic transect data are archived in the Geothermal Data Repository at: *http://gdr.openei.org/submissions/1102*.

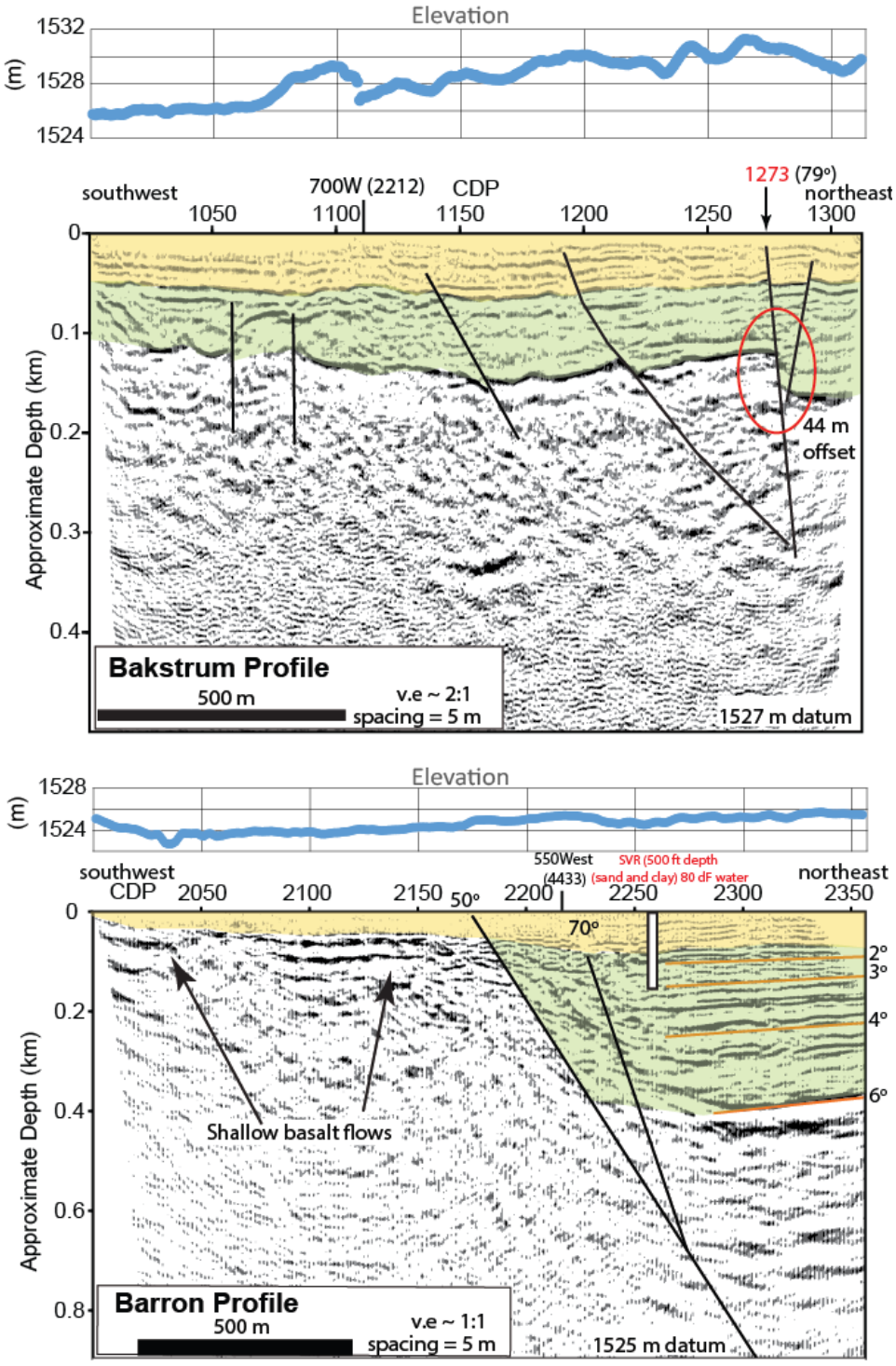

Figure 26. (top) Bakstrum seismic profile with elevation profile and interpretation. (bottom) Barron profile with elevation profile and interpretation.

12.4. Potential Fields (Gravity and Magnetics)

Potential field methods are used in geothermal exploration to facilitate imaging of subsurface structures (e.g., faults, fractures, and contacts) that may provide conduits or barriers to fluid flow. Variations in gravity and magnetic fields occur due to lateral contrasts in rock density and magnetic properties (magnetic susceptibility and remanent magnetization), respectively, and can be used to resolve the geometry and origin of buried sources, particularly when combined with other geologic constraints.

In the Camas Prairie, the physical properties of mafic igneous rocks contrast strongly with the surrounding tuffaceous, sedimentary, and silicic intrusive and extrusive rocks to produce prominent gravity and magnetic anomalies. As a result, potential field methods are particularly well-suited for mapping and modeling subsurface geologic structures such as faults and contacts that juxtapose these contrasting rock types and lead to distinct gravity and magnetic anomalies. Important constraints for potential field modeling typically come from other geophysical data (e.g., seismic reflection and MT), regional geologic mapping, borehole logs from wells, and rock-property measurements. Potential field data are summarized in Figure 27.

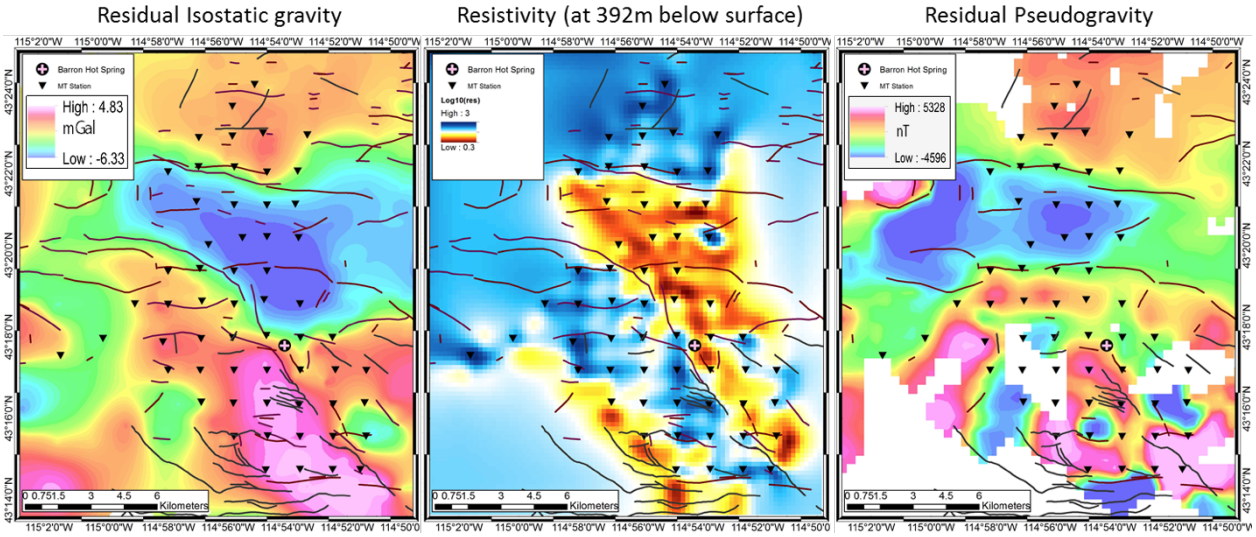

Figure 27: Regional maps of the western Camas Prairie of gravity (residual isostatic, left), resistivity (at 392m below the surface, middle), and magnetics (residual pseudogravity, right), showing geophysical lineations derived from maximum horizontal gradients of gravity (plotted on gravity and resistivity maps) and pseudogravity (plotted on the magnetic map).

12.4.1. Gravity. As part of the present study, a total of 1612 (1329 during Phase 2, 293 during Phase 3) new gravity data were collected in Camas Prairie to improve regional coverage in areas of sparse control and provide detailed coverage (100-200m station spacing) along a series of profile lines in the study area (Figures 19, 20). These were combined with existing data (*Glen et al., 2017; Shervais et al., 2012; PACES, 2016*). Gravity data were reduced using standard gravity reduction methods (*Dobrin and Savit, 1988; Blakely, 1995*), in order to produce a gravity grid reflecting lateral variations in density in the crust that is used to map faults and contacts, perform 2D modeling of subsurface structure, and perform a regional gravity inversion of the basement surface (Figure 27, left).

12.4.2. Magnetics. In the Camas Prairie, over 850 line-km of new high-resolution ground magnetic data (~725 km in 2017 and ~130 km in 2018) were collected on foot along off-road profile lines, and using ATV magnetometer systems (*Athens et al., 2011*) to collect data along roads and in agricultural fields (Figures 19 and 20).

12.4.3. Potential Field Mapping and Profile Modeling. We applied a variety of derivative and filtering methods to the magnetic and gravity data to help delineate structures, such as intra-basin or basin-bounding faults or contacts, and to constrain their geometries. Residual maps (Figures 28, 29, 30), produced by upward-continuing the observed anomalies and subtracting the result from the original grid, are useful for removing the contribution of deeper sources, and emphasizing surface and near-surface sources. The pseudogravity (or magnetic potential) transformation (Blakely, 1995), converts a magnetic anomaly into one that would be observed if the magnetic distribution of the body were replaced by an identical density distribution. Although there are significant assumptions that can limit its effectiveness, this method can be useful for simplifying the interpretation of magnetic sources by centering magnetic anomalies over their sources.

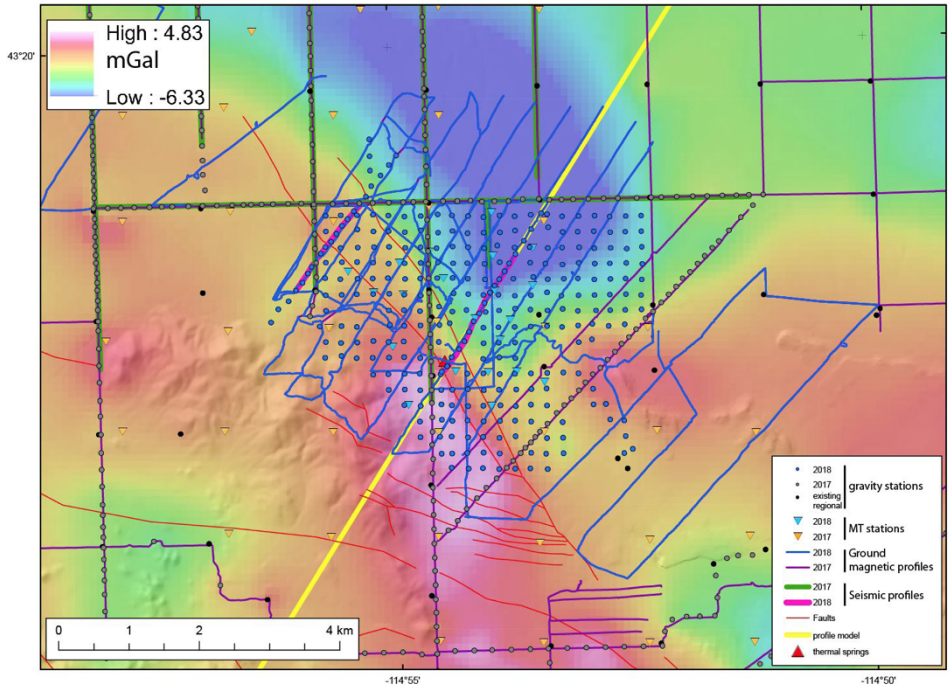

Figure 28: Colored residual isostatic gravity on shaded topographic relief map of the focus area around Barron's Hot Springs. Yellow line is profile in Figure 33.

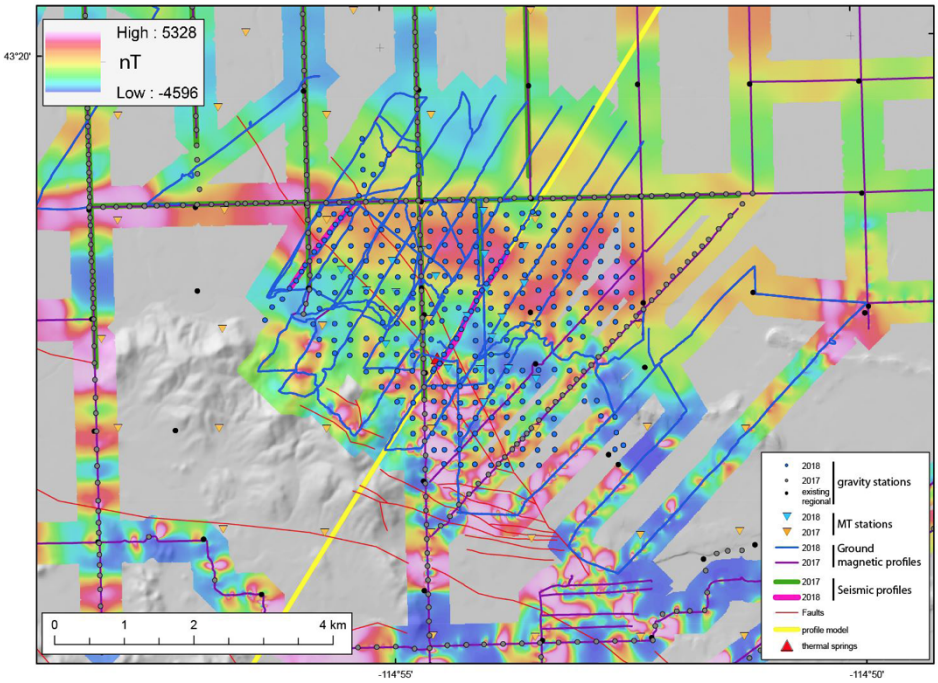

Figure 29: Colored reduced to pole magnetic field on shaded topographic relief map of the focus area around Barron's Hot Springs.

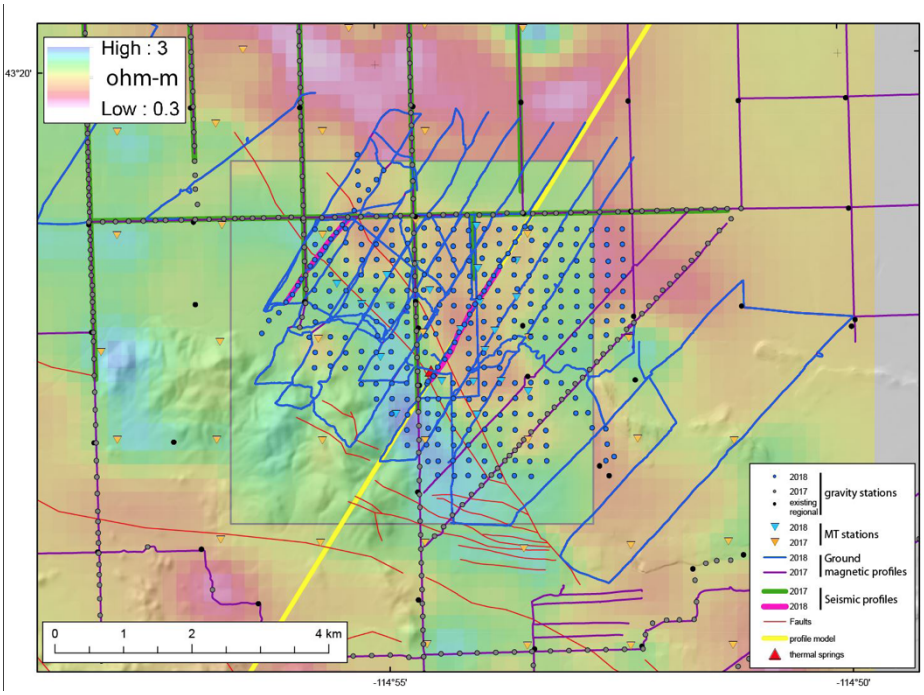

Figure 30: Colored MT resistivity (at ~500m depth) on shaded topographic relief map of the focus area around Barron's Hot Springs. The MT grid inside and outside the area indicated by the grey box reflect modeling results based on coarse- and fine-mesh inversions of the data, respectively.

Two-dimensional potential field models were constructed along profiles across the study area. Where possible, potential field, seismic and MT data collection was coordinated to facilitate modeling and interpretations (Figures 27 to 30). In the 2D modeling, subsurface geology is approximated by horizontal tabular prisms or blocks that vary in the ± Y directions (commonly referred to as 2¾-D modeling). The surface extents of model blocks were initially informed by geologic mapping, MT, and seismic cross sections. The geometries of the model bodies were adjusted iteratively through a series of forward and inverse calculations to match model anomalies with observed anomalies within the limits imposed by surface geology, seismic, rock property, and MT data. In addition, a 3D inversion of gravity was performed, using methods described by *Jachens and Moring (1990),* to yield an estimate of the depth to sediment-basement interface within the basin. Maximum Horizontal Gradients (MHG; *Blakely and Simpson, 1986*) of gravity and pseudogravity, which reflect abrupt lateral changes in the density or magnetization in the subsurface, and tend to lie over the edges of bodies with near vertical boundaries, are used to estimate the extent of buried sources (*Grauch and Cordell, 1987; Cordell and McCafferty, 1989*).

13.0 DATA INTEGRATION, MODELING, AND FINAL SITE SELECTION

13.1. GIS Methodology

Our GIS methodology was automated so the team could make changes to the model and easily assess the results. A 'processing model' was released along with the data, consisting of a Python script that reads parameters and coefficients used in a study from two data tables. This processing model was used to generate output data from input data for the Phase 1 study, Phase 2 Camas & Mt. Home studies, as well as 'independent assessments' of data from the Washington PFA project.

Additional interpretive layers were generated that are similar to the traditional CRS and CCRS layers that do not combine evidence and confidence data, but instead isolate them to see how each facet appears independently. A 'weighted evidence' and 'weighted confidence' layer was calculated for each component and for the CCRS equivalent, the layer that incorporates all components. Weighted evidence and weighted confidence calculations are identical to CRS & CCRS calculations, except that they use normalized evidence and confidence instead of risk in the weighted sum respectively. Additionally, a 'multiplied' CCRS, weighted evidence, and weighted confidence surface was created where components were combined by multiplying weight values instead of using a weighted sum. These 'multiplied' surfaces highlight areas where none of the components have low values.

13.1.1. GIS Processing Model. The GIS processing model developed for this project was gradually expanded to be able to perform each aspect of the functionality used in this project by reading instructions from tables. It is included with the data release as a Python script with data tables that contain model parameters and coefficients. A description is included with the processing model that details how a user could replicate this work, adapt the model to make changes to this work, or to use the model in another setting.

The model works by automating most of the geoprocessing and subsequent calculations. For any element, a user can specify in a 'parameter table' the name of the GIS file for evidence and confidence data, and instructions on how to use those data. For example, if an element uses a pre-existing grid (like an interpolated surface), those surfaces must be directly sampled. If a density function is used on input evidence data, such as lines or points (faults or vents), a kernel or simple density can be chosen, and a search radius can be specified. An option exists specifically for the approach used with volcanic vents, where a kernel density function was weighted by a value calculated as the product of two weight coefficients assigned based on categories of vent age and size. There is an option to sample weights associated with categories from polygon inputs, for example aquifer or lacustrine extent. There is also an option to assign weights based on the distance to a feature, where a user selects the weight assigned to any distance interval specified. Similarly, for confidence data, options exist to directly sample a pre-existing surface, to use weights associated with categories from polygon inputs, or to assign weights based on the distance from a feature.

There are many static coefficients chosen by expert opinion; those values are stored in the 'coefficient table.' Values in the coefficient table can represent the relative weights of layers

within a component, relative weights between components, confidence weights applied to confidence layers, normalization parameters, evidence weights, and distance thresholds. These lists of coefficients have unique names that are present in the parameter table. For example, each element with a confidence layer has a field in the parameter table with a unique name for the correct weight list. Weight lists that contain relative weights between elements in a component have names identical to the component name in the parameter table. Every list in the coefficient table has a name that is referenced by the parameter table.

The parameter table has additional options a user could choose. A user can specify whether or how to normalize evidence layers before they are combined in a component, which is a critical consideration before combining in a weighted sum. Data can be normalized from 0-1, not normalized, normalized using user-specified coefficients, or normalized based on the highest value from every element in a component. Other options include normalizing a density function's weighting values, applying a log-transform to evidence layers, and some special exceptions in processing made by the team to account for data layer properties. The processing model's documentation contains a detailed description of the options for each field in the parameter table.

To run the processing model, a user must correctly fill out the parameter and coefficient tables, then modify six options in the Python script that indicate the: location of all input GIS data, location to contain all GIS outputs, locations of the parameter and coefficient tables, the name of the study area raster (which will be used to define the processing extent and cell size of the study), and the name of a master points file that will contain all sampled and calculated data. When run, the script will produce a text output that describes each processing step and the actual values used in every calculation. More detailed information about how a user could modify the processing model can be found in its documentation (*https://gdr.openei.org/submissions/1287*).

13.1.2. SRP PFA Model Workflow. There are very few differences between the Phase 1 workflow (Figure 2) and that used on the Phase 2 Mountain Home and Camas studies.

The four elements representing permeability (mapped faults, magnetics, gravity mid, gravity deep) each had two fields (slip tendency, dilation tendency) that were normalized 0-1 then used to weight a kernel density function, producing 8 surfaces in total. Each surface was normalized using the highest value from any other density surface weighted by the same field. For example, mapped faults were more densely mapped than lineations from the geophysical layers (magnetics, gravity) and ended up producing a density surface with a greater maximum value. This maximum value was used to normalize the other surfaces derived from the geophysical layers for each weighting field. This was done so that the density represented by one line in any of the four surfaces generated using each field were of equal value prior to having weighting coefficients applied. These normalized values from all 8 layers were used in a weighted sum to calculate the weighted evidence layer for permeability. Risk was calculated for each element by multiplying the normalized evidence by a confidence value ranging from zero to one. These risk values were used in a weighted sum to calculate the CRS map for permeability. Similarly, a weighted evidence and weighted confidence were calculated from evidence and confidence. The only differences between Phase 1 and Phase 2 studies include: in Phase 1, the density functions

all used a search radius of 10 km, but in the Phase 2 studies, a 2.5 km radius was used, and the Phase 2 Camas study used the distance from magnetic sampling lines instead of a polygon map depicting the scale of sampling to depict confidence in magnetics.

The Heat component consisted of five elements in Phase 1 (vents, heat flow, groundwater temperatures, r-test temperatures, helium) and one additional element in Phase 2 (sill). Heat flow, groundwater temperatures, and r-test temperatures were all interpolated. The prediction and standard error surfaces were used as direct inputs depicting evidence and confidence. User assigned confidence values were assigned to equal intervals of the standard error surface to create the confidence layer for each element, except for r-test temperatures, custom intervals were specified to account for a large range in values. Evidence for heat flow was normalized using user-assigned values, r-test and groundwater temperatures were normalized from 0-1. Helium data were weighted by the $^{3}He/^{4}$ He ratio, then a simple density function was applied, with a 10 km radius in both Phase 1 and Phase 2, normalized from 0-1; no confidence data were used. Volcanic vents were weighted in a kernel density function by the product of weight values assigned to ranked categories for the vent's age and size with a 10 km radius in Phase 1 and a 2.5 km radius in Phase 2, normalized 0-1; no confidence data were used. In Phase 2, the location of a sill was used to create a layer that was directly sampled where areas within the sill were weighted 1.0 with weights decreasing to zero within a 10 km radius, no confidence data were used. Risk was calculated for each element by taking the product of the evidence layer and the confidence layer, when no confidence was used, risk was equal to evidence. The CRS for heat was calculated as the weighted sum of the risk layers. Similarly, a weighted evidence and weighted confidence were calculated from evidence and confidence.

The Seal component consisted of two elements: aquifers and sediments. Both elements consisted of polygons that had categories that corresponded to user-assigned weights. Weights varied from 1.0 in the most favorable areas, but areas with no features were still given a high weight ($\geq$ 0.9). The Seal component was calculated by multiplying the aquifer and sediment weights in study area cells, no confidence data were used. This resulted in a surface that contained values that varied over a high range (~0.81 – 1.0). This was done so that values from the Seal CRS could be multiplied by the weighted sum of the other two components to calculate the CCRS by slightly lowering favorability in areas without favorable Seal characteristics.

The CCRS was calculated by calculating the weighted sum of the normalized Permeability and Heat components, then multiplying by the Seal CRS, then normalizing the results from 0-1. Similarly, a weighted evidence and weighted confidence were calculated for each component. Additionally, 'multiplied' layers were generated for the CCRS, weighted evidence and weighted confidence data layers where layers were combined by multiplying component values instead of using a weighted sum.

13.1.4. Washington PFA. One task in our Phase 3 SOPO (Statement of Project Objectives) was to cross-validate our methodology by applying it to data from the Washington State PFA. This allows us to assess how well our method (based on GIS processing of bulk data) reproduces the results of projects with more subjective interpretations of relatively small areas. This cross-

validation effort was facilitated by having team members involved in both projects, and addresses DOE's goal of having different projects cross-fertilize ideas amongst their teams.

Data from the Phase 2 Washington PFA were examined using the approach and processing model from the present study as a possible way to compare results, demonstrate the application of the processing model to other settings, and provide an independent assessment of Washington. Seven data layers from the Phase 2 WA PFA were examined: Quaternary faults, seismicity, Quaternary vents, thermal gradient measurements, hot spring temperatures, geothermometry, and locations of intrusives. These data were acquired from publicly available data submissions. The WA PFA used more than seven layers in some parts of their analysis, the present study only used data that covered the entire extent of the three study areas, excluding MT, Vs, and Vp/Vs data. Weighted evidence maps were compared with the 'favorability at 2 km depth' maps from the WA Phase 2 PFA (Figures 31, 32) because the two studies accounted for confidence very differently. The units used between the two studies represent different phenomena, so no quantitative approach was attempted to compare results. Instead, a qualitative assessment of where relatively high and low patterns existed between the layers from the two different studies was undertaken to identify areas where the different approaches produced similar or different results.

The present study examined the same three regions examined by the WA PFA: Mt. Baker, Mt. St. Helens, and Wind River using a 100 m grid. Interpolation was performed on thermal gradient, spring temperature, and geothermometry data at a 500 m resolution, those surfaces were used as inputs in the processing model, each was normalized 0-1 prior to weights being applied. All other layers used a kernel density function on input data layers, with different search radii. None used any attribute weighting, and all were normalized 0-1. A polygon layer depicting locations of intrusives was converted to a 25 m point grid. That point file was used as an input in the processing model, with a 200 m search radius was used. The publicly available data for Quaternary faults, vents, and seismicity were used directly as inputs in the processing model, they used search radii of 500, 1000, and 300 m respectively. These model parameters were used with four different coefficient sets, producing four weighted evidence maps to compare with the WA Phase 2 favorability surface. The four weight sets used represent: weights used in the WA Phase 2 PFA (weight values were provided during personal communications with the WA PFA team), equal weighting (all layers and components of equal value), weights from the SRP Phase 1 PFA, weights from the SRP Phase 2 PFA (Table 1). The first two weight sets (WA PFA weights, equal weights) were chosen for the results to be directly compared with the WA PFA favorability map; the second two weight sets (from SRP PFA) were chosen to generate more of an independent perspective than a direct comparison.

Table 1 can be understood using the example of the Washington PFA weight set. In that example, the elements belonging to the heat component (vents, thermal gradient, springs, geothermometry, intrusives) were assigned relative weights (201, 304, 229, 128, 139) to normalized evidence layers. Elements belonging to permeability (faults, seismicity) were assigned weights (330, 138) in the same manner. Permeability was weighted relative to heat 344:322.

Table 1. Weights used to apply our PFA model to the Washington PFA data.

Element	Component	WA PFA	Equal	SRP P1	SRP P2
Faults	Permeability	330	1	1	1
Seismicity	Permeability	138	1	1	1
Vents	Heat	201	1	30	10
Thermal Gradient	Heat	304	1	55	10
Springs	Heat	229	1	5	5
Geothermometry	Heat	128	1	5	5
Intrusives	Heat	139	1	5	2
Permeability	CCRS	344	1	8	1
Heat	CCRS	322	1	5	1

A visual, qualitative comparison of the WA PFA favorability map and the weighted evidence surface using the approximate weights from the WA PFA (Table 1; WA Weights) in the Mt. St. Helens area shows three common areas with high values can be seen along a NNW striking trend; Mt. St. Helens is the central high. In the WA PFA, these highs appear to be driven largely by faults, seismicity, and intrusives. The weighted evidence surface shows the same trend observed in the WA PFA, but the highs are less pronounced, possibly at least in part because MT, Vs, and Vp/Vs data were not included. Along the favorable trend, the weighted evidence map produces similar contributions from faults, seismicity, and intrusives and qualitatively identifies many of the same areas identified in the WA PFA. Some differences likely relate to different interpolation approaches being used, but also the fact that there were very few measurements for geothermometry and spring temperature data within the Mt St Helens study area. Data that did exist varied greatly in magnitude, leading to predictive maps with stark contrasts that use very little information to make estimates about very large areas, especially in relation to the relatively small size of the Mt St Helen's study area.

In Wind River Valley, elevated favorability in the WA PFA appears to be driven by faults, vents, and temperature gradient. The same layers drive elevated favorability in the weighted evidence surface, though different search radii used on vents and a different interpolated surface for thermal gradient data contribute to the biggest qualitative differences. Color scales do not represent equal measures of favorability, but the patterns generally coincide between the two models across the entire study area. The fact that Wind River Valley did not use any MT, Vs, and Vp/Vs data may also help explain the general agreement between features seen in the two modeling approaches.

The maps of the Mt. Baker area looked very similar and tended to highlight areas near faults. An obvious difference exists between the maps in places that contain selective coverage in the WA PFA, but otherwise the same general patterns exist. One benefit of the weighted evidence map may stem from the use of a kernel density function, which may do a better job of highlighting fault intersections.

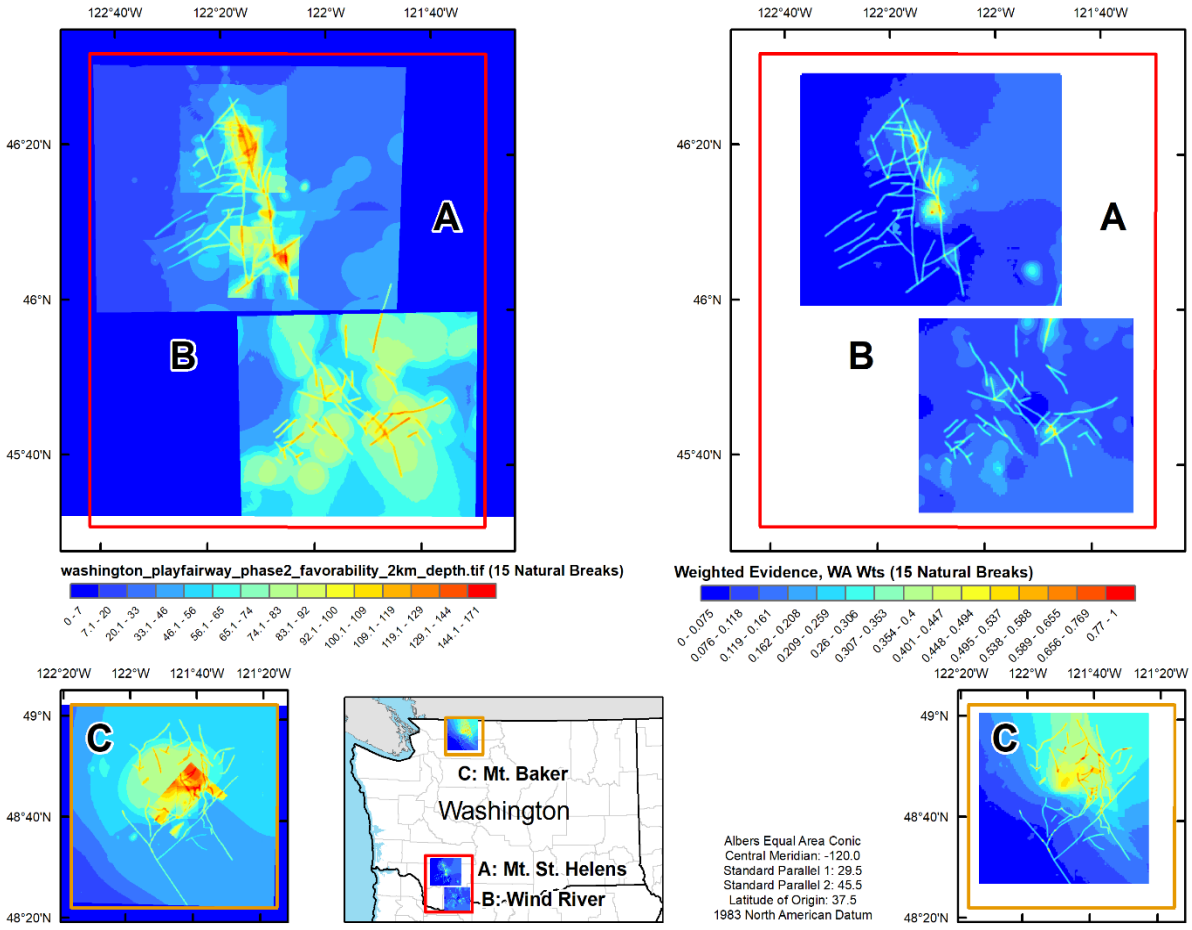

Figure 31. Comparison of the Washington State PFA results (left side panels) to models generated using a portion of their data within our automated GIS methodology (right side panels). (A) Mt. St. Helens area, (B) Wind River Valley area, and (C) Mt. Baker area. Right side panels were made using the evidence weights in Table 1. The weighted evidence surface in our models show the same trend observed in the WA PFA, but the highs are less pronounced, possibly at least in part because MT, Vs, and VpVs data were not included.

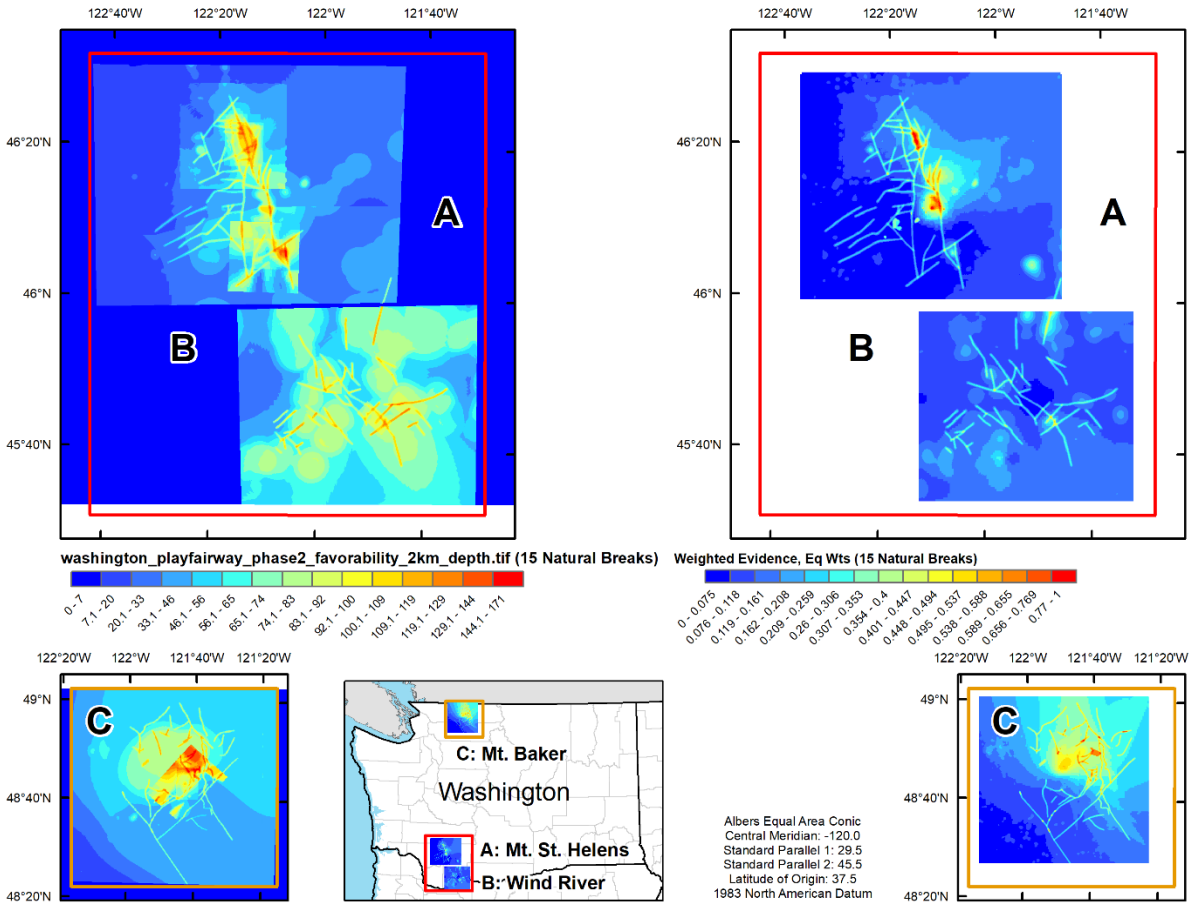

Figure 32. As in Figure 31, a comparison of the Washington State PFA results (left side panels) to models generated using a portion of their data within our automated GIS methodology (right side panels), except the right-side panels made using the equal weights instead of the weights in Table 1. (A) Mt. St. Helens area, (B) Wind River Valley area, and (C) Mt. Baker area. The weighted evidence surface in our models show the same trend observed in the WA PFA, but the highs are less pronounced, possibly at least in part because MT, Vs, and Vp/Vs data were not included.

13.2. Data Integration

Data integration and final site selection was carried out by the whole PFA team, with particular emphasis on the geophysical modeling, water chemistry data, and structural mapping.

13.2.1. Geophysical Data Integration. The geophysical mapping and modeling methods employed in this study were used to resolve subsurface structures that have little or no surface manifestation. Key goals of this work were to help delineate deep-seated features that likely represent important permeable pathways for hydrothermal fluid flow, constrain basin geometry, study fault interactions, and identify areas favorable to hydrothermal fluid flow.

Gravity and magnetic maps were gridded from a combination of new and existing data collected throughout the Camas Prairie valley and surrounding regions (Figures 19 and 20). Analyses of MHG of residual isostatic gravity and pseudogravity grids delineate a number of intrabasin structures that have little or no surface manifestation (Figures 21, 25). These structures represent two dominant fault trends; W to WNW-trending structures that likely reflect the major basin-bounding faults, and a NW-trending set that appears to control the major sub-basin geometry of the valley.

Potential field modeling was performed along several profiles at the western end of the valley (Figure 25, *Glen et al., 2017*). Seismic data collected along these lines constrain the upper several hundred meters of the models. The models reveal a deep (500-1000 m) structurally controlled sedimentary basin that displays offsets along numerous structures imaged in the seismic profiles and reflected in the potential field data. MT results support structures identified by gravity or seismic and provide depths to the base of basin sediments to constrain gravity inversions. The modeled basin is floored by crystalline basement that is, at least partly, capped with volcanic flows presumably derived from sources in the Mount Bennett Hills. The model also reveals that the basin stratigraphy includes interbedded volcanic flows that are offset along the same structures identified in the seismic profiles.

Regional gravity mapping indicates the valleys subsurface consists of several NW-elongate subbasins characterized by isolated gravity lows (*Glen et al., 2017*). The inferred sub-basin that resides on the western end of the Prairie just north of Barron's Hot Springs reflects the deepest part of the basin (up to 1 km). This area coincides with anomalously high groundwater temperatures and may represent the primary geothermal reservoir for fluids that feed the springs. A steep gradient bounding the southwest side of the gravity low likely reflects the more structurally active part of the basin. Seismic results show diminishing offsets of shallow strata from southeast to northwest away from Barron's Hot Springs, intersecting fault systems beneath the central basin region, and offset of the shallowest reflectors that support ongoing NW-trending basin extension.

The steep gradient bounding the sub-basin in the western end of the valley is aligned with inferred NW-trending structures that extend through Barron's Hot Springs. The location of hot springs appears to be related to the intersection of this NW-trending structure with more easterly oriented basin-bounding structures that delineate the southern edge of the valley. Analyses of new and existing geologic and structural mapping support the importance of these faults in

controlling basin geometry and possibly influencing hydrothermal fluid flow (Figure 33). Two dominant fault sets south of Barron's Hot Springs (WNW- and NNW-striking, E-dipping with dextral-normal to normal slip), though based on a limited dataset (a total of 37 fault surface measurements), are consistent with the trends of the major subsurface intra-basin features inferred from the geophysics. Under right lateral transtension, conditions conducive for dilation and fluid flow would be expected at releasing steps along intersections of these structural trends (Figure 13 and inset).

A conceptual model of the basin (*Glen et al., 2017*) illustrates the likely source and circulation of thermal fluids and involves 1) recharge from the Soldier Mountains to the north of the valley and Mount Bennett Hills to the south, and 2) deep circulation of fluids through the underlying granitic basement driven by the regional topographic head between the valley and the adjacent highlands. The system likely derives its heat from a magmatic source that is suggested by the presence of relatively young volcanic rocks emplaced within and around the valley (*Shervais et al., 2018*), but may also involve heat from deep basement circulation within a region characterized by elevated geothermal gradients.

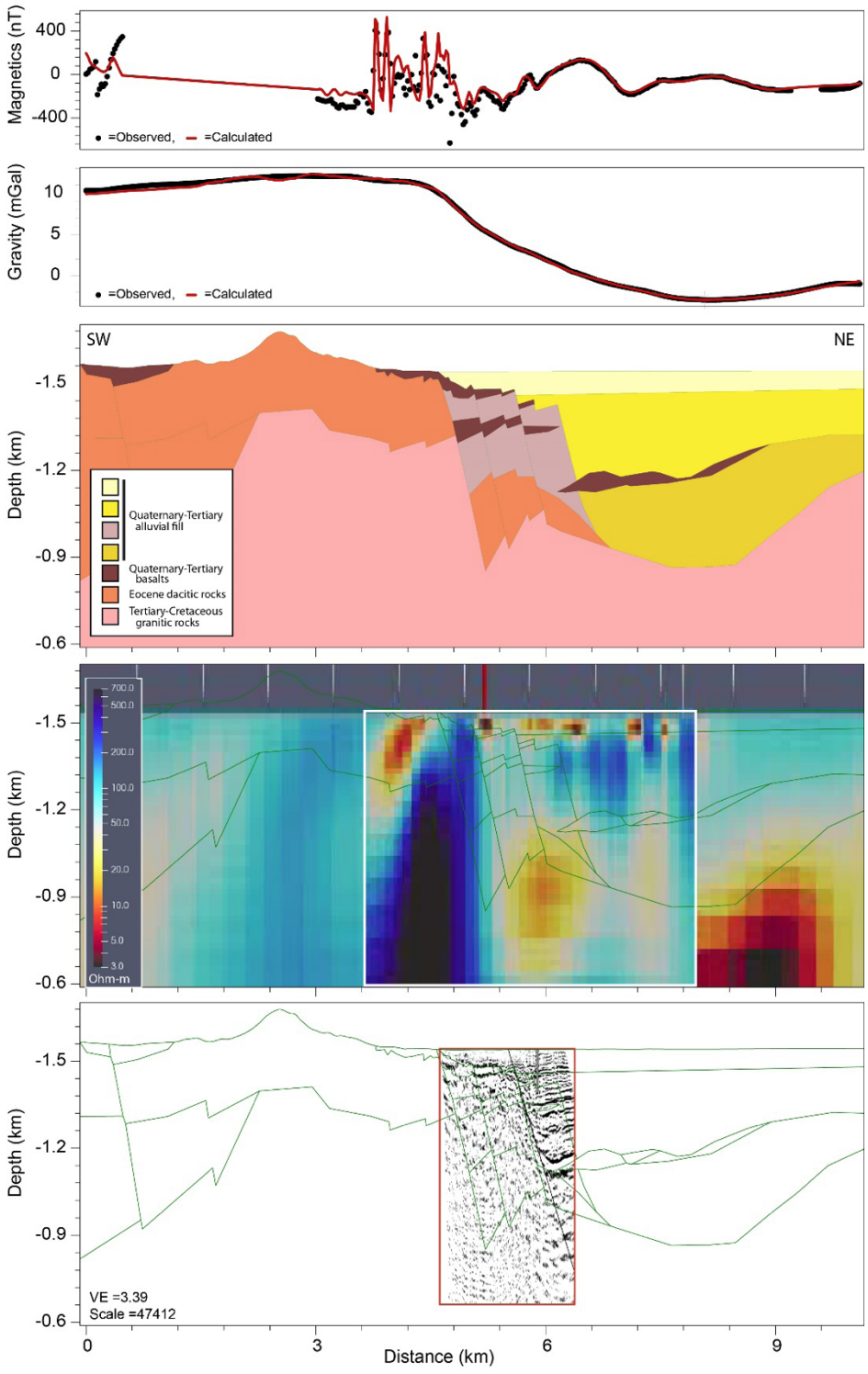

Figure 33: Two-dimensional geophysical model of the Camas Prairie along the Barron profile (see Figure 28 for location). Panels show (from top to bottom) magnetic field, gravity field, potential field model with individual model bodies colored by rock unit, MT resistivity model, and a seismic image with interpretation. Magnetic and gravity profiles show observed (black circles) and model (red line) anomalies. The MT cross-section inside and outside the area indicated by the white box reflect modeling results based on based on coarse- and fine-mesh inversions of the data, respectively.

13.2.2. Water Well Temperatures. Water well temperatures were used to establish a baseline for expected minimum temperatures in the region (Figures 34 and 35). Even though these wells are all less than 550 feet deep, some of them are fed by upflow from deeper geothermal waters and thus provide minimum expected resource temperatures. The most pertinent is the Barron well, situated just west of our proposed drill site target. This well had the drill string stuck in the hole, so that while the well does not flow, it is possible to lower a temperature logging tool down the borehole to measure the temperature profile – it has a maximum measured downhole temperature of 91°C. Three of the wells (SRV-1A, SRV-2, and SRV-3A) have deep temperatures close to 20°C, whereas the three wells that are closest to the USU-1 well site all have elevated (>65°C) temperatures.

Fig. 34. Location map of irrigation wells with measured downhole temperature profiles in Camas Prairie, along with play fairway well USU-1

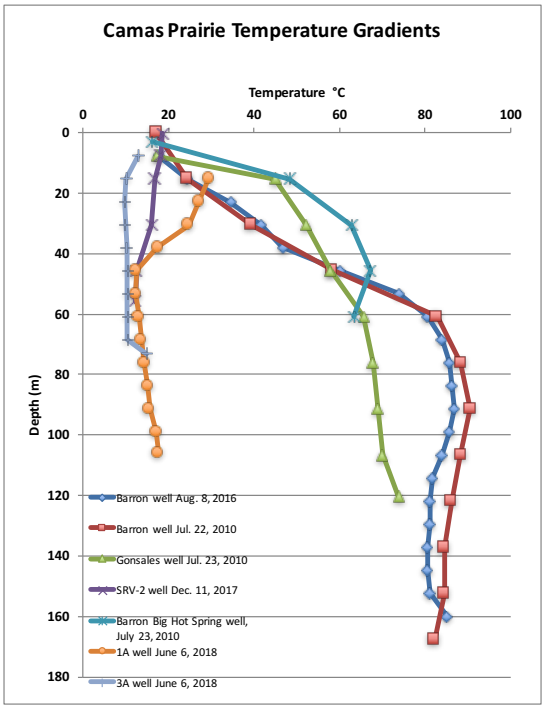

Fig. 35. Measured temperature gradients of six shallow wells in the western Camas Prairie area near the USU-1 borehole. Well locations are shown in Figure 34. Temperature logging performed by Roy Mink.

13.2.4. Structural Analysis. Structural mapping has shown that surface faults in the Barron's Hot Springs-Pothole area comprise two distinct structural trends: NW (~285-295°) and NNW (~325°), both of which dip predominantly NE. These faults pervasively cut the Pleistocene Pothole and other basalts, indicating that the faulting is Pleistocene or younger in age, while striated surfaces and relative offsets indicate that the dominant sense of slip is dextral-normal to normal.

In addition to mapped surface faults, geophysical data indicate a third structural domain of essentially EW-trending faults that parallel the range front of the Mount Bennett Hills. Although the physiographic range front lies some 5 km to the south, offsets in the potential fields data document the structural range front at depth in the area of Camas Creek. This structural range front represents offsets in basement (granites and rhyolites) that juxtapose it against basin fill sediments. A conceptual model of these relationships integrating geophysical results with the structural mapping is shown in Figure 36.

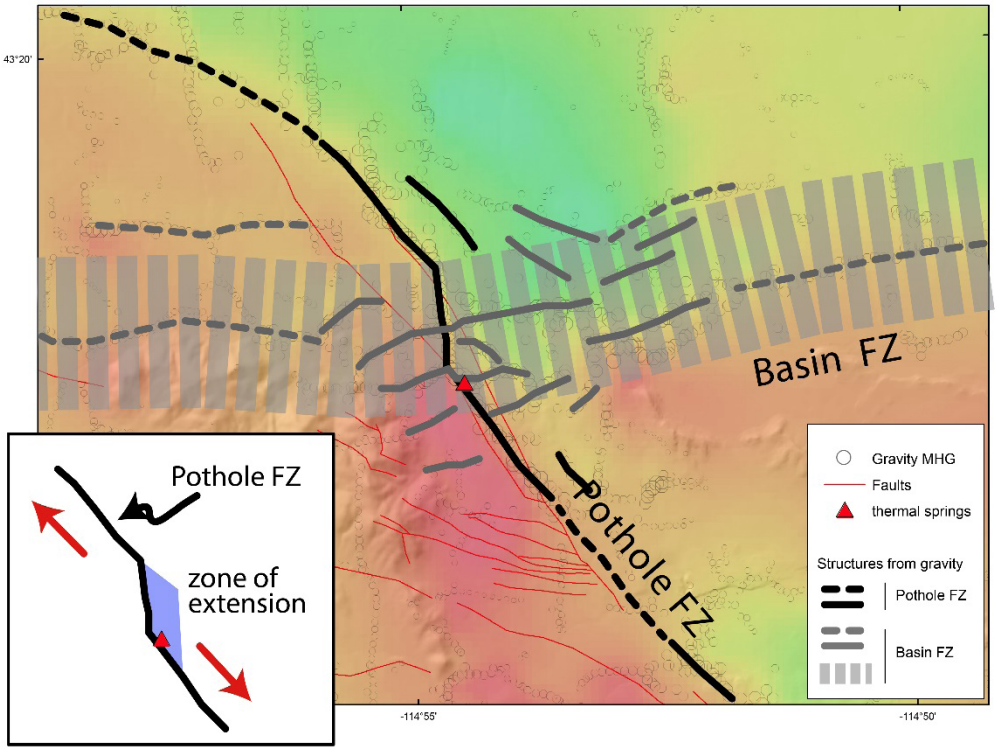

Figure 36: Conceptual model of the geophysical structural interpretation of the Barron's Hot Springs area showing geophysical lineations (faults) interpreted from Maximum Horizontal Gradients (MHG) of gravity, and illustrating the interaction of basin-bounding (Basin FZ) and Pothole (Pothole FZ) fault zones. The interpretation is superimposed on the residual gravity map. The Basin FZ is less well delineated where the fault zones intersect (in contrast to its expression in the central and eastern Camas Prairie), but is characterized by numerous roughly EW-trending geophysical lineations (highlighted here by a grey hatched area). The inset depicts an apparent right-stepover in the Pothole FZ that results in interpreted extension across the zone where the two fault systems intersect and coincident with Barron's Hot Springs.

This conceptual model also indicates that surface discharge of thermal fluids involves upflow along basin-controlling structures. We suggest that key intersections between ~EW-trending basin-bounding structures and prominent NW-trending faults associated with the Pothole fault system, and the apparent dilational right step-over in the dextral-normal Pothole fault, provide conduits for upward convection of thermal fluids at the southern margin of the valley adjacent to the deep structural subbasin (Figure 36). Active faulting along these structures, could stimulate and maintain zones of permeability that allow for upflow of thermal fluids at the Barron's Hot Springs. New high-resolution geophysical studies around Barron's Hot Springs reveal structural complexity at the intersection of the basin-bounding and Pothole fault systems. This is characterized by numerous fault segments that involve a prominent right-stepover in the Pothole fault.

13.3. Drill Site Selection

Potential field mapping delineates a NW-elongate gravity low on the western end of the valley just north of Barron's Hot Springs that reflects a deep (500-1000m) structurally controlled sedimentary sub-basin (Figure 37). A steep gradient bounding the southwest side of this low is interpreted as a major fault zone that likely reflects the more structurally active part of the basin. Seismic results document offsets of shallow strata that are consistent with potential field modeling and support ongoing extension across this fault zone. This NW-trending zone includes the Pothole fault, which cuts a Pleistocene basaltic vent and associated flows of the same name.

The BHS coincides with the intersection of the NW-trending Pothole fault system with an EW-trending fault zone that comprises basin-bounding faults delineating the southern extent of the valley and accommodating NS-extension. This intersection is characterized by a complex structural zone that is marked by numerous ~EW-trending geophysically-inferred faults, and a right stepover in the Pothole fault. We suspect that the dense faulting in this region plays a role in enhancing permeability and upflow. Furthermore, the dominant sense of dextral-normal to normal slip inferred for the Pothole fault, should result in extension across the stepover in the immediate vicinity of the Barron's Hot Springs.

MT modeling results show that this zone also coincides with a prominent conductive anomaly, characteristic of the presence of hydrothermal alteration or hydrothermal fluids. These results point to the importance of the fault intersection in localizing stresses that promote permeability, focus hydrothermal fluid flow, and result in sustained hydrothermal activity around the Barron's Hot Springs. Based on these results, we identified the fault intersection as the target for Phase 3 drilling.

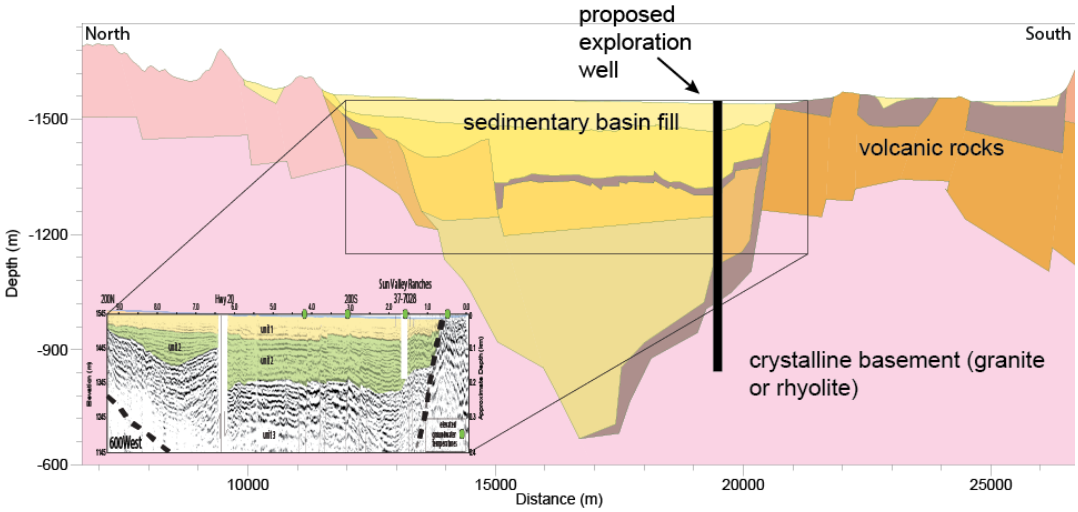

Figure 37. Interpreted N-S cross section through Camas Prairie intersecting The Pothole fault system near the location of Barron Hot Springs. The proposed well location is shown, targeting fracture zones associated with N-dipping normal faults near the south edge of basin.

Based on our combined datasets and Phase 2 CCRS map, we selected a location along the Pothole fault system to drill an exploratory well, near Barron Hot Springs and the southern margin of the basin. The high geothermal potential of this region is indicated by a number of data sets including thermal springs along a young fault system, thermal and irrigation well geochemistry indicating reservoir conditions >110°C, and elevated mantle-derived $^{3}He/^{4}He$ ratios in groundwater. Geophysical data (MT, gravity, and seismic) indicate major offsets in basement formed by faulting, with the Pothole fault system intersecting an EW-oriented range front system at depth. In addition, mapped faults and geophysics document step-over fault splays off the Pothole fault system which indicate dilational extension. Our drilling plan was to drill a 650 m (2000-foot) depth exploration well (Figure 38), with the goal of intersecting high permeability and elevated temperatures.

Figure 38. Satellite image map showing location of test well USU-1 just north of Camas Creek, Camas Prairie, Idaho.

14.0 VALIDATION WELL

14.1. Permitting

Permitting began early in Phase 3 with biological and cultural surveys of the potential drill sites. Since we had not yet selected a final site at this point, we needed to survey a relatively wide area around our potential sites to ensure that the final site could be permitted. This led to a cost overrun in the survey costs but allowed us wide latitude in our final site selection process. The proposed drill sites were located in an area of intense agricultural activity, so permitting was relatively easy. However, the proximity of the selected drill site to wetlands along Camas Creek required special measures to ensure that no run-off from the drill site entered the wetlands area.

Cannon Heritage Consultants, Inc, began collecting site data in December 2017. A USFWS IPaC report and an Idaho Natural Heritage Program data search was carried out first. Based on the agency reports, wildlife field surveys were conducted on all three sites, including a half mile buffer surrounding the areas, documenting suitable habitats (Camas Prairie Biological Report: *https://gdr.openei.org/submissions/1285*). Habitats were also mapped. This biological survey has been completed and final report submitted. A Class III Cultural/archeological survey, which meets Idaho SHPO standards, was carried out in May-June 2018 (*https://gdr.openei.org/submissions/1285*). Report forwarded to GTO on 29 June, along with further information on water sources for drilling and letter from landowner authorizing drilling. Final NEPA approval obtained 5 September 2018, and drilling funds released.

PIs Shervais and Nielson made a site visit to Camas Prairie in June 2018 to meet with Steve Crawford (USGS Research Drilling) and Camas Creek Ranch Manager Rod Gonsales. Potential drill sites within our target zone were reviewed for access to roads and water. The drilling plan, site footprint, water sources, sump pits, and expected weather conditions were discussed. Water wells belonging to Camas Creek Ranch were visited to establish proximity of water for drilling.

Also in June 2018, Nielson and Shervais met with Chad Hersley of Idaho Department of Water Resources (IDWR) to discuss well design, IDWR requirements for casing and cementing, and the impact of low-T versus high-T (geothermal) drilling rules. Further discussions were carried out via email, including our submission of a drilling plan and drilling prospectus to IDWR as part of our application for a drilling permit. The final drilling permit (#37-GR-8) was issued on 29 August 2018. A surety bond for $20,000 was also submitted as part of the application process. A copy of the drilling permit has been posted to the Geothermal Data Repository (*https://gdr.openei.org/submissions/1285*).

14.2. Drilling

Drilling was carried out by the USGS Research Drilling unit, on this and other PFA projects funded under the same umbrella. We worked interactively with the drillers to design the well to achieve our goals at minimal cost. Our plan was to drill to about 700 m depth, and to core the lower 200 m of the hole, depending on depth to basement. Our reservoir testing protocol required that we set casing in basement, in order to seal off aquifers in the basin fill sediments. Project personnel were present during drilling to oversee the process, to deal with drilling-related issues, and to receive core from the lower part of the hole.

At least one Senior Staff Scientist was assigned to be on site during drilling operations to monitor drilling progress, identify cuttings and core, and interact with the drilling crew as needed. The senior scientists would generally overlap during shift changes to ensure that the newly arriving senior was updated on current status and any problems. These senior scientists were generally co-PIs on the PFA project. Two Site Scientists (*Geology B.Sc. degrees*) were hired to be present on an alternating basis to assist the Senior Staff Scientists on site and to monitor activities when the senior staff were not present (e.g., during hole opening and casing operations). Site Geologists worked one week shifts on site and had one week off between shifts. Both received training in how to collect and log cuttings, and all personnel have received site safety training. USU personnel prepared an *Environmental Health and Safety Plan* (see *https://gdr.openei.org/submissions/1285*). A copy of this plan was kept on site and all site personnel received their own copy. The USU team assembled all relevant safety gear including personal protective equipment, fire extinguisher, and eye wash. The USU team also assembled supplies for sampling cuttings and core. Issues discussed during training included safety plans and gear, use of blow-out preventer, water sampling, and the reservoir test.

The staff scientists prepared and distributed a Daily Drilling Report that summarized both operations and geologic results each day (*https://gdr.openei.org/submissions/1285*). These daily reports provide a complete record of all site activities throughout the course of drilling, including any drilling related problems. These daily reports were distributed to all of the project principals as well as to all associated DOE personnel.

Two Senior Geologists mobilized to the site on 13-15 September 2018 with two additional USU personnel to setup work tent and logging operations. Protocols established for collecting cuttings, logging and sampling, and preparation of Daily Reports for DOE. A 20’x20’ canvas field tent was set up for logging and processing cuttings, with a generator, heater, lights, binocular microscope, and work tables. The same setup was used for Stage 3 drilling in 2019, with the addition of a diamond trim saw and photo stand for core box photos.

14.2.1. Stage 1 Drilling. The Camas Stage 1 well was drilled by the USGS Research Drilling unit in September-October of 2018, using a rotary drill rig, at coordinates Latitude 43.2994 and Longitude -114.9088 (5080 feet above sea level). A 14” surface casing was installed to a depth of 43’ and cemented into place. This was followed by a 7-7/8” rotary hole to 1140’ depth (completed on 27 September 2018). Geophysical logging of the open hole was carried out by the USGS Research Drilling Geophysical unit on 28 September 2018, prior to setting casing.

Casing was set to 1145’ after reaming the hole to 12” diameter and cemented into place. Hole opening took from 28 September to 5 October, followed by running in and welding casing (6-7 October 2018) and cementing. Cementing was delayed by weather for two days, until 10-11 October 2018. After cementing was complete, the well head was prepared for installation of a blowout preventer. This required hiring a backhoe and waiting for the archeology contractor to arrive to assess the area around the well head for artifacts. After being cleared by the archeologist, a pit was constructed and cemented to seat the BOP.

14.2.2. Stage 2 Drilling. Rotary drilling recommenced on 13 October 2018. After drilling through the cement plug in the casing, water began to enter the hole from an overlying aquifer, so the decision was made to drill a further five feet into basement and cement the hole, then to redrill through this section. The operation was successful, and rotary drilling continued with 5.5" bit. Drilling was continued until 18 October 2018, at which time financial concerns drove the decision to stop drilling and commence final wireline logging operations. Drilling was terminated at 1608 feet, about 200 feet short of our minimum target depth. Wireline logging and reservoir tested were carried out from 19-21 October 2018.

14.2.3. Stage 3 Drilling. Additional funds were allocated for drilling in the summer of 2019. Stage 3 drilling resumed in October 2019 using a CS1000 diamond core drill rig. Operations were carried out using the same protocols and personnel as in 2018. After consulting with IDWR, it was determined that a revised drilling permit was not needed as our original drilling prospectus including coring operations in the lower part of the hole. Prior to beginning operations, the USU Health and Safety Plan and contact numbers were updated, and site safety procedures were reviewed with all site personnel.

Stage 3 coring operations began on 2 October 2019 and continued through 29 October 2019, with logging and testing into early November 2019. A BOP was installed prior to coring, and an NQ core assembly was used (47.6 mm/1.87inch diameter core). HQ drill rods from the 2018 Stage 2 drilling were installed in the hole as a temporary casing and guide for the NQ drill rods. Mud temperatures were monitored with a temperature probe to conform to IDWR rules on geothermal drilling. On 12 October 2019, a HOBO temperature probe was deployed onsite to measure downhole temperatures directly, although monitoring of returned mud temperatures continued. The bottom hole temperature on 12 October was found to be 79.4ºC/174ºF. A subsequent run on 25 October 2019 hung up at ~1750 feet depth, with a maximum temperature of 80.3ºC/176.5ºF.

Core recovery was very good generally. Core was logged on site using a physical setup similar to that of 2018. Coring was relatively slow initially due to issues with the wireline core barrel. Drilling was halted early due to unseasonably cold temperatures in late October (-20ºF overnight; -14ºF at 0900 hours), causing diesel fuel to gel. Coring terminated on 30 October 2019 at a final depth of 2028.5 feet. The rate of core recovery (about 15 feet per day on average) was very low, due to the combination of equipment issues (with the core barrel assembly) and weather (unseasonably cold temperatures). A more typical recovery rate of ~50 feet per day would have tripled our depth of penetration in the same time period.

14.3 Lithologic Logging

Lithologic logging was carried out on site by the Senior Staff Scientist and the Site Geologist, using cuttings during Stages 1 and 2 drilling and core during Stage 3 drilling. During Stages 1 and 2 drilling in 2018, cuttings were collected approximately every 10 feet. Each sample was washed to remove drilling mud and placed in a marked cloth sample bag. In addition, a small split of each cuttings sample was placed in a special cuttings holder with space for 10 samples per holder (approximately 100 feet of depth interval). Core logging was carried out on field sheets for each core run.

As predicted from earlier models of the basin, the uppermost section of the Camas Prairie basin consists of silty to sandy poorly consolidated sediments. The borehole did not encounter any basalt flows in the uppermost section. Approximately 1045 ft (319 m) of basin-fill sediments were penetrated before encountering bedrock (*Shervais et al., 2020*). The 6 5/8" casing was set at 1138 ft (347 m) to isolate deeper hydrothermal systems from the basin fill – shortly after resuming drilling, a high permeability zone was encountered, which generated a short episode of flow through the drill string. Rotary drilling continued to 1608 ft (490 m) through granitoids, assumed to correlate with the Idaho Batholith, cut by dikes of rhyolite and andesite (inferred from well logs and cuttings).

Core drilling in October 2019 deepened the well to 2028.5 ft (618.4 m), with ~100% core recovery. The primary lithology is porphyritic granite cut by dikes of pink to grey andesite/rhyolite. Veins of calcite and quartz are common, often with chlorite and sulfide mineralization. Slickenlines are common on fracture surfaces, consistent with the interpretation that much of the cored interval consists of a fault zone.

Suites of geophysical logs (caliper, natural gamma, resistivity, SP, conductivity, and temperature) were run before running the 6 5/8" casing, after reaching the rotary drilled depth of 1608 ft, and after completing the core drilling (depth of 2028.5 ft). The well temperature was deemed too high to run an image log. Unfortunately, during the final logging run, the tool got wedged in the borehole, and the cable snapped off, resulting in the tool and a small section of cable being left in the borehole. The synthesized log results are depicted in Figures 39-41.

14.3.1. Stage 1 Drilling Lithology. Stage 1 drilling encompassed basin fill sediments and approximately 60 feet of bedrock (Figure 39). The basin fill sediments comprise a thin layer of coarse sand near the surface overlying ~180 feet of grey-green clay with a thin (40 foot) sand interbed. This clay layer is evident in many local water well logs and forms the seal for deeper confined aquifers. Below the clay layer lies ~300 feet of coarse pebbly sand comprising quartz, feldspar, and granitic pebbles that appear to be derived from the Idaho batholith to the north. The lowermost 200 feet of basin fill (to basement) consists of clay, clayey sand, and fine-grained sand. Basement chips consist largely of granite (derived from the Idaho batholith) and rhyolite ± altered rhyolite volcanics, which may correlate with the Challis Volcanic formation or with younger (Pliocene) rhyolites exposed nearby (e.g., Windy Butte). Calcite chips are common, suggesting hydrothermal veins in the parent rock (*https://gdr.openei.org/submissions/1285*).

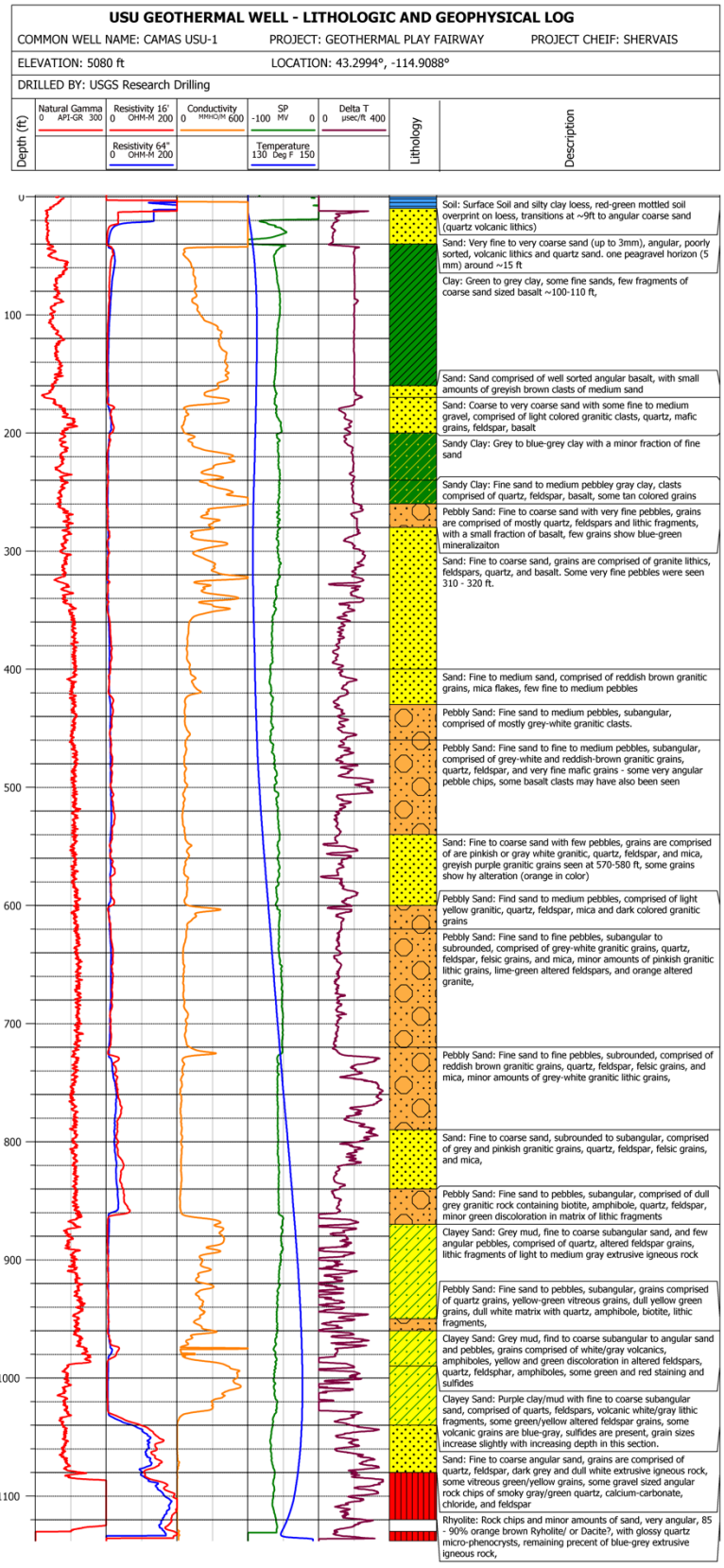

Figure 39. Combined lithologic and geophysical logs for Stage 1 drilling.

14.3.2. Stage 2 Drilling Lithology. Stage 2 drilling was entirely within basement, consisting here of granite/granodiorite cut by numerous dikes of rhyolite (Figure 40). The initial size and thickness of units was based on the footage of when cuttings were collected, but unit boundaries were refined using the geophysical logs. Specifically, natural gamma response peaked within the rhyolite dikes, owing to their somewhat higher K_2O, Th, and U contents. Of the 580 feet of basement drilled during Stages 1 and 2, about 23% (135 feet) are rhyolite dikes. The rhyolites are interpreted as dikes based on the dominance of granite, and on their occurrence in Stage 3 core with intrusive contacts against the granite (*https://gdr.openei.org/submissions/1285*).

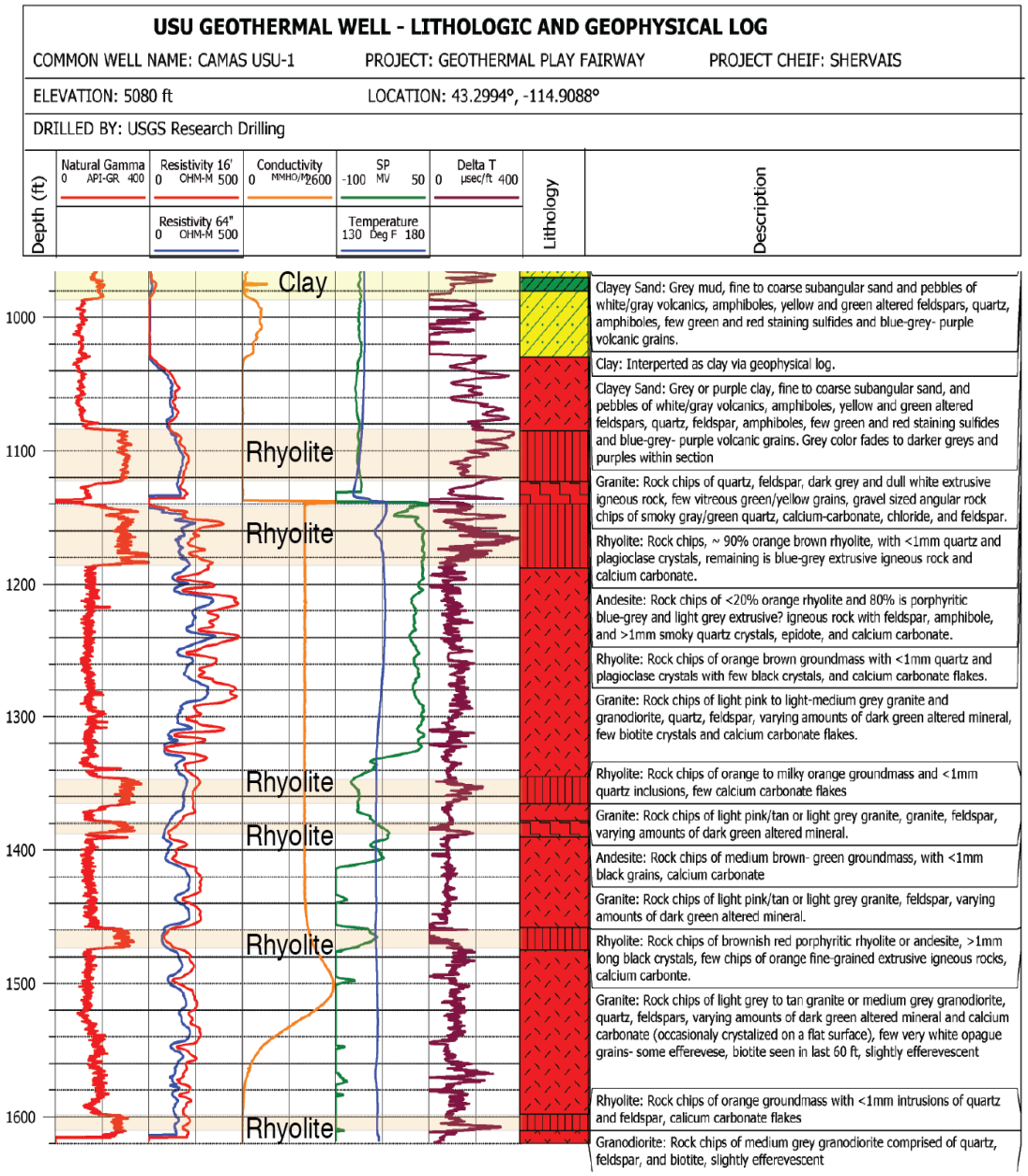

Figure 40. Combined lithologic and geophysical logs for Stage 2 drilling, annotated.

14.3.3. Stage 3 Drilling Lithology. Stage 3 drilling collected more-or-less continuous NQ-size core (47 mm) from the basement below the bottom of the Stage 2 hole. This allowed us to identify intrusive relationships between the rhyolite dikes and granite host rock, and to identify mineralized fractures and vein assemblages (Figure 41).

Stage 3 core can be divided into two sections: the upper section (1608-1928 feet) consists largely of granitic rock with minor rhyolite dikes, ranging from ~1 foot to 7 feet thick; the lower section (1928-TD) comprises pink to salmon-colored rhyolite with minor intercalations of granitic rock that range from ~1 foot to 6 feet thick. The contact at 1628 feet is brecciated and may be a fault. Sharp contacts of the rhyolite dikes with granite in the upper section imply intrusive contacts. In the lower section, the origin of the granite intercalations is unclear. Some granite-rhyolite contacts are brecciated, suggesting fault contacts, whereas others are not well exposed due to breakage in the core. These lower granites may be large blocks (olistoliths) within rhyolite ash flows. As in the Stage 2 section, the rhyolites are characterized by an enhanced natural gamma response (~250 API GR) relative to the granitic rocks (~100-150 API GR).

The Stage 3 granitic rocks are commonly characterized by pale greenish propylitic alteration, with disseminated pyrite, hairline calcite veins, and in places, abundant mineralized fractures. Rhyolites in the upper Stage 3 core are vitrophyres, with mm-size white phenocrysts (possibly sanidine) in a black (formerly?) glassy groundmass. The lower Stage 3 rhyolite is pale pink to salmon-colored with small (<1 mm) white phenocrysts that are also likely sanidine. More complete descriptions of the lithologies is found below (Post-Drilling Analyses).

See *https://gdr.openei.org/submissions/1285* for complete descriptions.

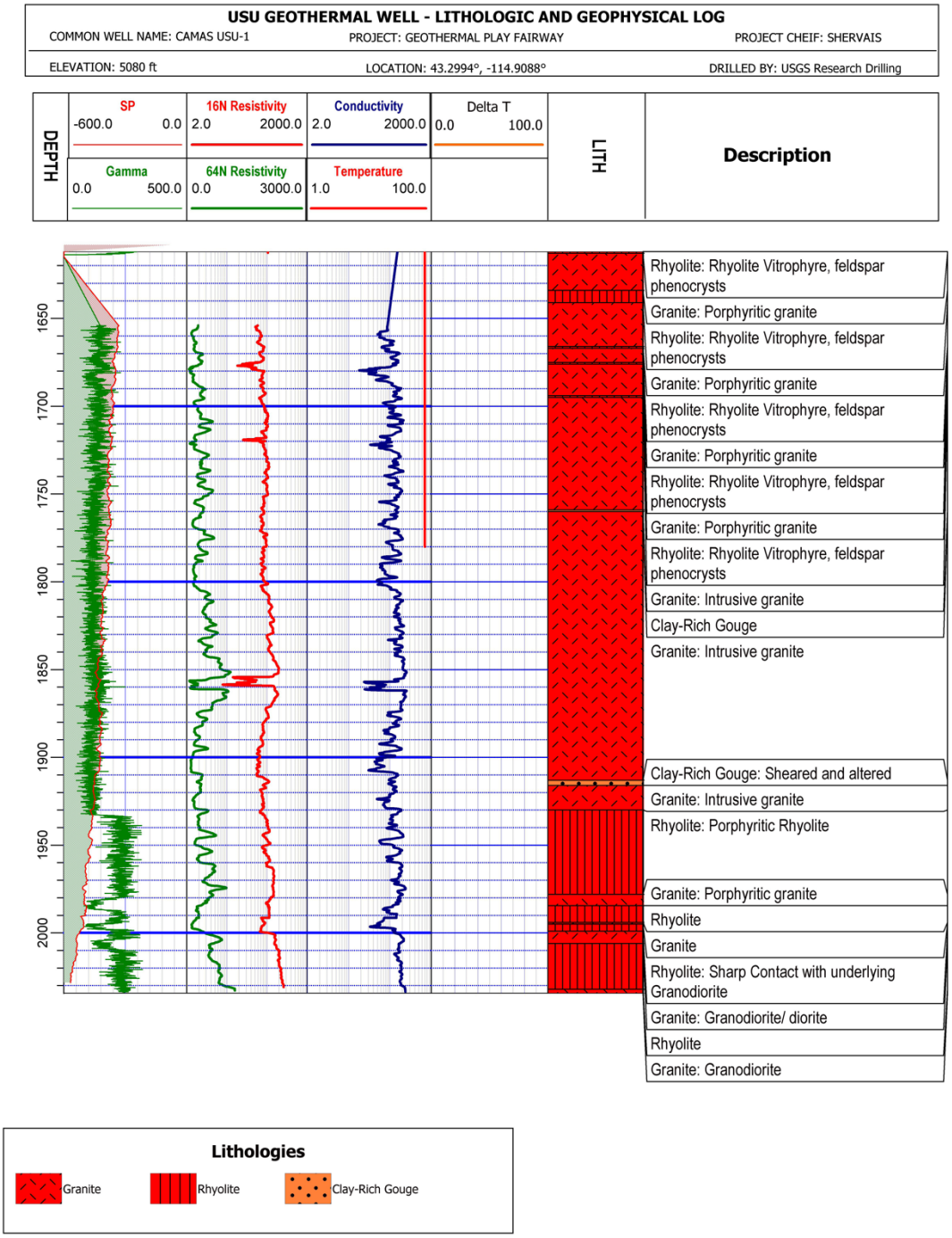

Figure 41. Lithologic log for Stage 3 coring from NQ-size core. Also shown are total gamma, self-potential, resistivity, and conductivity acquired by USGS Geosphysical Logging team.

14.4. Temperature Logs

The well site was revisited on several occasions by Roy Mink, who conducted two additional temperature surveys – one on Dec. 22, 2018, and a second on July 9, 2019 (Figure 42). During the July 2019 visit, Dr. Mink observed that the well now exhibited artesian flow – this prompted our team to return to the site to conduct geochemical sampling of the now discharging well, which had a surface discharge temperature of 71.9°C and a flow rate of 11.2 gpm. Hari Neupane (INL) and Patrick Dobson (LBNL) visited the site on July 21, 2019 and collected a full suite of water samples for geochemical and isotopic analysis. A $^{3}He/^{4}He$ Cu tube sample collected during this visit yielded the highest R/Ra value of any sample previously collected in the Camas Prairie area (2.45 Ra).

Temperature logs were run during and immediately following the two episodes of drilling by the USGS in 2018 and 2019, and additional temperature logging runs were conducted by Roy Mink in Dec. 2018 and July 2019 to capture the temperature profile of the borehole after the well had time to reequilibrate (Fig. 42). During the July 2019 survey, the well exhibited artesian flow, which prompted the team to mobilize later that month to collect a suite of fluid samples from the well. In addition to the conventional temperature logging runs, a HOBO sensor was run in the hole several times during breaks in drilling in 2019 to provide quick updates on the temperature profile of the borehole.

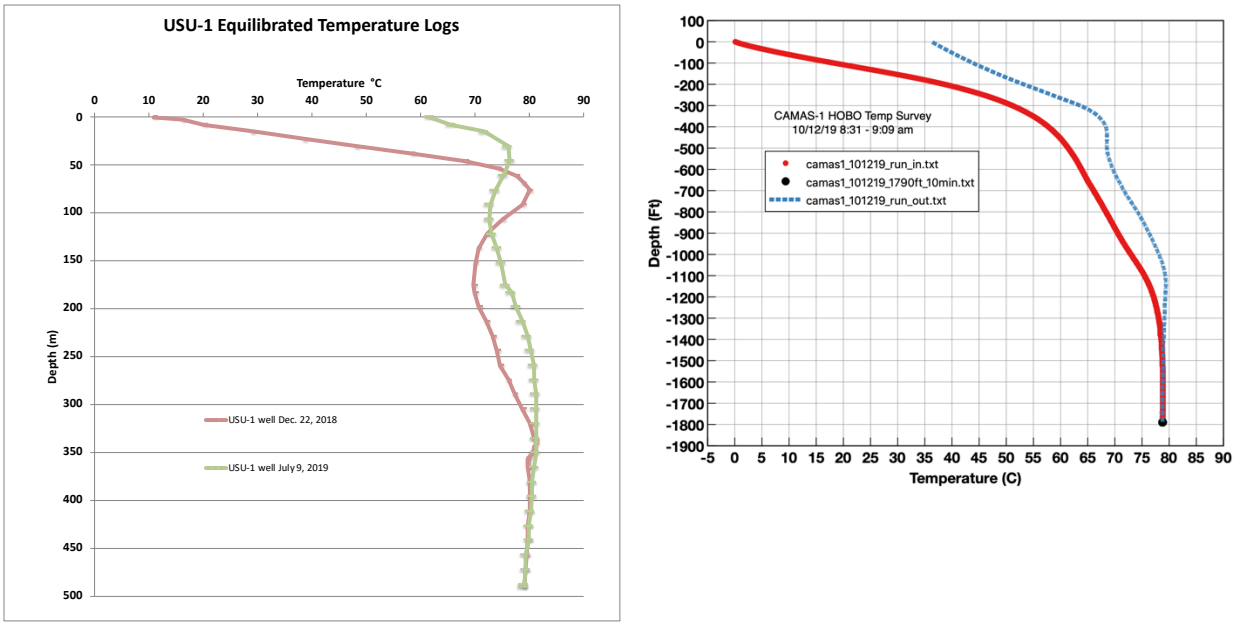

Fig. 42: Left – temperature surveys run on Dec. 22, 2018 and July 9, 2019 in USU-1 well by Roy Mink. Note the much higher shallow temperatures in the July 2019 survey – these reflect the rising water level and artesian flow that had dramatically heated up the shallow section of the borehole.

Right – HOBO temperature survey run on Oct. 12, 2019 during a drilling break in the core drilling of USU-1 well. Note the higher temperatures recorded when the tool was coming out of the hole – this likely reflects the delay in temperature equilibration of the instrument.

14.5. Geophysical Wireline Logging

Geophysical wireline logs were run after each drill stage. The Stage 1 hole was logged 27-28 September 2018 prior to setting casing. Tools run included the caliper, natural gamma, resistivity, conductivity, self-potential, and temperature. The Stage 2 hole was logged 19 October 2018 using the same tool set in the open hole, after removal of the HQ drill rods. A reservoir test was conducted on 22-24 October 2018 by the USGS Geophysics unit, under the supervision of Colin Goranson (see below). Finally, the Stage 3 hole logged on 31 October 2019, and further reservoir tests attempted 1-4 November 2019 (*https://gdr.openei.org/submissions/1285*).

A summary of the wireline log results is shown in Figure 43, along with a schematic of the well as built. Natural gamma is relatively low through the basin sediment section, and only slightly higher in the granite bedrock (typically around 200 API-GR), consistent with derivation of the basin-fill sediments from the adjacent granitic terranes. In contrast, rhyolite dikes are characterized by high natural gamma response (~380 API-GR; Figure 43). This contrast is consistent with whole rock geochemical analyses discussed below, which show that the rhyolites typically have slightly higher K_2O than the granites (~3.8 wt% average in rhyolite vs ~3.6 wt% in granite). In addition, the rhyolites have higher U+Th concentrations (~31 ppm average in rhyolite vs ~14 ppm in granite).

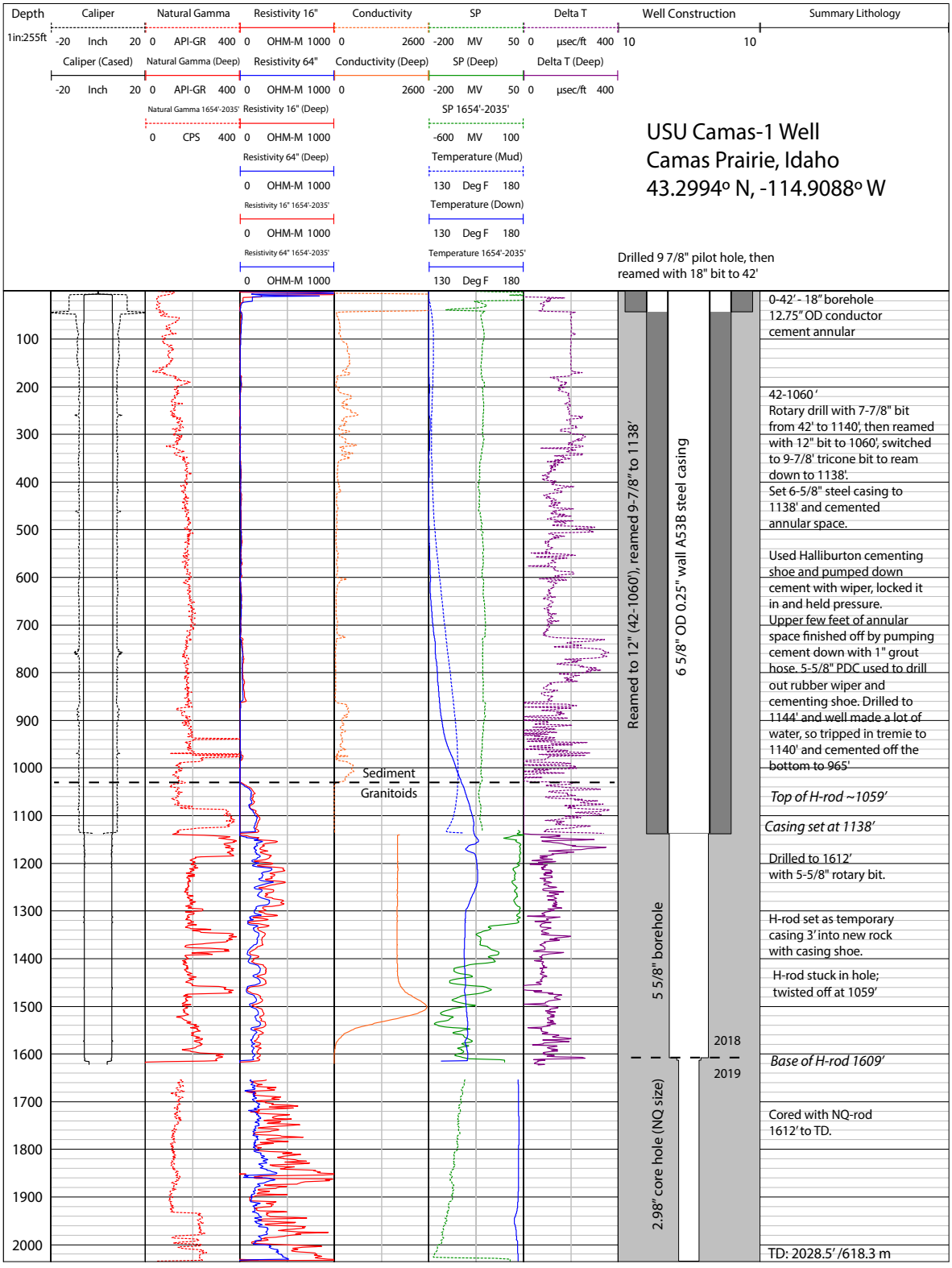

Figure 43. Summary of geophysical wireline logs in USU Camas-1 well, with diagram of well structure as built.

15.0 POST-DRILLING ANALYSIS

Post-Drilling Analyses included reservoir testing, a detailed study of recovered core (mineralogy, fluid inclusions, fractures, mechanical properties) and analytical data on any recovered water and gasses (elemental chemistry, isotopic composition of O, H, and dissolved He, multicomponent geothermometry).

15.1 Reservoir Testing of the Camas Prairie Validation Well

Reservoir tests were carried out by Colin Goranson, assisted on site by Tony Brown (USGS Research Drilling Geophysicist) and Thomas Lachmar (USU hydrologist). The reservoir test in 2018 indicated modest flow rates at moderate temperatures (66.7ºC/ 152ºF). This is lower than anticipated, but we failed to reach our projected target depth of 2000+ feet due to drilling and equipment issues. The results of these tests were analyzed by Sabodh Garg and Colin Goranson, and a full report is found at *https://gdr.openei.org/submissions/1284*.

Partial temperature survey of October 19, 2018 was taken just after well completion and prior to discharge and injection activities. The only other temperature survey was run on October 24, 2018 some 14 hours after cold water injection into the well. It is unlikely that the temperatures had equilibrated in the well at the time of the latter survey. Presence of a cold zone centered at ~357.5 m most likely indicates the permeable zone that accepted cold injection water. A maximum temperature of 77.2ºC was recorded at the bottom of the well (~490 m) on October 24, 2018; considering that the well was shut-in only for 14 hours after cold water injection, it is likely that the stable formation temperature at 490 m is considerably higher than 77.2ºC. By comparison between the temperature profiles of October 19 and 24, 2018, the feedzone temperature (~357.5 m) is estimated to be at least 70ºC. A pressure of 34.84 bars was measured at 357.5 m on October 24, 2018. The temperature survey recorded on October 24, 2018 in USU-1 exhibits a conductive gradient of ~7ºC/100 m below a depth of 420 m; it is thus possible that temperatures ≥100ºC may be encountered at depths of 700 to 800 m in the area.

15.1.1 Discharge test. The well was discharged for about 4 hours (10:38 LT to 14:33 LT) on October 20, 2018 by air lift through drill pipe (DP) lowered to 735 ft (224.0 m). The average discharge rate was about 60 gpm (~3.79 l/s = 3.71 kg/s) at a maximum surface temperature of 67.8ºC. During the discharge test, the pressure was steady at 155 psig (~11.53 bar) at 224 m. The static pressure at 224 m was ~22.03 bar on October 24, 2018. Therefore, the productivity index (PI) is given by:

PI = 3.71/ (22.03 – 11.53) = 0.35 kg/s-bar

The computed productivity index (PI) is relatively low. Continued injection (or discharge) is often found to lead to an improvement in the PI as a result of hole clean up.

15.1.2 Injection tests. Two injection tests were performed on October 21, 2018 (11:19 LT to 18:10 LT) and October 23, 2018 (09:26 LT to 17:16 LT). The injection rates had to be kept low (~22 gpm on October 21, 2018 and ~16 gpm on October 23) due to leakage of the surface packer. During both the injection tests, a PT (pressure and temperature) tool was installed at 1225 ft to record changes in downhole pressure and temperature. Unfortunately, the tool failed to

record properly on October 21, 2018; thus, downhole pressure data are only available for the second injection test performed on October 23, 2018. The injected water temperature was ~11.1ºC on October 24.

It was not possible to record the early injection rate on October 23, and the corresponding pressure record contains large oscillations. The pressure record was processed to remove the latter oscillations and resampled using a time interval of 0.005 hours; the resampled data were then filtered using a low pass filter (corner frequency = 10) to remove high frequency oscillations. Finally, the filtered data were resampled (decimated) using a minimum pressure interval of 0.0015 bar (~0.02 psi).

The resampled and filtered pressure data display an anomalous response. Normally, one would expect pressure to increase monotonically with continued injection; however, in this case, the pressure decreases. A decrease in pressure indicates an improvement in injectivity with continued injection. The final injection pressure just prior to shut-in at 17:19 LT on October 23, 2018 was ~35.90 bar (g). By the end of the downhole recording (about 8:20 LT on October 24, 2018), the pressure had declined to about 35.24 bar (g). With an injection rate of 16 gpm (~1.01 l/s = 1.01 kg/s), the injectivity index (II) is given by:

II = 1.01 / (35.90 – 35.24) = 1.53 kg/s-bar

The above injectivity index is more than 4 times the productivity index obtained from the brief discharge test on October 20, 2018. As noted earlier, the injectivity improved during the injection test.

Because of anomalous pressure response during the injection phase, the pressure data for this part of the test cannot be analyzed to obtain formation and well properties. Consequently, it was decided to focus on the fall-off pressure data. The latter data were at first analyzed using the standard Horner plot (see e.g. Streltsova, 1988).

With a discharge rate of 1.01 kg/s, a fluid density of 977.7 ºC and viscosity of 404 µPa-s (corresponding to a temperature of 70ºC), the formation permeability-thickness (kh) is given by:

*kh = 1.15 * (mass flow rate/density)*viscosity/ (2*pi*slope of semi-log line) ~1.09 darcy-meter.*

The fall-off data were also analyzed using an automatic inversion program DIAGNS (*Garg et al., 2002*); inversion was performed using the classical finite cylindrical source solution (*Streltsova, 1988; Garg et al, 2002*). Agreement between the data and the mathematical fit is only fair. Mathematical fit yields a permeability-thickness of about 4.17 darcy-meter, which is about 4 times that inferred from the Horner plot. In any event, it appears that the formation intercepted by USU-1 has a modest transmissivity (1 to 4 darcy-meter).

15.2. Water Chemistry and Equilibrium Water Temperatures

Water samples were collected from the Camas-1 well for major element, trace element, and isotopic analysis.

15.2.1. Water Sampling. After completion of the well, a flow test was conducted in the fourth week of October 2018. Prior to injection of cold water, an opportunity was provided to collect water samples. The water table was measured about 45 feet below ground surface. Water was airlifted to the surface and discharged onto the bed of an empty tank with a side kept open

all the time to drain water into the agricultural field. The flow rate was about 55 gal/min, and temperature of the water at discharge point was about 67.8ºC.

After 3.75 hours of pumping, water samples were collected for chemical and isotopic analysis. Once the water was discharged onto the bed, it was allowed to flow through the empty bed. A peristaltic pump (*Geotech Environmental Equipment, Inc. Denver, CO USA*) was used to pump water from the open side of the bed to the sample bottles through pre-cleaned, acid-washed, polytetrafluoroethene (PTFE) tubing fitted with a 0.45-um Gelman Sciences high-capacity capsule filter containing polyether sulfone membrane. Aliquots for cation and REE determinations were acidified to pH <2, using Optima-grade HNO3, and sealed with Parafilm M (*Bemis NA, Neenah, WI USA*). Anion samples were collected in 18 MΩ deionized water (DIW) rinsed bottles. To minimize the potential for environmental contamination, the exteriors of the sample containers were rinsed thoroughly with DIW and placed into acid-washed plastic bags, and the bagged sample bottles were placed in an ice-filled cooler and transported to laboratory.

Alkalinity was determined in the field by sulfuric acid titration using a digital titrator alkalinity test kit (*Hach Company, Loveland, CO USA*) with results expressed as mg/L of $CaCO_3$ and bicarbonate (Kehew 2001). The field pH was measured using a Beckman Coulter pH 400 series meter with a combination glass pH electrode. Field conductivity, dissolved oxygen, and redox potential were measured with YSI Professional Plus meter (YSI Inc.) equipped with a flow cell and multiple electrodes.

A subset of samples was collected for analyses of isotopes of O, H, and He. Filtered samples were collected for O and H isotopes in DIW rinsed HDPE bottles with no head space. Similarly, unfiltered water samples were collected in cold-sealed copper tube for He isotopes. Because the samples collected for He might have significant air contamination due to the airlifting of the well and open-air discharging of water prior to the collection of samples, these samples were not analyzed. A complete suite of drilling water samples (except He isotopes) was also collected from a storage tank. The drilling water was acquired from a shallow irrigation well located a few hundred feet east of the Camas PFA well.

15.2.2. Water Chemistry Methods. Cation and anion analytical measurements were made at the Center for Advanced Energy Studies (CAES) in Idaho Falls, Idaho. Cations concentrations were measured in triplicate using an Inductively Couple Plasma Mass Spectrometer (ICP-MS; Agilent Technologies, Inc., Santa Clara, CA USA) and Inductively Couple Plasma Optical Emission Spectrometer (ICP-OES; ThermoFisher Scientific, Sunnyvale, CA USA). Calibration standards were prepared by dilution of commercial concentrated standards (Inorganic Ventures Inc., Christiansburg, VA USA). For REE analyses, plasma oxide formation was maintained at <0.5% for $^{156}CeO/^{140}Ce$. Instrumental drift was accounted for by periodically analyzing a fixed concentration Rh internal standard, instrument blanks, and quality-control standards. Analytical results have ≤5% relative standard deviations as estimated from replicate analyses.

Anions were analyzed in triplicates using a Dionex Model ICS-2100 ion chromatograph (ThermoFisher Scientific) equipped with an IonPac™ AS18 column and a conductivity detector using a potassium hydroxide eluent (Dionex EluGen Cartridge EGC-KOH). Replicate analyses of each sample yielded a relative standard deviation of ≤3%. All samples collected for isotopes

were shipped to Utah State University, Logan, UT and Lawrence Berkeley National Laboratory, Berkeley, CA.

15.2.3. Water Chemistry Results. The analytical results of the new PFA well in Camas Prairie are given in Table 2. This includes the results of an air-lifted water sample collected just following drilling in October 2018 (CAES#150), a nearby water well that was used for drilling fluid (CAES#151), and sampling of the well in July 2019 when it exhibited artesian flow (CAES#152). Full results are at *https://gdr.openei.org/submissions/1264*.

15.2.4. Water Chemistry Isotopic Results. The collected water samples were analyzed for $^{18}O/^{16}O$, D/H, $^{13}C/^{12}C$ (dissolved carbon in water) and $^{3}He/^{4}He$ (dissolved gas in water). Results are reported in Table 3.

Figure 44 depicts the water stable isotopic compositions of spring and well water samples collected in the Camas Prairie area. Note that the Camas Creek Ranch samples and the water from USU-1 well are shifted further away from the global meteoric water line than the remaining samples, suggesting either more extensive water-rock interaction (*Taylor, 1974*) or mixing of meteoric water with a volcanic water component (*Giggenbach, 1992*). A similar shift was observed for other thermal water samples within the Snake River Plain (*Conrad et al., 2016*). The well at Camas Creek Ranch was sampled on four different occasions, and each time the resulting water had a different discharge temperature and distinct stable isotopic composition. The samples from these wells appear to depict a trend where the higher temperature fluids have more negative δD and $\delta^{18}O$ values.

The helium isotopic composition of the USU-1 well fluid (2.45) is the highest water He value measured within the Snake River Plain region outside of Yellowstone (*Dobson et al., 2015*), and indicates that there is a significant mantle-derived component to the He in this fluid. The relatively elevated He R/Ra values observed in the Camas Prairie area in the vicinity of Camas Creek was interpreted as reflecting the presence of young sills and dikes intruding into the crust of this region, supplying heat and serving as a source of mantle helium via degassing.

Table 2. Analytical results of PFA Camas-1 well water

Sample	Units	Camas PFA Well (CAES ID # 150)	Camas Drilling Water (CAES ID # 151)	Camas PFA Well (CAES ID # 152)
Longitude	Degree	43.2996	43.298831	43.2996
Latitude	Degree	-114.9088	-114.906666	-114.9088
Temperature	˚C	67.8	10.2	71.9
Sampling Date		10/20/18	10/20/18	7/21/19
Alkalinity	(as mg of $CaCO_3$)	222	158	164
Dissolved Oxygen	mg/L	5.2		
Conductivity	uS/cm	523		925
pH			8.27	8.76
F	mg/L	13.2	11.5	12.5
Cl	mg/L	14.4	12.0	13.3
SO4	mg/L	29.9	14	16
Br	mg/L	<5	<5	
NO3	mg/L	0.08	0.81	
Li	mg/L	0.22	0.08	
Al	mg/L	30*	0.063	0.0227
As	mg/L	0.004	0.0008	
Mg	mg/L	3.88	0.62	
Se	mg/L	<0.005	<0.005	
Sr	mg/L	0.321	0.03	0.098
Cs	mg/L	0.008	<0.0001	
Ba	mg/L	0.635	0.0	
Ge	mg/L	0.013	0.01	
SiO2 (aq)	mg/L	119.4	71.7	81.2
Na	mg/L	118	89	98
Ca	mg/L	7.27	3.9	2.3
K	mg/L	4.18	2.8	2.5

* Aluminum value is likely to be erroneous. Even though the water was filtered through the 0.45 um filter, it may have particles (<0.45 um) of clay (drilling mud). The airlifted water was cloudy.

Table 3: Isotopic analyses of water samples from the USU-1 well.

Sample	Units	Camas PFA Well (CAES ID # 150)	Camas Drilling Water (CAES ID # 151)	Camas PFA Well (CAES ID # 152)
Longitude	Degree	43.2996	43.298831	43.2996
Latitude	Degree	-114.9088	-114.906666	-114.9088
Temperature	˚C	67.8	10.2	71.9
Sampling Date			10/20/18	7/21/19
$^{18}O/^{16}O$	Permil (V-SMOW)		-18.8	-18.5
D/H	Permil (V-SMOW)		-151.8	-147.9
$^{13}C/^{12}C$	Permil (PDB)			-6.67
$^{3}He/^{4}He$	R/R_{air}			2.45

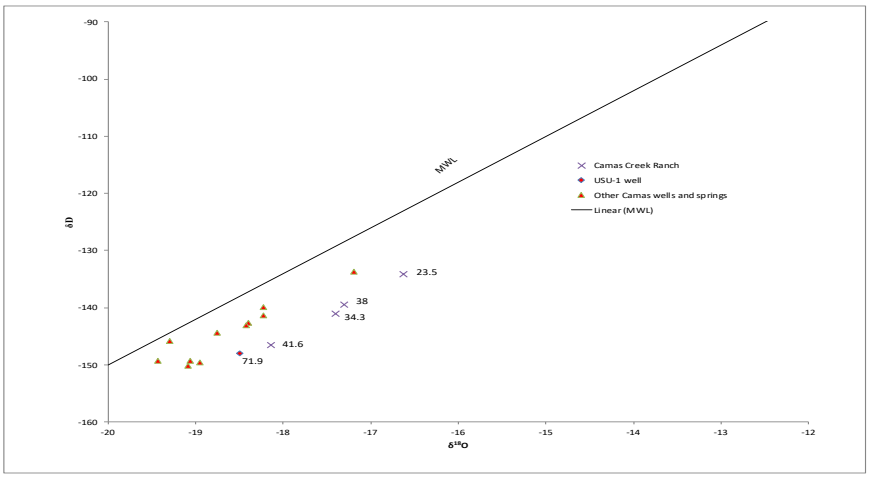

Figure 44. Water stable isotopic compositions of spring and well water samples collected in the Camas Prairie area.

15.2.5. Post-drilling Water Sampling. After many months of being static, the Camas well flowed under artesian conditions in the summer of 2019 – this was noted by Roy Mink when he went to run a temperature log in the well on July 9, 2019. Based on that observation, we mobilized a team to conduct water chemistry sampling on July 21, 2019. The well was discharged for several hours on July 9th, and it was discharged for several hours prior to collecting the water samples to ensure that the wellbore was fully purged. The discharge flow rate was ~11 gallons/minute, with a well discharge temperature of 71.9°C. Flow was captured by inserting tubing into the 2" wing valve to eliminate air contamination issues. Quite a number of gas bubbles were observed to be forming in the Tygon discharge lines as the fluid cooled. The gas had no odor, suggesting that it was mainly CO_2. As the well continued to discharge, it appeared that the amount of gas bubbles decreased. One possibility is that during the months when the well lay fallow, the water in the upper portion of the well may have become gas charged, leading to artesian flow. By September, the water level of the well dropped a few feet and it was no longer flowing.

Samples were collected for anion, cation, $^{18}O/^{16}O$, D/H, and $^{3}He/^{4}He$ in dissolved gas using a Cu tube. A field alkalinity titration was conducted on site, along with a pH measurement. The water chemistry results of this sampling visit are listed in Table 2 and 3.

15.2.6. Water Chemistry Equilibrium Water Temperatures. The multicomponent geothermometry program GeoT (*Spycher et al., 2014*) was used to estimate equilibrated fluid chemistry temperatures using a suite of water samples that was collected from the USU-1 well in July 2019 under artesian flow conditions. These samples were deemed to be the most equilibrated and least contaminated by residual drilling fluids. Figure 45 depicts the estimated equilibration temperature for the source fluids, along with the estimated error. To obtain the optimal fitting of the data, the sample was diluted by a factor of two. This implies a very dilute (meteoric) mixing water with concentrations of dissolved species much lower than in the native thermal brine (such that their effect on the mixing can be neglected). The best fit was obtained by using chalcedony as the silica phase.

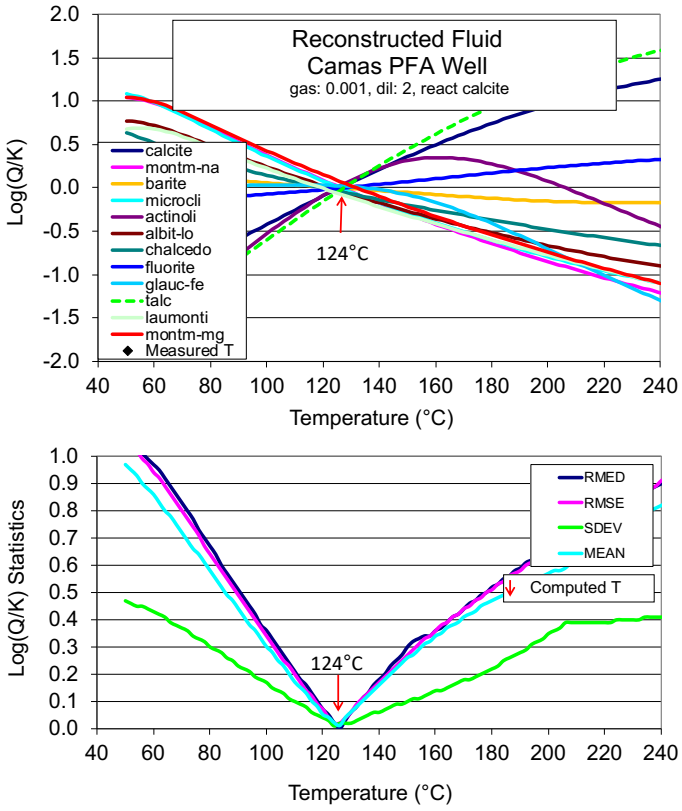

Fig. 45. Estimated equilibration temperature for the source fluids (top), along with the estimated error (bottom). The best fit was obtained by using chalcedony as the silica phase. This temperature is somewhat higher than that estimated from nearby hot springs (~110ºC).

15.3. Whole rock geochemistry and Petrography

Eight representative samples were chosen for whole rock major and trace element analysis. Commercial analyses were obtained from ALS Global Laboratory Services (Reno, Nevada). Major elements were analyzed by ICP-OES (optical emission spectroscopy) and trace elements were analyzed by ICP-MS (quadrupole mass spectrometry). The results are presented in Table 4, and complete sample descriptions are listed below.

Camas 3-6 [depth 1639.0 feet]. This is a rhyolite vitrophyre with mm-size phenocryst of sanidine in a black glassy or cryto-crystalline groundmass. It occurs as a seven-foot thick dike in the upper part of the granitic section, and has sharp intrusive contacts with the adjacent granite. Its high silica content (SiO_2 = 75 wt%) is consistent with Pliocene rhyolites of the older SRP. It has a La/Lu ratio = 103, K_2O ~4.6%, and U+Th ~10 ppm. Its high natural gamma response is largely due to its high K content.

Camas 9-18 [depth 1710.0 feet]. This sample is a mylonitic biotite gneiss, with a strong foliation dipping ~55º relative to the core axis. This sample is interpreted as a xenolith of metamorphic wall rock within the granitic rocks, based on its size (<1 foot thick) and unusual chemistry (low silica ~54% SiO_2), with high alumina (~24% Al_2O_3) and potassium (~7.4 K_2O). This composition is consistent with its biotite-rich mode.

Camas 9-20 [depth 1721.2 feet]. This is a granite with pale green propylitic alteration. It is nearly identical in composition to Camas 25-59, located over 150 feet deeper in the hole, with 69% SiO_2, a La/Lu ratio of 288, and U+Th ~12.5 ppm.

Camas 25-59 [depth 1883.5 feet]. This is a granite with pale green propylitic alteration. It is nearly identical in composition to Camas 9-20, located over 150 feet higher in the hole, with 69% SiO_2, a La/Lu ratio of 202, and U+Th ~19 ppm.

Camas 26-61 [depth 1889.7 feet]. This is a granodiorite with pale pink alteration, 63.6% SiO_2, a La/Lu ratio of 261, and U+Th ~12 ppm.

Camas 26-69 [depth 1929.6 feet]. This is a granodiorite with whitish alteration, 66.6% SiO_2, a La/Lu ratio of 296, and U+Th ~11 ppm.

Camas 29-70 [depth 1931.0 feet]. This is a pale salmon-colored rhyolite, with 71.4% SiO_2, a La/Lu ratio of 377, and U+Th= 30 ppm. The high U+Th accounts for its high natural gamma response in wireline logs. It is interpreted to represent the Challis Volcanic group.

Camas 32-78 [depth 1972.8 feet]. This is a pale salmon-colored rhyolite, with 70.7% SiO_2, a La/Lu ratio of 345, and U+Th= 31 ppm. The high U+Th accounts for its high natural gamma response in wireline logs. It is interpreted to represent the Challis Volcanic group.

Table 4. Whole rock chemical analyses of core from Camas1 well.

		Camas 3-6	Camas 9-18	Camas 9-20	Camas 25-59	Camas 26-61	Camas 29-69	Camas 29-70	Camas 32-78
Depth		1639.0	1710.0	1721.2	1883.5	1889.7	1929.6	1931.0	1972.8
		Rhyolite vitro-phyre	Mylonitic Biotite Gneiss	Granite propylitic alteration	Granite altered	Granite pink	Altered Granite	Rhyolite	Rhyolite
		Pliocene rhyolite	inclusion	Granite	Granite	Grano-diorite	Grano-diorite	Challis Volcanics	Challis Volcanics
SiO2	%	75	54.9	69.1	69.1	63.6	66.6	71.4	70.7
TiO2	%	0.15	0.2	0.28	0.22	0.3	0.29	0.39	0.35
Al2O3	%	13	23.8	15.7	13.1	16.95	13.7	14.35	13.75
Fe2O3*	%	1.26	5.04	1.97	1.92	1.64	2.02	2.28	1.97
MnO	%	0.02	0.06	0.04	0.1	0.03	0.05	0.03	0.03
MgO	%	0.24	2	0.44	0.61	0.3	0.37	0.76	0.68
CaO	%	1.69	1.19	2.32	4.48	5.3	4.41	1.76	1.8
Na2O	%	3.51	1.17	4.62	3.33	2.46	3.97	4.18	3.68
K2O	%	4.57	7.36	3.73	4.4	2.97	3.18	3.52	4.21
P2O5	%	0.02	0.03	0.08	0.09	0.07	0.06	0.16	0.13
Cr2O3	%	<0.02	<0.02	<0.02	<0.02	<0.02	<0.02	0.003	0.002
SrO	%	0.03	0.02	0.11	0.12	0.18	0.1	0.05	0.05
BaO	%	0.08	0.21	0.22	0.25	0.24	0.21	0.16	0.19
LOI	%	1.84	4.98	2.41	4.22	7.06	4.58	2.3	2.84
Total	%	101.41	100.96	101.02	101.94	101.1	99.54	101.34	100.38
total alkali		8.08	8.53	8.35	7.73	5.43	7.15	7.7	7.89
Cr	ppm	<10	10	10	10	<10	<10	20	20
V	ppm	9	85	24	19	22	22	37	31
Ga	ppm	20.4	62.1	22.7	18	22.7	18.4	21.7	19.9
Sn	ppm	1	1	1	1	1	1	2	1
W	ppm	940	510	450	715	321	930	450	135
Ba	ppm	707	1735	1800	2100	1970	1695	1360	1545
Cs	ppm	1.49	29	3.29	2.34	18.75	1.87	2.95	2.87
Rb	ppm	110.5	356	99.1	90.5	79	60.4	119.5	137.5
Sr	ppm	261	188.5	899	1005	1445	812	399	429
Y	ppm	8.3	5.4	10.7	12.2	9.8	14.1	12.1	11.2
Zr	ppm	57	69	218	187	227	250	227	207
Nb	ppm	15.8	9	19.6	13.4	20.1	19.4	18.7	16.9
La	ppm	9.3	14.5	46.1	34.4	41.7	50.4	56.6	51.8
Ce	ppm	19.1	25.4	81.4	59.3	74.7	87.5	96.1	88.3
Pr	ppm	2.26	2.54	8.27	5.85	7.55	8.89	9.26	8.55
Nd	ppm	8.9	8.8	29	20.5	26.6	31.1	32.4	29.1
Eu	ppm	0.61	0.51	1.39	1.11	1.34	1.46	1.09	1.09
Sm	ppm	2.05	1.34	4.09	2.95	3.82	4.55	4.36	4.13
Gd	ppm	1.99	1.11	3.29	2.37	2.93	3.67	3.51	3.33
Tb	ppm	0.28	0.17	0.4	0.35	0.42	0.46	0.45	0.44
Dy	ppm	1.59	0.93	1.9	1.86	2.09	2.56	2.27	2.19
Ho	ppm	0.31	0.18	0.41	0.4	0.42	0.53	0.45	0.41
Er	ppm	0.8	0.59	1.04	1.11	1.11	1.49	1.16	1.17
Tm	ppm	0.1	0.09	0.15	0.16	0.15	0.18	0.15	0.16
Yb	ppm	0.62	0.72	1.06	1	1.08	1.18	1.04	1.09
Lu	ppm	0.09	0.11	0.16	0.17	0.16	0.17	0.15	0.15
Ta	ppm	1.2	0.5	1.4	1	1.5	1.5	1.6	1.4
Hf	ppm	2	1.7	5	4.5	5.4	5.7	5.6	5.1
Th	ppm	7.73	5.31	10.25	16.6	8.82	9.55	23.9	25.3
U	ppm	2.49	2.12	2.28	2.64	3.01	1.73	6.16	6.14

16.0 SUMMARY AND CONCLUSIONS

We present an approach to Play Fairway Analysis, based on previously discussed conceptual models, that is adapted for use in geothermal exploration *(e.g., Nielson and Shervais, 2014; Nielson et al., 2015; DeAngelo et al., 2016)*. We have developed a systematic workflow in ArcGIS by creating custom Python scripts that use ArcGIS functions and Python scripts to automate data analysis. ArcGIS may use either raw data or synthetic data products (*e.g.,* fault dilation and slip tendency) derived from other programs for primary evidence layers. ArcMap *Geostatistical Analyst* was used for all geostatistics and data interpolation (*Empirical Bayesian Kriging*), and other ArcMap toolbox tools were used to derive density functions (simple density or kernel density functions).

In Stage 1, we applied our methodology to data compiled from publicly available sources to all of southern Idaho (south of 44.7ºN). Our assessment of these data suggests that important undiscovered geothermal resources exist in several areas of the Snake River Plain. These include four areas in the WSRP (all blind systems associated with concealed structures inferred from geophysics), two areas in the CSRP (eastern end of the Mount Bennett Hills and King Hill areas) and two Basin-and-Range play types in eastern and SE Idaho. In addition, four potential EGS prospects were located.

In Stage 2, we filled data gaps in our knowledge base with new geological, geophysical, and geochemical data for two of these undiscovered resource areas: Mountain Home and Camas Prairie, Idaho. These data allowed us to refine our conceptual model and select potential drill sites for geothermal test wells at both localities. Data acquisition and integration continued into Stage 3, which culminated with the drilling of USU Camas-1 geothermal test well. This well validated our approach to geothermal PFA by supporting our predictions based on integrated geological, geochemical, and geophysical studies interpreted in the context of a conceptual model for this play type.

All of the hydrothermal prospects identified in this study are potentially commercially viable, with favorability that equals or exceeds our training sites (*e.g.,* Raft River). Many of these prospects have large geographic extents, estimated temperatures of 150ºC or more, and the potential to produce 10s of MW of power. Most are near transmission corridors and have extensive private or non-excluded public land available for lease.

The most successful outcome of this project, however, has been the development and refining of our GIS-based approach to Play Fairway Analysis, which uses Python scripts to semi-automate data processing, and can be applied to a wide range of geothermal systems and conceptual models.

References Cited

Adams, M.C., Moore, J.N., Bjornstad, S. and Norman, D.I., 2000. Geologic history of the Coso geothermal system. Transactions-geothermal resources council, pp.205-210.

Anderson, J.E., Bideganeta, K. and Mitchell, J.C., 1985. Water information bulletin No. 30, part 13: geothermal investigations in Idaho. Preliminary geologic reconnaissance of the geothermal occurrences of the Wood River Drainage Area (No. DOE/ET/28407-T6). Idaho Dept. of Water Resources, Boise (USA).

Anderson, SR, Akerman, DJ, Liszewski, MJ, 1996, Stratigraphic data for wells at and near the Idaho National Engineering Laboratory, Idaho. USGS Open File Report OFR-96-248, 27 pp.

Anderson, SR, Kuntz, MA, and Davis, LC, 1999, Geologic controls of hydraulic conductivity in the Snake River Plain aquifer at and near the Idaho National Engineering and Environmental Laboratory, Idaho: US Geological Survey Water Resources Investigations Report 99-4033 (DOE/ID-22155), 38 p.

Anderson, SR, Liszewski, M.J., and Cecil, L.D., 1997, Geologic ages and accumulation rates of basalt-flow groups and sedimentary interbeds at the Idaho National Engineering Laboratory, Idaho. USGS Water Resources Investigation Report 97-4010, 39 pp.

Anderson, E., Crosby, D., and Ussher, G., 2000, Bulls-Eye - Simple Resistivity Imaging to Reliably Locate the Geothermal Reservoir. Proceedings World Geothermal Congress 2000 Kyushu - Tohoku, Japan, May 28 - June 10, 2000.

Arney, B.H., 1982, Evidence of former higher temperatures from alteration minerals, Bostic 1-A well, Mountain Home, Idaho, Geothermal Resources Council Trans., 6, 3-6.

Arney, B.H., F. Goff, and Harding Lawson, 1982, Evaluation of the hot dry rock geothermal potential of an area near Mountain Home, Idaho, Los Alamos Nat. Lab Report LA-9365-HDR, 65 pp.

Atkinson, T. A., 2015, Geochemical characterization of the Mountain Home geothermal system, Masters Thesis, Utah State University, All Graduate Theses and Dissertations, 4599, 105 pp.

Atkinson, TA, Newell, DL, and Shervais, JW, 2017, Geochemical and thermal evidence of high temperature geothermal activity from the MH-2B slimhole, Western Snake River Plain, Idaho. Proceedings, 42nd Workshop on Geothermal Reservoir Engineering, Stanford University, Stanford, California, February 13-15, 2017, SGP-TR-212.

Bacon, C.R., Duffield, W.A. and Nakamura, K., 1980. Distribution of Quaternary rhyolite domes of the Coso Range, California: Implications for extent of the geothermal anomaly. Journal of Geophysical Research: Solid Earth, 85(B5), pp.2425-2433.

Baker, S.J. and P.M. Castelin, 1990, Geothermal resource analysis in Twin Falls County, Idaho Part II. Idaho Department of Water Resources Water Information Bulletin, 30/16, 1990, 36 p.

Bankey, V., Cuevas, A., Daniels, D., Finn, C.A., Hernandez, I., Hill, P., Kucks, R., Miles, W., Pilkington, M., Roberts, C., Roest, W., Rystrom, V., Shearer, S., Snyder, S., Sweeney, R., Velez, J., 1999, A New Magnetic Anomaly Map of North America, http://crustal.usgs.gov/projects/namad/the_project.html

Barton, C.A., Hickman, S.H., Morin, R., Zoback, M.D., Benoit, D., 1998. Reservoir-scale fracture permeability in the Dixie Valley, Nevada, geothermal field. Proceedings, Soc. Pet. Eng. Annu. Meet. 315–322. doi:10.2523/47371-MS

Barton, C.A., Zoback, M.D., Moos, D., 1995, Fluid flow along potentially active faults in crystalline rock. Geology 23, 23–27. doi:10.1130/0091-7613(1995)023<0683

Blackwell et al 2002

Blackwell, DD and M. Richards. 2004. Geothermal Map of North America. Amer. Assoc. Petroleum Geologists, Tulsa, Oklahoma, 1 sheet, scale 1:6,500,000.

Blackwell, DD, 1980, Geothermal-gradient and heat-flow data, pp. 23-29, in Preliminary geology and geothermal resource potential of the Western Snake River Plain, Oregon, eds. D. E. Brown, G. D. McLean, G. L. Black, and J. F. Riccio, Ore. DOGAMI Open File Rep. 0-80-5, Portland.

Blackwell, DD, 1989, Regional implications of heat flow of the Snake River Plain, Northwestern United States, Tectonophysics, 157, 241-250.

Blackwell, DD, SA Kelley, and JL Steele, 1992, Heat flow modeling of the Snake River Plain, Idaho, Dept. of Geological Sciences, Southern Methodist Univ, US Dept of Energy Contract DE-AC07-761DO1570, 109 pp.

Blackwell, DD, Steele, J.L., and Carter, L.C., 1989, Heat flow data base for the United States, in Hittleman, A.M., Kinsfather, J.O., and Meyers, H., eds., Geophysics of North America CD-ROM, Boulder, Colo, Natl. Oceanographic and Atmospheric Adm., Natl. Geophys. Data Center.

Blake, K. and Davatzes, N.C., 2011. Crustal stress heterogeneity in the vicinity of Coso Geothermal Field, CA. In Proceedings, Thirty-Sixth Workshop on Geothermal Reservoir Engineering (p. 11).

Blake, K. and Davatzes, N.C., 2012, February. Borehole image log and statistical analysis of FOH-3D, Fallon Naval Air Station, NV. In Proceedings, Thirty-Seventh Workshop on Geothermal Reservoir Engineering Stanford University, Stanford, California.

Blakely, R.J., and Simpson, R.W., 1986, Approximating edges of source bodies from gravity or magnetic data. Geophysics, 51, 1494–1498, doi: 10.1190/1.1442197.

Bodvarsson, G. and J.M. Hanson. 1977. Forced Geoheat Extraction from Sheetlike Fluid Conductors. Proceedings of the Second NATOCCMS Information Meeting on dry hot rock geothermal energy. Los Alamos Scientific Laboratory report, LA7021:85.

Bouligand, C., J.M.G. Glen, and R.J. Blakely, 2014, Distribution of buried hydrothermal alteration deduced from high resolution magnetic surveys in Yellowstone National Park, Jour Geophys. Res., DOI: 10.1002/2013JB010802

Bradford, J., Liberty, L.M., Lyle, M.W., Clement, W.P., and Hess, S.S., 2006, Imaging complex structure in shallow seismic-reflection data using pre-stack depth migration, Geophysics, v. 71, p. B175-B181.

Breckenridge, RM, Gillerman, VS and Wray-Macomb, E., 2006, Oil and Gas Exploration in Idaho. Idaho Geological Survey, Digital Web Map 81.

Breckenridge, RP, Shervais, JW, Nielson, DE, Wood, TR, 2012, Exploration and Resource Assessment at Mountain Home Air Force Base, Idaho Using an Integrated Team Approach. Geothermal Resources Council Trans, v36, 615-619.

Brook C.A., Mariner R.H., Mabey D.R., Swanson J.R., Guffanti M., Muffler L.J.P., 1979, Hydrothermal Convection Systems With Reservoir Temperatures & 90°C. in Assessment of Geothermal Resources of the United States - 1978, U.S. Geological Survey Circular 790, 170 p.

Brott, CA, DD Blackwell, and JC Mitchell, 1976, Heat flow study of the Snake River Plain region, Idaho, p. 195 pp., in Geothermal Investigations in Idaho, Idaho Dept. Water Resour., Water Info. Bull., 30.

Brott, CA, DD Blackwell, and JC Mitchell, 1978, Tectonic implications of the heat flow of the western Snake River Plain, Idaho, Geol. Soc. Am. Bull., 89, 1697-1707, 1978.

Brott, CA, DD Blackwell, and JP Ziagos, 1981, Thermal and tectonic implications of heat flow in the eastern Snake River plain, Idaho, J. Geophys. Res., 86, 11709-11734, 1981.

Brown, DE, GD McLean, and GL Black, 1980, Preliminary geology and geothermal resource potential of the western Snake River plain, Oregon, Oregon Dept. Geol. Min. Indus, Open-File Rep O-80-5, 114p.

Cannon, C., Wood, T., Neupane, G., McLing, T., Mattson, E., Dobson, P., and Conrad, M., 2014, Geochemistry sampling for traditional and multicomponent equilibrium geothermometry in southeast Idaho. Geothermal Resources Council Transactions v. 38, 425-431.

Christiansen, E., and McCurry, M., 2008, Contrasting origins of Cenozoic silicic volcanic rocks from the western Cordillera of the United States: Bulletin of Volcanology, v. 70, no. 3, p. 251-267.

Christiansen, RL, 2001, The Quaternary and Pliocene Yellowstone Plateau Volcanic Field of Wyoming, Idaho, & Montana, Geology of Yellowstone National Park, U.S. Geological Survey Professional Paper 729, 1-156.

Cluer, J.K., and Cluer, B.L., 1986, The late Cenozoic Camas Prairie Rift, south-central Idaho. Contributions to Geology, University of Wyoming, 24, (1986), 91–101.

Conrad, ME, Dobson, PF, Sonnenthal, EL, Kennedy, BM, Cannon, C., Worthing, W., Wood, T., Neupane, G., Mattson, E, and McLing, T., 2016, Application of Isotopic Approaches for Identifying Hidden Geothermal Systems in Southern Idaho. Proceedings, 41st Workshop on Geothermal Reservoir Engineering, Stanford University, Stanford, California, SGP-TR-209.

Coolbaugh, M., Zehner, R., Kreemer, C., Blackwell, D., Oppliger, G., Sawatzky, D., Blewitt, G., Pancha, A., Richards, M., Helm-Clark, C., Shevenell, L., Raines, G., Johnson, G., Minor, T., Boyd, T., 2005. Geothermal potential map of the Great Basin, western United States: Nevada. Bur. Mines Geol. Map (151).

Coolbaugh, M., Zehner, R., Kreemer, C., Blackwell, D.D., Oppliger, G.L., 2005, A map of geothermal potential for the Great Basin, USA: Recognition of multiple geothermal environments. Geothermal Resources Council Transactions, v. 29.

Coolbaugh, M.F., Taranik, J.V., Raines, G.L., Shevenell, L.A., Sawatzky, D.L., Minor, T.B., Bedell, R., 2002, A geothermal GIS for Nevada: defining regional controls and favorable exploration terrains for extensional geothermal systems. Geothermal Resources Council Transactions v. 26, p. 485-490.

Cordell, L., and McCafferty, A.E., 1989, A terracing operator for physical property mapping with potential field data. Geophysics, 54, (1989), 621–634, doi:10.1190/1.1442689.

Criss, R.E. and Taylor Jr, H.P., 1983. An 18O/16O and D/H study of Tertiary hydrothermal systems in the southern half of the Idaho batholith. Geological Society of America Bulletin, 94(5), pp.640-663.

Crone, A.J., Machette, M.N., Bonilla, M.G., Lienkaemper, J.J., Pierce, K.L., Scott, W.E. and Bucknam, R.C., 1987. Surface faulting accompanying the Borah Peak earthquake and segmentation of the Lost River fault, central Idaho. Bulletin of the Seismological Society of America, 77(3), pp.739-770.

Cumming, W., 2016, Resource Conceptual Models of Volcano-Hosted Geothermal Reservoirs for Exploration Well Targeting and Resource Capacity Assessment: Construction, Pitfalls and Challenges. GRC Transactions, Vol. 40, 2016.

Davatzes, N.C, and Hickman, S. (2006), Stress and faulting in the Coso Geothermal Field: Update and recent results from the East Flank and Coso Wash, Proceedings 31st Workshop on Geothermal Reservoir Engineering, Stanford Univ., Stanford, CA, SGP-TR-179.

Davatzes, N.C. and Hickman, S., 2005, January. Comparison of acoustic and electrical image logs from the Coso geothermal field, CA. In Proceedings, Thirtieth Workshop on Geothermal Reservoir Engineering, Stanford University (pp. 1-11).

DeAngelo, J, Shervais, JW, Glen, JM, Nielson, DL, Garg, S, Dobson, P, Gasperikova, E, Sonnenthal, E, Visser, C, Liberty, LM, Siler, D, Evans, JP, and Santellanes, S., 2016, GIS Methodology for Geothermal Play Fairway Analysis: Example from the Snake River Plain Volcanic Province. Proceedings Forty-First Workshop on Geothermal Reservoir Engineering, Stanford University, Stanford, California, February 22-24, 2016 SGP-TR-209.

Delahunty, C., Nielson, DL, and Shervais, JW, 2012, Coring of three deep geothermal holes, Snake River Plain, Idaho. Geothermal Resources Council Trans., v36, 641-647.

DeNosaquo, K.R., R.B. Smith and A.R. Lowry, 2009, Density and lithospheric strength models of the Yellowstone-Snake River Plain volcanic system from gravity and heat flow data. Journal of Volcanology and Geothermal Research, 188, 2009, 108-127.

Desborough, GA, Raymond, W.H. Marvin, R.F. and Kellogg, K.S., 1989, Pleistocene sediments and basalts along the Snake River in the area between Blackfoot and Eagle Rock, southeastern Snake River Plain, southeastern Idaho. U.S. Geological Survey Open-File Report 89-436, 18 pp.

Dobrin, M.B., and Savit, C.H., 1988, Introduction to Geophysical Prospecting, 4th ed.: New York, McGraw-Hill, 867 p.

Dobson, P.F., B.M. Kennedy, M.E. Conrad, T. McLing, E. Mattson, T. Wood, C. Cannon, R. Spackman, M. van Soest, and M. Robertson, 2015, He Isotopic Evidence for Undiscovered Geothermal Systems in the Snake River Plain. Proceedings, Fortieth Workshop on Geothermal Reservoir Engineering Stanford University, Stanford, California, January 26-28, 2015 SGP-TR-204.

Doherty, DJ, 1979, Drilling data from exploration well 1, NE1/4, Sec 22, T2N R32E, Bingham County, Idaho. USGS Open File Report OFR-79-1225, plate.

Doherty, DJ, McBroome, LA and Kuntz, MA, 1979, Preliminary geological interpretation and lithologic log of the exploratory geothermal test well (INEL-1), Idaho National Engineering Laboratory, eastern Snake River Plain, Idaho. USGS Open File Report OFR-79-1248, 9 pp.

Doust, H., 2010. The exploration play: What do we mean by it? AAPG bulletin, 94(11), pp.1657-1672.

Druschel, G.K. and Rosenberg, P.E., 2001. Non-magmatic fracture-controlled hydrothermal systems in the Idaho Batholith: South Fork Payette geothermal system. Chemical Geology, 173(4), pp.271-291

Eager et al., 2001;

Egbert, G, 1997, Robust multiple-station magnetotelluric data processing, Geophysical Journal International. 130, 475-496.

Egbert, G.D. and Kelbert, A., 2012. Computational recipes for electromagnetic inverse problems. Geophysical Journal International, 189(1), pp.251-267.

Egbert, G.D., and Kelbert, A., 2012, Computational recipes for electromagnetic inverse problems. Geophys. J. Int., 189, (2012), 251-267.

Ekren, EB, DH McIntyre and EH Bennett, 1984, High-temperature, large-volume, lavalike ash-flow tuffs without calderas in southwestern Idaho: U.S. Geological Survey Professional Paper 1272, 76 p.

Elders, W.A., Friðleifsson, G.Ó., Zierenberg, R.A., Pope, E.C., Mortensen, A.K., Guðmundsson, Á., Lowenstern, J.B., Marks, N.E., Owens, L., Bird, D.K. and Reed, M., 2011. Origin of a rhyolite that intruded a geothermal well while drilling at the Krafla volcano, Iceland. Geology, 39(3), pp.231-234.

Embree, GF, Lovell, MD, and Doherty, DJ, 1978, Drilling data from Sugar City exploration well, Madison County, Idaho. USGS Open File Report OFR78-1095, plate.

Faulds, J.E., Coolbaugh, M., Blewitt, G. and Henry, C.D., 2004. Why is Nevada in hot water? Structural controls and tectonic model of geothermal systems in the northwestern Great Basin. Geothermal Resources Council Transactions, 28, pp.649-654.

Faulds, J.E., Coolbaugh, M.F., Vice, G.S., and Edwards, M.L., 2006, Characterizing Structural Controls of Geothermal Fields in the Northwestern Great Basin: A Progress Report: Geothermal Resources Council Transactions, v. 30, p. 69–76.

Faulds, J.E., N.H. Hinz, G.M. Dering and D.L. Siler, 2013, The Hybrid Model-The Most Accommodating Structural Setting for Geothermal Power Generation in the Great Basin, Western USA. Geothermal Resources Council Transactions 37, 3–10.

Ferrill, D.A., Winterle, J., Wittmeyer, G., Sims, D., Colton, S., Armstrong, A., Horowitz, A.S., Meyers, W.B., Simons, F.F., 1999, Stressed rock strains groundwater at Yucca Mountain, Nevada. GSA Today 9, 2–9.

Fleischmann, D.J., 2006, Geothermal development needs in Idaho, Geothermal Energy Association, 51 pp.

Fridleiffson, G. O and Richter, B.: The geological significance of two IDDP-ICDP spot cores from the Reykjanes geothermal field, Iceland: Proceed. World Geothermal Congress (2010).

Fridleifsson, G. O., Sigurdsson, O., Thorbjornsson, D., Karlsdottir, R. and Gislason, Th.: Preparation for drilling IDDP-2 at Reykjanes: Geothermics, 49 (2014) 119-126.

Fugelli, E.M. and Olsen, T.R., 2005. Risk assessment and play fairway analysis in frontier basins: Part 2—Examples from offshore mid-Norway. AAPG bulletin, 89(7), pp.883-896.

Gao, Z.J., Wu, L.J. and Cao, H., 2009. The summarization of geothermal resources and its exploitation and utilization in Shandong Province. Journal of Shandong University of Science and Technology (Natural Science), 28, 2, 1-7.

Gao, K., Huang, L. and Cladouhos, T., 2020. Three-dimensional seismic characterization and imaging of the Soda Lake geothermal field. Geothermics, 90, p.101996.

Garabedian, SP, 1992, Hydrology and digital simulation of the regional aquifer system, eastern Snake River Plain, Idaho. USGS Professional Paper 1480F, 102 p.; 10 Plates.

Garg, S, Nielson, DL, Shervais, JW, Sonnenthal, E, 2016, Thermal modeling of the Mountain Home Geothermal Area. Proceedings Forty-First Workshop on Geothermal Reservoir Engineering, Stanford University, Stanford, California, February 22-24, 2016 SGP-TR-209.

Garg, S. Gasperikova, E, Nielson, DL, Shervais, JW, 2017, Mountain Home Geothermal Area: Natural State Model. Geothermal Resources Council Transactions, v41, 2731-2742.

Geist, D, Teasdale, R, Sims, E, and Hughes, S, 2002, Subsurface volcanology at TAN and controls on groundwater flow, GSA Special Paper 353, 45-59.

Genter, A., Traineau, H., 1996, Analysis of macroscopic fractures in granite in the HDR geothermal well EPS-1, Soultz-sous-Forêts, France, Journal of volcanology and geothermal research, vol. 72, no1-2, pp. 121-141.

Giggenbach W.F., Goguel R.L., 1989, Collection and Analysis of Geothermal and Volcanic Water and Gas Discharges. Report No. CD 2401, Chemistry Division, DSIR, Petone, New Zealand (1989).

Giggenbach, W.F., 1992, Isotopic shifts in waters from geothermal and volcanic systems along convergent plate boundaries and their origin. Earth and Planetary Science Letters 113, 495-510.

Giggenbach, W.F.: Geothermal Solute Equilibria. Derivation of Na–K–Mg–Ca Geoindicators, Geochim. Cosmochim. Acta, 52, (1988), 2749–2765.

Glen JMG, Payette S, Bouligand M, Helm-Clark C, Champion D, 2006, Regional geophysical setting of the Yellowstone Hotspot track along the Snake River Plain, Idaho, USA. EOS Trans. AGU, 87(52), V54-1698.

Glen, JMG, Liberty, L, Gasperikova, E, Siler, D, Shervais, JW, Ritzinger, B, Athens, N, Earney, T, 2017, Geophysical Investigations and Structural Framework of Geothermal Systems in west and southcentral Idaho; Camas Prairie to Mountain Home. Proceedings, 42nd Workshop on Geothermal Reservoir Engineering, Stanford University, Stanford, California, February 13-15, 2017, SGP-TR-212.

Grauch, V.J.S., and Cordell, L., 1987, Limitations of determining density or magnetic boundaries from the horizontal gradient of gravity or pseudogravity data. Geophysics, (1987), 118–121, doi: 10.1190/1.1442236.

Hackett, W.R., Anders, M., and Walter, R.C., 1994, Preliminary stratigraphic framework of rhyolites from corehole WO-2, Idaho National Engineering Laboratory: Caldera-related late Tertiary Silicic volcanism in the eastern Snake River plain, Abstracts, VIIth International Symposium on the Observation of Continental Crust Through Drilling, Santa Fe, New Mexico, 1994.

Hanan, BB Shervais, JW, and Vetter, SK, 2008, Yellowstone plume-continental lithosphere interaction beneath the Snake River Plain, Geology, v. 36, 51-54. DOI:10.1130/G23935A.1

Heidbach, O., Tingay, M., Barth, A., Reinecker, J., Kurfeß, D. and Müller, B., 2010. Global crustal stress pattern based on the World Stress Map database release 2008. Tectonophysics, 482(1-4), pp.3-15.

Hickman, S., Zoback, M.D., Barton, C., Benoit, R., Svitek, J. and Summers, R. (2000), Stress and permeability heterogeneity within the Dixie Valley geothermal reservoir: Recent results from well 82-5, Proceedings 25th Workshop on Geothermal Reservoir Engineering, Stanford Univ., Stanford, CA, p. 256-265.

Hickman, S., Zoback, M.D., Benoit, R. (1998), Tectonic controls on fault-zone permeability in a geothermal reservoir at Dixie Valley, Nevada, in Rock Mechanics in Petroleum Engineering, v. 1, R. M. Holt et al. (eds.), Soc. Petroleum Eng., Richardson, TX., p. 79-86.

Hickman, S.H., and Davatzes, N.C., 2010, In-situ stress and fracture characterization for planning of an EGS stimulation in the Desert Peak Geothermal Field, Nevada, in Proceedings, Thirty-Fifth Workshop on Geothermal Reservoir Engineering, Stanford University, p. 13.

Hill DP and Pakiser, LC, 1967, Crustal structure between the Nevada test site and Boise Idaho from seismic refraction measurements, in Steinhart and Smith (eds), The Earth beneath the Continents: American Geophysical Union Monograph 10, (1967), 391-419.

Hughes SS, PH Wetmore, and JL Casper, 2002, Evolution of Quaternary tholeiitic basalt eruptive centers on the eastern Snake River Plain, Idaho, in Idaho Geological Survey Bulletin 30, p. 363-385.

Ito, T., Zoback, M.D., 2000, Fracture permeability and in situ stress to 7 km depth in the KTB Scientific Drillhole. Geophys. Res. Lett. 27, 1045–1048.

Jachens, R.C., and Moring, B.C., 1990, Maps of the Thickness of Cenozoic Deposits and the Isostatic Residual Gravity over Basement for Nevada. USGS Open-File Report, 90-404, (1990), 15p.

James, ER Manga, M, Rose, TP, Hudson, GB, 2000, The use of temperature and the isotopes of O, H, C, and noble gases to determine the pattern and spatial extent of groundwater flow. Journal of Hydrology 237, 100–112.

Janik, A., Lyle, M., and Liberty, L.M., 2004, Seismic expression of Pleistocene paleoceanographic changes in the California Borderland from digitally acquired 3.5 kHz subbottom profiles and Ocean Drilling Program Leg 167 drilling: Journal of Geophysical Research, v. 109.

Jean, M.M., Christiansen, E.H., Champion, D.E., Vetter, S.K., Phillips, W.M., Schuth, S., Shervais, J.W., 2018, Caldera Life-Cycles of the Yellowstone Hotspot Track: Death and Rebirth of the Heise Caldera, Journal of Petrology, egy074, doi.org/10.1093/petrology/egy074.

Jean, MM, Hanan, BB, and Shervais, JW, 2014, Yellowstone Hotspot – Continental Lithosphere Interaction: Earth and Planetary Science Letters, v389, 119-131. doi.org/10.1016/j.epsl.2013.12.012.

Jean, MM, Shervais, JW, Champion, DE, and SK Vetter, 2013, Geochemical and paleomagnetic variations in basalts from the Wendell Regional Aquifer Systems Analysis (RASA) drill core: evidence for magma recharge and assimilation–fractionation crystallization from the central Snake River Plain, Idaho: Geosphere. doi:10.1130/GES00914.1

Johnson, S.D. and Hulen, J.B., 2002. Subsurface stratigraphy, structure, and alteration in the Senator thermal area, northern Dixie Valley geothermal field, Nevada. Transactions-Geothermal Resources Council, pp.533-542.

Jolie, E., Faulds, J.E., and Moeck, I., 2012, The Development of a 3D structural-geological model as part of the geothermal exploration strategy - A case study from the Brady's geothermal system, Nevada, USA, in Proceedings, Thirty-Seventh Workshop on Geothermal Reservoir Engineering, Stanford University, p. 421–425.

Jolie, E., Moeck, I., and Faulds, J.E., 2015, Quantitative structural–geological exploration of fault-controlled geothermal systems—A case study from the Basin-and-Range Province, Nevada (USA): Geothermics, v. 54, p. 54–67, doi: 10.1016/j.geothermics.2014.10.003.

Kauffman, JD, Othberg, KL, Gillerman, VS, Garwood, DL, 2005a, Geologic Map of the Twin Falls 30x60 minute Quadrangle, Idaho: Idaho Geological Survey, Moscow Idaho; DWM-43, Scale: 1:100,000.

Kauffman, JD, Othberg, KL, Shervais, JW, Cooke, MF, 2005b, Geologic Map of the Shoshone Quadrangle, Lincoln County, Idaho: Idaho Geological Survey, Moscow Idaho; DWM-44, Scale: 1:24000.

Kelbert, A., Egbert, G.D. and deGroot-Hedlin, C., 2012. Crust and upper mantle electrical conductivity beneath the Yellowstone Hotspot Track. Geology, 40(5), pp.447-450.

Kelbert, A., Meqbel, N., Egbert, G.D. and Tandon, K., 2014. ModEM: A modular system for inversion of electromagnetic geophysical data. Computers & Geosciences, 66, pp.40-53.

Kennedy, B.M., and van Soest, M.C., 2007, Flow of Mantle Fluids through the Ductile Lower Crust: Helium Isotope Trends. Science, 318, (2007), 1433–1436.

Kessler, JA, Bradbury, KK, Schmitt, DR, Shervais, JW, Pulsipher, MA, Rowe, FE, Varriale, J, Evans, JP, 2017, Geology and In Situ Stress of the MH-2 Borehole, Idaho, U.S.A.: Insights into Western Snake River Plain Structure from Geothermal Exploration Drilling, Lithosphere, doi:10.1130/L609.1.

Kessler, JA, Schmitt, DR Chen, X, Evans, JP, Shervais, JW, 2017, Predicting Uniaxial Compressive Strength From Empirical Relationships Between Ultrasonic P-Wave Velocities, Porosity, and Core Measurements in a Potential Geothermal Reservoir, Snake River Plain, Idaho; 51st US Rock Mechanics/Geomechanics Symposium, 25-28 June, San Francisco, California, USA, 9 pp.

Kreemer, C., Blewitt, G. and Klein, E.C., 2014. A geodetic plate motion and Global Strain Rate Model. Geochemistry, Geophysics, Geosystems, 15(10), pp.3849-3889.

Krieger, L. and Peacock, J.R., 2014. MTpy: A Python toolbox for magnetotellurics. Computers & geosciences, 72, pp.167-175.

Krieger, L., and Peacock, J.R., 2014, MTpy: a Python toolbox for magnetotellurics. Computers & Geoscience, 72, 167-175.

Kuntz, M. A., 1992, A model-based perspective of basaltic volcanism, eastern Snake River plain, Idaho, in Link, Kuntz, and Platt, eds., Regional geology of eastern Idaho and western Wyoming, Memoir 179: Boulder, Co, Geological Society of America, p. 289-304.

Lachmar, T.E., Freeman, T.G., Kessler, J.A., Batir, J.F., Evans, J.P., Nielson, D.L., Shervais, J.W., Chen, X., Schmitt, D.R., and Blackwell, D.D., 2019, Evaluation of the geothermal potential of the western Snake River Plain based on a deep corehole on the Mountain Home AFB near Mountain Home, Idaho. Geothermal Energy 7, 26. https://doi.org/10.1186/s40517-019-0142-7

Lachmar, TE, Freeman, TG, Sant, CJ, Walker, JR, Batir, JF, Shervais, JW, Evans, JP, Nielson, DL, Blackwell, DD, 2017, Effect of an 860-m thick, cold, freshwater aquifer on geothermal potential along the axis of the eastern Snake River Plain, Idaho. Geothermal Energy, 5:28, https://doi.org/10.1186/s40517‑017‑0086‑8.

Lachmar, TL, Freeman, T., Shervais, JW, Nielson, DE, 2012, Preliminary Results: Chemistry and Thermometry of Geothermal Water from MH-2B Test Well. Geothermal Resources Council Transactions, vol. 36, 689-692.

Lewis RE, and HW Young, 1989, The Hydrothermal System in Central Twin Falls County, Idaho, USGS Water-Resources Investigations Report 88-4152, 44 pages.

Lewis, R.E. and Stone, M.A.J., Geohydrologic data from, a 4,403-foot geothermal test hole, Mountain Home Air Force Base, Elmore County, Idaho: USGS Open-file report 88-166, 30 p (1988).

Lewis, R.E. and Young, H.W., 1982. Geothermal Resources in the Banbury Hot Springs Area, Twin Falls County, Idaho (No. 2186). United States Dept. of the Interior, Geological Survey.

Liberty, L.M., W.P. Clement, and M.D. Knoll, 1999, Surface and borehole seismic characterization of the Boise Hydrogeophysical Research Site, Proc. Environmental and Engineering Geophysical Society, 723-732.

Liberty, LM, Schmitt, DR, and Shervais, JW, 2015, Seismic imaging through the volcanic rocks of the Snake River Plain: Insights from Project Hotspot. Geophysical Prospecting, DOI: 10.1111/1365-2478.12277.

Lindholm, G.F., 1996, Summary of the Snake River regional aquifer-system analysis in Idaho and eastern Oregon: U.S. Geological Survey Professional Paper 1408-A, 59 p.

Link, PK and L. L. Mink, LL (editors), 2002, Geology, hydrogeology, and environmental remediation: Idaho National Engineering and Environmental Laboratory, Eastern Snake River Plain, Idaho: Geological Society of America Special Paper 353, Boulder, 316 pp.

Machette, M.N., Haller, K.M., Dart, R.L., Rhea, S.B., 2003, Quaternary fault and fold database of the United States: U.S. Geological Survey Open-File Report 03-417, http://qfaults.cr.usgs.gov/faults/.

Mansure, A. J. and Blankenship, D. A.: Geothermal well cost update 2011, Transactions, GRC, 35, (2011) 189-192.

Mansure, A. J and Blankenship, D. A., 2013, Geothermal well cost update 2013, Geothermal Resources Council Transactions, 17, 2013, 437-442.

McCafferty, A.E., Kucks, R.P., Hill, P.L., Racey, S.D., 1999, Aeromagnetic Map for The State of Idaho, U.S. Geological Survey Open-File Report 99-371. http://pubs.usgs.gov/of/1999/ofr-99-0371/idaho.html

McCurry, M, Hackett, WR, Hayden, K, 1999, Cedar Butte and cogenetic Quaternary rhyolite domes of the eastern Snake River Plain, in Guidebook to the geology of eastern Idaho: Idaho. Idaho Museum of Natural History, 169-179.

McCurry, M, Welhan, J, Polun, S, Autenrieth, Rodgers, DW, 2011, Geothermal potential of the Blackfoot Reservoir-Soda Springs volcanic field: hidden geothermal resource and natural laboratory in SE Idaho. Geothermal Resources Council Transactions 35:917-924.

McCurry, M., and Welhan, J., 2012, Do Magmatic-Related Geothermal Energy Resources Exist in Southeast Idaho? GRC Transactions, Vol. 36, 2012.

McCurry, M., Hayden, K.P., Morse, L.H., and Mertzman, S., 2008. Genesis of post-hotspot, A-type rhyolite of the Eastern Snake River Plain volcanic field by extreme fractional crystallization of olivine tholeiite. Bulletin of Volcanology 70: 361-383.

McCurry, M., Pearson, DM, Welhan, J, Natwotniak, SK, and Fisher, M., 2015, Origin and Potential Geothermal Significance of China Hat and Other Late Pleistocene Topaz Rhyolite Lava Domes of the Blackfoot Volcanic Field, SE Idaho. Geothermal Resources Council Transactions 39, 2-5.

McIntyre, DH, 1979, Preliminary description of Anschutz Federal No. 1 Drill Hole, Owyhee County, Idaho. USGS Open File Report OFR 79-651, 15 pp.

McLing, T.L., R.W. Smith and T.M. Johnson, 2002, Chemical characteristics of thermal water beneath the eastern Snake River Plain, in Link, P.K., and Mink, L.L., (eds.), Geology, Hydrogeology, and Environmental Remediation: Idaho National Engineering and Environmental Laboratory, Eastern Snake River Plain, Idaho: Geological Society of America Special Paper 353, 2002), 205–211.

McLing, T.L., Smith, R.P., Smith, R.W., Blackwell, D.D., Roback, R.C., and Sondrup, A.J., 2016, Wellbore and groundwater temperature distribution eastern Snake River Plain, Idaho: Implications for groundwater flow and geothermal potential. Journal of Volcanology and Geothermal Research, 320, 144-155.

Melosh, G., 2015. Geothermal well targeting method using structural irregularities. In Proceedings, 40th Workshop on Geothermal Reservoir Engineering, Stanford University, Stanford, CA.

Mink, L.L., 2010, Camas Creek Ranch Geothermal Assessment Preliminary Report. (unpublished).

Mitchell, JC, 1981, Geological, Hydrological, Geochemical and Geophysical Investigations of the Nampa-Caldwell And Adjacent Areas, Southwestern Idaho. Geothermal Investigations in Idaho, Idaho Department of Water Resources, Water Information Bulletin No. 30.

Moeck I.S., Hinz, N., Faulds J., Bell J., Kell-Hills A., Louie J., 2010, 3D geological mapping as a new method in geothermal exploration: a case study from central Nevada. Geothermal Resources Council Transactions 34, 807-812

Moeck, I.S., 2014, Catalog of geothermal play types based on geologic controls, Renewable and Sustainable Energy Reviews, 37, 867-882.

Morris, A., Ferrill, D.A., Henderson, D.B., 1996, Slip-tendency analysis and fault reactivation. Geology 24, 275–278.

Morse, L.H., and McCurry, M., 2002, Genesis of alteration of Quaternary basalts within a portion of the eastern Snake River Plain Aquifer. In Link, P.K., and Mink, L.L., Eds.), Geology, Hydrogeology, and Environmental Remediation; Idaho National Engineering and Environmental Laboratory, Eastern Snake River Plain, Idaho. GSA Special Paper, 353:213–224.

Nathenson, M, TC Urban, WH Diment, and NL Nehring, 1980, Temperatures, heat flow, and water chemistry from drill holes in the Raft River geothermal system, Cassia County, Idaho, U.S. Geol. Survey Open-File Report. 80-2001, 29 pp., 1980.

Neely, KW and Galinato, G, 2007, Geothermal power generation in Idaho: an overview of current developments and future potential, Open File Report, Idaho Office of Energy Resources, 18 pp.

Neely, KW, 1996, Production history for the four geothermal district heating systems in Boise, Idaho, Geothermal Resources Council Transactions, vol. 20, pp. 137-144.

Neupane, G., E.D. Mattson, T.L. McLing, C.D. Palmer, R.W. Smith, T.R. Wood, 2014, Deep Geothermal Reservoir Temperatures in the Eastern Snake River Plain, Idaho using Multicomponent Geothermometry. Proceedings, Thirty-Eighth Workshop on Geothermal Reservoir Engineering Stanford University, Stanford, California, Feb 24-26, 2014 SGP-TR-202.

Neupane, G., Mattson, E.D., Spycher, N., Dobson, P.F., Conrad, M.E., Newell, D.L., McLing, T.L., Wood, T.R., Cannon, C.J., Atkinson, T.A., Brazell, C.W., and Worthing, W.C., 2017, Geochemical evaluation of the geothermal resources of Camas Prairie, Idaho. Proceedings, 42nd Workshop on Geothermal Reservoir Engineering, Stanford University, Feb 13-15, 2017.

Nielson, D.L., 1993, The temperature-volume relationship in convective hydrothermal systems: Geothermal Resources Council Transaction, 17, 437-442.

Nielson, DL and Shervais, JW, 2014, Conceptual Model for Snake River Plain Geothermal Systems. Proceedings Thirty-Ninth Workshop on Geothermal Reservoir Engineering Stanford University, Stanford, California, February 24-26, 2014 SGP-TR-202.

Nielson, DL, Atkinson TA, and Shervais JW, 2018, Evaluation of the Mountain Home AFB Geothermal System for the Play Fairway Project. Proceedings, 43rd Workshop on Geothermal Reservoir Engineering, Stanford University, Stanford, California, February 12-14, 2018, SGP-TR-213.

Nielson, DL, Shervais, JW, Evans, JP, Liberty, L, Garg, SK, Glen, J., Visser, C., Dobson, P, Gasperikova, E. and Sonnenthal, E., 2015, Geothermal Play Fairway Analysis of The Snake River Plain, Idaho. Proceedings Fortieth Workshop on Geothermal Reservoir Engineering, Stanford University, Stanford, California, January 26-28, 2015 SGP-TR-204.

Nielson, DL, Sonnenthal, E., Shervais JW and Garg, SK, 2017, Mafic Heat Sources for Snake River Plain Geothermal Systems. Proceedings, 42nd Workshop on Geothermal Reservoir Engineering, Stanford University, Stanford, California, February 13-15, 2017, SGP-TR-212.

Nielson, DL., Delahunty, C., and Shervais, JW, 2012, Geothermal Systems in the Snake River Plain, Idaho, Characterized by the Hotspot Project. Geothermal Resources Council Transactions, v36, 727-730.

Noorollahi, Y., Itoi, R., Fujii, H. and Tanaka, T., 2008. GIS integration model for geothermal exploration and well siting. Geothermics, 37(2), pp.107-131.

Paillet, F.L., 1999, Geophysical reconnaissance in bedrock boreholes--finding and characterizing the hydraulically active fractures, in Morganwalp, D.W. and Buxton, H.T., eds., U.S. Geological Survey Toxic Substances Hydrology Program--Proceedings of the Technical Meeting, Charleston, South Carolina, March 8-12, 1999: U.S. Geological Survey Water-Resources Investigations Report 99-4018C, v. 3, p. 725-733.

Paillet, F.L., 2000, Using borehole wireline methods to delineate fracture flow paths in bedrock formations (Chapter 7), in Inyang, H.I., and Bruell, C.J., eds., Remediation in rock masses: Reston Vir., American Society of Civil Engineers.

Plamer, C.D., Ohly, S.R., Smith, R.W., Neupane, G., McLing, T. and Mattson, E., 2015. Mineral selection for multicomponent equilibrium geothermometry. Transactions-Geothermal Resources Council, 38(INL/JOU-15-34930).

Payne, S.J., McCaffrey, R., King, R.W. and Kattenhorn, S.A., 2012, A new interpretation of deformation rates in the Snake River Plain and adjacent basin and range regions based on GPS measurements, Geophysical Journal International, Volume 189, Issue 1, pages 101–122; DOI: 10.1111/j.1365-246X.2012.05370.x

Payne, SJ, McCaffrey, R and King, RW, 2008, Strain rates and contemporary deformation in the Snake River Plain and surrounding Basin and Range from GPS and seismicity. Geological Society of America Bulletin 36(8): 647-650.

Peng, X and ED Humphreys, 1998, Crustal velocity structure across the eastern Snake River plain and the Yellowstone Swell. Journal of Geophysical Research, B, Solid Earth and Planets 103(4): 7171-7186.

Phillips, WM, and Welhan, JA, 2006, Geologic Map of the Idaho Falls North Quadrangle, Bonneville County, Idaho. Idaho Geological Survey, Digital Web Map DWM-77, 1:24,000.

Phillips, WM, and Welhan, JA, 2011, Geologic Map of the Idaho Falls South Quadrangle, Bingham and Bonneville County, Idaho. Idaho Geological Survey, Digital Web Map DWM-78, 1:24,000.

Potter, K.E., Champion, D.E., Duncan, R.A., and Shervais, J.W., 2019, Volcanic stratigraphy and age model of the Kimama deep borehole (Project Hotspot): Evidence for 5.8 million years of continuous basalt volcanism, central Snake River Plain, Idaho: Geosphere, 15, 1–23, doi.org/10.1130/GES01679.1.

Potter, K.E.; Bradshaw, R., Sant, C.J., King, J., Shervais, J.W., and Christiansen, E.H., 2011, Project Hotspot: Insight into the Subsurface Stratigraphy and Geothermal Potential of the Snake River Plain. Geothermal Resources Council Transactions, vol. 35, 967-971.

Potter, KA, Shervais, JW, Christiansen, EH, and Vetter, SK, 2018, Evidence for cyclical fractional crystallization, recharge, and assimilation in basalts of the Kimama drill core, central Snake River Plain, Idaho: 5.5-million-years of petrogenesis in a mid-crustal sill complex. Frontiers in Earth Science, doi.org/10.3389/feart.2018.00010.

Powell, T. and Cumming, W., 2010, February. Spreadsheets for geothermal water and gas geochemistry. In Proceedings (pp. 4-6).

Pribnow, D.F., Schütze, C., Hurter, S.J., Flechsig, C. and Sass, J.H., 2003. Fluid flow in the resurgent dome of Long Valley Caldera: implications from thermal data and deep electrical sounding. Journal of Volcanology and Geothermal Research, 127(3-4), pp.329-345.

Pritchett, J.W., 2011, STAR User's Manual Version 11.0. Leidos Inc., San Diego, CA (2011).

Prodehl, C., 1979. Crustal structure of the western United States - a reinterpretation of seismic-refraction measurements from 1961 to 1963 in comparison with the crustal structure of central Europe. U.S. Geol. Survey Prof. Paper 1034, 74 pp.

Putirka, K, Kuntz, M, Unruh, D, and Vaid, N, 2009, Magma Evolution and Ascent at the Craters of the Moon and Neighboring Volcanic Fields, Southern Idaho, USA: Implications for the Evolution of Polygenetic and Monogenetic Volcanic Fields: Journal of Petrology, v. 50, no. 9, p. 1639-1665.

Robertson-Tait, A., Lutz, S.J., Sheridan, J., and Morris, C.L. (2004), Selection of an interval for massive hydraulic stimulation in well DP 23-1, Desert Peak East EGS project, Nevada, Proceedings, 29th Workshop on Geothermal Reservoir Engineering, Stanford University, Stanford CA, SGP-TR-175.

Ryan, M.P., 1987. Neutral buoyancy and the mechanical evolution of magmatic systems. Magmatic process: physicochemical principles, pp.259-287.

Sant, Christopher J. and John W. Shervais, 2011, Project Hotspot: Preliminary Analysis of Secondary Mineralization in Basaltic Core, Central Snake River Plain. Geothermal Resources Council Transactions, vol. 35, 987-989.

Schmitt, A.K. and Hulen, J.B., 2008. Buried rhyolites within the active, high-temperature Salton Sea geothermal system. Journal of Volcanology and Geothermal Research, 178(4), pp.708-718.

Schmitt, DR, Liberty, LM, Kessler, JE, Kück, J., Kofman, R., Bishop, R., Shervais, JW, Evans, JP, Champion, DE. 2012, The ICDP Snake River Geothermal Drilling Project: Preliminary overview of borehole geophysics. Geothermal Resources Council Transactions, v36., 1017-1022.

Shell Exploration & Production, 2013, Play Based Exploration Guide. Graphics Media and Publishing Services (GMP), Rijswijk, Netherlands.

Sherman, FB, 1982, Characterization of the geothermal resources of southeastern Idaho, pp. 76-87, in Geothermal Direct Heat Program Roundup Technical Conference Proceedings, ed. C. A. Ruscetta, Earth Sci. Lab., Univ. of Utah, DOE/ID/12079-71.

Shervais, J. W., Glen, J. M., Liberty, L. M., Dobson, P., Gasperikova, E., Sonnenthal, E., Visser, C., Nielson, D., Garg, S., Evans, J. P., Siler, D., DeAngelo, J., Athens, N., Burns, E., 2015, Snake River Plain Play Fairway Analysis - Phase 1 Report. Geothermal Resources Council Transactions, v39, 761-769.

Shervais, J.W., and Hanan, B.B., 2008, Lithospheric topography, tilted plumes, and the track of the Snake River-Yellowstone Hotspot, Tectonics, 27, TC5004, doi:10.1029/2007TC002181.

Shervais, J.W., Branney, M.J., Geist, D.J., Hanan, B.B., Hughes, S.S., Prokopenko, A.A., Williams, D.F., 2006a, HOTSPOT: The Snake River Scientific Drilling Project – Tracking the Yellowstone Hotspot Through Space and Time. Scientific Drilling, no 3, 56-57. Doi:10.2204/iodp.sd.3.14.2006.

Shervais, J.W., Evans, J.P., Glen, J.M., DeAngelo, J., Dobson, P., Gasperikova, E., Sonnenthal, E., Siler, D., Liberty, L.M., Visser, C., Nielson, D.L., Garg, S., Athens, N., Burns, E., 2016, Snake River Plain Play Fairway Analysis: Phase 1 Final Report, Report to Department of Energy Geothermal Technology Office, Project number DE-EE 0006733, January 2016, 171 pp.

Shervais, J.W., Kauffman, J.D., Gillerman, V.S., Othberg, K.L., Vetter, S.K., Hobson, V.R., Meghan Zarnetske, M., Cooke, M.F., Matthews, S.H., and Hanan, B.B., 2005, Basaltic Volcanism of the Central and Western Snake River Plain: A Guide to Field Relations Between Twin Falls and Mountain Home, Idaho; in J. Pederson and C.M. Dehler, Guide to Field trips in the western United States, Field Guide volume 6, Geological Society of America, Boulder Colorado, 26 pages.

Shervais, J.W., Kauffman, J.D., Gillerman, V.S., Othberg, K.L., Vetter, S.K., Hobson, V.R., Meghan Zarnetske, M., Cooke, M.F., Matthews, S.H., and Hanan, B.B., 2005, Basaltic Volcanism of the Central and Western Snake River Plain: A Guide to Field Relations Between Twin Falls and Mountain Home, Idaho; in J. Pederson and C.M. Dehler, Guide to Field trips in the western United States, Field Guide volume 6, Geological Society of America, Boulder Colorado, 26 pages.

Shervais, J.W., Shroff, G., Vetter, S.K., Matthews, S., Hanan, B.B., and McGee, J.J., 2002, Origin of the western Snake River Plain: Implications from stratigraphy, faulting, and the geochemistry of basalts near Mountain Home, Idaho. in Bill Bonnichsen, C.M. White, & Michael McCurry (eds) Tectonic and Magmatic Evolution of the Snake River Plain Volcanic Province, Idaho Geological Survey Bulletin 30, Moscow, Idaho, 343-361.

Shervais, J.W., Vetter, S.K. and Hanan, B.B., 2006, A Layered Mafic Sill Complex beneath the Eastern Snake River Plain: Evidence from Cyclic Geochemical Variations in Basalt, Geology, v. 34, 365-368. https://doi.org/10.1130/G22226.1

Shervais, J.W., Vetter, S.K. and Hanan, B.B., 2006b, A Layered Mafic Sill Complex beneath the Eastern Snake River Plain: Evidence from Cyclic Geochemical Variations in Basalt, Geology, v. 34, 365-368.

Shervais, J.W., Vetter, S.K., and Hackett, W.R., 1994, Chemical Stratigraphy of Basalts in Coreholes NPR-E and WO-2, Idaho National Engineering Laboratory, Idaho: Implications for Plume Dynamics in the Snake River Plain, in Proceedings of the VIIth International Symposium on the Observation of Continental Crust Through Drilling, Santa Fe, New Mexico, 1994, 93-96.

Shervais, JW and Vetter, SK, 2009, High-K Alkali Basalts of the Western Snake River Plain: Abrupt Transition from Tholeiitic to Mildly Alkaline Plume-Derived Basalts, Western Snake River Plain, Idaho, Journal of Volcanology and Geothermal Research, doi:10.1016/j.jvolgeores.2009.01.023.

Shervais, JW, Evans, JP, Christiansen, EH, Schmitt, DR, Kessler, JA, Potter, KE, Jean, MM, Sant, CJ, Freeman, TG, 2011, Project Hotspot – The Snake River Scientific Drilling Project. Geothermal Resources Council Transactions, vol. 35, 995-1003.

Shervais, JW, Glen, JM, Nielson, DL, Garg, S, Dobson, P, Gasperikova, E, Sonnenthal, E, Visser, C, Liberty, LM, DeAngelo, J, Siler, D, Varriale, J, and Evans, JP, 2016, Geothermal Play Fairway Analysis of the Snake River Plain Volcanic Province: Phase 1. Proceedings Forty-First Workshop on Geothermal Reservoir Engineering, Stanford University, Stanford, California, February 22-24, 2016 SGP-TR-209.

Shervais, JW, Glen, JM, Nielson, DL, Garg, S, Liberty, LM, Siler, D, Dobson, PF, Gasperikova, E, Sonnenthal, E, Neupane, G, DeAngelo, J, Newell, DL, Evans, JP, Snyder, N. 2017, Geothermal Play Fairway Analysis of the Snake River Plain: Phase 2. Geothermal Resources Council Transactions, v41, 2352-2369.

Shervais, JW, Glen, JM, Siler, D, Deangelo, J, Liberty, LM, Nielson, DL, Garg, S, Neupane, G., Dobson, P, Gasperikova, E, Sonnenthal, E, Newell, DL, Evans, JP, Snyder, N, Mink, LL, 2018, Provisional Conceptual Model of the Camas Prairie (ID) Geothermal System from Play Fairway Analysis. Proceedings, 43rd Workshop on Geothermal Reservoir Engineering, Stanford University, Stanford, California, February 12-14, 2018, SGP-TR-213.

Shervais, JW, Glen, JM, Siler, D, Liberty, LM, Nielson, DL, Garg, S, Dobson, P, Gasperikova, E, Sonnenthal, E, Newell, DL, Evans, JP, Deangelo, J, Peacock, J, Earney, T, Schermerhorn, W., Neupane, G., 2020. Play Fairway Analysis in Geothermal Exploration: The Snake River Plain Volcanic Province. Proceedings, 45th Workshop on Geothermal Reservoir Engineering, Stanford University, Stanford, California, February 10-12, 2020, SGP-TR-216.

Shervais, JW, Nielson, DL, Evans, JP, Lachmar, T, Christiansen, EH, Morgan, L., Shanks, WCP, Delahunty, C, Schmitt, DR, Liberty, LM, Blackwell, DD, Glen, JM, Kessler, JE, Potter, KE, Jean, MM, Sant, CJ, Freeman, TG., 2012, Hotspot: The Snake River Geothermal Drilling Project -- Initial Report. Geothermal Resources Council Transactions, v36., 767-772.

Sibson, H., 1996, Structural permeability of fluid-driven fault-fracture. J. Struct. Geol. 18, 1031–1042.

Sibson, R.H., 1994, Crustal stress, faulting and fluid flow, in: Parnell, J. (Ed.), Geofluids: Origin, Migration and Evolution of Fluids in Sedimentary Basins. Geological Society, London, Special Publications. 69–84.

Siler, D.L. and Kennedy, B.M., 2016, Regional crustal-scale structures as conduits for deep geothermal upflow. Geothermics 59, 27-37, https://doi.org/10.1016/j.geothermics.2015.10.007.

Siler, D.L., Zhang, Y., Spycher, N.F., Dobson, P.F., McClain, J.S., Gasperikova, E., Zierenberg, R.A., Schiffman, P., Ferguson, C., Fowler, A., and Cantwell, C., 2017, Play-fairway analysis for geothermal resources and exploration risk in the Modoc Plateau region. Geothermics, 69, 15-33.

Smith, R.L., and H.R. Shaw, 1975, Igneous-related geothermal systems, Assessment of Geothermal Resources of the United States – 1975. edited by D.E. White and D.L. Williams, U.S. Geol. Survey Circ. 726, 58-83.

Smith, R. B., Jordan M, Steinberger, B., Puskas, CM, Farrell, J., Waite, GP, Husen, S. Chang, W.L., O'Connell, J, 2009, Geodynamics of the Yellowstone hotspot and mantle plume: seismic and GPS imaging, kinematics, mantle flow: Jour. Volcanology and Geothermal Research 188 (2009), 26-65.

Smith, RP, 2004, Geologic setting of the Snake River Plain Aquifer and vadose zone. Vadose Zone Journal 3:47-58.

Sonnenthal, E.L., Spycher, N., Xu, T., Zheng, L., Miller, N., Pruess, K. (2014). TOUGHREACT V3.0-OMP, http://esd.lbl.gov/research/projects/tough/software/toughreact.html.

Sparlin, MA, Braile, LW, and Smith, RB, 1982, Crustal structure of the eastern Snake River Plain determined from ray trace modeling of seismic refraction data, Journal of Geophysical Research, 87, 2619-2633.

Spear, D.B. and King, J.S., 1982. The geology of Big Southern Butte, Idaho. Cenozoic geology of Idaho: Idaho Bureau of Mines and Geology Bulletin, 26, pp.395-403.

Spycher, N., Peiffer, L., Sonnenthal, E., Saldi, G., Reed, M.H., and Kennedy, B.M., 2014, Integrated multicomponent solute geothermometry. Geothermics, v. 51, p. 113-123.

Stanley, W.D., 1982. Magnetotelluric soundings on the Idaho National Engineering Laboratory facility, Idaho. Journal of Geophysical Research: Solid Earth, 87(B4), pp.2683-2691.

Street, L.V., 1990, Geothermal resource analysis in the Big Wood River Valley, Blaine County, Idaho. IDWR Water Information Bulletin No. 30, Part 17, 26 pages, 1 plate.

Street, LV and DeTar, RE, 1987, Geothermal resource analysis in Twin Falls County, Idaho; in Geothermal Investigations in Idaho, Idaho Dept. Water Resour., Water Info. Bull., 30 (15).

Street, LV and RE DeTar, 1987, Geothermal Resource Analysis in Twin Falls County, Idaho, IDWR Water Information Bulletin No. 30, Part 15, 46 pages.

Tanaka, T., 2008

Teplow, W., Marsh, B., Hulen, J., Spielman, P. Kaleikini, M. Fitch, D. and Rickard, W.: Dacite melt at the Puna Geothermal Venture wellfield, Big Island of Hawaii: Geothermal Resources Council Transactions 33 (2009) 989-994.

Tester, J., 2006, The Future of Geothermal Energy: Impact of Enhanced Geothermal Systems (EGS) on the United States in the 21st Century. Massachusetts Institute of Technology.

Tester, JW and MC Smith, 1977, Energy Extraction Characteristics of Hot Dry Rock Geothermal Systems. Proceedings of the Twelfth Intersociety Energy Conversion Engineering Conference, Washington, D.C. American Nuclear Society, 1:816.

Tester, JW, HD Murphy, CO Grigsby, R. M. Potter, and B.A. Robinson. 1989. Fractured Geothermal Reservoir Growth Induced by Heat Extraction. SPE J. Reservoir Engineering, 3:97104.

Townend, J., and Zoback, M. D., 2000, How faulting keeps the crust strong. Geology, v. 28, p. 399–402.

Trumpy, E., Donato, A., Gianelli, G., Gola, G., Minissale, A., Montanari, D., Santilano, A., Manzella, A., 2015, Data integration and favourability maps for exploring geothermal systems in Sicily, southern Italy. Geothermics, Volume 56, Pages 1-16. doi:10.1016/j.geothermics.2015.03.004

Vozoff, K., 1991, The magnetotellurics method. Investigations in Geophysics, 3, 2.

Walker, G. P. L., 1987, The dike complex of Koolau volcano, Oahu: internal structure of a Hawaiian rift zone, in Decker, R. W, Wright, T. L. and Stauffer, P. H. (eds.) Volcanism in Hawaii, USGS Professional Paper 1350, 961-993.

Walker, J. and Wheeler, J., 2016, The smectite to corrensite transition: X-ray diffraction results from the MH-2B core, western Snake River Plain, Idaho: Clay Minerals, 51, 691-696.

Ward, SH, Ross, HP, and Nielson, DL, 1981, Exploration strategy for high-temperature hydrothermal systems in the Basin and Range Province: American Association Petroleum Geologists Bulletin, 65/1, 86-102.

Welhan, J.A., 2016, Gigawatt-scale power potential of a magma-supported geothermal system in the fold and thrust belt of southeast Idaho. Proceedings, 41st Workshop on Geothermal Reservoir Engineering, Stanford, California, February 2016, SGP-TR-209, 13 p.

Welhan, J.A., Gwyunn, M., Payne, S., McCurry, M., Plummer, M. and Wood, T., 2014, February. The Blackfoot volcanic field, southeast Idaho: a hidden high-temperature geothermal resource in the Idaho thrust belt. In Proceedings of the 39th Workshop on Geothermal Reservoir Engineering Stanford University, Stanford, California, Vol. 2426.

White, C.M., 2007, The Graveyard Point intrusion: an example of extreme differentiation of Snake River Plain basalt in a shallow crustal pluton. Journal of Petrology 48, 303-325.

White, CM, WK Hart, B Bonnichsen, and D Matthews, 2002, Geochemical and Sr-isotopic variations in western Snake River Plain basalts, Idaho, in: Bonnichsen, B., White, C., and McCurry, M., eds., Tectonic and Magmatic Evolution of the Snake River Plain Volcanic Province: Idaho Geological Survey Bulletin 30, Moscow, ID, United States, p. 329-342.

Whitehead RL, and Lindholm GF, 1985, Results of Geohydrologic test drilling in the Eastern Snake River Plain, Gooding County, Idaho. US Geological Survey, Water–Resources Investigations Report 84–4294.

Whitehead, R.L., 1986. Geohydrologic framework of the Snake River Plain. Idaho and eastern Oregon: US Geological Survey Hydrologic Investigations Atlas HA-681, 3.

Whitehead, R.L., 1992. Geohydrologic framework of the Snake River Plain regional aquifer system, Idaho and eastern Oregon (No. 1408-B). US Government Printing Office.

Williams, C.F. and J. DeAngelo, 2008, Mapping Geothermal Potential in the Western United States. Geothermal Resources Council Transactions v. 32, 181-188.

Williams, C.F., and J. DeAngelo, 2011, Evaluation of approaches and associated uncertainties in the estimation of temperatures in the upper crust of the western United States. Geothermal Resources Council Transactions, v. 35, 1599-1605.

Williams, C.F., Reed, M.J., DeAngelo, J. and Galanis Jr, S.P., 2009. Quantifying the undiscovered geothermal resources of the United States. In Geothermal Resources Council 2009 Annual Meeting, Vol. 33.

Wilmarth, M. and Stimac, J., 2015. Power density in geothermal fields. Power, 19, p.25.

Wohletz. K. and Hieken, G., 1992, Volcanology and geothermal energy, University of California Press, 432 p.

Wood, S. H., 1994, Seismic expression and geological significance of a lacustrine delta in Neogene deposits of the western Snake River plain, Idaho, AAPG Bulletin, 78, 1, 102-121.

Wood, S.H. and Anderson, J.E., 1981. Part II: Geological, Hydrological, and geochemical and geophysical investigation of the Nampa-Caldwell and the adjacent areas, Southwestern Idaho. Geothermal Investigations in Idaho, Idaho Department of Water Resources.

Wood, S.H. and D.M. Clemens, 2002, Geologic and tectonic history of the western Snake River Plain, Idaho and Oregon, in: Bonnichsen B., White C., and McCurry M., eds., Tectonic and magmatic evolution of the Snake River Plain volcanic province, Idaho Geological Survey Bulletin 30. Moscow, ID, United States. p. 69-103.

Xu, T., N. Spycher, E. Sonnenthal, G. Zhang, L. Zheng, and K. Pruess (2011), TOUGHREACT Version 2.0: A simulator for subsurface reactive transport under non-isothermal multiphase flow conditions, Computers & Geosciences, 37(6), 763–774.

Young, H.W. and Lewis, R.E., 1982. Hydrology and geochemistry of thermal ground water in southwestern Idaho and north-central Nevada (No. USGS-PP-1044-J). Geological Survey, Boise, ID (USA).

Young, H.W., 1978, Water resources of Camas Prairie, south-central Idaho, U.S. Geological Survey, Water· Resources Investigations 78-82, Open File Report, 34 pp.

Young, H.W., 1985. Geochemistry and Hydrology of Thermal Springs in the Idaho Batholith and Adjacent Areas, Central Idaho. U.S. Geological Survey Water-Resources Investigations Report 85-4172, 44 pp.

Zierenberg, R.A., Schiffman, P., Barfod, G.H., Lesher, C.E., Marks, N.E., Lowenstern, J.B., Mortensen, A.K., Pope, E.C., Bird, D.K., Reed, M.H. and Friðleifsson, G.Ó., 2013. Composition and origin of rhyolite melt intersected by drilling in the Krafla geothermal field, Iceland. Contributions to Mineralogy and Petrology, 165(2), pp.327-347.

Zoback, M.D., Townend, J., 2001. Implications of hydrostatic pore pressures and high crustal strength for the deformation of intraplate lithosphere. Tectonophysics 336, 19–30. doi:10.1016/S0040-1951(01)00091-9.